

Zygmunt Kowalik<sup>1</sup> and John Luick<sup>2</sup>

# The Oceanography of Tides

Fairbanks, January, 2013

---

<sup>1</sup> University of Alaska Fairbanks

<sup>2</sup> Austides Consulting and South Australian Research and Development Institute

## Table of Contents

<b>Chapter I: Tidal forces</b>	5
1. Basics of celestial mechanics	5
2. Tide-producing forces	8
3. Equilibrium tides	13
4. The orbits of Earth and Moon	20
5. The harmonic constituents of the equilibrium tide	26
6. The origins of major tidal variations	34
7. Nodal phase	36
8. Longitude formulas	38
References	40
<b>Chapter II: Basic equations</b>	43
1. Rectangular and spherical system of coordinates	43
2. Total tidal potential	45
3. Energy equation	48
4. Free tidal waves in a channel	50
5. Energy considerations	53
5a. Energy flux	53
5b. Kinetic and potential energy	55
6. Free tidal waves in two-dimensional geometry	56
7. Kelvin wave	59
8. Sverdrup wave	62
9. Shelf waves	64
10. Tidal motion enhancement around islands and seamounts	66
10a. Trapped tidal motion around islands	68
10b. Residual tidal circulation around islands	70
References	74
<b>Chapter III: Tidal current</b>	77
1. Bottom boundary layer	77
2. Vertical changes in the eddy viscosity	81
3. Influence of the stratification	84
4. St. Lawrence Island region	88
5. Tidal data and comparison of full records against the vertically averaged model	91
6. Structure of temporal and vertical variability	95
7. Rotary spectra	98
8. Elliptical motion along the vertical direction	100
9. Tidal ellipses	101

10. Nonlinear effects in the tidal currents . . . . .	106
11. Nonlinear tidal interactions in the Sea of Okhotsk . . . . .	109
References . . . . .	117
<b>Chapter IV: Tide distribution and tidal power . . . . .</b>	<b>120</b>
1. Introduction . . . . .	120
2. Short description of tides in the World Ocean . . . . .	121
3. Short description of extreme tide ranges . . . . .	126
4. Rudimentary notions related to transfer of energy . . . . .	133
5. Tidal energy balance in local water bodies . . . . .	135
6. Tidal power from bays of high tidal energy . . . . .	140
7. Tidal power from the sea level difference . . . . .	142
8. Tidal power from currents . . . . .	147
8.1 The future of tidal power . . . . .	147
8.2 Power generation from currents . . . . .	149
9. Conclusion . . . . .	153
10. The last page from Gibrats Lenergie des marees . . . . .	154
11. Acknowledgements . . . . .	154
References . . . . .	155

# CHAPTER I: TIDAL FORCES

## 1. BASICS OF CELESTIAL MECHANICS

Newton's Second Law states a relationship between net force and acceleration  $F = ma$ . For a falling object at the surface of the earth, the acceleration due to the force of gravity is usually written  $g$ , so that

$$F = mg. \quad (\text{I.1})$$

Here  $g \approx 9.8 \frac{m}{s^2}$ , and  $m$  is the mass of the falling object.

Newton's Law of Gravitation is an expression of the mutual gravitational attraction between two masses,  $m_1$  and  $m_2$ . The attraction is proportional the product of the masses of the two bodies and inversely proportional to the square of the distance separating their centers of mass ( $l$ ). In the case of the falling object of mass  $m$ , and the earth, with mass  $M_e$ , we write

$$F_g = G \frac{M_e m}{l^2} \quad (\text{I.2})$$

Here  $G$  is the gravitational constant. At the earth's surface  $l = r_e$ , and Eqs (I.1) and (I.2) yield,

$$mg = G \frac{M_e m}{r_e^2} \quad (\text{I.3})$$

The **earth's mass** is  $5.97 \times 10^{24}$  kg, and the **earth's radius** is  $6.371 \times 10^6$  m. Therefore, from Eq (I.3), the magnitude of the **gravitational constant** follows:

$$G = 6.673 \times 10^{-11} \left( \frac{m^3}{kg \ s^2} \right). \quad (\text{I.4})$$

The masses of the sun and moon relative to earth are

$$\text{Sun } 333420; \quad \text{Earth } 1; \quad \text{Moon } \frac{1}{81.53};$$

Kepler's First Law states that the orbit of a planet is an **ellipse** with the sun located at one focus. Fig. I.1 depicts an ellipse with the sun (S) at one of the foci. Denoting the distance  $A'C = AC = a$  as the major semi-axis, the distance from the center (C) to the focus is  $ae$ . Then  $e = ae/a$  is called eccentricity of the ellipse. The distance of the planet from the sun is the shortest at **perihelion**

$$SA = a - ae = a(1 - e) \quad (\text{I.5a})$$

At **aphelion** (point  $A'$ ) the planet is at the longest distance from the sun,

$$SA' = a + ae = a(1 + e) \quad (\text{I.5b})$$

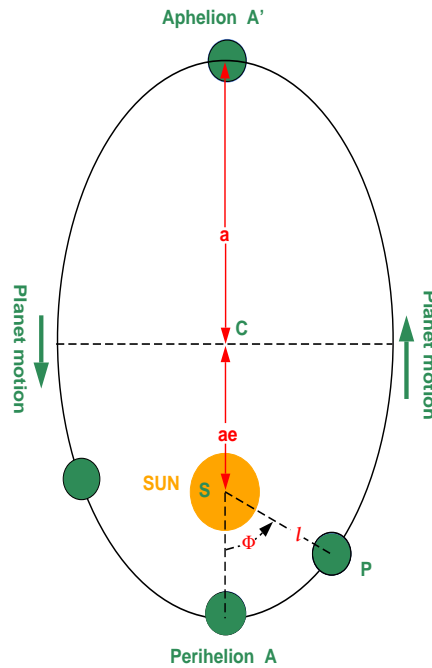


**Figure I.1**

**Elliptical orbits. Semi-major axis  $a$ , eccentricity  $e = ae/a$ ,  $l$  is the distance from the center of the sun (S) to the center of the planet (P),  $\phi$  is the true anomaly.**

The measured distances in eq(I.5a) and eq(I.5b) give for the **eccentricity of the Earth's orbit**  $e = 0.01674$ . Equation of an ellipse can be also written in the polar coordinates. Denoting distance from the focus (S) to the planet (P) as the radius vector  $l$  and the angle ASP (from perihelion counterclockwise) as  $\phi$ , we can write;

$$l = \frac{a(1 - e^2)}{1 + e \cos \phi} \quad (\text{I.6})$$

The angle  $\phi$  is often called the **true anomaly** of the planet. For  $\phi = 0^\circ$  (perihelion)  $l$  is equal to eq(I.5a) and for  $\phi = 180^\circ$  (aphelion),  $l$  is equal to eq(I.5b).

Consider polar coordinates  $(l, \phi)$  given in Fig. I.2. Setting the origin of coordinates at the center of the sun, the radius vector  $\vec{l}/l$  is directed from the sun to the planet. Vector  $\vec{s}$  denotes direction along the planet's path and vector  $\vec{n}$  is normal to  $s$ . To define components of velocity let the planet P travels a small distance  $ds$  along the arc from the point 1 to the point 2.

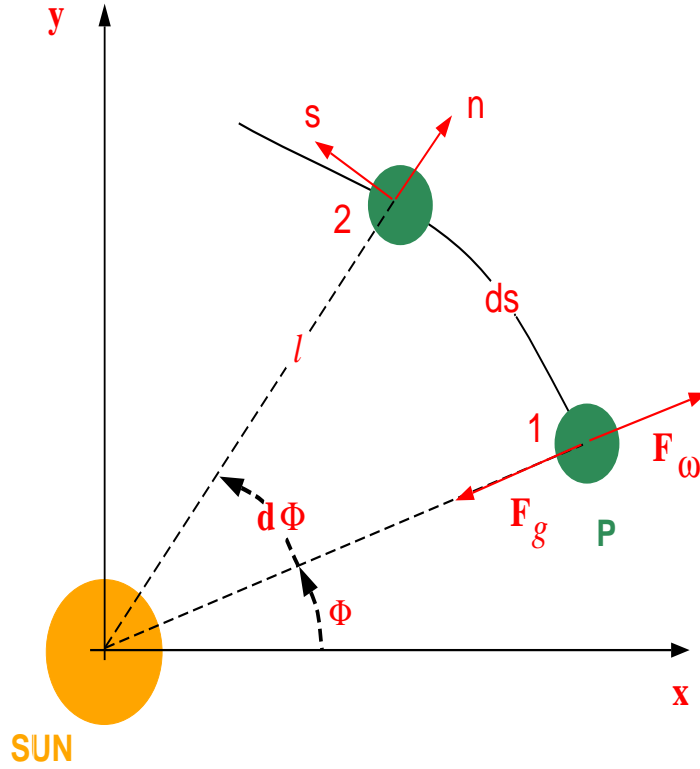


**Figure I.2**

**System of coordinates for the rotating planet. Center of coordinate located at the sun.  $l$  is radius vector,  $ds$  is the element of the orbit and  $d\phi$  is the angle related to  $ds$ .  $F_g$  is force of attraction and  $F_\omega$  is centrifugal force.**

Components of the velocity vector  $\vec{v} = \frac{d\vec{l}}{dt}$  along the tangential and normal directions can be defined as,

$$v_s = l \frac{d\phi}{dt} = v \quad v_n = 0 \quad (\text{I.7a})$$

and the components of acceleration vector  $\frac{d^2\vec{l}}{dt^2}$  are,

$$\frac{dv_s}{dt} = \frac{dv}{dt} \quad \frac{dv_n}{dt} = \frac{v^2}{l} \quad (\text{I.7b})$$

Setting  $M_s$  as the mass of the sun and  $M_p$  that of a planet, the force of attraction expressed by eq(I.2) can be written in the vector form as,

$$\vec{F}_g = -G \frac{M_s M_p}{l^2} \frac{\vec{l}}{l} \quad (\text{I.8})$$

Using above defined expression for the acceleration along the direction normal to the planet's arc the centrifugal force is

$$\vec{F}_\omega = M_p \frac{v^2}{l} \frac{\vec{l}}{l} \quad (\text{I.9})$$

To gain insight into the second Kepler law which states that the radius vector from the sun to the planet describes equal areas in equal times; we specify the moment of force. Introducing moment of the force  $\vec{N}$  as the vector product of the force  $\vec{F}_g$  and the radius vector

$$\vec{N} = \vec{l} \times \vec{F}_g \quad (\text{I.10})$$

it follows that  $\vec{N} = 0$ , since both force and radius vector are parallel.

For the planet in its motion around the sun the vector sum of the two forces ought to be zero,

$$M_p \frac{d^2 \vec{l}}{dt^2} - G \frac{M_s M_p}{l^2} \frac{\vec{l}}{l} = 0 \quad (\text{I.11})$$

Vector product of this equation by radius vector  $\vec{l}$  yields

$$M_p \vec{l} \times \frac{d^2 \vec{l}}{dt^2} = 0 \quad \text{and therefore} \quad M_p \vec{l} \times \frac{d\vec{l}}{dt} = \text{Const} \quad (\text{I.12})$$

Since the angular momentum of planet is constant it will be easy to conclude that the areal velocity is constant as well. Eq(I.12) leads to the following results

$$M_p |l| \left| l \frac{d\phi}{dt} \right| \sin(90^\circ) = M_p l^2 \frac{d\phi}{dt} = \text{Const} \quad (\text{I.13})$$

Introducing polar coordinates as in Fig. I.2, with the radius  $l$  and the polar angle  $\phi$ , the element of surface is

$$ds = \frac{1}{2} l^2 d\phi \quad (\text{I.14})$$

or differentiating above equation with respect to time it follows from eq(I.13) that,

$$2 \frac{ds}{dt} = l^2 \frac{d\phi}{dt} = \text{Const} \quad (\text{I.15})$$

Thus the law of angular momentum leads to conclusion that planets move with the constant areal velocity. Which in turn confirm well known observations that linear velocity along the orbit of the planet is variable with the largest velocity at perihelion (shortest radius vector) and smallest at aphelion (see Fig. I.1).

## 2. TIDE-PRODUCING FORCES

Tides are oscillations of the ocean caused by gravitational forces of the sun and earth. Although the nature of the tide generating forces is well understood the details of the tidal phenomena in the various water bodies require knowledge of the wide range of variables including bathymetry and frictional forces. To simplify consideration we shall make assumption that the tidal phenomenon is dominated by the moon. As is well known the centers of gravity of earth and of moon are moving around the **common center of gravity (barycentre)**. Actually, this system is a twin planets system moving around the common center. Barycentre, due to the difference of the mass of earth and moon, is located approximately 3/4 of the earth's radius from the earth center. To find the position

of the common center lets use Fig. I.3 and denote the distance from the common center to the center of the earth as  $r_{oe}$  and to the center of the moon as  $r_{om}$ .

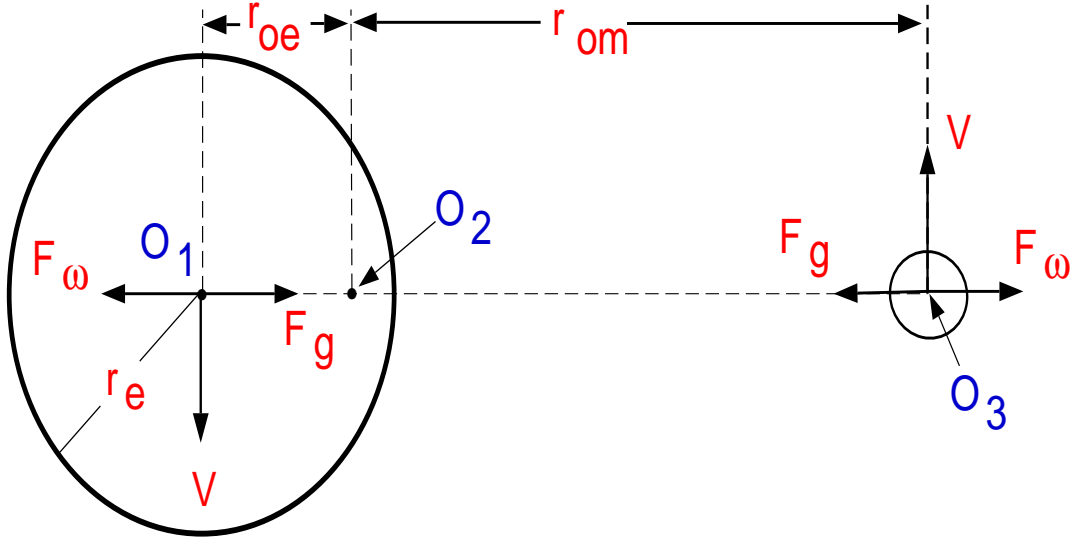


**Figure I.3**

**Earth-moon interaction.  $O_2$  location of the common center of mass.  $V$  tangential velocity to the trajectory.**

The coordinate of the barycentre  $r_c$  are defined as,

$$r_c(M_m + M_e) = r_1M_e + r_2M_m \quad (\text{I.16})$$

Setting the origin of the coordinates at the center of the earth, yields  $r_c = r_{oe}$ ,  $r_1 = 0$ ,  $r_2 = l = r_{oe} + r_{om}$ , therefore, eq(I.16) simplifies to

$$r_{oe} = \frac{M_m l}{M_m + M_e} \quad (\text{I.17})$$

The mean distance between the center of the earth and the center of the moon is close to 60 earth radii,  $l = 60.3r_e$ . Since  $M_e = 81.53M_m$ , from eq(I.17)  $r_{oe} = r_e 60/82$ .

The earth and moon are locked in the motion, rotating with the period of one month. The earth-moon system is kept in the dynamical equilibrium by two forces. One of them is the centrifugal force:

$$F_\omega = M \frac{V^2}{r_o} \quad (\text{I.18})$$

Here  $M$  is the mass of earth or the moon,  $V$  is the velocity of the earth or moon and  $r_o$  is the radius of the orbit either of the earth ( $r_o = r_{oe}$ ) or the orbit of the moon ( $r_o = r_{om}$ )

(see Fig. I.3). The second force ( $F_g$ ) is the force of gravitational attraction. For the earth-moon system it is expressed as:

$$F_g = G \frac{M_e M_m}{l^2} \quad (\text{I.19})$$

Here  $l = r_{oe} + r_{om}$  is the time-dependent distance between the center of the earth and the center of the moon. For the system earth-moon to be in the equilibrium the vector sum of the two forces ought to be zero, both in the center of the earth and in the center of the moon (see Fig. I.3). Therefore,  $\vec{F}_\omega$  must be equal  $\vec{F}_g$ ,

$$\vec{F}_\omega = \vec{F}_g \quad (\text{I.20})$$

The rotational motion around common center of gravity is somewhat different from the motion described by a wheel. Earth and moon revolves around the common center without rotation through a simple translation. To explain this revolution without rotation we invoke geometrical interpretation given by [Darwin \(1901\)](#) and [Defant \(1960\)](#). Consider points  $A$  and  $B$  on the earth (Fig. I.4).

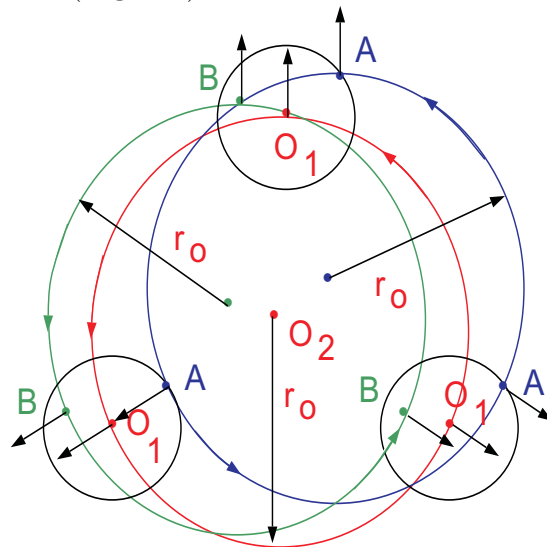


**Figure I. 4**

**Rotation around common center  $O_2$ . System of the centrifugal forces and circular orbits traced by points  $A$ ,  $B$ , and  $O_1$ .**

To simplify considerations and to make picture more lucid we shall move the barycentre  $O_2$  from inside the earth to the outside. The revolution of the earth around point  $O_2$  proceeds in such way that every particle located on earth describe a circle of the same radius  $r = r_o$  (Fig. I.4). Therefore, for each particle, accordingly to eq(I.20)

$$(F_\omega)_A = (F_\omega)_B = (F_\omega)_{O_1} = F_g \quad (\text{I.21})$$

Thus, every point in the revolving motion is subject to the equal and parallel centrifugal forces. Stability of the earth-moon system will require that the sum of all centrifugal and

attraction forces should be zero. While this statement is true for the centers of the earth and moon the balance does not occur in every point leading to the forces generating tides.

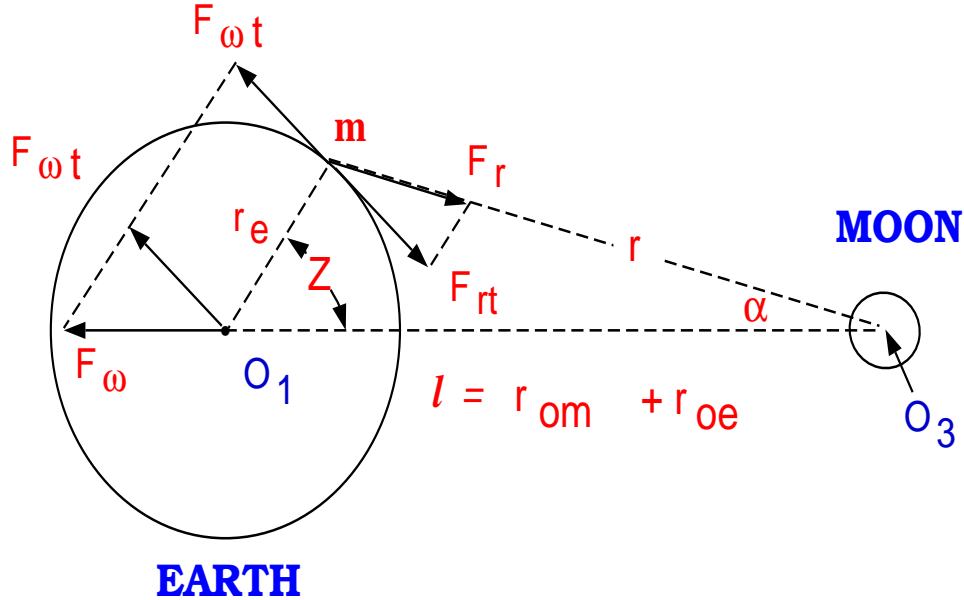


**Figure I.5**

**Earth-moon interaction. Forces acting on the mass  $m$  located on the surface of the earth.**

To find these forces let us consider a mass  $m$  located on the earth's surface (Fig. I.5). The centrifugal force  $F_\omega$  is the same for the every point on the earth and according to eq(I.21) is equal to the force of attraction which moon exerts on the mass ( $m$ ) located at the center of the earth;

$$F_\omega = F_g = G \frac{M_m m}{l^2} \quad (\text{I.22})$$

The force of the moon attraction acting on the mass  $m$  located on the earth's surface (see Fig.I.5) is

$$F_r = G \frac{M_m m}{r^2} \quad (\text{I.23})$$

Projection of these forces on the tangential direction to the earth's surface yield,

$$F_{\omega t} = G \frac{M_m m}{l^2} \sin Z \quad (\text{I.24})$$

and

$$F_{rt} = G \frac{M_m m}{r^2} \sin(Z + \alpha) \quad (\text{I.25})$$

Where  $Z$  is zenith angle.

Summing up these forces we arrive at the tide generating force  $F_t$

$$F_t = GM_m m \left[ \frac{\sin(Z + \alpha)}{r^2} - \frac{\sin Z}{l^2} \right] \quad (\text{I.26})$$

From the triangle  $O_1, m, O_3$  we can find:

$$\frac{\sin Z}{r} = \frac{\sin(\pi - Z - \alpha)}{l} = \frac{\sin(Z + \alpha)}{l} \quad (\text{I.27})$$

Therefore in eq(I.26)  $\sin(Z + \alpha)$  can be expressed by  $\sin Z$  and

$$F_t = GM_m m \left[ \frac{\sin(Z + \alpha)}{r^2} - \frac{\sin Z}{l^2} \right] = GM_m m \sin Z \left( \frac{l}{r^3} - \frac{1}{l^2} \right) \quad (\text{I.28})$$

Again using the triangle  $O_1, m, O_3$  the distance  $r$  is defined as:

$$r^2 = l^2 + r_e^2 - 2r_e l \cos Z \quad (\text{I.29})$$

Since the **equatorial parallax ratio** for the moon  $r_e/l$  is very small number (1/60.3) and for the sun this number is even smaller

$$\frac{r_e}{l_m} = 0.01658 \quad \frac{r_e}{l_s} = 4.2615 \times 10^{-5}$$

the terms of the higher order ( $r_e^2/l^2 \simeq 1/3600$ ) will be neglected. Developing above equation into binomial series we arrive at,

$$\frac{1}{r^3} \simeq \frac{1}{l^3} \left( 1 + \frac{3r_e}{l} \cos Z \right) \quad (\text{I.30})$$

Introducing this result into the **horizontal component of the tide generating force**, yields,

$$F_t = GM_m m \sin Z \left( \frac{l}{r^3} - \frac{1}{l^2} \right) = 3GM_m m \frac{r_e}{l^3} \sin Z \cos Z = \frac{3}{2} GM_m m \frac{r_e}{l^3} \sin 2Z \quad (\text{I.31})$$

Repeating similar considerations for the forces directed along the normal direction to the surface of the earth, we arrive at,

$$F_n = F_{rn} - F_{\omega n} = 3GM_m m \frac{r_e}{l^3} (\cos^2 Z - \frac{1}{3}) \quad (\text{I.32})$$

To the tidal forces the notion of the potential ( $\Omega$ ) can be ascribed assuming that force per unit mass ( $F/m$ ) and potential are connected as follows

$$\frac{\vec{F}}{m} = -\nabla \Omega_T \quad (\text{I.33})$$

In the system of coordinate from Fig. I.5, normal direction is away from the center of the earth and tangential direction is along  $F_{\omega t}$  (compare also Fig I.2),

$$-F_t/m = -\frac{\partial\Omega_T}{\partial s} = -\frac{1}{r_e} \frac{\partial\Omega_T}{\partial Z} \quad (\text{I.34})$$

$$F_n/m = -\frac{\partial\Omega_T}{\partial n} = -\frac{\partial\Omega_T}{\partial r_e} \quad (\text{I.35})$$

Using eqs(I.31) and (I.32) the **potential of the tidal force** follows,

$$\Omega_T = \frac{3}{2}GM_m \frac{r_e^2}{l^3} \left( \frac{1}{3} - \cos^2 Z \right) \quad (\text{I.36})$$

This expression is of the first approximation. It works well for the sun-earth interaction but because of the moon proximity to the earth sometimes higher order effects become important. For such case the distance in eq(I.29) can be developed to derive next term in series;

$$\Omega_T = \frac{3}{2l}GM_m \left[ \frac{r_e^2}{l^2} \left( \frac{1}{3} - \cos^2 Z \right) + \frac{r_e^3}{l^3} (3 - 5 \cos^2 Z) \right] \quad (\text{I.37})$$

One possible approach for the evaluation of **the magnitude of the tide generating force** is to compare it with the gravity force acting on mass  $m$  located on the earth's surface. Expressing gravitational constant from eq(I.4) and taking  $\sin 2Z = 1$ , the magnitude of  $F_t$  equals

$$F_t = mg \frac{3}{2} \frac{M_m}{M_e} \left( \frac{r_e}{l} \right)^3 \quad (\text{I.38})$$

for the moon  $F_t = mg 8.43 \times 10^{-8}$  and for the sun  $F_t = mg 3.87 \times 10^{-8}$

Thus the moon and the sun tide producing forces are very small in comparison to the gravity force  $mg$ . The tide generating force due to the moon is approximately 2.2 times greater than the tide generating force due to the sun. Such force will cause a man weighing 100 kg to loose (maximum)  $12.3 \times 10^{-8}$  of 100 kg, which is equal  $12.3 \times 10^{-3}$  g. To understand why such a small force has such a strong influence on the ocean dynamics it is enough to recall that the pressure force due to sea level change in the storm surge phenomena possesses the same order of magnitude.

### 3. EQUILIBRIUM TIDES

Equilibrium or static theory of tides has its root in the Newton works. Later it was developed by Bernoulli, Euler and MacLaurin (see **Cartwright, 1999**). Considerations involve assumption that the entire globe is covered by water, but the main tenet of the theory assumes an equilibrium between hydrostatic pressure and external (disturbing) forces. Henceforth the sea level change is defined by a simple equation;

$$-mg \frac{d\zeta^e}{ds} = F_t \quad (\text{I.39})$$

Here  $\zeta^e$  denotes elevation of the free surface above mean (undisturbed) sea level. According to Fig.I.5  $ds = r_e dZ$ . Introducing this dependence and expression for the  $F_t$  from eq(I.31) into eq(I.39), and using eq(I.3), we arrive at

$$-\frac{mg}{r_e} \frac{d\zeta^e}{dZ} = mg \frac{3}{2} \frac{M_m}{M_e} \left(\frac{r_e}{l}\right)^3 \sin 2Z \quad (\text{I.40})$$

and after integration

$$\zeta^e = \frac{r_e M_m}{M_e} \left(\frac{r_e}{l}\right)^3 \left(\frac{3}{2} \cos^2 Z + c\right) \quad (\text{I.41})$$

Assuming that the tide does not change the water volume, the above constant can be defined from (**Proudman, 1953**),

$$\int_0^\pi \left(\frac{3}{2} \cos^2 Z + c\right) \sin Z dZ = 0$$

Thus  $c = -1/2$ , and eq(I.41) defines the sea level change

$$\zeta^e = \frac{3}{2} \frac{r_e M_m}{M_e} \left(\frac{r_e}{l}\right)^3 \left(\cos^2 Z - \frac{1}{3}\right) = K \left(\cos^2 Z - \frac{1}{3}\right) \quad (\text{I.42})$$

where

$$K = \frac{3}{2} \frac{r_e M_m}{M_e} \left(\frac{r_e}{l}\right)^3$$

Using the lunar values,  $K \approx 0.54$ ; using the solar analogs we find  $K \approx 0.24$ . For the combined lunar and solar effect,  $K \approx 0.79$ . Here we may also relate the sea level to the previously introduced (eq.I.36) tidal potential. Comparing eq.(I.36) and eq.(I.42) we arrive at the expression,

$$\Omega_T = -g\zeta^e \quad (\text{I.43})$$

According to eq.(I.42) the free surface of the ocean is deformed from the globe to an ellipsoid (see Fig.I.6). Sectors in syzygy with the moon (around points 1 and 2), where  $Z = 0$  and  $\pi$  will depict the maximum tide, equal to:

$$\zeta^e_{max} = \frac{r_e M_m}{M_e} \left(\frac{r_e}{l}\right)^3 = \frac{2}{3} K \quad (\text{I.44})$$

Sectors in quadrature with the moon (proximity of points 3 and 4), where  $Z = \pi/2$  and  $3\pi/2$  will depict the minimum tide, equal to:

$$\zeta^e_{min} = -\frac{r_e M_m}{2M_e} \left(\frac{r_e}{l}\right)^3 = -\frac{1}{3} K \quad (\text{I.45})$$

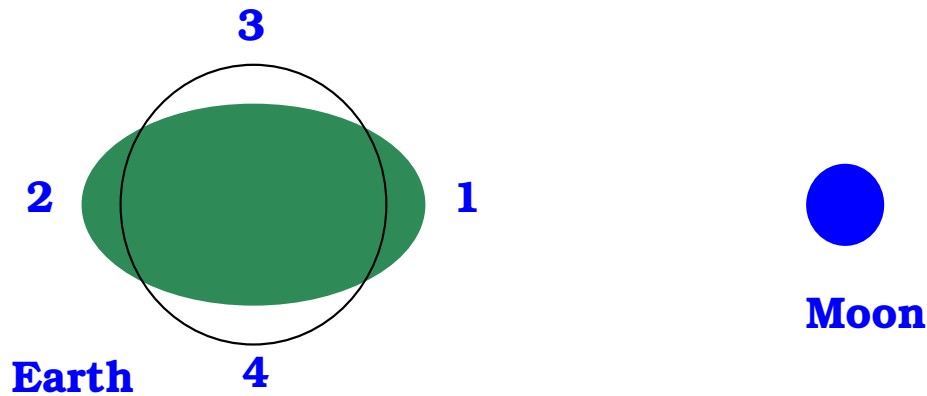


**Figure 1.6**

**Change of the shape of the oceanic free surface from the globe to an ellipsoid due to tidal forces.**

Above theory has its roots in Newton research but it was first proposed by Bernoulli in 1740 who used it to explain many tidal features such as periodicity or inequalities between successive high waters and low waters. It was used by subsequent researchers and practitioners as a simple tool to recognize the basic tidal processes and for computing tide tables. This is called equilibrium or static theory. We shall investigate the dynamic tidal theory in Chapter 2. For now let's consider a channel along the earth's equator and ask a question whether the tide generated by Moon or Sun in this channel will follow the Moon or Sun without delay? The equatorial distance is close to 40,000km. If this distance is traveled in 24h the speed is 1,667km/h. The long wave whose celerity is defined as  $\sqrt{gH}$  will travel the same distance in 24h assuming the ocean depth is 21.8km. Such depth does not exist in the oceans and therefore the tidal wave will follow the Moon or Sun, but with a time delay which cannot be described solely from the static tidal theory. Actually the mean ocean depth is close to 4 km, therefore the mean celerity is approximately 200 m/s which for the wave period of 24 hr results in the wave length of 18000 km. This simple example demonstrates that the tide wavelength is much bigger than the ocean depth. For such long waves the motion will be influenced by the bottom drag thus slowing the progression of the wave forced by the moon (or sun) attraction.

The tide-producing forces and tidal potential are functions of the zenith angle. Now we turn our attention to express this angle through the system of coordinate which takes into account the position of the external body and position of the observer. In Fig.I.7 the observer at the point O, can define the point on **the celestial sphere** which is located directly above his head.

This is zenith (ZN) and an associated point in opposite direction is called nadir (ND). The line connecting the center of the earth with the north pole if continued to the celestial sphere define a point called celestial north pole (NP).

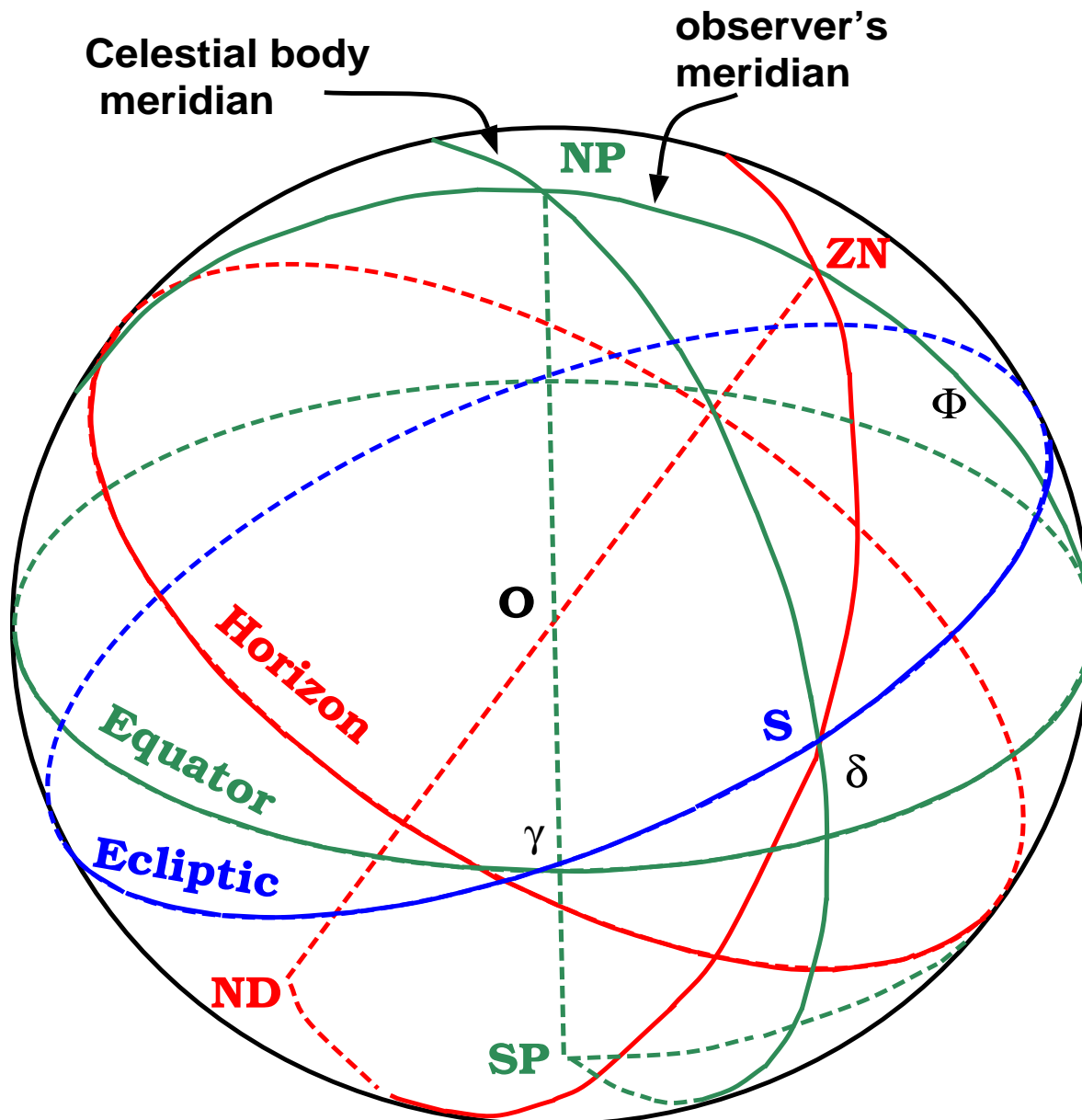


Figure I. 7

Celestial sphere. Observer is at the point O. The red color denote local system of coordinates: horizon, zenith (ZN) and nadir (ND). The green color denotes geographical coordinates: equator, north pole(NP), south pole (SP), observer's meridian (points NP, ZN, SP),  $\Phi$  latitude of the observer,  $\delta$  latitude of the celestial body (S), also called declination. Point  $\gamma$  where ecliptic crosses equator is called vernal equinox

Opposite point is called celestial south pole (SP) and continuation of the equatorial plane onto celestial sphere defines celestial equator. Therefore, the two systems of coordinates can be used on the celestial sphere: the local one related to the observer (red color in Fig.I.7), it is defined by the zenith, nadir and the plane of horizon, and the general system

(green color in Fig.I.7), defined by the north and south poles and the equatorial plane. Both system of coordinate play important role in tidal calculations. Observer's meridians joins the north pole, zenith point and south pole.

Sun, moon, planets rise in the east, climb the celestial sphere until they transit observer's meridian and then a decrease in altitude follows. The **declination** of the moon, sun or any celestial body denoted  $\delta$  is the angle defined from the equator plane along the meridian of the body to the body's position on the celestial sphere. In case of the sun the plane in which it travels is called **ecliptic**. Hence for the sun the declination is an angle between the planes of the equator and ecliptic. The declination of the body is measured in the similar fashion as the latitude of the observer. To relate zenith angle  $Z$  to position of the celestial body and to position the observer let consider Fig.I.8 with the three main meridians: observer's meridian, celestial body (S) meridian (hour circle) and Greenwich meridian. First we define **the hour angle** as an angular distance along celestial equator from the meridian of an observer to the meridian of the celestial body. The hour angle is also contained in the spherical triangle S, NP, ZN. The hour angle is measured from the moment a celestial body will transit observer's meridian. It increases by  $360^\circ$  in one day. Moreover this angle is closely related to the longitude and to the time. The longitude of the observer's meridian is measured from the Greenwich meridian to the east. The time is measured westwards from the Greenwich meridian to the celestial body meridian (see Fig.I.8). Denoting hour angle as  $\alpha$ , longitude of the observer as  $\lambda$  and time angle of celestial body as  $t$ , one can write

$$\alpha = \lambda + \frac{360^\circ}{T}t \quad (\text{I.46})$$

Here  $T$  denotes period required by celestial body to return to the observer's meridian. This time should be close to one day, but it is different for the moon and the sun. Before proceeding to develop formulas for the zenith angle let us notice an important point for the reckoning on the celestial sphere. This is a point where ecliptic intersects the equatorial surface ( $\gamma$ ), see Fig.I.7. This the first point of Aries or vernal equinox when the sun crosses equatorial plane ascending from southern to northern hemisphere. This point is often taken as beginning of coordinate system to calculate the longitude of the celestial bodies. The longitude is calculated positive eastward from  $\gamma$ .

From the spherical triangle S, NP, ZN in Fig.I.7 and Fig.I.8 the zenith angle  $Z$  is defined as,

$$\cos Z = \cos \delta \cos \phi \cos \alpha + \sin \delta \sin \phi \quad (\text{I.47})$$

Defining the zenith angle in terms of the declination (of the sun or moon), the latitude of the observer, and the hour angle is a key step in placing the equilibrium sea level in terms of readily available parameters.



Eq. I.47 into Eq I.42, we obtain

$$\begin{aligned} \zeta^e &= K(\cos^2 Z - \frac{1}{3}) \\ &= \frac{2K}{3} \left[ \left(\frac{3}{2} \cos^2 \phi - 1\right) \left(\frac{3}{2} \cos^2 \delta - 1\right) + \frac{3}{4} \sin 2\phi \sin 2\delta \cos \alpha + \frac{3}{4} \cos^2 \phi \cos^2 \delta \cos 2\alpha \right] \end{aligned} \quad (\text{I.48})$$

The equilibrium sea level can be split into three terms based on frequency.

The first term:

$$\zeta_{long-period}^e = \frac{2K}{3} \left(\frac{3}{2} \cos^2 \phi - 1\right) \left(\frac{3}{2} \cos^2 \delta - 1\right), \quad (\text{I.49})$$

does not include the hour angle (hence has no longitudinal dependence), but does depend on the declination of the celestial body (moon or sun) and the latitude of the observer. The latitude dependence produces a maximum at the poles and a minimum at the latitudes  $\pm 35^\circ 16'$ . The declination  $\delta$  undergoes monthly variations in case of the moon, and yearly variations in case of the sun. Since  $\cos^2 \delta = 0.5(1 + \cos 2\delta)$ , the periodicity is one-half of the above periods. Thus this term is the source for **the semi-monthly and semi-annual periods**.

The second term:

$$\zeta_{diurnal}^e = \frac{K}{2} \sin 2\phi \sin 2\delta \cos \alpha, \quad (\text{I.50})$$

depends on the hour angle, declination and latitude. The  $\cos \alpha$  dependence on the hour angle shows that this term generates **the diurnal oscillations**. The latitude dependence generates the maximum tide at the latitudes  $\pm 45^\circ$  and the minimum at the equator and at the poles. The declination imparts a slow amplitude modulation and the sign of this modulation will change from positive to negative when the celestial body crosses the equator from the northern to the southern hemisphere. In all three terms the distance  $l$  changes over one month for the moon (one year for the sun) in accordance with the usual elliptical motion of celestial bodies.

The third term:

$$\zeta_{semi-diurnal}^e = \frac{K}{2} \cos^2 \phi \cos^2 \delta \cos 2\alpha, \quad (\text{I.51})$$

generates **the semi-diurnal periods** since it is proportional to  $\cos 2\alpha$ , and since  $\alpha$ , the hour angle, moves through  $360^\circ$  each lunar (or solar in the case of the sun) day. The sea level also depends on the declination  $\delta$  of the celestial body, and the latitude ( $\phi$ ) of the observer. The change of the declination over the semidiurnal period is slow. Since the semi-diurnal term is proportional to  $\cos^2 \delta$  the maximum occurs when the celestial body is above the equator and is at a minimum at the poles.

Had additional terms in the approximation (Eq. I.30) been retained, higher frequency constituents (ter-diurnal etc.) would have been obtained. We may now proceed to express the equilibrium tide in terms of harmonic constituents; before doing so, however, we will review the basic elements of the earth-moon-sun orbital motions.

#### 4. THE ORBITS OF EARTH AND MOON

The sea level produced by the tidal forcing is a function of the various astronomical parameters. As we have seen, primary among these are the revolution of the moon around the earth, the earth around the sun, and the rotation of the earth around own axis. These result in the three main tidal periods, i.e, monthly, yearly and daily.

The Earth orbit around the sun is ellipse with eccentricity  $e=0.01674$ . The shortest distance along the major axis at perihelion is reached on January 2, and the longest distance at aphelion is reached on July 2, see Fig. I.9. Therefore, dependence of the equilibrium tides on the distance suggests that tide producing force due to the sun is larger in the winter. The fundamental period is equal 365.24 days. During one year the moon completes about twelve elliptical orbits around the earth with the period of 29.5 days.

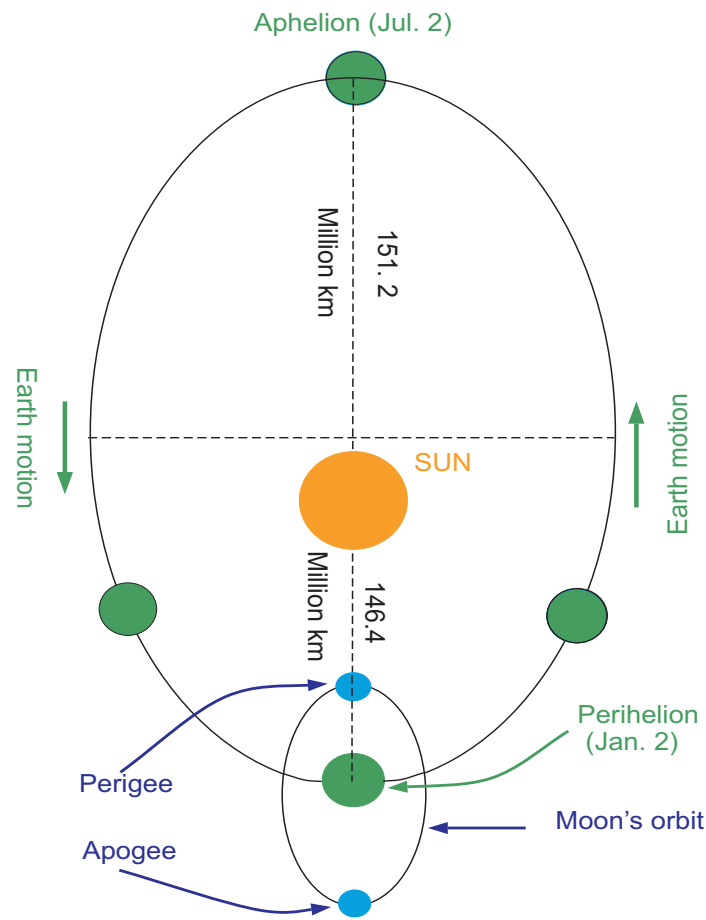


**FIGURE I. 9**

Sun, earth and moon in the orbital motion. Aphelion denotes the earth's longest distance from the sun, perihelion is the shortest distance. The moons shortest distance from the earth is called perigee, apogee is the longest distance

The shortest distance of the moon from the earth being called **perigee** and the longest **apogee**. The eccentricity of the moon orbit is  $e=0.055$ . Therefore, the moon ellipse is much more elongated than the sun orbit. This will result in the large difference of the tide

producing forces between apogee and perigee. The ratio of the tidal forces at apogee and perigee is 1.4:1 for the moon and 1.11:1 for the sun. The line joining apogee and perigee (the line of apsides) rotates slowly, making one complete revolution in about 8.85 years. The period of the lunar perigee is one of the important data in computing tide parameters. None of the described motions take place in the equatorial plane. Among many factors which influence tidal cycles the inclination of the ecliptic to the equator and the inclination of the lunar orbit to the ecliptic are the most important. In Fig. I.7 we have defined the declination as the inclination of the ecliptic (i.e. the sun trajectory on the celestial sphere) to the equatorial plane. The declination (or latitude) of the ecliptic changes from  $23^{\circ}27'$  north of the equator to  $23^{\circ}27'$  south of the equator. The moon is also slightly inclined to the ecliptic with an angle of  $5^{\circ}9'$ , see Fig.I. 10. The moon maximum declination changes from  $28^{\circ}36'$  to  $18^{\circ}18'$ . These limits are reached every 18.6 years. The plane of the moon orbit intersect during one month the ecliptic plane at least at two points, called nodal points. If entire system were the earth and moon only, the moon will be always repeating the same trajectory with the same nodal points.

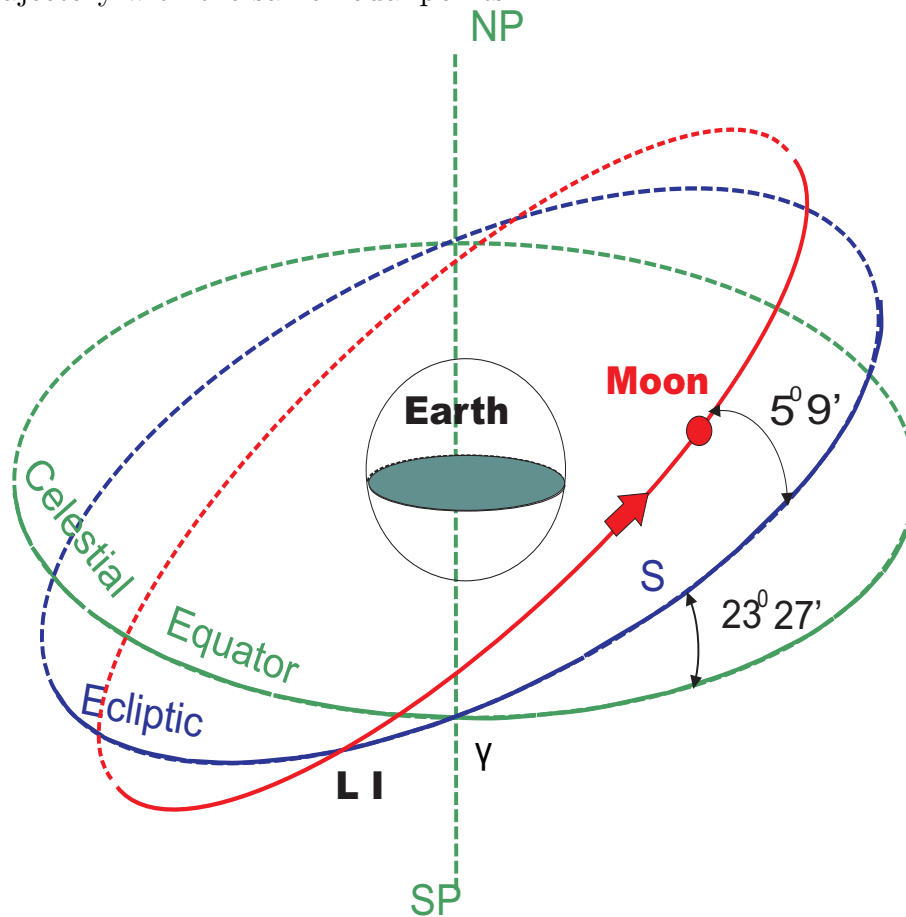


**FIGURE I. 10**

**Moon in the orbital motion as seen from earth. Lunar orbit intersection with ecliptic (point LI) is called nodal point.**

The effect of the sun is perturbation of the moon orbit. As a result of the perturbation the nodal points do not remain in the fixed position. They moved westward on the ecliptic

completing one cycle in 18.6 years. This is one of the major period of the tide producing forces.

The monthly cycle of the moon latitudinal movement from  $28^{\circ}36'$  N to  $28^{\circ}36'$  S should have a strong modulating effect over semidiurnal and diurnal tides with a monthly period. During one day period the moon position on the celestial sphere will change only slightly thus in the first approximation one can assume that the shape of tidal envelope is permanent over diurnal cycle. The tidal ellipsoid stays aligned with the moon, but due to the moon declination the observer in the fixed point on the rotating earth will encounter various sea level of the tidal ellipsoid, as he is carried by earth's rotation through the various phases of the tidal envelope. To describe this effect let consider the tidal ellipsoid generated by the moon (or sun) when the moon is not located in the equatorial plane so the declination is not equal to zero. We use in Fig.I.11 examples suggested by [Dronkers \(1964\)](#).

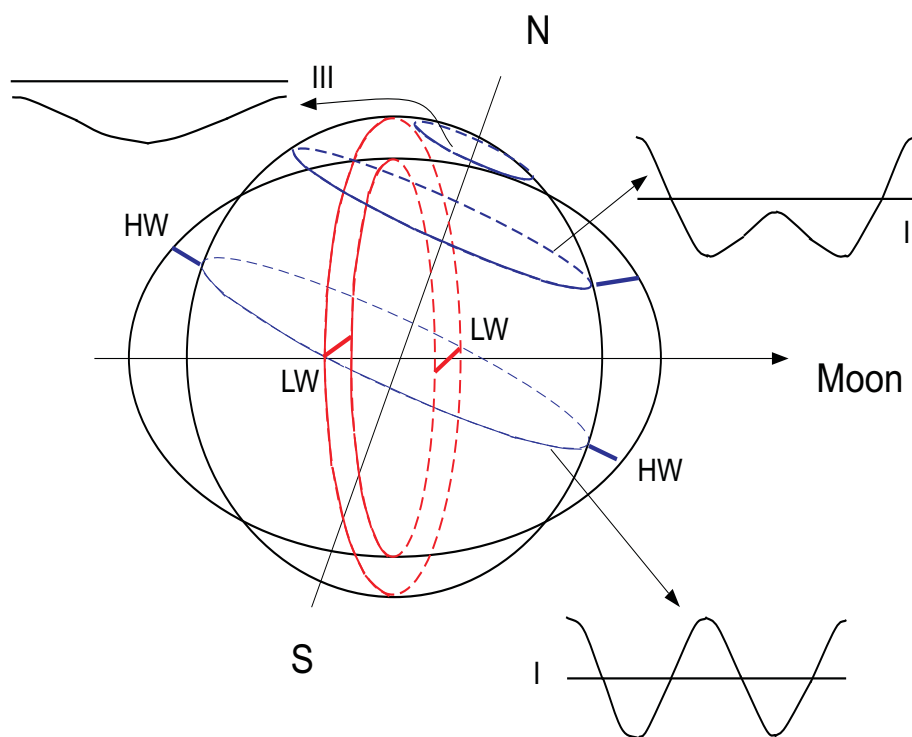


**FIGURE I. 11**

**Tidal envelope and generation of diurnal and semidiurnal tides, according to Dronkers (1964)**

Consider observational point on the earth's surface located at the equator. Due to the daily rotation this point will travel along latitudinal circle (equator). The high water level (HW) occurs when the observational point pass under the moon (moon passes the observer's meridian) and when this point is on the opposite side of the earth. The low water level (LW) occurs when the moon rises or sets in the observational point. Henceforth, the observational point will encounter two low and two high sea levels during one day, see tidal record I in Fig.I.11. At the equator the semidiurnal tide is quite symmetrical. This symmetry is broken at higher latitudes. Record II in Fig.I.11 depicts quite strong daily inequality in the semidiurnal tides. Away from the equator the diurnal tides are growing

stronger and eventually at the high latitudes (record III in Fig.I.11) this period completely dominates the tidal record. Daily inequalities can be studied precisely by using formulas for the semidiurnal equilibrium tide (eq I.50) and for the diurnal tide (eq I.51).

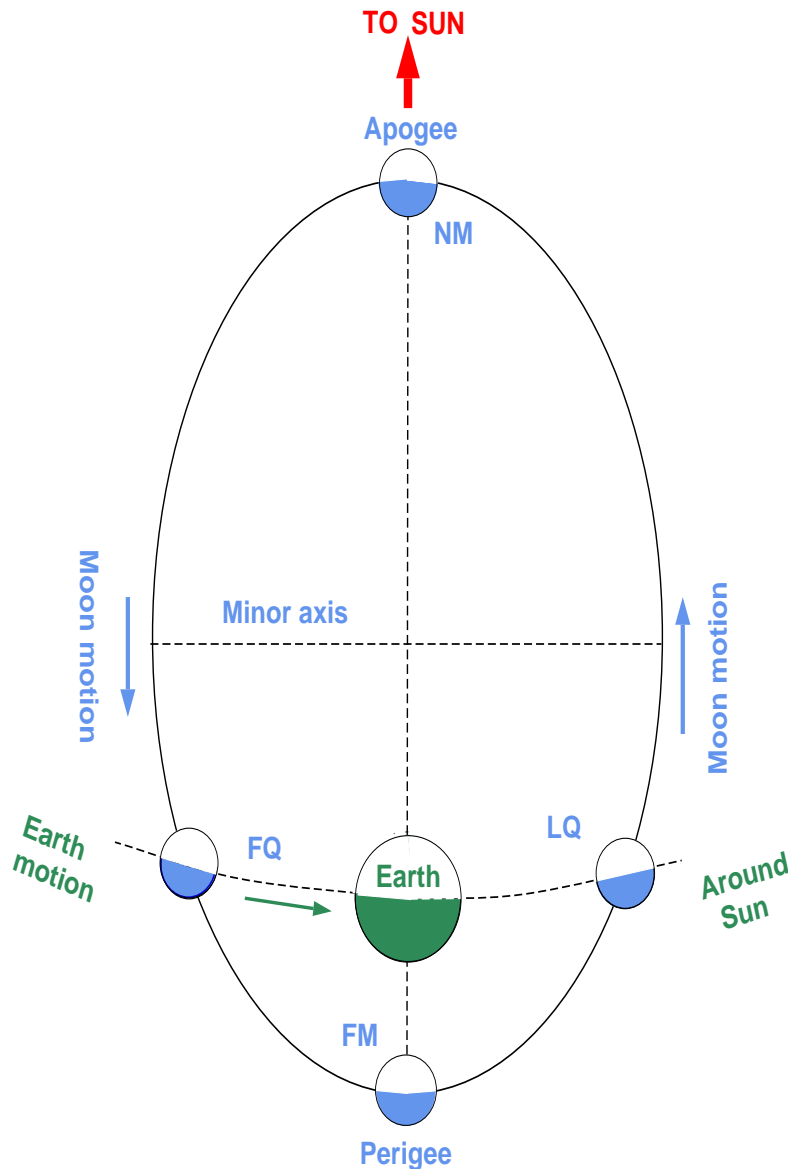


**FIGURE I. 12a**

**Moon orbital motion.** Maximum tides (spring tide) occur at both new (NM) and full moon (FM). Minimum tides (neap tides) occur at the first quarter (FQ) and the last quarter (LQ). The alignment of the sun, earth and moon is called syzygy.

The moon revolves around the earth in one synodic cycle from the new moon (NM) through the first quarter (FQ), the full moon (FM), the last quarter (LQ) and back to the new moon in one synodic cycle equal to 29.53 days (Fig.I.12a). The various positions of these celestial bodies will result in the various magnitude of the tide producing force. The maximum of tides (**spring tide**), occur at the new moon and at the full moon when the earth moon



will occur during new moon (NM) perigee.

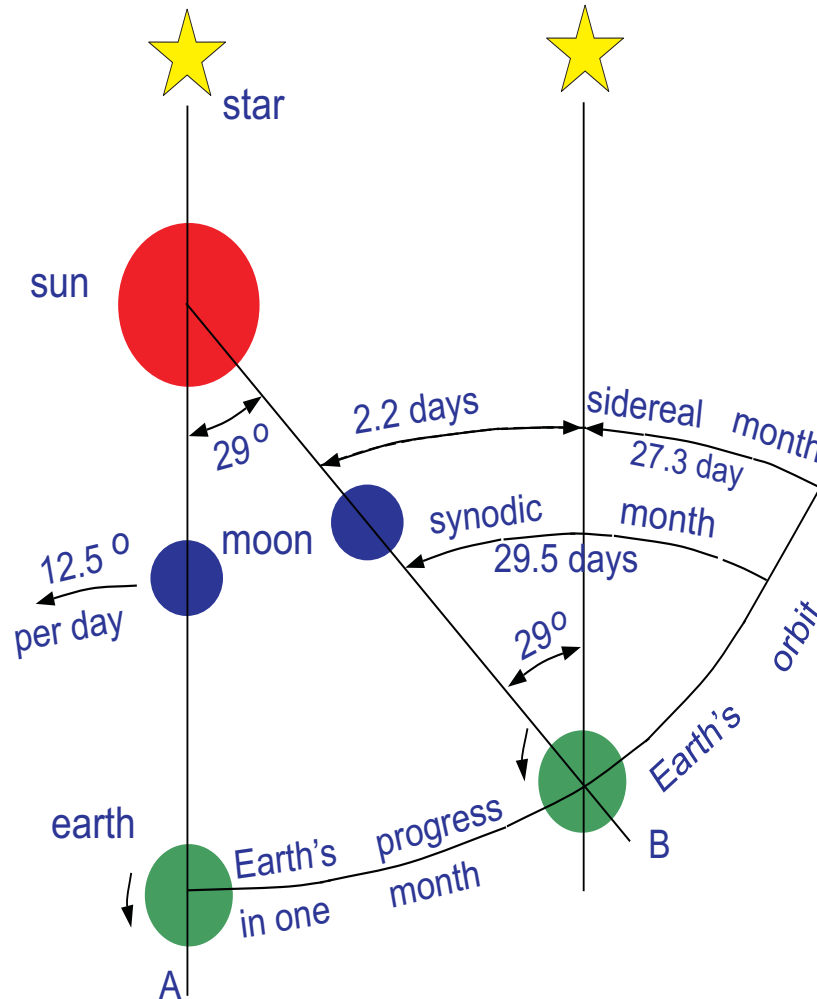


**FIGURE I. 13**

**Moon revolution around the earth and earth revolution around the sun, according to Macmillan (1966)**

The spring/neap cycle may be understood in terms of two signals (in this example the semi-diurnal tides ("M<sub>2</sub>" and "S<sub>2</sub>") going in and out of phase over the course of a fortnight. This phenomenon is known as a "beats" or "beating" and in the context of tides is not confined to M<sub>2</sub> and S<sub>2</sub>. When any pair of slightly-different frequencies (of similar amplitude) add together, their sum undergoes a regular cycle between near-zero magnitude (neaps), and a magnitude equal to the sum of the pair (springs). The period between successive "neaps" is equal to the inverse of the absolute value of the difference between the two frequencies. The frequencies of M<sub>2</sub> and S<sub>2</sub> are 1.9322 d<sup>-1</sup> and 2.0 d<sup>-1</sup> respectively (where d is mean solar day); their difference is the beat frequency 0.0678 d<sup>-1</sup>, the inverse of which, 14.75 d<sup>-1</sup>, is the beat period - also known as the fortnightly or spring-neap cycle. In the case of M<sub>2</sub> and S<sub>2</sub>, the average of the pair is slightly less than 2 d<sup>-1</sup> - thus, about two highs and two lows per day. The modulation frequency is half the difference, which comes to a period of 29.49 days. Because the modulation is indistinguishable over the two halves of

the cosine cycle, there are two neaps and two springs per 29.49 days - thus, a neaps every 14.75 days.

The diurnal period related to the moon producing forces is equal about 24.84 h. Every day transit of the moon across the observer's meridian is 0.84 h (50 min) later. To deduce the moon successive transits let's consider closely the motion of the earth and moon during one month - Fig.I.13. The moon moves counterclockwise about  $12.5^\circ$  per day, because the earth's rotation takes place in the same direction, the observer's meridian (see Fig.I.13) will not be aligned with the moon in 24 h period. Additional, about  $12.5^\circ$  will require about 50 min, since one degree (on the earth) corresponds to 4 min time lag. Moon periodic motion around the earth defined by **synodic month** (period between two identical moon phases) is not equal to the lunar sidereal month (sidereal meaning with respect to a fixed reference frame). The reason for this difference is that the earth and moon jointly revolve around the sun. The results of combining the moon monthly revolution and the earth's annual revolution are shown in Fig.I.13, according to **Macmillan (1966)**. During one sidereal month the earth moves from point A to B, thus advancing about  $29^\circ$ . After that period the star, the moon and the earth are aligned again. The period is called sidereal month and is equal 27.3 days. However the sun is not aligned, because during the one sidereal month the earth moved around the sun, for the moon to be in line with the sun, it must revolve additionally about  $29^\circ$  or about 2.2 days, thus completing one synodic month in about 29.5 days. This alignment will also result in the strongest tides since the shortest distance from the earth to both the sun and moon will occur during new moon (NM) perigee. Generally, we can deduce from the above considerations that the time of one complete revolution of the moon around the earth will depend on the system of reference. Frequently, together with the synodic and sidereal definitions, the nodical and anomalistic months are used as well (see below table).

**Table I.1 Duration of the month according to the reference system**

Reference system	Month	Duration
Moon node	Nodical	27.2122 d
Star	sidereal (tropical)	27.3216 d
Moon perigee	anomalistic	27.5546 d
Moon phase	synodic	29.5306 d

## 5. THE HARMONIC CONSTITUENTS OF THE EQUILIBRIUM TIDE

The sea level in eq(I.48) depends in a quite complicated fashion on the latitude of the observer, the distance to and declination of the celestial body, and the hour angle, with the latter three all being functions of time. This does not make a convenient basis for the representation of the tides. The harmonic model (Eq.I.52) proposed by **Thomson (Lord Kelvin) (1882)**, and developed chiefly by **Darwin (1901)** and **Doodson (1921; reprinted in 1954)** enabled tidal scientists to analyse tidal records in terms of a set of parameters (such as the current longitude of the moon) which vary in a simple clocklike

fashion. Doodson's (1921) tidal potential model became the basis for most tidal analysis and prediction schemes through the 20th century. Summaries may be found in **Neumann and Pierson (1966)**, **Dronkers (1964)**, **Dietrich et al. (1980)**, and **Pugh (1987)**. The theory was put on a more modern foundation by **Cartwright and Tayler (1971)**, with minor corrections published by **Cartwright and Edden 1973** (collectively "CTE"). **Kantha and Clayson (2000)** give an excellent elaboration of the methods of CTE.

The names of the basic tidal constituents ( $M_2$ ,  $K_1$ , etc.) originated with Sir William Thomson (Lord Kelvin) and Sir George Darwin in the 19th and early 20th centuries. **Cartwright (1999)**, pp. 100-103, provides an interesting account of how the convention developed. Aside from "S" for solar and "M" for moon (lunar), the rationale for the letters is not obvious. The subscript specifies the species. The harmonic analysis introduced by Thomson found primary application in harmonic development of the tide-generating potential by **Darwin (1901)** who introduced the basic tidal constituents and their names. Further extension to about 400 constituents was made by **Doodson (1921)**. In Tables I.3 and I.4 we define 11 major constituents in the semidiurnal, diurnal and long period range of oscillations. General symbols like M and S refer to lunar and solar origin. The subscripts 1 and 2 refer to diurnal and semidiurnal species respectively. Hence  **$M_2$  is semidiurnal constituent due to the moon attraction** with the period equal to half of the mean lunar day.  **$S_2$  is semidiurnal constituent due to sun attraction** with the period equal to half of the solar day. The constituent  **$N_2$  is called the lunar elliptic semidiurnal** because it depends on the changes of distance. The constituents  **$K_2$  is called a luni-solar declinational semidiurnal constituent** because it depend on the changes in the moon and sun declination and not on the changes in distance. Both declinational constituent due to the sun and the moon have the same period. Similarly  **$K_1$  constituents** for the moon and sun have the same period, therefore they are combined into one luni-solar diurnal constituent. It is interesting to see from the Tables I.3 and I.4 that the main solar and lunar constituents are not identified as  $S_1$  and  $M_1$ . These should have periods of the mean solar day and the mean lunar day but these diurnal constituents depend on the declination as  $\sin 2\delta$ , hence the input of these terms is equal zero. Three long-period constituents Mf, Mm and Ssa are considered. The most important constituent is the **lunar fortnightly (Mf)** with period 13.661 day. It is associated with the variation of the moon's monthly declination. The **monthly lunar period Mm** is related to the monthly variation of the moon's distance and therefore this period is also named as elliptic. This period is equal to 27.555 day it is so called anomalistic month.

Doodson represented the equilibrium sea level as a sum of  $n$  individual harmonic waves, each having one of two forms:

$$\zeta_n^e = \frac{1}{g} C_n S_D G_{ms} F_D(\phi) \cos(V_n(t) + d_1 \lambda) \quad \text{or} \quad \zeta_n^e = \frac{1}{g} C_n S_D G_{ms} F_D(\phi) \sin(V_n(t) + d_1 \lambda). \quad (\text{I.52})$$

The meaning of the terms in Eq.I.52 are as follows.

$C_n$  is the relative amplitude of the  $n^{\text{th}}$  wave. Values of  $C_n$  are listed in a series of "Schedules" in **Doodson (1921)**. The value listed for  $M_2$ , for example, is 0.90812.

$S_D$  is a scaling factor chosen such that all the products  $S_D G_m F(\phi)$  (which Doodson referred to as the "geodetic coefficients") have identical maximum values. For long-period, diurnal, and semi-diurnal harmonics, the values of  $S$  are 0.5, 1, and 1 respectively, but for ter-diurnal and higher harmonics, the values range between 0.125 and 3.079.

$G_{ms}$  is a constant. For lunar and solar terms respectively it takes on the values

$$G_m = \frac{3}{4} G M_m \frac{R_e^2}{\langle l_m \rangle^3} \quad \text{and} \quad G_s = \frac{3}{4} G M_s \frac{R_e^2}{\langle l_s \rangle^3}$$

where the angle brackets indicate mean values.

$F_D(\phi)$  is a function of earth latitude. For  $M_2$ ,  $F_D(\phi) = \cos^2 \phi$ .

$V_n(t)$  is the phase of the  $n^{\text{th}}$  equilibrium harmonic on the Greenwich meridian. Further discussion may be found in the following section.

$d_1 \lambda$  advances the phase with west longitude  $\lambda$ .  $d_1 = 0, 1, 2$  for long-period, diurnal, and semi-diurnal tides respectively.

The lunar tidal potential has an 18.6 year periodicity known as the "regression of the lunar nodes" (see Sec. 7) which for time series of less than 18.6 years is usually accounted for using a factor and phase shift known as "f and u". Also, in order to let the phase advance in time at a frequency  $\omega_n$ , we add a term  $\omega_n t$ , where  $t$  is the time elapsed since  $t_0 = 0000$  hours UT, and we explicitly reference the phase to that time by writing  $V_n(t_0)$ . With these changes, and assuming appropriate phase changes have been made in order to use exclusively cosine terms with positive coefficients, Eq.I.52 becomes (for all terms, lunar and solar):

$$\zeta_n^e = \frac{f_n}{g} C_n G_m F(\phi) \cos(\omega_n t + V_n(t_0) + u_n) \quad (\text{I.53})$$

The full equilibrium sea level with  $n$  harmonics, using **Doodson's (1921)** scalings, is given by the sum:

$$\zeta^e = \sum_n \frac{f_n}{g} C_n G_m F(\phi) \cos(\omega_n t + V_n(t_0) + u_n) \quad (\text{I.54})$$

The expansion of CTE results in a simpler scaling and more accurate coefficients, although for the most part the differences were found to be minor. For example, CTE lists  $H_{M_2} = 0.63192$  for the coefficient based on the most recent data (centered on 1960). When scaled to compare with Doodson's coefficient ( $C_{M_2} = 0.90812$ ), CTE found that  $H_{M_2} = 0.90809$ . More recently, other authors (e.g. **Tamura, 1987**) have taken the CTE expansion to higher order, adding some additional precision. With CTE coefficients, Eq.I.53 is written

$$\zeta_n^e = S_{CTE} H_n F_{CTE}(\phi) \cos(\omega_n t + V_n(t_0) + u_n). \quad (\text{I.55})$$

Here

$S_{CTE} = \left(\frac{5}{4\pi}\right)^{1/2}$ ,  $\frac{3}{2}\left(\frac{5}{24\pi}\right)^{1/2}$ , and  $3\left(\frac{5}{96\pi}\right)^{1/2}$  for long-period, diurnal, and semi-diurnal harmonics respectively, and

$F_{CTE}(\phi) = \frac{3}{2}\cos^2\phi - 1$ ,  $\sin 2\phi$ , and  $\cos^2\phi$  for long-period, diurnal, and semi-diurnal harmonics.

For example,  $M_2$  then becomes:

$$\zeta_{M_2}^e = 3\left(\frac{5}{96\pi}\right)^{1/2} H_{M_2} \cos^2\phi \cos(\omega_{M_2}t + V_{M_2}(t_0) + u_{M_2}). \quad (\text{I.56})$$

The equilibrium sea level, using the scaling and coefficients of CTE, including the  $f$  and  $u$  factors, is given by the sum:

$$\zeta^e = \sum_n f S_{CTE} H_n F_{CTE}(\phi) \cos(\omega_n t + V_n(t_0) + u_n) \quad (\text{I.57})$$

The period of each term in the harmonic model derives directly from the orbital and rotational periods of discussed in Sec. 4. These include:

the mean solar hour (msh) (lunar hours and lunar days may also be used, but see below),

**the sidereal month (period of lunar declination)**, 27.321582 mean solar days,

**the tropical year (period of solar declination)**, 365.24219879 mean solar days,

**the period of the lunar perigee**, 8.8475420 years

**the period of the lunar node**, 18.613188 years, and

**the period of the solar perihelion**, 20,940 years.

The "year" in the definitions of the latter three is the Julian year (1 Julian Year 365.24219879 days). Although the longitude of the perihelion changes by less than  $.02^\circ$  per year, this is enough to cause a noticeable effect in the frequencies of certain constituents, and that is why it must be retained.

The letters  $s$ ,  $h$ ,  $p$ ,  $N$  and  $p_s$  (sometimes  $p'$  or  $p_1$ ) are well-established in the tidal literature, but usage varies. Most commonly they are time-dependent functions of longitude on the celestial sphere and have units of degrees. In other words, many authors use  $s$  for the longitude of the moon,  $p$  for the longitude of the moon's perigee, etc. Elsewhere they are understood to mean the time rate of change of those longitudes, in which case the meaning is clear only if the dot notation is used (as in " $\dot{s}$ "), but unfortunately the dot is sometimes omitted. We use  $\dot{s}$ ,  $\dot{h}$ ,  $\dot{p}$ ,  $\dot{N}$ , and  $\dot{p}_s$  for the rates of change, and  $s(t)$ ,  $h(t)$ ,  $p(t)$ ,  $N(t)$ , and  $p_s(t)$  to indicate the time-dependent longitudes.

It is conventional in tidal practice to use "speed", usually in degrees per msh, rather than radians per second, as the unit of frequency. In terms of speed (with  $msh$  = mean solar hour and  $msd$  = mean solar day), the above periodicities become:

$$\omega_t = 15.0^\circ/msh = 360^\circ/msd$$

$$\omega_m = 14.4920521^\circ/msh = 360^\circ/\text{mean lunar day},$$

$$\dot{s} = 5.490165 \times 10^{-1} \text{ }^\circ/msh = 13.17644^\circ/msd = 360^\circ/\text{sidereal month},$$

$$\dot{h} = 4.106863 \times 10^{-2} \text{ }^\circ/msh = 0.98565^\circ/msd = 360^\circ/\text{tropical year},$$

$\dot{p} = 4.641878 \times 10^{-3} \text{ }^\circ/msh = 0.11140^\circ/msd = 360^\circ/\text{lunar perigee cycle}$ ,  
 $\dot{N} = 2.206413 \times 10^{-3} \text{ }^\circ/msh = 0.052955^\circ/msd = 360^\circ/\text{nodal cycle}$ , and  
 $\dot{p}_s = 1.96125 \times 10^{-6} \text{ }^\circ/msh = 0.000047^\circ/msd = 360^\circ/\text{solar perihelion cycle}$ .

Conversion between speed in  $^\circ/hour$  and circular frequency in radians per second is straightforward: e.g., for the  $K_1$  wave:

$$\omega_{K1} = 15.041068^\circ \times (\pi/180)/3600. = 0.7292110^{-4} s^{-1} \quad (\text{I.58})$$

In the list above, two different types of day are used. Both are slightly longer than a sidereal day as a result of the orbit of the earth around the sun (in the case of the solar day) and the orbit of the moon around the earth (in the case of the lunar day). Hence the solar and lunar diurnal frequencies are related to the sidereal frequency  $\omega_s$  by (respectively)  $\omega_t = \omega_s - \dot{h}$  and  $\omega_m = \omega_s - \dot{s}$ . Table I.2 shows the respective periods.

**Table I.2 Fundamental Daily Periods (Platzman (1971))**

Period (msd)	Description
$360^\circ/\omega_s = 0.997270$ ( $23^h 56^m 4^s$ )	Sidereal day
$360^\circ/\omega_t = 1$	Mean solar day
$360^\circ/\omega_m = 1.035050$ ( $24^h 50^m 28^s$ )	Mean lunar day

The frequency of any tidal constituent can be computed by:

$$\omega_n = d_1\omega_t + d_2\dot{s} + d_3\dot{h} + d_4\dot{p} + d_5\dot{N} + d_6\dot{p}_s \quad (\text{I.59})$$

where the numbers ( $d_1, d_2, d_3, d_4, d_5, d_6$ ) are a set of six small integers known as the "Doodson Number" of the constituent. The **Doodson Number** identifies both the speed and the equilibrium phase.

The Doodson Number was originally written NNN.NNN where each N was an integer in the range 0 - 9 (or "X" for ten). In some tabulations five was added to each integer (except the first) to avoid negative values. This practice is no longer of much value, so we will write the Doodson Number simply as ( $d_1, d_2, d_3, d_4, d_5, d_6$ ). Each Doodson Number takes on a value ranging between -12 and +12 (between -4 and +4 for most major tidal constituents).

The first digit of the Doodson Number is the species of the constituent. The second and third digits ( $d_2$  and  $d_3$ ) of the Doodson Number take on different values depending on whether solar or lunar time is being used, and this may not always be spelled out. For example, the Doodson Number for  $M_2$  would be written (2 0 0 0 0 0) or (2 2 2 0 0 0) respectively\*. The first one tells us that the constituent oscillates twice per lunar day, as one expects for  $M_2$ . The latter tells us that the same constituent oscillates twice per solar day, less twice per month, plus twice per tropical year, which of course must come to the

same thing. Given a Doodson Number of (2 0 0 0 0 0), there is no way to know if it is  $M_2$  or  $S_2$ , unless we are told whether the "2" refers to "twice per lunar day" or "twice per solar day". Obviously the time base must always be clearly specified. Unless otherwise specified, we will use the solar-day based Doodson Numbers exclusively. Conversion of the Doodson Number from one time base to the other is quite simple.

\*In a table that adds five to all digits except the first, the representation of  $M_2$  is either (2 5 5 5 5 5) or (2 3 7 5 5 5).

**Table I.3 Doodson Numbers and speeds of the major tidal constituents**

Constituent semidiurnal	Doodson number, solar time						speed in °/h
	d <sub>1</sub>	d <sub>2</sub>	d <sub>3</sub>	d <sub>4</sub>	d <sub>5</sub>	d <sub>6</sub>	
$M_2$	2	-2	2	0	0	0	28.984
$S_2$	2	0	0	0	0	0	30.000
$N_2$	2	-3	2	1	0	0	28.440
$K_2$	2	0	2	0	0	0	30.082
diurnal							in °/h
$K_1$	1	0	1	0	0	0	15.041
$O_1$	1	-2	1	0	0	0	13.943
$P_1$	1	0	-1	0	0	0	14.958
$Q_1$	1	-3	1	1	0	0	13.399
long period							in °/h
Mf	0	2	0	0	0	0	1.098
Mm	0	1	0	-1	0	0	0.544
Ssa	0	0	2	0	0	0	0.082

The following may be used to convert to solar time:

Diurnal constituents ( $d_1 = 1$ ):

$$d_2(solar) = d_2(lunar) - 1, \text{ and } d_3(solar) = d_3(lunar) + 1,$$

Semi-diurnal constituents ( $d_1 = 2$ ):

$$d_2(solar) = d_2(lunar) - 2, \text{ and } d_3(solar) = d_3(lunar) + 2,$$

Ter-diurnal constituents ( $d_1 = 3$ ):

$$d_2(solar) = d_2(lunar) - 3, \text{ and } d_3(solar) = d_3(lunar) + 3,$$

...and so forth for higher frequency constituents. Note that only  $d_2$  and  $d_3$  differ.

For example, to compute the speed of  $S_2$ , with solar day Doodson Number (2 0 0 0 0 0), and lunar day Doodson Number (2 2 -2 0 0 0), we have:

$$\omega_{S_2} = 2\omega_t = 30^\circ/\text{msh}, \text{ or}$$

$$\omega_{S_2} = 2\omega_m + 2\dot{s} - 2\dot{h} = 30^\circ/\text{msh}.$$

For  $M_2$  and  $K_1$ , using only the solar day Doodson Numbers,  $\omega_{M_2} = 2\omega_t - 2\dot{s} + 2\dot{h} = 28.984^\circ/h$ ,  $\omega_{K_1} = \omega_t + \dot{h} = 15.041068^\circ/h$

In case of nonlinear interactions through the advective terms or bottom friction terms in the equation of motion the new constituents are generated. These are called overtides or compound tides. Compound tides have speeds that are linear combinations of the basic

constituents. For example,  $2SK_2$  has twice the speed of  $S_2$  less that of  $K_2$ , i.e.  $2\omega_{S_2} - \omega_{K_2}$  (some authors write this as " $2S_2 - K_2$ "). Using the Doodson Numbers for  $S_2$  and  $K_2$ , (2 0 0 0 0 0) and (2 0 2 0 0 0) respectively,  $\omega_{S_2}$  and  $\omega_{K_2}$  are expanded as:

$$\omega_{S_2} = 2\omega_t, \text{ and}$$

$$\omega_{K_2} = 2\omega_t + 2\dot{h}. \text{ Then the expression is written}$$

$$2\omega_{S_2} - \omega_{K_2} = 2(2\omega_t) - 2\omega_t - 2\dot{h} = 2\omega_t - 2\dot{h},$$

indicating a constituent with Doodson Number (2 0 -2 0 0 0), i.e.  $2SK_2$ . Had lunar day Doodson Numbers been used, the result would have been (2 2 -4 0 0 0), which is of course also  $2SK_2$ . The names of the compound constituents, described in [Rossiter and Lennon \(1968\)](#) includes the more basic constituents from which they arise. A few examples shows the logic behind them. While the names are suggestive of the origins, they don't always identify them completely.

$2MS_6$ , which oscillates six times per day, arises from  $M_2$  and  $S_2$ . The speed is determined as  $2\omega_{M_2} + \omega_{S_2}$ , that is, twice the speed of  $M_2$  plus the speed of  $S_2$ .

$2MQ_3$  arises from  $M_2$  and  $Q_1$  and the speed is given by  $2\omega_{M_2} + \omega_{Q_1}$ .  $2MQ_3$  is a bit unusual because most compound tides involve only constituents of the same species (i.e., all diurnal or all semi-diurnal).

$2(MN)S_6$  arises from  $M_2$ ,  $N_2$ , and  $S_2$  and the speed is given by  $2\omega_{M_2} + 2\omega_{N_2} - \omega_{S_2}$ . Note that the sign can be negative, and that the parenthesis indicates that  $M_2$  and  $N_2$  have the same sign. The only way for the speeds to add up to six is to have factors of positive two on  $M_2$  and  $N_2$ , and a factor of negative one on  $S_2$ . Thus,  $2 \times 2 + 2 \times 2 - 2 = 6$ .

$V_n(t_0)$ , the phase of the equilibrium tide at a given place and time, can be written as a function of  $s(t)$ ,  $h(t)$ ,  $p(t)$ ,  $N(t)$ ,  $p_s(t)$ :

$$V_n(t_0) = d_2s(t_0) + d_3h(t_0) + d_4p(t_0) + d_5N(t_0) + d_6p'(t_0) + \Phi_n \quad (\text{I.60})$$

In the expansion, the angle  $\Phi$  arises due to the requirement that the summation (Eq. I.52) is over cosines only (not sines) (adding  $\Phi$ , which is always a multiple of  $\pi/2$ , converts a sine term to a cosine), and also that the tabulated coefficients be positive. The latter is achieved by applying one of the following identities:  $\cos(\theta - 90^\circ) = \sin \theta$ , and  $\cos \theta = -\cos(\theta - 180^\circ)$ .

In Eq.I.60 we have written  $t_0$  rather than  $t$  to emphasise that the expression is normally evaluated at  $t_0$ , the start of a solar day (i.e., at 0000 Hours UT). At that time,  $\alpha$ , the hour angle of the sun, is zero. If  $V_n(t)$  is required at some time other than 0000 Hours UT, a term  $d_1\omega_n t$  could be added, where  $\omega_n$  is the speed of the  $n^{th}$  constituent and  $t$  is the time in hours since the start of the day.

The values in Eq.I.60 are sometimes referred to collectively as the "astronomical argument" of constituent  $n$ . For example, for  $O_1$ , with Doodson Number (1 -2 1 0 0 0) (note that the Doodson Numbers used in the computation of  $V_n(t_0)$  must be in solar time), and  $\Phi = 270^\circ$  (see Table I.4), the astronomical argument would be written  $-2s+h+270$ . Hence, the equilibrium phase for  $O_1$  and  $M_2$  are simply:

$$V_{O_1}(t_0) = -2 s(t_0) + h(t_0) + 270^\circ$$

and

$$V_{M_2}(t_0) = -2 s(t_0) + 2h(t_0) \quad (\text{I.61})$$

Values of  $s(t_0)$  and  $h(t_0)$  are easily computed using one of the equations of time given at the end of the chapter. In this notation, Eq.I.56 is written:

$$\zeta_{M_2}^e = 3 \left( \frac{5}{96\pi} \right)^{1/2} H_{M_2} \cos^2 \phi \cos(\omega_{M_2} t + 2s(t_0) - 2h(t_0) + u_{M_2}).$$

**Table I.4 Tidal parameters of the major tidal constituents**

Constituent	Astronomical argument*	Speed °/h
<b>Semidiurnal</b>		
M <sub>2</sub>	$-2s + 2h$	28.984
S <sub>2</sub>	0	30.000
N <sub>2</sub>	$-3s + 2h + p$	28.440
K <sub>2</sub>	$2h$	30.082
<b>Diurnal</b>		
K <sub>1</sub>	$h + 90^\circ$	15.041
O <sub>1</sub>	$-2s + h - 90^\circ$	13.943
P <sub>1</sub>	$-h - 90^\circ$	14.958
Q <sub>1</sub>	$-3s + h + p - 90^\circ$	13.399
<b>Long period</b>		
Mf	$2s$	1.098
Mm	$s - p$	0.544
Ssa	$2h$	0.082

\* Some tables add  $360^\circ$  to the phase, e.g. list  $270^\circ$  instead of  $-90^\circ$ .

In Table I.5 we define 11 major constituents in the semidiurnal, diurnal and long period ranges. The term  $\zeta_n^e$  represents the magnitude of the constituent in the tidal potential. The largest such term is M<sub>2</sub>, with amplitude 0.24 m, followed by K<sub>1</sub>, with amplitude 0.14 m. The frequencies of the constituents in the harmonic model (Eq. I.57) can be expressed either by speeds in °/h (Table I.4) or radian/s (Table I.5). From Table I.5 tidal constituents are clustered around the main diurnal and semidiurnal periods.

**Table I.5 Parameters of the Major Tidal Constituents**

Constituent		Period <sup>1</sup>	Freq. (s <sup>-1</sup> )	$\zeta_n^e$ (m)
<b>Semidiurnal</b>				
Principal Lunar	M <sub>2</sub>	12.421 msh	1.40519·10 <sup>-4</sup>	0.242334
Principal Solar	S <sub>2</sub>	12.000 msh	1.45444·10 <sup>-4</sup>	0.112841
Elliptical Lunar	N <sub>2</sub>	12.658 msh	1.37880·10 <sup>-4</sup>	0.046398
Declination Luni-Solar	K <sub>2</sub>	11.967 msh	1.45842·10 <sup>-4</sup>	0.030704
<b>Diurnal</b>				
Declination Luni-Solar	K <sub>1</sub>	23.934 msh	0.72921·10 <sup>-4</sup>	0.141565
Principal lunar	O <sub>1</sub>	25.819 msh	0.67598·10 <sup>-4</sup>	0.100574
Principal solar	P <sub>1</sub>	24.066 msh	0.72523·10 <sup>-4</sup>	0.046843
Elliptical lunar	Q <sub>1</sub>	26.868 msh	0.64959·10 <sup>-4</sup>	0.019256
<b>Long-Period</b>				
Fortnightly Lunar	M <sub>f</sub>	13.661 msd	0.053234·10 <sup>-4</sup>	0.041742
Monthly Lunar	M <sub>m</sub>	27.555 msd	0.026392·10 <sup>-4</sup>	0.022026
Semiannual Solar	S <sub>sa</sub>	182.621 msd	0.0038921·10 <sup>-4</sup>	0.019446

<sup>1</sup> msh: mean solar hour    msd: mean solar day

## 6. THE ORIGINS OF MAJOR TIDAL VARIATIONS

The fortnightly or spring/neap cycle of tides may be understood in terms of two signals going in and out of phase. This phenomenon is known as a "beats" or "beating". When a pair of slightly-different frequencies of similar amplitude add together, their sum undergoes a regular cycle between near-zero magnitude (neaps), and a magnitude equal to the sum of the pair (springs). This may be seen using the identity

$$\begin{aligned} \cos(\omega_1 t) + \cos(\omega_2 t) &= 2 \cos \frac{1}{2}(\omega_1 - \omega_2)t \cos \frac{1}{2}(\omega_1 + \omega_2)t = \\ &= 2 \cos \omega_m t \cos \omega_c t \end{aligned} \quad (\text{I.62})$$

where  $\omega_c = \frac{1}{2}(\omega_1 + \omega_2)$  and  $\omega_m = \frac{1}{2}(\omega_1 - \omega_2)$  are carrier and modulation frequencies. The shorter (carrier) and the longer (modulation) periods are expressed as,

$$\frac{2\pi}{T_c} = 0.5\left(\frac{2\pi}{T_1} + \frac{2\pi}{T_2}\right) \quad \text{or} \quad T_c = \frac{2T_1 T_2}{T_1 + T_2} \quad (\text{I.63a})$$

$$\frac{2\pi}{T_m} = 0.5\left(\frac{2\pi}{T_1} - \frac{2\pi}{T_2}\right) \quad \text{or} \quad T_m = \frac{2T_1 T_2}{T_2 - T_1} \quad (\text{I.63b})$$

This shorter wave period  $T_c$  is modulated by the longer wave period  $T_m$ . The most important tidal beat is between M<sub>2</sub> and S<sub>2</sub>, in whose case the shorter-period wave is semidiurnal. The frequencies of M<sub>2</sub> and S<sub>2</sub> are 1.9322 d<sup>-1</sup> and 2.0 d<sup>-1</sup> respectively (where d is mean solar day); hence the modulation has frequency 0.0678 d<sup>-1</sup>, the inverse of which, 14.75 days, is the beat period (fortnightly cycle). Of course, a power spectrum of the two

combined signals would contain no power at the beat period. The fortnightly tide "Msf" is caused by a fortnightly variation in the declination of the moon.

If the earth, sun and moon orbits were circular rather than elliptical, and in the same plane, and the earth's axis of rotation were perpendicular to that plane, the only important tidal frequencies would be  $M_2$ ,  $S_2$ , and their multiples and compounds ( $M_6$ ,  $MS_4$ , etc.). All the other tidal frequencies arise because of the orbital ellipticities, the angle between the orbital planes, and the tilt of the earth's axis. All the other tidal frequencies arise from these three variations and as a consequence can be expressed as simple linear combinations of their rates of change.

The modulation of the amplitude ( $a_c$ ) of the harmonic wave ( $a_c \cos(\omega_c t)$ ) by a signal of lower amplitude and frequency ( $a_m \cos(\omega_m t)$ ) can be represented as

$$(a_c + a_m \cos(\omega_m t)) \cos(\omega_c t)$$

which we can write

$$a_c \cos(\omega_c t) + a_m \cos(\omega_m t) \cos(\omega_c t).$$

Then using  $2 \cos \alpha \cos \beta = \cos(\alpha + \beta) + \cos(\alpha - \beta)$ , we have

$$a_c \cos(\omega_c t) + \frac{a_m}{2} \cos(\omega_c + \omega_m)t + \frac{a_m}{2} \cos(\omega_c - \omega_m)t. \quad (\text{I.64})$$

Thus we have our original frequency (whose amplitude is unaffected), plus two "sidebands" whose frequencies are slightly above and below it. This type of modulation is associated with many of the constituents of the equilibrium tide. For example, the ellipticity of the moon's orbit adds two sidebands ( $N_2$  and  $L_2$ ) to the  $M_2$  constituent due to the changing distance between the centers of mass of earth and moon. The period of  $M_2$  is 12.421 hours, and the period required for the moon to complete an orbit (i.e., to reach successive perigees, known as the anomalistic month) is 27.5546 days. Thus, the  $M_2$  speed is  $28.984^\circ/\text{hour}$  and the modulation speed is  $0.544^\circ/\text{hour}$ . In accordance with Eq. I.64, our new sideband speeds are  $28.984 \pm 0.544^\circ/\text{hour}$ , i.e.,  $28.44$  and  $29.53^\circ/\text{hour}$  – the speeds associated with  $N_2$  and  $L_2$ .  $N_2$  and  $L_2$  are known as the larger and smaller elliptical lunar semidiurnal constituents. If effects of angular speed are considered, it can be shown that the tidal potential of  $N_2$  is larger than that of  $L_2$ .

The terms  $T_2$  and  $R_2$  are the solar equivalents of  $N_2$  and  $L_2$ . Their origin is in the ellipticity of earth's orbit around the sun and they are known respectively as the larger and smaller solar elliptic semidiurnals. Their speeds are  $\omega_{S_2} + \omega_{S_a}$  and  $\omega_{S_2} - \omega_{S_a}$  ( $30. \pm 0.041 = 29.941$  and  $30.041^\circ/\text{hour}$ ).  $T_2$  and  $R_2$  are known as the larger and smaller elliptical solar semidiurnal constituents.

In the expansion of the equilibrium tide, the diurnals  $M_1$  and  $S_1$  have zero amplitude because they are defined in the equatorial plane ( $\delta = 0$ ), and the diurnal species are proportional to  $\sin 2\delta$  (Eq. I.50). Nevertheless, the amplitudes of the sum and difference frequencies of Eq. I.62 are nonzero due to the changing declinations of the moon and sun. In the case of the moon, the declination changes with a period 27.3217 days (the sidereal month), i.e. with a speed of  $0.549^\circ/\text{hour}$ . The speeds associated with these changes are

$14.492 \pm 0.549^\circ/\text{hour} = 13.943$  and  $15.041^\circ/\text{hour}$ . These are the speeds of  $O_1$  and  $K_1$ .  $O_1$  is the lunar declinational diurnal constituent, and  $K_1$ , because as we shall see it also contains a contribution from the solar tidal potential.

The origin of the solar analogs of  $O_1$  and  $K_1$  is similar. In this case, the central frequency is  $15^\circ/\text{hour}$  ( $360^\circ/\text{msd}$ ). The period of the solar declination is 365.2564 days (the sidereal year), so the speed is  $0.041^\circ/\text{hour}$ . Hence, the sum and difference frequencies are  $15. \pm 0.041^\circ/\text{hour} = 14.959$  and  $15.041^\circ/\text{hour}$ . The first is the speed of  $P_1$ , and the latter is the same as we found for  $K_1$ .  $P_1$  is known as the solar declinational diurnal constituent.

Although as we have said there is no harmonic in the equilibrium tide with speed  $15^\circ/\text{hour}$ , there is a constituent with this frequency, known as  $S_1$ , that is included in many tidal analyses. It owes its origin to meteorological effects and is commonly referred to as a "radiational tide".

## 7. NODAL PHASE

The moon's elliptical orbit around earth is at an angle to the earth's axis of rotation, and over time the orientation of the plane defined by the elliptical orbit rotates. As it does so, its nodes – the intersections of the orbit with the plane of the earth's equator – circuit westward through  $360^\circ$  of longitude. It does this once every 18.61 years. This regression of the lunar nodes or nodal cycle has a modulating effect on the amplitude and phase of all lunar tidal constituents, because over its course the maximum declination of the moon varies between  $28^\circ 36'$  and  $18^\circ 18'$  latitude north and south of earth's equator.

For each important line in the spectrum of the lunar equilibrium tide, there is a small sideband line, due to the nodal modulation, which cannot be resolved in typical tidal data (due to geophysical noise and limited duration). For example  $M_2$  and  $N_2$ , the two largest lunar constituents, each have significant sidebands whose frequency is less than the principal lines by an amount  $2\pi/N$ . The Doodson Numbers of the sidebands are identical to those of the principals except for the value of  $N$ , which equals one as opposed to zero (as is the case for  $M_2$  and  $N_2$ ). In both cases, the sideband signals are also out of phase from the principals by  $180^\circ$ .

The procedure normally adopted in tidal analysis was originally proposed by **Darwin (1901)**. Rather than attempt to resolve the small sideband frequencies due to the nodal modulation, the nodal cycle is accounted for by modulating the lunar and partly-lunar constituents with "corrections" known as the nodal factor  $f_n(t)$  and nodal phase  $u_n(t)$  (a subscript  $n$  is added here to emphasise that there are different factors and angles for different harmonics). The nodal factor is close to unity, and the phase angle is always small (they are identically unity and zero for purely solar terms). Hence, they amount to small, time-varying modulations of the principal lunar constituents.

We first write  $M_2$  and its sideband, which we will call  $M_{2-}$  in the following form

$$\zeta_{M_2}^e \cos(2\omega t - 2s(t) + 2h(t))$$

$$\zeta_{M_{2-}}^e \cos(2\omega t - 2s(t) + 2h(t) - N(t) + 180^\circ)$$

These two waves are of the form  $a \cos \omega t$  and  $b \cos(\omega t + \theta(t))$  where  $a \gg b$  and  $\theta$  is a small angle. We wish to express their sum as a single cosine term of amplitude  $a$  modulated by  $f(t)$ , and with phase shift  $u(t)$ :

$$a \cos \omega t + b \cos(\omega t + \theta(t)) = f(t)a \cos(\omega t + u(t)) \tag{I.65}$$

Using a standard trigonometric identity and identifying like terms on either side of Eq.I.65, it follows that:

$$a + b \cos \theta(t) = f(t)a \cos u(t) \quad \text{and} \quad b \sin \theta(t) = f(t)a \sin u(t) \tag{I.66}$$

From the above equalities we obtain the following relations:

$$\tan u(t) = \frac{b \sin N(t)}{a + b \cos N(t)} \quad \text{and} \quad a^2 + 2ab \cos N(t) + b^2 = f(t)^2 a^2 \tag{I.67}$$

Because amplitudes  $a \gg b$ , therefore the following approximations hold:

$$u(t) \simeq \tan u(t) = \frac{b}{a} \sin N(t) \quad \text{and} \quad f(t) = [1 + (\frac{b}{a})^2 + 2\frac{b}{a} \cos N(t)]^{1/2} \tag{I.68}$$

The regression of the lunar nodes also produces a small but measurable long-period constituent of the equilibrium tide, called the nodal tide, of period 18.61 years. Since the nodal sidebands (e.g. the one we called "M<sub>2-</sub>") contain a phase shift of 180°, when the nodal tide is a maximum, the modulation is a minimum. The nodal tide is often ignored as it is smaller than long-term oceanographic and geophysical changes. Its latitudinal dependence is the same as that of all the long period tides (cf. Eq.I.49):  $\frac{3}{2} \cos^2 \phi - 1$ . It is about 9 mm at the equator, falls to zero at 35° north and south, and reaches a maximum of 18 mm at the poles - about 13 mm when the elasticity of the earth is accounted for.

The  $f$  and  $u$  factors may be held constant for as much as a year without adding significant error to the prediction of a principle tidal constituent. Generally a value is calculated for the center of each prediction interval of up to one year. For predictions spanning longer than 18.6 years, the  $f$  and  $u$  factors may be eliminated, and terms included in the prediction to explicitly model the satellite sidebands as well as the 18.6 year nodal tide.

The nodal corrections are shown in Table I.6 for the important lunar and lunisolar constituents. Tabulations can also be found in [Shureman \(1958\)](#) and [Doodson and Warburg \(1941\)](#).

**Table I.6 Nodal Parameters of the Major Tidal Constituents**

Constituent	amplitude factor $f$	phase factor $u$
Mm	$1.000 - 0.130 \cos N(t)$	$0.0^\circ$
Mf	$1.043 + 0.414 \cos N(t)$	$-23.7^\circ \sin N(t)$
O <sub>1</sub> , Q <sub>1</sub>	$1.009 + 0.187 \cos N(t)$	$10.8^\circ \sin N(t)$
K <sub>1</sub>	$1.006 + 0.115 \cos N(t)$	$-8.9^\circ \sin N(t)$
N <sub>2</sub> , M <sub>2</sub>	$1.000 - 0.037 \cos N(t)$	$-2.1^\circ \sin N(t)$
K <sub>2</sub>	$1.024 + 0.286 \cos N(t)$	$-17.7^\circ \sin N(t)$

In Fig. I.14, the time dependence of the amplitude factor ( $f$ ) in the 20<sup>th</sup> century and beginning of 21<sup>st</sup> century is shown for  $M_2$ ,  $O_1$  and  $K_1$ . In 2006, the nodal cycle is acting to suppress  $M_2$  while enhancing  $O_1$  and  $K_1$ .

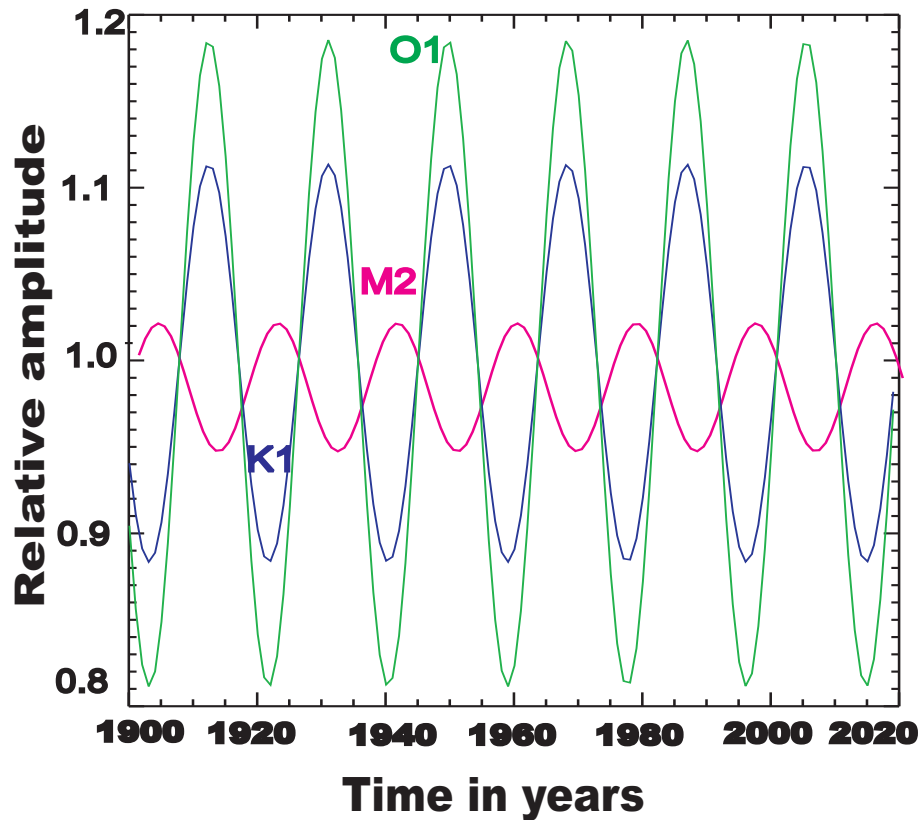


FIGURE I.14

Amplitude factor  $f(t)$  for the  $M_2$ ,  $K_1$  and  $O_1$  constituents

## 8. LONGITUDE FORMULAS

Algebraic formulas for  $s(t)$ ,  $h(t)$ ,  $p(t)$ ,  $N(t)$ , and  $p_s(t)$  are given in a number of sources, including [Cartwright \(1982\)](#), [Doodson \(1921\)](#), [Franco \(1988\)](#), [Schureman \(1958\)](#) and the tidal package TASK-2000 (IOS, UK), and may be easily programmed. Several of these are given below, starting with Cartwright's. In each case, the results are phases valid at 0000 hours UT of the input day.

Cartwright's formula is based on an "epoch" of 1200 hours ET, 31 December 1899. Let  $d$  be the number of calendar days counted from the epoch, and  $T=d/36525$ . (A subroutine known as `zeller.for` is widely available for counting day numbers.) Noon on 1 January 1900 would be  $d = 1$ . Units are "revolutions", so must be multiplied by 360 to convert to degrees, for example. (The modulus would of course also be taken, eg.  $2765.4^\circ$  is equivalent to  $245.4^\circ$ .) Then:

$$s(t) = 0.751206 + 1336.855231 * T - 0.000003 * T^2$$

$$h(t) = 0.776935 + 100.002136 * T + 0.000001 * T^2$$

$$\begin{aligned}
p(t) &= 0.928693 + 11.302872 * T - 0.000029 * T^2 \\
N(t) &= 0.719954 - 5.372617 * T + 0.000006 * T^2 \\
p_s(t) &= 0.781169 + 0.004775 * T + 0.000001 * T^2
\end{aligned} \tag{I.69}$$

Phase increases linearly in time aside from a small quadratic factor which accounts for small secular trends in the speeds.

TASK-2000 is based on an epoch of 0000 hours UT, 1 January 1900. The formula is said to be accurate for at least the period 1800-2100:

$$\begin{aligned}
s(t) &= 277.0247 + 129.38481IY + 13.17639DL \\
h(t) &= 280.1895 - 0.23872IY + 0.98565DL \\
p(t) &= 334.3853 + 40.66249IY + 0.11140DL \\
N(t) &= 259.1568 - 19.32818IY - 0.05295DL \\
p_s(t) &= 281.2209 + 0.017192IY
\end{aligned} \tag{I.70}$$

In the above, IY = year -1900 (for example, for the year 1905, IY = 5, and for the year 1895, IY = -5), and DL = IL + IDAY -1, where IL is the number of leap years from 1900 (which was not a leap year) up to the start of year IY. Thus, IL = (IY-1)/4 in FORTRAN, and IDAY is the day number in the year in question. For example, for 12 January 1905, DL = 12. For years less than 1900 then one can compute IL = IABS(IY)/4 and DL = -IL + IDAY - 1 in FORTRAN.

**Schureman (1958)** is very similar to TASK-2000, using the same epoch, but with the Julian century (36526 days) as a unit of time.

$$\begin{aligned}
s(t) &= 277.0248 + 481267.8906T + 0.0011T^2 \\
h(t) &= 280.1895 + 36000.7689T + 3.0310^{-4}T^2 \\
p(t) &= 334.3853 + 4069.0340T - 0.0103T^2 \\
N(t) &= 259.1568 - 1934.142T + 0.0021T^2 \\
p_s(t) &= 281.2209 + 1.7192T + 0.00045T^2
\end{aligned} \tag{I.71}$$

The time T in the 20 century is

$$T = [365(Y - 1900) + (D - 1) + i]/36526$$

where i is the integer part of 0.25(Y-1901). The time is defined for 0000 hour UT on day D in year Y. Similar formula can be written for the 21 century time

$$T = [365(Y - 2000) + (D - 1) + i]/36526$$

Here i=INT[0.25(Y-2001)].

**Franco's (1988)** algorithms are given in terms of the Gregorian century, which may make them more convenient for dates further into the past or future. However, they carry one decimal place less on many terms than the foregoing algorithms, implying slightly less accuracy for the present time.

Three algorithms were given for computing reference phase,  $V_n(t_0)$ .  $V_n(t_0)$  is computed as a function of the number of days elapsed between an epoch (e.g. 0000 hours UT on 1 January 1900) and the start of a day on which predictions are required. UT, or Universal Time, was the basis for the formulas of Doodson (1921) and Schureman (1976), while ET, or Ephemeris Time, was the basis for the formulas of Cartwright and Tayler (1971). At the start of the 1900s, the two time scales coincided. At the present time, however, they differ by about one minute. Estimates of  $V_n(t_0)$  for a particular time in the present, using the two formulas, differ by an equivalent amount in degrees, depending on the speed of the constituent.

All of the above formulas are still in use at different institutions, and for most practical tide predictions the differences are negligible. However, Cartwright (1985) argues that compelling reasons exist for adopting new formulas which were published in the USA/UK Astronomical Almanac for 1984. These new formulas are based on the TDT time scale. TDT, which stands for Terrestrial Daylight Time, differs from UT by a varying amount, whose value can also be found in the almanac. The new formulas are also based on a more recent epoch: 1200 hours TDT on 31 December, 1999.

Where reference is found to GMT (Greenwich Mean Time), or Z (Zulu time), one can safely substitute in the term UT, which is essentially synonymous. However, data supplied by most observatories actually conform to a specific version of UT, such as UT1 or UTC. If accuracy greater than one second is required, then the version must be specified. The instantaneous difference between UTC and UT1 is available electronically.

## REFERENCES

- Cartwright, D. E. 1999. *Tides, A Scientific History*. Cambridge University Press, 292pp.
- Cartwright, D.E. and R.J. Tayler 1971. New Computations of the Tide-Generating Potential. *Geophys. J. R. astr. Soc.*, v. 23, 45–74.
- Cartwright, D.E. and A. C. Edden 1973. Corrected Tables of Tidal Harmonics. *Geophys. J. R. astr. Soc.*, v. 33, 253–264.
- Darwin, G. H. 1901. *The Tides*. John Murray, London, 346pp.
- Defant, A. 1960. *Physical Oceanography*, vol. II, Pergamon Press, Oxford, 598pp.

- Dietrich, G., K. Kalle, W. Krauss, G. Siedler. 1980. *General Oceanography*, A Wiley-Interscience Publication, New York, 626pp.
- Dronkers, J. J. 1964. *Tidal Computations*. North-Holland Publishing Company, Amsterdam, 518pp.
- Doodson, A. T. 1921. The harmonic development of the tide-generating potential. *Proceedings of the Royal Society, A*. v. 100, 305–329. (reprinted in *Int. Hydr. Review*, 31, 11-35, 1954)
- Doodson, A. T. and H.D.Warburg. 1941. *Admiralty Manual of Tides*, HMSO, 270 pp.
- Franco, S. 1988. *Tides: fundamentals, analysis and prediction*. Fundacao Centro Tecnologico de Hidraulica, Sao Paulo, Brazil.
- Godin, G. 1988. *Tides*. , CICESE, Ensenada, Mexico, 290pp.
- Kantha L. H. and C. A. Clayson. 2000. *Numerical Model of Ocean and Oceanic Processes*. Academic Press, San Diego, 936pp.
- Macmillan, D. H. 1966. *Tides*. American Elsevier Publishing Company, Inc., New York, 240pp.
- Neumann, G. and W. J. Pierson 1966. *Principles of Physical Oceanography*, Prentice-Hall (Englewood Cliffs, N.J) , 545pp.
- Platzman, G. W. 1971. *Ocean Tides and Related Waves*. In *Mathematical Problems in the Geophysical Sciences*, Editor H. Reid, American Mathematical Society, Providence, 239–291.
- Proudman, J. 1953. *Dynamical Oceanography*, Methuen& Co., London, 409pp.
- Pugh, D. T., 1987. *Tides, Surges and Mean Sea-Level*, John Wiley & Sons, 472pp.
- Rossiter, J. R. and G. W. Lennon. 1968. An intensive analysis of shallow water tides, *J. R. Astr. Soc.*, 16, 275-293.
- Schureman, P. 1958. *Manual of Harmonic Analysis and Prediction of Tides*, US Government Printing Office, Washington, 317pp.

Tamura Y., 1987. A harmonic development of the tide-generating potential, *Bull. Inf. Marr. Terr.*, 99, 6813-6855.

Thomson, W. (Lord Kelvin). 1882. *The Tides*. Evening Lecture to the British Association at the Southampton Meeting, Friday, August 25th, 1882.

## CHAPTER II: BASIC EQUATIONS

### 1. Rectangular and spherical system of coordinates

The effects of the Earth's curvature on the motion of a fluid at the relatively small scales of the order of 1000 km may be neglected. To describe this motion a **rectangular (Cartesian) system** of coordinates will be employed, thus making the equations and discussion much simpler. We shall rewrite the set of equations of motion to describe tides in the Cartesian system as (Gill, 1982; Kowalik and Murty, 1993)

$$\frac{\partial u}{\partial t} + u \frac{\partial u}{\partial x} + v \frac{\partial u}{\partial y} - fv = -\frac{1}{\rho} \frac{\partial p_a}{\partial x} - g \frac{\partial \zeta_s}{\partial x} - \frac{\partial \Omega_T}{\partial x} + \tau_x^s / \rho D - \tau_x^b / \rho D + N_h \Delta u \quad (\text{II.1})$$

$$\frac{\partial v}{\partial t} + u \frac{\partial v}{\partial x} + v \frac{\partial v}{\partial y} + fu = -\frac{1}{\rho} \frac{\partial p_a}{\partial y} - g \frac{\partial \zeta_s}{\partial y} - \frac{\partial \Omega_T}{\partial y} + \tau_y^s / \rho D - \tau_y^b / \rho D + N_h \Delta v \quad (\text{II.2})$$

These are so-called vertically averaged equations with velocity being the function of the horizontal coordinates and time. In these equations:  $x$  and  $y$  are coordinates directed towards East and North, respectively; velocities along these coordinates are  $u$  and  $v$ ;  $t$  is time; **Coriolis parameter**  $f = 2\Omega \sin \phi$  is a function of the **Earth's angular velocity**  $\Omega = 7.29 \times 10^{-5} \text{ s}^{-1}$  and the latitude —  $\phi$ ;  $p_a$  is the atmospheric pressure;  $\rho$  denotes density of the sea water;  $\zeta_s$  is the sea level change around the mean sea level;  $\Omega_T$  is the tide producing potential as defined in Ch.I;  $\tau_x^s$  and  $\tau_y^s$  are components of the stress at the free surface, and  $\tau_x^b$  and  $\tau_y^b$  are components of the stress at the bottom;  $D = H + \zeta_s$  is the total depth equal to the average depth  $H$  plus the sea level variations  $\zeta_s$ . The horizontal friction terms are defined by the horizontal eddy viscosity  $N_h$  and two-dimensional Laplace operator  $\Delta = \frac{\partial^2}{\partial x^2} + \frac{\partial^2}{\partial y^2}$ . In the above equations the vertical friction expressed by the stresses and the horizontal friction expressed by the horizontal eddy viscosity serve to dissipate the oceanic motion. This motion is variable in time and also display space variability, therefore the above simple formulas describe the first approximation of the complicated physics of dissipation. In the tidal motion the main dissipation of the energy is caused by frictional forces at the bottom. Measurements of the bottom stress have been performed under the different flow conditions. An excellent review of the measurements and processes in the tidal bottom boundary layer was given by **Marchuk and Kagan (1977)**. **G. I. Taylor (1919)** showed that the **bottom stress** is proportional to the square of the average velocity:

$$\tau_x^b = \rho r u \sqrt{u^2 + v^2} \quad \text{and} \quad \tau_y^b = \rho r v \sqrt{u^2 + v^2} \quad (\text{II.3})$$

The dimensionless friction coefficient  $r$  depends on the various factors but mainly it is defined by the bottom roughness. Mean value of  $r$  ranges from  $r = 2 \times 10^{-3}$  to  $r = 3.5 \times 10^{-3}$ .

The horizontal friction expressed in the above equation by the horizontal eddy viscosity coefficient is less amenable to the definition. Often in the first approximation it is assumed to be constant, frequently used coefficient is both variable in space and time, see, **Smagorinsky (1963)**.

The tidal dissipation estimates based on the above terms show that the major work is done by the bottom stress. This process occurs mainly in the shallow water where tidal velocities are large enough. In the deep ocean the dissipation processes take place due to generation of an internal tide over the rough bottom topography. Recent estimates (**Jayne and Laurent, 2001**) show that inclusion of the internal wave dissipation mechanism increases the amount of tidal dissipation. Proposed new stress is proportional to the average velocity and is a function of the vertical stratification and the bottom roughness. Generally, such stress can be applied only in the deeper ocean at the depth greater than 200m. Internal stress is formulated as

$$\tau_i^x = r_1 u \quad \text{and} \quad \tau_i^y = r_1 v \quad (\text{II.4})$$

Here  $r_1 \simeq 10^{-5}$ , is dimensional coefficient expressed in the CGS units.

The tidal potential in eqs. II.1 and II.2 is related to the equilibrium tides discussed in Ch.I. It is given by the equilibrium surface elevation ( $\zeta_{eql,s}$ ) as (see eq. I.39)

$$\zeta_{eql,s} = -\frac{\Omega_T}{g} \quad (\text{II.5})$$

Eqs. II.1 and II.2 are often called the long wave equations or shallow water equations. The assumption is made that the horizontal velocities do not change along the vertical direction, vertical motion is absent and instead of the vertical equation of motion a simple hydrostatic relation holds for pressure.

For the three unknown variables ( $u, v, \zeta_s$ ) only two equations have been introduced, therefore one additional equations is required — this will be the equation of continuity. In the tidal problems the sea water can be regarded as an incompressible fluid, for such fluid the equation of continuity expresses the conservation of volume,

$$\frac{\partial \tilde{u}}{\partial x} + \frac{\partial \tilde{v}}{\partial y} + \frac{\partial w}{\partial z} = 0 \quad (\text{II.6})$$

Here vertical velocity  $w$  is included to delineate the way the sea level ( $\zeta_s$ ) and the bottom deformation ( $\zeta_b$ ) are introduced into equation of continuity. Integrating eq. II.6 along the vertical direction from the free surface  $z = \zeta_s$  to the bottom  $z = -H + \zeta_b$  we arrive at,

$$\frac{\partial}{\partial t}(\zeta_s - \zeta_b) + \frac{\partial u D}{\partial x} + \frac{\partial v D}{\partial y} = 0 \quad (\text{II.7})$$

$D$  is the **total depth defined as  $D = H + \zeta_s - \zeta_b$** .

Velocities  $\tilde{u}$  and  $\tilde{v}$  depend on three coordinates  $x, y$ , and  $z$ . These velocities are usually averaged along the vertical  $z$  coordinate to derive the component  $u$  and  $v$  occurring in the long wave equations (II.1 and II.2), thus

$$u = \frac{1}{D} \int_{-H+\zeta_b}^{\zeta_s} \tilde{u} dz \quad \text{and} \quad v = \frac{1}{D} \int_{-H+\zeta_b}^{\zeta_s} \tilde{v} dz \quad (\text{II.8})$$

Actual observations of the tidal currents show that the variability along the vertical direction is quite small. Therefore, in all practical applications for the tide analysis the equations (II.1, II.2 and II.7) are written for the vertically averaged horizontal velocities  $u$  and  $v$ . Whenever an integration domain stretches over 1000 km the use of a spherical system is advisable. Equations of motion in the spherical system ( $\lambda$  is longitude and  $\phi$  is latitude) can be written as ( Gill, 1982)

$$\begin{aligned} \frac{\partial u}{\partial t} + \frac{u}{R \cos \phi} \frac{\partial u}{\partial \lambda} + \frac{v}{R} \frac{\partial u}{\partial \phi} - (2\Omega + \frac{u}{R \cos \phi})v \sin \phi = \\ - \frac{1}{\rho R \cos \phi} \frac{\partial p_a}{\partial \lambda} - \frac{g}{R \cos \phi} \frac{\partial \zeta}{\partial \lambda} - \frac{1}{R \cos \phi} \frac{\partial \Omega_T}{\partial \lambda} + \frac{\tau_\lambda^s - \tau_\lambda^b}{\rho D} + A'_1 u \end{aligned} \quad (\text{II.9})$$

$$\begin{aligned} \frac{\partial v}{\partial t} + \frac{u}{R \cos \phi} \frac{\partial v}{\partial \lambda} + \frac{v}{R} \frac{\partial v}{\partial \phi} + (2\Omega + \frac{u}{R \cos \phi})u \sin \phi = \\ - \frac{1}{\rho R} \frac{\partial p_a}{\partial \phi} - \frac{g}{R} \frac{\partial \zeta}{\partial \phi} - \frac{1}{R} \frac{\partial \Omega_T}{\partial \phi} + \frac{\tau_\phi^s - \tau_\phi^b}{\rho D} + A'_1 v \end{aligned} \quad (\text{II.10})$$

The horizontal friction term has been simplified in (II.9) and (II.10) by introducing the operator  $A'_1$

$$A'_1 = N_h \left( \frac{1}{R^2 \cos^2 \phi} \frac{\partial^2}{\partial \lambda^2} + \frac{1}{R^2 \cos \phi} \frac{\partial}{\partial \phi} (\cos \phi \frac{\partial}{\partial \phi}) \right) \quad (\text{II.11})$$

For the equation of continuity in the spherical system of coordinates the following form will be used

$$\frac{\partial(\zeta_s - \zeta_b)}{\partial t} + \frac{1}{R \cos \phi} \frac{\partial u D}{\partial \lambda} + \frac{1}{R \cos \phi} \frac{\partial}{\partial \phi} (Dv \cos \phi) = 0 \quad (\text{II.12})$$

## 2. Total tidal potential

The actually recorded tide by the tide gauges defines a surface oscillation ( $\zeta$ ) relative to the ocean bottom, therefore the surface ( $\zeta_s$ ) and the bottom ( $\zeta_b$ ) displacements are connected as,

$$\zeta = \zeta_s - \zeta_b \quad (\text{II.13})$$

In the equilibrium tide the displacement relative to the bottom is

$$\zeta_{eql} = \zeta_{eql,s} - \zeta_{eql,b} \quad (\text{II.14})$$

Equations of motion and continuity introduced in the previous section will serve to compute distribution of tides in the ocean. The tide generating potential ( $\Omega_T$ ) for the ocean as defined in Ch.I has to be corrected for the contribution due to the solid earth tides and atmospheric tides. The latter, enter the equation of motion through the terms  $\frac{\partial p_a}{\partial x}$  and  $\frac{\partial p_a}{\partial y}$ . The change of pressure arising from the atmospheric tides is of the order of 1mb which leads to the static sea level change of approximately 1 cm. If the Earth

were the rigid body none of the deformation will occur, but the elastic yielding to the tide generating forces generates quite big tides. Additionally the ocean and earth tides generate disturbance in the earth gravity field which contributes to the tide modifications. The ocean bottom changes caused by tides can be expressed by the tidal potential as,

$$\zeta_{eql,b} = -h \frac{\Omega_T}{g} \quad (\text{II.15})$$

Here  $h \approx 0.6$  is the Love number. From this expression we conclude that the amplitude of the equilibrium earth tide are 0.6 of the amplitude of the equilibrium ocean tides. The correction arising from the gravity field disturbance increases the surface displacement due to the equilibrium tide (**Hendershott, 1977**),

$$\zeta_{eql,s1} = -k \frac{\Omega_T}{g} \quad (\text{II.16})$$

Here  $k \approx 0.3$  is a different Love number.

Invoking this correction the surface displacement due to the tidal potential defined by eq.II.5 changes to

$$\zeta_{eql,s} = -(1+k) \frac{\Omega_T}{g} \quad (\text{II.17})$$

The equilibrium displacement relative to the bottom (II.14) can be defined with the help of II.17 and II.15 as

$$\zeta_{eql} = \zeta_{eql,s} - \zeta_{eql,b} = -(1+k-h) \frac{\Omega_T}{g} \quad (\text{II.18})$$

Introducing surface displacement as defined by eqs. II.13 and II.14 and equilibrium surface elevation from II.5 into eqs. II.1 and II.2 we arrive at the following set of equations of motion,

$$\frac{\partial u}{\partial t} + u \frac{\partial u}{\partial x} + v \frac{\partial u}{\partial y} - fv = -\frac{1}{\rho} \frac{\partial p_a}{\partial x} - g \frac{\partial \zeta + \zeta_b}{\partial x} + g \frac{\partial \zeta_{eql} + \zeta_{eql,b}}{\partial x} + \tau_x^s / (\rho D) - \tau_x^b / (\rho D) + N_h \Delta u \quad (\text{II.19})$$

$$\frac{\partial v}{\partial t} + u \frac{\partial v}{\partial x} + v \frac{\partial v}{\partial y} + fu = -\frac{1}{\rho} \frac{\partial p_a}{\partial y} - g \frac{\partial \zeta + \zeta_b}{\partial y} + g \frac{\partial \zeta_{eql} + \zeta_{eql,b}}{\partial y} + \tau_y^s / (\rho D) - \tau_y^b / (\rho D) + N_h \Delta v \quad (\text{II.20})$$

In equation of continuity II.7 the difference of the surface and bottom displacements is given by eq. II.13. Analyzing eqs. II.19 and II.20 we assume that the bottom deformation is described by the equilibrium deformation, therefore,

$$\zeta_{eql,b} = \zeta_b \quad (\text{II.21})$$

This assumption eliminates the bottom displacement from the equations of motion.

Usually the tidal forcing in eqs.II.19 and II.20 is described through the terms which are multiplied by coefficients  $\alpha$  and  $\beta$ .

$$\frac{\partial u}{\partial t} + u \frac{\partial u}{\partial x} + v \frac{\partial u}{\partial y} - fv = -\frac{1}{\rho} \frac{\partial p_a}{\partial x} - g \frac{\partial \alpha \zeta}{\partial x} + g \frac{\partial \beta \zeta_{eql}}{\partial x} + \tau_x^s / (\rho D) - \tau_x^b / (\rho D) + N_h \Delta u \quad (\text{II.22})$$

$$\frac{\partial v}{\partial t} + u \frac{\partial v}{\partial x} + v \frac{\partial v}{\partial y} + fu = -\frac{1}{\rho} \frac{\partial p_a}{\partial y} - g \frac{\partial \alpha \zeta}{\partial y} + g \frac{\partial \beta \zeta_{eql}}{\partial y} + \tau_y^s / (\rho D) - \tau_y^b / (\rho D) + N_h \Delta v \quad (\text{II.23})$$

Coefficient  $\alpha$  defines additional correction due to ocean loading and self-attraction of the ocean tides. Its value ranges from 0.940 (for diurnal tides) to 0.953 (for semi-diurnal tides) according to **Ray and Sanchez (1989)**. The higher-order correction for the loading effect can be implemented as well, e.g., **Francis and Mazzega, (1990)**. The term  $\beta$  follows from eq.II.18 as

$$\beta \zeta_{eql} = (1 + k - h) \zeta_{eql} \quad (\text{II.24})$$

Here  $k$  and  $h$  denote Love numbers, which are equal to 0.302 and 0.602 for the semi-diurnal tides respectively. These values for the individual diurnal constituent may differ and according to **Wahr (1981)** for  $K_1$  constituent  $k = 0.256$  and  $h = 0.520$  and for  $O_1$  constituent  $k = 0.298$  and  $h = 0.603$ .

The equilibrium tide for the diurnal constituents is defined in Ch.I by formula I.66, in the following way,

$$\zeta_{eql} = fK \sin 2\phi \cos(\omega t + \kappa + \lambda + u)$$

which we rewrite as,

$$\zeta_{eql} = f_n \zeta_n \sin 2\phi \cos(\omega_n t + \kappa_n + \lambda + u_n) \quad (\text{II.25a})$$

to underline that each harmonic constituent has different amplitude, frequency and astronomical argument. If in numerical calculations only one constituent is considered we may disregard both nodal corrections and astronomical argument, and use above as:

$$\zeta_{eql} = \zeta_n \sin 2\phi \cos(\omega_n t + \lambda) \quad (\text{II.25b})$$

Here  $H_n = 14.565$  cm,  $\omega_n = 0.729221 \cdot 10^{-4}$  s<sup>-1</sup> for  $K_1$ , and  $H_n = 10.0514$  cm,  $\omega_n = 0.675981 \cdot 10^{-4}$  s<sup>-1</sup> for  $O_1$ ;  $\lambda$  denotes the longitude angle (see Table I.4).

From eq.I.65 the semidiurnal equilibrium sea level is

$$\zeta_{eql} = fK \cos^2 \phi \cos(\omega t + \kappa + 2\lambda + u)$$

this can be rewritten as,

$$\zeta_{eql} = f_n H_n \cos^2 \phi \cos(\omega_n t + \kappa_n + 2\lambda + u_n) \quad (\text{II.26a})$$

If and only if computations are done for one constituent in isolation we may simplify the expression for the equilibrium sea of semi-diurnal constituents as:

$$\zeta_{eql} = \zeta_n \cos^2 \phi \cos(\omega_n t + 2\lambda) \quad (\text{II.26b})$$

Here (see Table I.4),  $\zeta_n = 24.2334$  cm,  $\omega_n = 1.495189 \cdot 10^{-4}$  s<sup>-1</sup> for M<sub>2</sub>, and  $\zeta_n = 11.2841$  cm,  $\omega_n = 1.454410 \cdot 10^{-4}$  s<sup>-1</sup> for S<sub>2</sub>.

### 3 Energy equation

We shall continue by constructing energy equation because it is closely related to the physics of tide generation, propagation and dissipation. In order to derive this equation let us multiply (II.1) by  $Du$ , (II.2) by  $Dv$ , and (II.7) by  $\rho g \zeta_s$ . Adding the resulting equation on either side, we arrive at

$$\begin{aligned} & \frac{1}{2} \frac{\partial}{\partial t} [\rho D(u^2 + v^2) + \rho g \zeta_s^2] + \frac{\partial}{\partial x} \{ \rho u D[(u^2 + v^2)/2 + g \zeta_s] \} + \frac{\partial}{\partial y} \{ \rho v D[(u^2 + v^2)/2 + g \zeta_s] \} \\ & = (\tau_x^s u + \tau_y^s v - \tau_x^b u - \tau_y^b v) + \rho u D N_h \Delta u + \rho v D N_h \Delta v - \frac{\partial p_a}{\partial x} u D - \frac{\partial p_a}{\partial y} v D \\ & \quad - \rho \frac{\partial \Omega_T}{\partial x} u D - \rho \frac{\partial \Omega_T}{\partial y} v D + \rho g \zeta_s \frac{\partial \zeta_b}{\partial t} \end{aligned} \quad (\text{II.27})$$

The various terms in the above equation can be defined as follows:

1.  $e_k = \rho D(u^2 + v^2)/2$  denotes surface density of the **kinetic energy**; it is defined by velocity of the tidal motion and the total depth.
2.  $e_p = \rho g \zeta_s^2/2$  denotes surface density of the **potential energy**; it is defined by the sea level oscillations around mean sea level (MSL).
3. The second and the third terms in (II.27) represent the components of an **energy flux vector**. This vector characterizes the flux of energy through a unit width surface extended from the ocean surface to the bottom (**Kowalik and Untersteiner, 1978**). The components of the vector along latitude and longitude are

$$\mathbf{E}_h = \{ \rho u D[(u^2 + v^2)/2 + g \zeta], \rho v D[(u^2 + v^2)/2 + g \zeta] \} \quad (\text{II.28})$$

The first order approximation (not valid in very shallow water)

$$\mathbf{E}_{h1} = \{ \rho g H u \zeta, \rho g H v \zeta \} \quad (\text{II.29})$$

serves often to describe the energy transfer from the source to various locations.

4. Two terms in the eq. II.27 define the energy sources; the energy input is caused by the wind stress  $\tau_x^s u + \tau_y^s v$  and by the surface (atmospheric) pressure  $-\frac{\partial p_a}{\partial x} u D - \frac{\partial p_a}{\partial y} v D$ . These terms are not related to the tide motion, therefore they will be neglected in the tidal energy considerations.

5. The tidal **energy dissipation** takes place through the bottom stress:  $-\tau_x^b u - \tau_y^b v$  and the horizontal friction  $\rho u D N_h \Delta u + \rho v D N_h \Delta v$ .

6. The generation of the tidal energy is described by

$$-\rho \frac{\partial \Omega_T}{\partial x} u D - \rho \frac{\partial \Omega_T}{\partial y} v D + \rho g \zeta_s \frac{\partial \zeta_b}{\partial t}$$

To investigate behavior of various terms in the equation of energy balance an integration is carried out over the entire domain  $\Omega$ . Here we assume that the component of velocity normal to the boundary  $\Gamma$  is equal to zero. The domain  $\Omega$  represents surface of the water body closed by coastline  $\Gamma$ . Neglecting terms unrelated to tides, and averaging in time over period  $T$  yields to:

$$\begin{aligned} & \frac{1}{T} \int \left\{ \int \int \left[ \frac{\partial}{\partial x} \{ \rho u D [(u^2 + v^2)/2 + g \zeta_s] \} + \frac{\partial}{\partial y} \{ \rho v D [(u^2 + v^2)/2 + g \zeta_s] \} \right] dx dy \right\} dt \\ &= -\frac{1}{T} \int \left\{ \int \int \left[ (\tau_x^b u + \tau_y^b v) \right] dx dy \right\} dt + \frac{1}{T} \int \left\{ \int \int \left[ \rho u D N_h \Delta u + \rho v D N_h \Delta v \right] dx dy \right\} dt \\ & \quad - \frac{1}{T} \int \left\{ \int \int \left[ \rho \frac{\partial \Omega_T}{\partial x} u D + \rho \frac{\partial \Omega_T}{\partial y} v D + \rho g \zeta_s \frac{\partial \zeta_b}{\partial t} \right] dx dy \right\} dt \end{aligned} \quad (\text{II.30})$$

In local water bodies, like Cook Inlet, the energy generated due to tidal potential is small and often can be neglected. **LeProvost and Lyard (1997)** described detailed development of this term. The full solution, as can be gleaned from the last term requires not only tidal potential by the knowledge of the bottom deformation  $\zeta_b$ . In the energy balance computation for the local body, it is important to see how the energy flux is calculated. Denoting the components of an energy flux (cf. II.28) as  $E_{hx}$  and  $E_{hy}$  the first term in the above equation is

$$\frac{1}{T} \int \left\{ \int \int \left[ \frac{\partial}{\partial x} E_{hx} + \frac{\partial}{\partial y} E_{hy} \right] dx dy \right\} dt$$

and changing surface integral into contour integral we arrive at energy flux across the contour

$$\frac{1}{T} \int \left\{ \int \left[ E_{hx} dy + E_{hy} dx \right] \right\} dt \quad (\text{II.31})$$

Along with the above general equation a simpler problem can be tackled by considering equations II.22 and II.23 together with continuity equation II.7, for  $\zeta = \zeta_s - \zeta_b$ . Thus again multiplying II.22 by  $uD$ , II.23 by  $vD$  and II.7 by  $g\alpha\zeta$ , an equation for the energy balance follows,

$$\begin{aligned} & \frac{1}{2} \frac{\partial}{\partial t} [\rho D (u^2 + v^2) + \rho \alpha g \zeta^2] \\ & + \frac{\partial}{\partial x} \{ \rho u D [(u^2 + v^2)/2 + g(\alpha\zeta - \beta\zeta_{eql})] \} + \frac{\partial}{\partial y} \{ \rho v D [(u^2 + v^2)/2 + g(\alpha\zeta - \beta\zeta_{eql})] \} = \\ & -\tau_x^b u - \tau_y^b v + \rho u D N_h \Delta u + \rho v D N_h \Delta v - \beta \rho g \zeta_{eql} \left( \frac{\partial u D}{\partial x} + \frac{\partial v D}{\partial y} \right) \end{aligned} \quad (\text{II.27a})$$

Notice important changes in this equation when compared against II.27. Definition of energy flux now includes equilibrium sea level as well. The rate of work by astronomical forces became explicit

$$-\beta\rho g\zeta_0\left(\frac{\partial uD}{\partial x} + \frac{\partial vD}{\partial y}\right)$$

and it can be calculated with the help of continuity equation, as

$$\beta\rho g\zeta_{eq}\frac{\partial\zeta}{\partial t}$$

#### 4. Free tidal waves in a channel

In the previous section we have formulated the general equations for the tide generation and propagation. These can be solved over world ocean and its local water bodies by application of the numerical solutions. Let's first consider a simplified problem of the free tidal wave propagation in the simplified geometry. To understand main features important for propagation of a tidal wave we consider a simplified set of equation of motion in a narrow channel of the constant depth.

$$\frac{\partial u}{\partial t} = -g\frac{\partial\zeta}{\partial x} \quad (\text{II.32})$$

$$\frac{\partial\zeta}{\partial t} + \frac{\partial uD}{\partial x} = 0 \quad (\text{II.33})$$

Here  $D = H$ . Let's first consider solution of II.32 and II.33 in the form  $\zeta = \zeta_1(x)\exp i(\omega t)$  with  $\omega > 0$ . Introducing the above solution into II.32 and II.33 we arrive at equation for the sea level amplitude,

$$\frac{\partial^2\zeta_1}{\partial x^2} + \frac{\omega^2}{gH}\zeta_1 = 0 \quad (\text{II.34})$$

Searching solution in the form  $\zeta_1 = A\exp -i\kappa x + B\exp i\kappa x$ , the dispersive equation will take form

$$\omega^2 = gH\kappa^2 \quad (\text{II.35})$$

The sea level is represented as superposition of two waves:

$$\zeta = A\exp i(\omega t - \kappa x) \quad (\text{II.36a})$$

running towards positive  $x$  direction, and

$$\zeta = B\exp i(\omega t + \kappa x) \quad (\text{II.36b})$$

running towards negative  $x$  direction. Introducing solutions for the sea level into II.32 and using the dispersive relation II.35, the velocity of the waves propagating towards the positive and negative directions, follow

$$u = A\sqrt{\frac{g}{H}}\exp i(\omega t - \kappa x) - B\sqrt{\frac{g}{H}}\exp i(\omega t + \kappa x) \quad (\text{II.37})$$

One important observation related to this linear system without external force is that the sea level defines velocity through II.37. The conclusion is that it is sufficient in such system to prescribe only one dependent variable, i.e., velocity or sea level.

Two waves described by II.37 are called **progressive waves** since they propagate in the endless channel without any boundaries. Comparing II.36 and II.37 one can see that velocity and sea level have the same argument, therefore the phase of oscillation is identical. From the point of view of an observer moving with the wave, the phase of the wave remain constant. Consider oscillations described by II.36a, the constant argument is expressed as

$$(\omega t - \kappa x) = \text{Const} \quad (\text{II.38})$$

In order to keep II.38 as constant while the wave is moving (and assuming that both frequency  $\omega$ , and wave number  $\kappa$  do not change) we arrive at

$$\frac{\partial}{\partial t} \text{Constant} = 0 = \omega - \kappa \frac{\partial x}{\partial t} \quad (\text{II.39})$$

This relations defines the wave propagating towards the positive x direction with the **phase velocity**

$$c = \frac{\partial x}{\partial t} = \frac{\omega}{\kappa} = \sqrt{(gH)} \quad (\text{II.40})$$

Since  $\omega = 2\pi/T$  and  $\kappa = 2\pi/\lambda$  the phase velocity can be expressed by the **wavelength**  $\lambda$  and the wave period  $T$ ,

$$c = \frac{\lambda}{T} = \sqrt{(gH)} \quad (\text{II.41})$$

In Fig.II.1 a wavelength is given; it was computed by the II.41 for the  $K_1$  wave ( $T=23.93$  hr) and  $M_2$  wave ( $T=12.42$  hr) and for the variable depth. Tides display a very long wavelength in the range of  $10^4$  km at the depth of 6 km. Only at the very shallow water (less than 50 m for  $M_2$  and 20 m for  $K_1$ ) the wavelength becomes less than 1000 km.

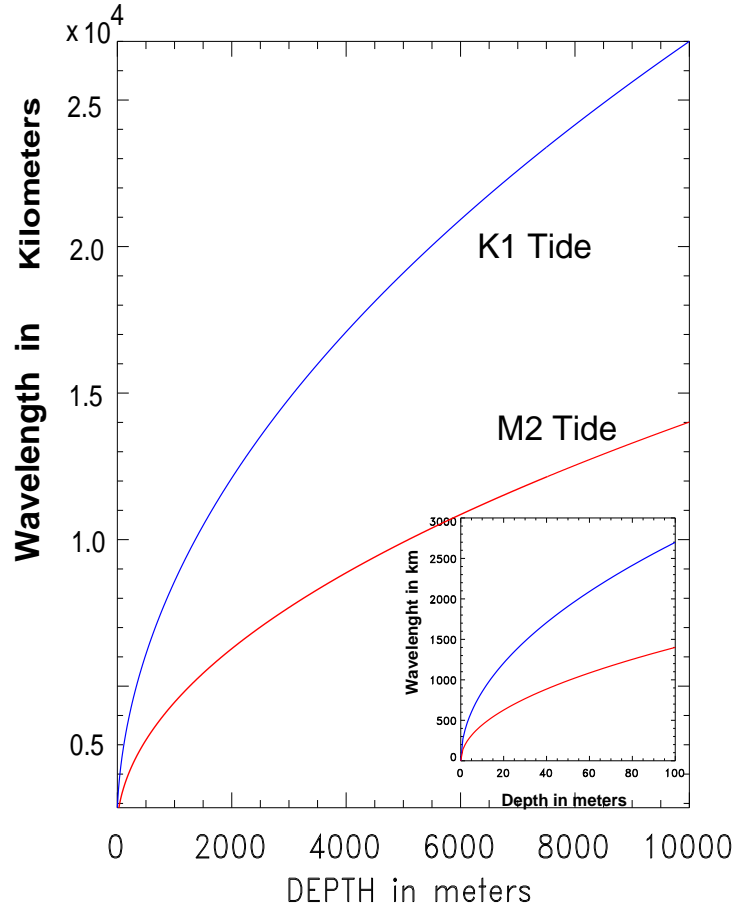


**Figure II.1** Wavelength of the  $K_1$  and  $M_2$  tides in the depth varying ocean.

The situation becomes more complicated if channel is closed by one wall or two walls. The waves reflected from the wall start to interact with the progressive waves resulting in the complicated field of standing and progressive waves. The channel closed on both ends is characterized by the **own (natural) oscillations**, often called eigenoscillations. We shall investigate these oscillations in a channel of length  $l$ , closed at  $x = 0$  and  $x = l$ . At the both ends, velocity of the water particles is zero,

$$u(x = 0) = 0 \quad \text{and} \quad u(x = l) = 0 \quad (\text{II.42})$$

Boundary conditions for the sea level can be formulated through II.32 as

$$\left. \frac{\partial \zeta}{\partial x} \right|_{x=0} = 0 \quad \text{and} \quad \left. \frac{\partial \zeta}{\partial x} \right|_{x=l} = 0 \quad (\text{II.43})$$

General solutions given by II.36 and II.37 with the above boundary conditions define the oscillations in the closed channel. Consider first the sea level, through condition at  $x = 0$ , it follows that  $A=B$ , thus

$$\zeta = A(\exp -i\kappa x + \exp i\kappa x) \exp i(\omega t) = 2A \cos \kappa x \exp i(\omega t) \quad (\text{II.44a})$$

Boundary condition at  $x = l$  requires that

$$\left. \frac{\partial \zeta}{\partial x} \right|_{x=l} = 0 = \sin \kappa l \quad (\text{II.44b})$$

Above is fulfilled if  $\kappa l = n\pi$ ; or introducing period through the dispersion equation II.35 we arrive at the expressions for the own period of oscillations (often called seiche) in the closed (narrow) channel

$$T = \frac{2l}{n\sqrt{gH}} \quad (\text{II.45})$$

Here  $n = 1, 2, \dots$  are nodes of oscillations. First node ( $n=1$ ) denotes the longest period oscillations. The seiche is uninodal for  $l = \lambda/2$ , binodal for  $l = \lambda$ , trinodal for  $l = 3\lambda/2, \dots$ ,  $n$ -nodal for  $l = n\lambda/2$ .

For a channel of a length  $l$  open at the one end and uniform depth  $H$ , the seiche period is given by (**Kowalik and Murty, 1993, p.344**)

$$T_n = \frac{4l}{n\sqrt{gH}} \quad (\text{II.46})$$

Here  $n = 1, 3, 5, \dots$

## 5. Energy considerations

### 5a. Energy flux

Generally, the tidal wave at any location along the channel, can be describe by the sea level

$$\zeta = \zeta_a \cos(\omega t - \phi) \quad (\text{II.47})$$

and velocity

$$u = u_a \cos(\omega t - \phi_u) \quad (\text{II.48})$$

In the channel the energy flux vector II.29 will have only one component

$$E_{h1} = \rho g H u \zeta \quad (\text{II.49})$$

Substituting II.47 and II.48 in II.49 an expression for the **energy flux** is obtained

$$\begin{aligned} E_{h1} = & \frac{1}{2} \rho g H u_a \zeta_a \cos(\phi_u - \phi) [1 + \cos 2(\omega t - \phi)] + \\ & \frac{1}{2} \rho g H u_a \zeta_a \sin(\phi_u - \phi) \sin 2(\omega t - \phi) \end{aligned} \quad (\text{II.50})$$

The first term in the above expression, averaged over one cycle defines the mean flux of the tidal energy (**Nekrasov, 1992**):

$$\bar{E}_{h1} = \frac{1}{2} \rho g H u_a \zeta_a \cos(\phi_u - \phi) \quad (\text{II.51})$$

The first part of II.50 is known also as a pulsating vector. The second part of II.50 averaged over one tidal cycle does not contribute to the average energy flux. The energy flux can serve well to differentiate between progressive and standing waves. To demonstrate the concept let's consider the progressive wave II.36 and II.37 in the form

$$\zeta = \zeta_a \cos(\omega t - \kappa x) \quad (\text{II.52})$$

$$u = \zeta_a \sqrt{\frac{g}{H}} \cos(\omega t - \kappa x) \quad (\text{II.53})$$

Introducing above expressions in II.50 we arrive at,

$$E_{h1} = \frac{1}{2} \rho g \sqrt{gH} \zeta_a^2 [1 + \cos 2(\omega t - \kappa x)] \quad (\text{II.54})$$

The energy flux of the progressive wave is always positive, it propagates into the same direction as the sea level and velocity, and its period of propagation is two times shorter than that of the sea level or velocity. **The mean energy flux** is equal to:

$$\bar{E}_{h1} = \frac{1}{2} \rho g \sqrt{gH} \zeta_a^2 \quad (\text{II.55})$$

Somewhat different behaves the energy flux for the standing wave. The sea level for the standing wave follows from II.44a

$$\zeta = 2\zeta_a \cos \kappa x \cos \omega t \quad (\text{II.56})$$

The solution for the velocity follows from II.32, first by differentiating II.56 over  $x$  and afterwards integrating in time

$$u = 2\zeta_a \sqrt{g/H} \sin \kappa x \sin \omega t \quad (\text{II.57})$$

The energy flux defined by II.49 equals to:

$$\rho g \sqrt{gH} \zeta_a^2 \sin 2\kappa x \sin 2\omega t \quad (\text{II.58})$$

The energy flux of the standing wave is a standing wave as well. The period is two times shorter than the original wave; it changes sign every half of the period and the mean over tidal period equals to zero. We can conclude that the standing wave do not transport the tidal energy. Going back the general expression for the energy flux II.50 we can conclude that as the first term is responsible for all the energy flux, henceforth velocity and sea level elevation are in phase in this term (**Henry and Foreman, 2002**). The second term which does not generate the energy flux, represents the standing wave, therefore velocity is in quadrature with elevation in this term.

### 5b. Kinetic and potential energy

According to II.27 the kinetic and potential energy are

$$E_k = \frac{1}{2} \int \int \rho D(u^2 + v^2) dx dy \quad (\text{II.59})$$

$$E_p = \frac{1}{2} \int \int \rho g \zeta^2 dx dy \quad (\text{II.60})$$

Here the integration area is the sea surface confined within boundary  $\Gamma$ . Since in the kinetic energy expression the total depth  $D$  is not very different from the depth  $H$  we shall assume that both are equal in all energy formulas. If we consider energy stored in progressive wave within one wave length ( $\lambda$ ) for the wave traveling along  $x$  direction in a channel of width  $b$ , the above expression for the kinetic energy simplify to:

$$E_k = \frac{1}{2} \int_0^b \int_0^\lambda \rho D(u^2) dx dy \quad (\text{II.61})$$

and introducing from II.53  $u = \zeta_a \sqrt{\frac{g}{H}} \cos(\omega t - \kappa x)$ , the **kinetic energy along the one wavelength** is obtained

$$E_{k,\lambda} = \frac{1}{4} \rho g \lambda b \zeta_a^2 \quad (\text{II.62})$$

The same expression can be obtained for the potential energy, thus the **total energy for the traveling wave**, within one wavelength is

$$E_{tot} = E_{k,\lambda} + E_{p,\lambda} = \frac{1}{2} \rho g \lambda b \zeta_a^2 \quad (\text{II.63})$$

The energy flux of the progressive wave given by Eq. II.55 now can be redefined in terms of the wave energy per unit area and the shallow water **group velocity**  $c_g = \sqrt{gH}$

$$\bar{E}_{h1} = \frac{1}{2} \rho g \zeta_a^2 c_g = \frac{1}{2} \rho g \zeta_a^2 \sqrt{gH}$$

Somewhat different are energy formulas for the standing wave. Using expressions II.56 and II.57 the kinetic energy can be written as

$$E_k = \frac{1}{2} \int_0^b \int_0^\lambda \rho D(u^2) dx dy = \frac{1}{2} \int_0^b \int_0^\lambda \rho D 4 \zeta_a^2 (g/H) \sin^2 \kappa x \sin^2 \omega t dx dy \quad (\text{II.64})$$

The kinetic energy contained within one wavelength is

$$E_{k,\lambda} = \frac{1}{2} \rho g b \lambda \zeta_a^2 (1 + \cos 2\omega t) \quad (\text{II.65})$$

Potential energy of the standing wave is defined in the following way,

$$E_{p,\lambda} = \frac{1}{2} \rho g b \lambda \zeta_a^2 (1 - \cos 2\omega t) \quad (\text{II.66})$$

Thus both potential and kinetic energy in the standing wave are variable in time with the period two times shorter than the period of the tidal wave. The **total energy for the standing wave** is equal to:

$$E_{tot} = E_{k,\lambda} + E_{p,\lambda} = \rho g b \lambda \zeta_a^2 \quad (\text{II.67})$$

thus both kinetic and potential energies are transformed in time in such a fashion that the total energy always is constant.

## 6. Free tidal waves in two-dimensional geometry

Let's consider now a simplified problem of the free tidal wave propagation in the two-dimensional geometry. To understand main features important for propagation of a tidal wave we consider a simplified set of equations of motion in the ocean of the constant depth.

$$\frac{\partial u}{\partial t} - f v = -g \frac{\partial \zeta}{\partial x} \quad (\text{II.68})$$

$$\frac{\partial v}{\partial t} + f u = -g \frac{\partial \zeta}{\partial y} \quad (\text{II.69})$$

$$\frac{\partial \zeta}{\partial t} + \frac{\partial u D}{\partial x} + \frac{\partial v D}{\partial y} = 0 \quad (\text{II.70})$$

Here  $D = H$ .

In these equations the nonlinear, frictional and forcing terms have been neglected. In consideration to follow the dependent variables in the system (II.68)–(II.70) will change in time as  $\exp(i\omega t)$ . From the above set of equations one equation for the sea level can be obtained ( **Lamb, 1945**),

$$g H \nabla^2 \zeta + (\omega^2 - f^2) \zeta = 0 \quad (\text{II.71})$$

Using II.68 and II.69 the components of velocity are expressed through the sea level

$$u = (\omega^2 - f^2)^{-1} g \left( f \frac{\partial \zeta}{\partial y} + i \omega \frac{\partial \zeta}{\partial x} \right) \quad (\text{II.72})$$

$$v = (\omega^2 - f^2)^{-1} g \left( i \omega \frac{\partial \zeta}{\partial y} - f \frac{\partial \zeta}{\partial x} \right) \quad (\text{II.73})$$

Therefore, when a solution of II.71 is sought, a condition at the coast can be introduced through II.72 and II.73, since the component of velocity perpendicular to the coast is equal to zero.

Let's first consider solution of II.71 in the form  $\zeta = \zeta_1(x) \exp i(\omega t - k_y y)$  with  $k_y > 0$ . For  $\omega$  and  $k_y$  positive, this wave travel in the positive  $y$  direction. Introducing the above solution into II.71 we arrive at equation for the sea level amplitude,

$$\frac{\partial^2 \zeta_1}{\partial x^2} + \left( \frac{\omega^2 - f^2}{gH} - k_y^2 \right) \zeta_1 = 0 \quad (\text{II.74})$$

Denoting

$$\frac{\omega^2 - f^2}{gH} - k_y^2 = k_x^2 \quad (\text{II.75})$$

and assuming that  $k_x > 0$ , solution to II.74 can be written as

$$\zeta_1 = A \exp ik_x x + B \exp -ik_x x \quad (\text{II.76})$$

The wave number  $k_x$  is real if  $\frac{\omega^2 - f^2}{gH} - k_y^2 > 0$ . The waves with the real wave numbers  $k_x$  are called Sverdrup waves. The limiting frequency for Sverdrup waves is  $\omega = f$ , therefore, this wave cannot exist where  $f > \omega$ . Since  $f = 2\Omega \sin \phi$  is a function of the latitude, the **Sverdrup wave** for the tidal frequencies cannot occur poleward above the so-called critical latitudes. Sverdrup (1926) explained this class of motion by the introduction of the wave motion on an unlimited rotating disc.

Different solution will be obtained when  $k_x$  is imaginary. The dispersion relation defined by II.75 changes to,

$$\frac{\omega^2 - f^2}{gH} - k_y^2 = -k_x'^2 \quad (\text{II.77})$$

Here  $k_x = ik_x'$ . The total solution for this case can be obtained by introducing the new value of  $k_x$  into II.76,

$$\zeta = (A \exp -k_x' x + B \exp k_x' x) \exp i(\omega t - k_y y) \quad (\text{II.78})$$

From the point of view of an observer looking along the positive  $y$  axis the wave at the coefficient  $A$  is right-decreasing and the one at the coefficient  $B$  is left-decreasing. This class of waves are prototype waves used for explanation of the various phenomena occurring in the tidal waves. Therefore we consider these waves propagating in the rotating (wide) channel to see what kind of boundary condition is required to sustain such wave. In the system of equations II.68–II.70, the  $x$  axis is directed across of the channel (Fig. II.2) and the  $y$  axis along the wall of the channel (positive to the south), the beginning of the reference system is set on the left-hand wall (looking along the positive  $y$  axis). The application of the boundary condition at the walls  $x = 0$  and  $x = b$  ( $b$  is width of the channel), requires that velocity  $u = 0$ . From expression II.72 it follows that

$$f \frac{\partial \zeta}{\partial y} + i\omega \frac{\partial \zeta}{\partial x} = 0$$

at the walls, which leads to the two independent systems of roots,

$$\omega k_x' = f k_y; \quad \omega k_x' = -f k_y \quad (\text{II.79})$$

and

$$e^{k_x' b} - e^{-k_x' b} = 0 \quad (\text{II.80})$$

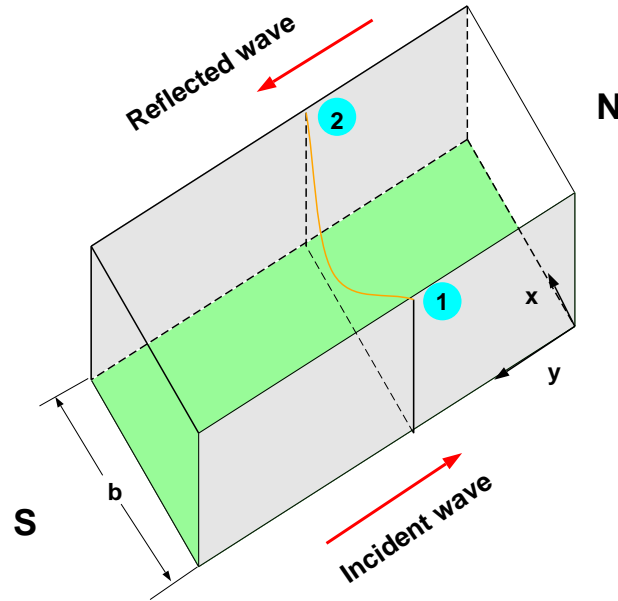


**Figure II.2 Propagation of a long wave in the channel**

The latter can take the form of an oscillatory wave if  $k'_x b = in\pi$  (where  $n = 1, 2, 3, \dots$ ). This is the so-called **Poincare wave**, it exists when  $k'_x{}^2 < 0$ . Under this condition, it follows from II.77 that

$$\frac{\omega^2 - f^2}{gH} - k_y^2 > 0 \quad (\text{II.81})$$

Above the "critical" latitudes where  $f^2 > \omega^2$ , the inequality II.81 is not fulfilled and the Poincare waves are not admissible. From II.80 by setting  $k'_x b = in\pi$  we derive the dispersion equation,

$$\frac{\omega^2 - f^2}{gH} - k_y^2 = \left(\frac{n\pi}{b}\right)^2 \quad (\text{II.82})$$

Propagation towards the critical latitude shows that the left-hand-side of II.82 tends to zero, whereas the right-hand-side is always positive. Considering the different modes ( $n$ ) of oscillations it is easy to deduce from the above equation that the width of the channel will also limit the admissible Poincare waves. Setting very large channel width brings back the solution on the rotating disc,  $\frac{\omega^2 - f^2}{gH} - k_y^2 = 0$ . Actually solution given by II.78 defines two different waves according to the boundary condition II.79 and II.80. If the boundary conditions are taken at the  $x = 0$  and  $x = b$  the Poincare solution follows if on the other hand only condition at the  $x = 0$  is used and  $B = 0$  in II.78 the Kelvin wave will be derived.

Turning to II.79, we obtain through II.77

$$k_y = \pm \frac{\omega}{\sqrt{gH}} \quad (\text{II.83})$$

and

$$k'_x = \frac{|f|}{\sqrt{gh}} \quad (\text{II.84})$$

The wave with these wave numbers can exist both below and above the critical latitude and is called **Kelvin wave**. In Table II.1, critical latitudes are defined for major semidiurnal and diurnal constituents, by equating tidal periods to the inertial period. The numbers cluster around two latitudes: for the diurnal constituents approximately at  $30^\circ$  and for the semidiurnal constituents approximately at  $75^\circ$ .

Table II.1

Critical latitudes for the tidal waves

Tidal wave	$\omega_i$	$\phi_{cr}$
M <sub>2</sub>	$1.40519 \cdot 10^{-4}$	$74^\circ 29'$
S <sub>2</sub>	$1.45444 \cdot 10^{-4}$	$85^\circ 47'$
N <sub>2</sub>	$1.37880 \cdot 10^{-4}$	$70^\circ 59'$
K <sub>2</sub>	$1.45842 \cdot 10^{-4}$	No
K <sub>1</sub>	$0.72921 \cdot 10^{-4}$	$30^\circ 00'$
O <sub>1</sub>	$0.67598 \cdot 10^{-4}$	$27^\circ 37'$
P <sub>1</sub>	$0.72523 \cdot 10^{-4}$	$29^\circ 49'$
Q <sub>1</sub>	$0.64959 \cdot 10^{-4}$	$26^\circ 27'$

## 7. Kelvin wave

Kelvin waves are often used as prototype to explain tidal dynamics in the coastal domains. Classical solution obtained by **Taylor (1921)** considered a couple of Kelvin waves (incident and reflected) in a channel imitating an idealized North Sea.

To derive equations for the Kelvin wave a simplified equations of motion and continuity will be investigated in the geometry of the previously considered channel (Fig.II.2) with an additional assumption that the crosssectional velocity  $u = 0$ . Hence from the set II.68-II.70 the following equations are derived,

$$-fv = -g \frac{\partial \zeta}{\partial x} \quad (\text{II.85})$$

$$\frac{\partial v}{\partial t} = -g \frac{\partial \zeta}{\partial y} \quad (\text{II.86})$$

$$\frac{\partial \zeta}{\partial t} + \frac{\partial v H}{\partial y} = 0 \quad (\text{II.87})$$

Considering solution to this set in the form

$$\zeta = \zeta_0 \exp -k_x x \exp i(\omega t - k_y y) \quad \text{and} \quad v = v_0 \exp -k_x x \exp i(\omega t - k_y y) \quad (\text{II.88})$$

(here  $k'_x$  is changed to  $k_x$ ) from II.86 and II.87 an equation of dispersion follows

$$\omega = \pm \sqrt{gH} k_y \quad (\text{II.89})$$

This equation defines the wave number along the  $y$  direction. Considering II.85 and II.87 we arrive at the expression for the wave number along  $x$  direction,

$$k_x = -\frac{f}{\sqrt{gH}} \quad (\text{II.90})$$

Introducing this wave number into II.88 we arrive at the conclusion that wave propagating along the coast towards the south is depicting an amplitude growing away from the shoreline (the coastline is to the left when looking into wave propagation). On other hand the wave propagating towards the north will have amplitude diminishing away from the shoreline. This solution is

$$\zeta = \zeta_0 \exp -\frac{f}{\sqrt{gH}} x \exp i(\omega t + k_y y) \quad \text{and} \quad v = v_0 \exp -\frac{f}{\sqrt{gH}} x \exp i(\omega t + k_y y) \quad (\text{II.91})$$

Using II.85 it follows that the amplitudes of the sea level and velocity are related as

$$v_0 = \zeta_0 \sqrt{\frac{g}{H}} \quad (\text{II.92})$$

This solution is for the northern hemisphere. The wave is propagating into negative  $y$  direction. An observer looking into the negative  $y$  axis will see that the wave amplitude is right-increasing and left-decreasing. The distance of the signal decay ( $x = R_d$ ) along the channel crosssection can be estimated by setting in II.91:

$$\frac{\zeta}{\zeta_0} = e^{-1}, \quad \text{whence} \quad \frac{f R_d}{\sqrt{gH}} \simeq 1 \quad (\text{II.93})$$

The decay-distance is called the **Rossby radius of deformation**. This distance as function of the latitude and depth is shown in Figure II.3. For the deep ocean ( $H > 2000$  m) the Rossby radius is greater than 1000km. Only in the shallow water of approximately 200 m depth, the Rossby radius is less than 500 km. The dependence of the Coriolis parameter on the latitude tends to diminish the Rossby radius poleward from equator. The tides propagating north often described by the Kelvin wave along the wall of the channel located at  $x = 0$ . If in turn we consider the second wall of the channel at the distance  $x = b$  and delete the wall at  $x = 0$ , the Kelvin wave solution take the following form :

$$\zeta = \zeta_0 e^{-f(b-x)/c} \exp i(\omega t - k_y y) \quad \text{and} \quad v = v_0 e^{-f(b-x)/c} \exp i(\omega t - k_y y) \quad (\text{II.94})$$

Here  $\sqrt{gH} = c$ . Thus along the right-hand wall (looking north) the Kelvin wave propagates towards the north, at the left-hand wall the Kelvin wave propagates southward (Fig.II.2). Let us consider these two waves as a superposition of an incident wave propagating towards north and a reflected wave propagating towards south.

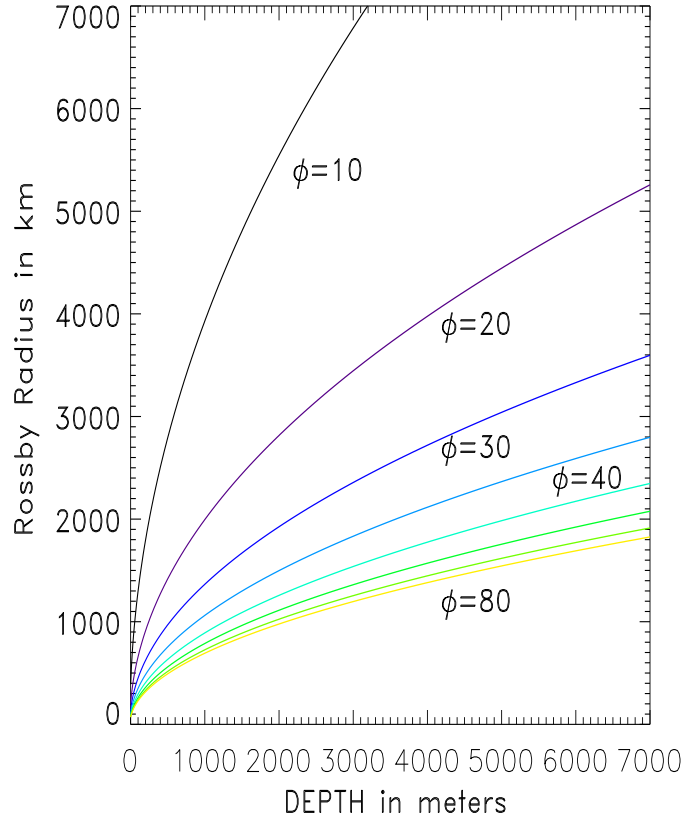


**Figure II.3** Rossby radius of deformation (II.93) as a function of latitude and depth

Denoting the amplitude at the coast in the point 1 (Fig.II.2) as  $\zeta_{x_1}$  and the amplitude in the point 2 as  $\zeta_{x_2}$ , we can conclude that in certain point inside the channel the amplitudes of both waves are equal. Taking into account II.93 and II.94

$$\zeta_{x_1} \exp\left(-\frac{fx_a}{c}\right) = \zeta_{x_2} \exp\left(-\frac{f(b-x_a)}{c}\right) \quad (\text{II.95})$$

the coordinate of such point along the  $x$  axis is specified, as,

$$x_a = \frac{b}{2} + \frac{c}{2f} \ln \frac{\zeta_{x_1}}{\zeta_{x_2}} \quad (\text{II.96})$$

This is so-called **amphidromic point**. It is located at the center of the channel when amplitudes of the incident and reflected waves are equal. Usually the amplitude of the reflected wave is smaller than the amplitude of the incident wave, this assumption will move an amphidromic point towards the left-hand wall (looking towards north). The

amplitude decay along the  $x$  direction is a function of the depth, therefore in the channel of greater depth the amphidromic point will be shifted stronger from the central location. Similar conclusions follow when the left and the right sides of the channel display different depths, to find the shift for such case, the different depths ought to be introduced into the RHS and LHS of II.95.

### 8. Sverdrup wave

Equations II-74 – II.76 describe a general class of waves called Sverdrup waves, their equation of dispersion reads,

$$\frac{\omega^2 - f^2}{gH} - k_y^2 = k_x^2 \quad (\text{II.97})$$

This general relation is completely symmetrical with respect to  $x$  and  $y$  coordinates, therefore for the convenience sake we consider progressive wave along the  $y$  direction only, thus  $k = k_y$ , and  $k_x = 0$ . Since the dependent variables in such wave do change along  $y$  direction only, the equations of motion and continuity are,

$$\frac{\partial u}{\partial t} - fv = 0 \quad (\text{II.98})$$

$$\frac{\partial v}{\partial t} + fu = -g \frac{\partial \zeta}{\partial y} \quad (\text{II.99})$$

$$\frac{\partial \zeta}{\partial t} + \frac{\partial vH}{\partial y} = 0 \quad (\text{II.100})$$

Looking as before for the oscillatory solution  $\zeta, u, v \approx \exp i(\omega t - k_y y)$  we will arrive at the dispersion equation, similar to II.97, namely,

$$k_y = \pm \sqrt{\frac{\omega^2 - f^2}{gH}} \quad (\text{II.101})$$

The phase velocity for the Sverdrup wave ( $c_s$ ) follows from the above relation

$$c_s = \frac{\omega}{k_y} = c \sqrt{\frac{\omega^2}{\omega^2 - f^2}} \quad (\text{II.102})$$

Here  $c = \sqrt{gH}$ . Inspection of this result shows that the Sverdrup phase velocity is always greater than the velocity of the long waves ( $c$ ). This velocity also increases towards the critical latitudes. The Sverdrup wave can not propagate above the critical latitude, since in this domain  $f < \omega$ . The wave amplitude above critical latitude decays quickly; this mode of propagation is often called an evanescent mode. The properties of the Sverdrup wave are also changing under the influence of the bottom friction, it is possible to construct Sverdrup wave in the shallow water with a dispersion relation allowing for propagation across the critical latitudes **Kowalik (1979)**.

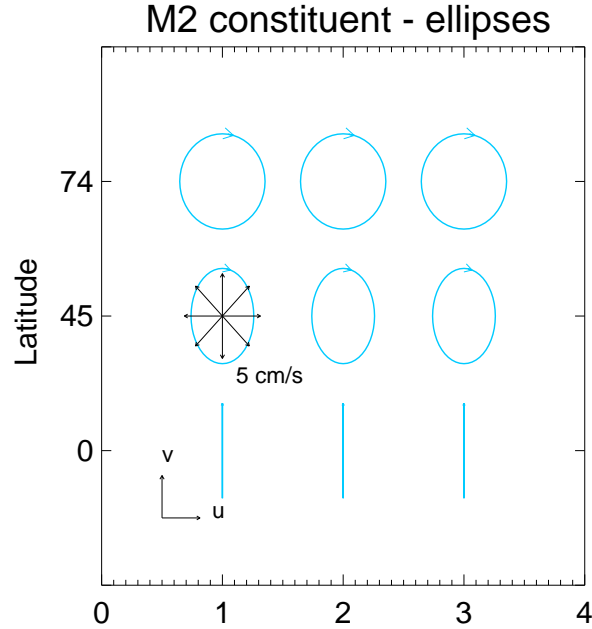


**Figure II.4 Trajectories of water particles in Sverdrup wave. Velocity scale (5 cm/s) is given at 45° latitude.**

Solution for the Sverdrup wave progressing along  $y$  direction, can be written as

$$\zeta = \zeta_0 \exp i(\omega t - k_y y) \quad (\text{II.103})$$

and using II.72 and II.73 with  $\frac{\partial}{\partial x} = 0$ ,

$$u = (\omega^2 - f^2)^{-1} g (f \frac{\partial \zeta}{\partial y}) \quad (\text{II.104})$$

$$v = (\omega^2 - f^2)^{-1} g (i\omega \frac{\partial \zeta}{\partial y}) \quad (\text{II.105})$$

Considering only the real part of the complex solution and taking into account II.99, the solution is,

$$\zeta = \zeta_0 \cos(\omega t - k_y y) \quad (\text{II.106})$$

$$u = \frac{\zeta_0 f}{H k_y} \sin(\omega t - k_y y), \quad v = \frac{\zeta_0 \omega}{H k_y} \cos(\omega t - k_y y) \quad (\text{II.107})$$

Trajectories of water particles form an ellipse with the axes along  $y$  direction depending on frequency  $\omega$  while the axes along the  $x$  direction is a function of the Coriolis parameter. The ratio  $u/v = f/\omega$  changes along the circle of latitude from zero at the equator to 1 in proximity to the critical latitude. In Fig II.3 an elliptical motion is depicted for the semidiurnal  $M_2$  constituent at the various latitudes. The rotation in time is clockwise,

often the sense of this rotation is described as *cum sole* or anticyclonic. It is of interest to notice that the Sverdrup wave amplitude is everywhere the same (wave with horizontal crests). It is difficult to imagine that such property will be preserved upon this wave interaction with the shoreline.

### 9. Shelf waves

Incident tidal waves arriving to the shore modify their pattern and travel along the shore as Kelvin waves. Often before arriving to the shore they undergo interaction with the shelf. In this section we will look into process of transforming tides by trapping their energy into the shelf waves. A simple model of a step shelf will be considered (Fig.II.5).

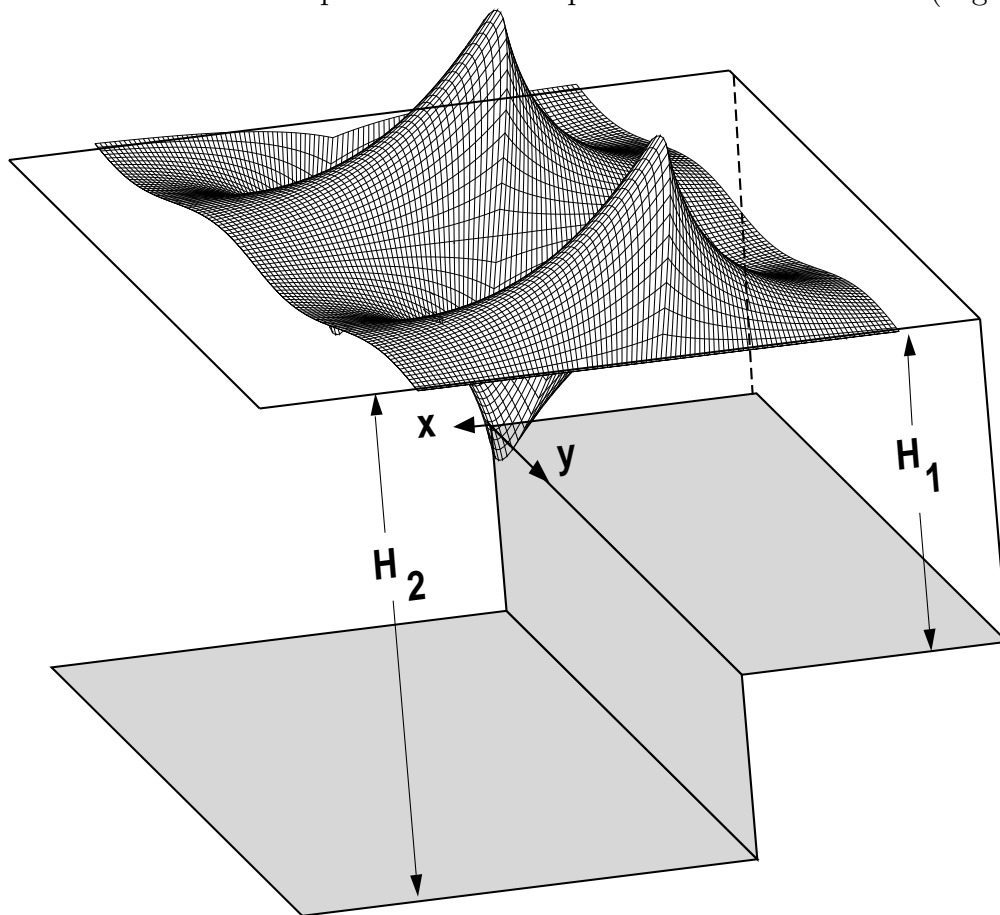


**Figure II.5 A model of a step shelf**

The general idea is that if such geometry in the presence of rotation possesses own modes (eigenmodes) of oscillations whose period is close to the tidal period then the resonance phenomena can occur. This process will transfer energy into the shelf (trapped) modes, thus generating enhanced currents. Let's consider depth discontinuity located at the origin of coordinates with the  $x$  axis pointing towards deep water, Fig.II.5. Deep basin depth is constant and equal to  $H_2$ , the shallow water depth is  $H_1$ . The matching boundary condition relate the sea level and water transport across the discontinuity depth (**Mei, 1989**),

$$\zeta_1 = \zeta_2 \quad \text{and} \quad u_1 H_1 = u_2 H_2 \quad (\text{II.108})$$

Additionally, we assume that the shoreline is located far enough from the shelf break, therefore its influence will be neglected. Such approach allows us (among quite a few possibilities) to suggest that the solution across discontinuity will be described as an exponential function, in the shallow water domain,

$$\zeta_1 = A_1 \exp k'_1 x \exp i(\omega t - k_y y) \quad (\text{II.109})$$

Here  $x$  is negative; and in the deep water domain,

$$\zeta_2 = A_2 \exp -k'_2 x \exp i(\omega t - k_y y) \quad (\text{II.110})$$

Indeed if such oscillations exist they will be "trapped" across the shelf due to exponential decay of the amplitude. Combining these two solutions through the first boundary condition in II.108, a simple result follows that  $A_1 = A_2$ . The second boundary condition needs velocity along the  $x$  direction, for this we use II.72, and rewrite the boundary condition as ( $x = 0$ ),

$$\begin{aligned} A_1 H_1 [(\omega^2 - f^2)g(-i f k_y + i \omega k'_1)] \exp i(\omega t - k_y y) = \\ A_1 H_2 [(\omega^2 - f^2)g(-i f k_y - i \omega k'_2)] \exp i(\omega t - k_y y) \end{aligned}$$

This simplifies to:

$$k_y = -\frac{\omega(k'_1 H_1 + k'_2 H_2)}{(H_2 - H_1)f} \quad (\text{II.111})$$

Here the wave number of the propagating wave is expressed as a function of the frequency. The actual computation of this dispersive equation requires the wave numbers along the  $x$  directions, these we calculate from equation II.75 assuming the form of solution given by II.109 and II.110. Thus in the shallow domain from II.75 we obtain,

$$k_1'^2 = k_y^2 - \frac{\omega^2 - f^2}{gH_1} \quad (\text{II.112})$$

Unfortunately the RHS of II.112 is not always positive. It will be always positive in the subinertial frequency range when  $\omega < f$ . In the deep water the wave number is defined as

$$k_2'^2 = k_y^2 + \frac{f^2 - \omega^2}{gH_2} \quad (\text{II.113})$$

Here we already changed sign in the RHS of II.112, so it is defined in the subinertial frequency range as well. Introducing  $k'_1$  and  $k'_2$  from the above equations into II.111 we arrive at dispersive equation which define resonance frequencies for the shelf waves.

$$\begin{aligned} k_y = -\frac{\delta_\omega}{H_2(1 - \delta_H)} \left[ (k_y^2 + \frac{f^2 - \omega^2}{gH_1})^{1/2} H_1 \right. \\ \left. + (k_y^2 + \frac{f^2 - \omega^2}{gH_2})^{1/2} H_2 \right] \quad (\text{II.114}) \end{aligned}$$

In the above the following notation is introduced,  $\delta_\omega = \omega/f$  and  $\delta_H = H_1/H_2$ . It is obvious from the above equation that the wave number is not expressed explicitly by the frequency  $\omega$ . The iterative search for solution works well. In the computational example given in Fig.II.6 we have assumed depth  $H_2 = 1000$  m, and the relative depth contrast ( $\delta_c$ )

$$\delta_c = \frac{H_2 - H_1}{H_2} = 1 - \delta_H \quad (\text{II.115})$$

was changed by using different  $\delta_H$ . Solution behaves well for the large depth contrast  $\delta_c = 0.8-0.9$  (small  $\delta_H = 0.1-0.2$ ) when the depth contrast diminishes ( $\delta_H = 0.5$ ) solution exists only for small values of the relative frequencies  $\delta_\omega < 0.4$  and small wavenumbers. The small depth contrast ( $\delta_c < 0.2$ ,  $\delta_H > 0.8$ ) eliminates the large part of the spectra, for example, when  $\delta_H = 0.8$ , shelf waves exist only if  $\omega < 0.1f$ .

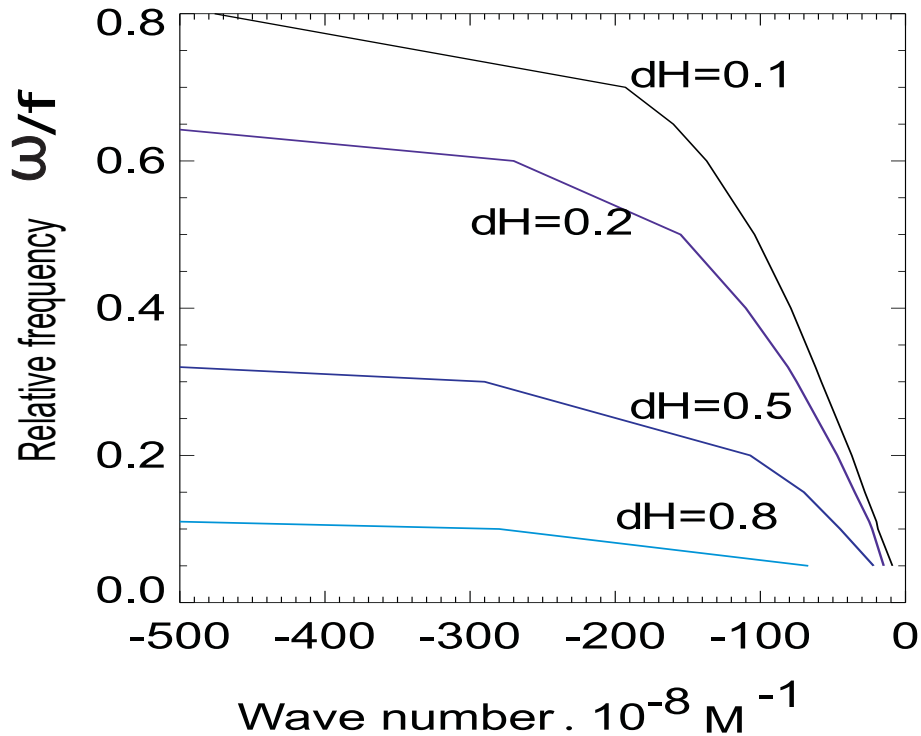


Figure II.6. Wave number (should be multiplied by  $10^{-8} \text{ m}^{-1}$ ) of the shelf waves as a function of the relative frequency. Waves are generated in geometry shown in Fig.II.5.

As the resonance frequencies for the shelf waves are located in the subinertial range or above the critical latitude, the dominant tidally-generated shelf waves will belong to the diurnal oscillations. The possibility of the shelf wave generation by the semidiurnal tide can only occur poleward from  $75^\circ$  latitude.

## 10. Tidal motion enhancement around islands and seamounts

Measurements and tidal theories are primarily concerned with the semidiurnal  $M_2$  tide whose amplitude generally dominate over all tidal constituents. This is typical for

many regions of the Atlantic Ocean but **Mooers and Smith (1968)** on the Oregon shelf and **Cartwright (1969)** off the west coast of Scotland found that in the field of velocity the reverse situation can occur, i.e., diurnal tidal currents can dominate over semidiurnal currents. This phenomenon has been found in many locations and has been identified with continental shelf waves of tidal origin, e.g. **Yefimov et al., (1985)**. In the Arctic Ocean, local response to the tidal forcing is especially conspicuous in the diurnal range of a velocity field. Critical latitude for the semidiurnal tidal wave occurs within the AO domain. Just below the critical latitude for the  $M_2$  tide, the frequencies of diurnal and semidiurnal tides straddle the local Coriolis frequency, and therefore, diurnal and semidiurnal constituents have different tidal wave dynamics for given Coriolis force, gravity, stratification, and bathymetry.

Tide modification by the shorelines is a vast and important subject, as we are unable to dwell on all possible interactions therefore we present some extended results related to tidal motion around islands and seamounts. This section will be divided into two subsection first the motion trapped around islands and seamounts in both **subinertial ( $\omega < f$ ) and superinertial ( $\omega > f$ ) bands** of oscillations will be considered and second part will be devoted to the shelf waves generated in the subinertial range of oscillations. Tidally-generated, trapped motions can significantly enhance and modify sea level and currents in the island proximity. Observations often depict maximum and minimum tidal sea levels at the opposite sides of the islands. Investigations of the tidal wave pattern lead to the conclusion that a tidal wave around an island is a superposition of two types of waves: a primary wave arriving from a distant source and secondary waves generated by the island. The primary wave consists of incoming propagating and reflected propagating waves. The secondary wave is trapped around the island and decays offshore from the island. While the primary wave influences sea level in the entire domain, the trapped wave affects only the island's vicinity, propagating clockwise (in the northern hemisphere) around the island with the same period as the primary wave. The distortion caused by the island modifies the amplitude of the tidal sea level, changes the time of the arrival of low and high tides, and enhances tidal currents.

**Proudman (1914)** investigated scattering of a tidal wave by small circular and elliptical islands (see also Figs. 149 and 150 in **Defant 1960, vol. II**). **Larsen (1977)** analyzed a systematic variation in amplitude and phase around the Hawaiian Islands and applied the solution of the scattering problem around an elliptical island to explain the observations. Analytical solutions for the tidal wave scattering around small islands were further developed by **Lee and Kim (1993)** by introducing bottom friction. The basic facts can be summarized in the following: Observations and numerical modeling show specific peculiarities in the amplitude and phase distribution both for semidiurnal and diurnal tides. These peculiarities are sometimes stronger for semidiurnal tides and sometimes for the diurnal tides.

In **Kowalik and Marchenko (2002)** theoretical approach we assumed that these peculiarities were related to the trapping effects around the islands and to the interaction of the incident waves with the islands. The constructed model of an island in the ocean of a constant depth was found to be insufficient to explain the behavior of tidal waves in the region of the Pribilof Islands in the Bering Sea. However, the inclusion of a sill changed

the situation. The “skirt” around the Pribilof Islands was found to play an important role in formation of the observed tidal peculiarities. The differences between diurnal and semidiurnal tides are found to be associated with : a) different incident waves for these two types of tides, and b) different eigenmodes (own oscillations). Computations of the island and circular sill response to the incident Sverdrup and Kelvin waves demonstrate that the former produces a more pronounced difference structure and phase contrast for the semidiurnal wave and wider sill around the island. Kelvin waves and diurnal Sverdrup waves do not appear to have much effect on tidal waves around the islands.

An additional question to be answered is how the general picture derived from the investigation of the scattering tide is changed in the case of resonance response? Of special interest is the response in the subinertial frequency band due to influence of the shelf waves trapped around the islands and seamounts ( **Rhines, 1969**). Observations show that these modes of oscillations strongly affect diurnal tides in high latitudes ( **Huthnance, 1974; Hunkins, 1986; Kowalik and Proshutinsky, 1995; Rabinovich and Thomson, 2001**). Hunkins (1986) reported a significant topographic amplification of the diurnal tide over the Yermak Plateau, with high velocities and enhanced mixing. **Huthnance (1981)** described the high velocities in the vicinity of Bear Island.

#### 10a. Trapped tidal motion around islands.

Observations and numerical computations by Kowalik and Proshutinsky (1995) around Bear Island in the Barents Sea, of approximately 20 km diameter, located at  $74^{\circ}30'N$ , and by **Kowalik and Stabeno (1999)** around the Pribilof Islands (the diameters less than 20 km), located at approximately  $57^{\circ}N$  in the Bering Sea, delineated a dipole structure in the tidal sea level distribution. Maximum and minimum sea levels occur at the opposite sides of the islands. According to Proudman (1914) and Lee and Kim (1999) this feature depends on the direction of propagation of the incident wave relative to the island. From the point of view of an observer looking in the propagation direction of the incident wave, the tidal amplitude increases to the left and decreases to the right of the island. A linear wave (a wave with a straight crest) propagating from east to west should generate the local sea level maximum at the southern side of the island. Observations in the Cheju Island region (**Lee and Kim, 1993**), show that the  $M_2$  wave arrives from the east, therefore amplitudes are much larger on the southern side of this island than on the northern. In the Barents and Bering Seas the  $M_2$  waves arrive from the west, setting the maximum amplitude at the northern shores of the islands.

The interaction of tides and currents with the bottom topography around islands, often leads to current enhancement and, as a consequence, nonlinear interactions become stronger in such regions. Observations and model computations of the oscillatory tidal flow interacting with bottom topography demonstrate well developed rectilinear motion around banks and islands (**Loder and Wright, 1985**).

Here we use observations and computations to explain the trapped tidal wave pattern around the Pribilof Islands in the Bering Sea. In Figure II.7 the depth distribution is coded by colors, and continuous lines denote the pattern of the amplitude of the  $M_2$  tidal wave. Islands are located on a shelf plain of approximately 80 m depth at some distance from the shelf break. The 50 m depth contour shows that St. Paul Island (northern island)

is surrounded by a wide area of shallow water extending 15–20 km beyond the island perimeter, while around St. George Island (southern island) the shallow water extends only 3–5 km beyond the island perimeter. A tide wave enters the Bering Sea as a progressive wave from the North Pacific Ocean through the Aleutian passages ( [Sünderman, 1977](#); [Pearson \*et al.\*, 1981](#); [Kantha, 1995](#); [Kowalik, 1999](#) ). The Pribilof Islands are located on the shelf, but close to the deep Bering Basin. Here tides propagate from the deep basin onto the shallow domain, which strongly enhances the tidal amplitudes and currents. The  $M_2$  amplitude of the surface elevation is shown in Figure II.7. It slowly changes from 24 cm in the deep basin to 31 cm over the open shelf. The sea level depicts the dipole structure around islands with the minimum located at the southeastern shores and the maximum at the northern shores. Especially conspicuous is the 14 cm sea level change across St. Paul Island. Around St. George Island the sea level change is only 7 cm. Due to topographic amplification by the shallow water,  $M_2$  currents up to 50–70  $\text{cm s}^{-1}$  are generated around St. Paul Island (Kowalik and Stabeno, 1999). The driving mechanism which generates these strong currents around the islands is the dipole structure of the sea level (shown in Fig.II.7) because the strength of the tidal stream is proportional to the sea level difference in the dipole structure.

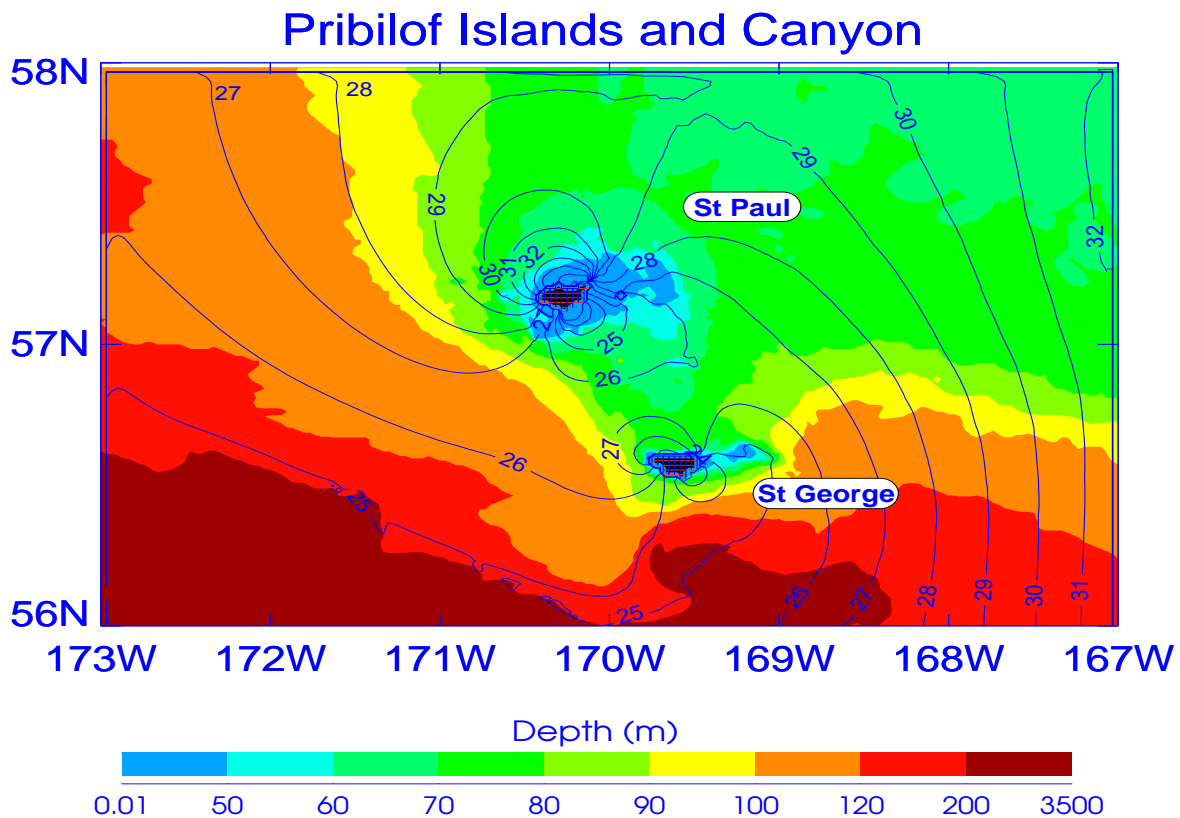


**Figure II.7.** Amplitude (in cm) of the  $M_2$  tide in the Pribilof Islands and Canyon, Bering Sea. The depth is coded by colors. Based on Kowalik and Stabeno (1999).

The dynamics of diurnal tides can be described using the major constituent  $K_1$ . Al-

though this wave has an amplitude of approximately 35 cm in the region of the Pribilof Islands, it does not generate the dipole structure of the same strength as the  $M_2$  wave. The difference in sea levels across St. Paul Island is only 5 cm and across St. George only 2 cm. Consequently, the diurnal currents are significantly smaller than semidiurnal currents (Kowalik and Stabeno, 1999).

The important difference in wave trapping around the Pribilof Islands is apparently related to the local topography, since both diurnal and semidiurnal tides are stronger at St. Paul Island. Observations also demonstrate that the different types of tides are enhanced in different ways, because at both islands the dipole structures are stronger for the  $M_2$  wave, despite the fact that the amplitude of the incident  $K_1$  wave being larger than the  $M_2$  wave. To explain the peculiarities of tidal dynamics around the Pribilof Islands we may use a simple model of Sverdrup or Kelvin waves approaching the islands. As [Mofjeld \(1984\)](#) has suggested, the tidal waves in the Bering Sea shelf region resemble a Sverdrup wave generated by an incident wave from the Deep Bering Basin. The Sverdrup wave model predicts well the amplitudes and phases of the tides on the Bering Sea shelf (Kowalik and Marchenko, 2002). These waves, in a frictionless ocean, below the critical latitude, propagate as free waves; above this latitude they change to subinertial evanescent waves. The tide on the Bering Sea shelf along the Alaska Peninsula is determined by the barotropic Kelvin wave ([Mofjeld 1980](#)). Kelvin wave exists both in subcritical and supercritical latitudes, and hence, this wave strongly influences the Bering Sea semidiurnal (superinertial) and diurnal (subinertial) tides.

### 10b. Residual tidal circulation around islands

Observations in the region of the Pribilof Islands and Canyon reveal a clockwise circulation around the group of islands and around each of the two largest islands, St. Paul and St. George (Kowalik and Stabeno, 1999). Six current meters deployed around St. Paul Island revealed a steady clockwise flow around the island, that was strongest south of the island, and weakest to the east. A high-resolution tidal model in this region showed that this flow pattern results from tidal rectification over the shallow topography tides. Tidal residual currents of 10-15  $\text{cm s}^{-1}$  were predicted by the model, compared to mean currents of 5-20  $\text{cm s}^{-1}$  observed at the mooring sites. Both diurnal and semi-diurnal tidal oscillations contribute to the clockwise circulation around the islands. To define a slowly changing subtidal motion, a low-pass filter (half amplitude 35 hours) was applied to the current records obtained around St. Paul Island. The low frequency currents are directed along bathymetry and support clockwise circulation around the island as observed in drifter trajectories. The flow around island for the whole measuring period depicts amazing stability in direction, only once, the flow reversal occurred (Kowalik and Stabeno, 1999). Currents around the island can be forced by density gradients or wind; but neither of these mechanisms would result in the described stable behavior through the various seasons. The only constant mechanism is rectifying tidal currents into low frequency currents. The high-resolution model constructed around St. Paul Island was used to study a permanent circulation induced through the nonlinear interactions. Residual velocities and sea level were obtained by averaging an hourly time series over period of 29 days.

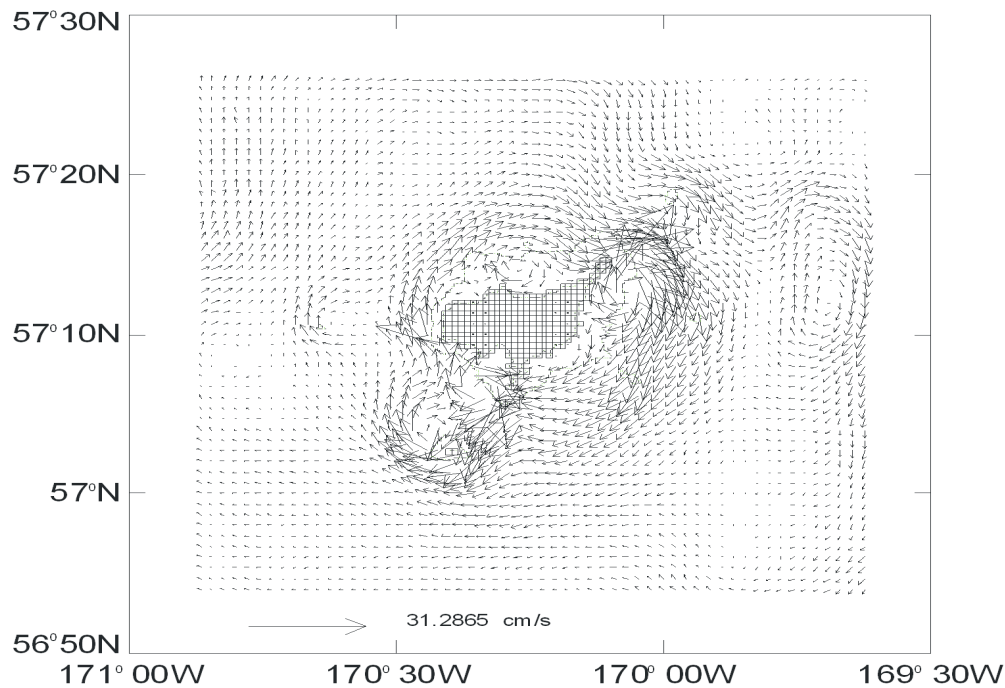


**Figure II.8. Residual tidal currents around St. Paul Island. Four major constituents ( $M_2$ ,  $N_2$ ,  $K_1$  and  $O_1$ ) are considered, numerical space step is 617 m.**

The horizontal resolution was increased around St. Paul Island to 617 m. This resolution is close to the grid distance recommended by [Zimmerman \(1978\)](#) and used by [Abraham et al., \(1987\)](#) for reproduction of the bottom topography with significant production of vorticity. In the island's vicinity the residual circulation is small and tends to be organized in local coastal eddies. At a distance of about 1 to 3 km from St. Paul Island the residual velocity attains greatest values and circles the island in continuous fashion. The average residual currents in this region are of the order of 10 to 15  $\text{cm s}^{-1}$ . Additional results obtained for the  $M_2$  constituent computed alone, without interaction with the remaining tidal constituents, show that this constituent is primarily responsible for the generation of residual currents around St. Paul Island.

A comparison of the measured residual currents with the currents obtained from the computation is given in the Figure II.9. Computed current magnitude and direction turned out to be in good agreement with the current obtained from the observations. The most interesting is current pattern at northern and southern sites. There, due to the local interaction with the bottom slope and coastline, the measured currents have been deflected from the general clockwise circulation. The local coastal eddies, evident in the fine resolution model (Figure II.8), are responsible for this deflected flow pattern.

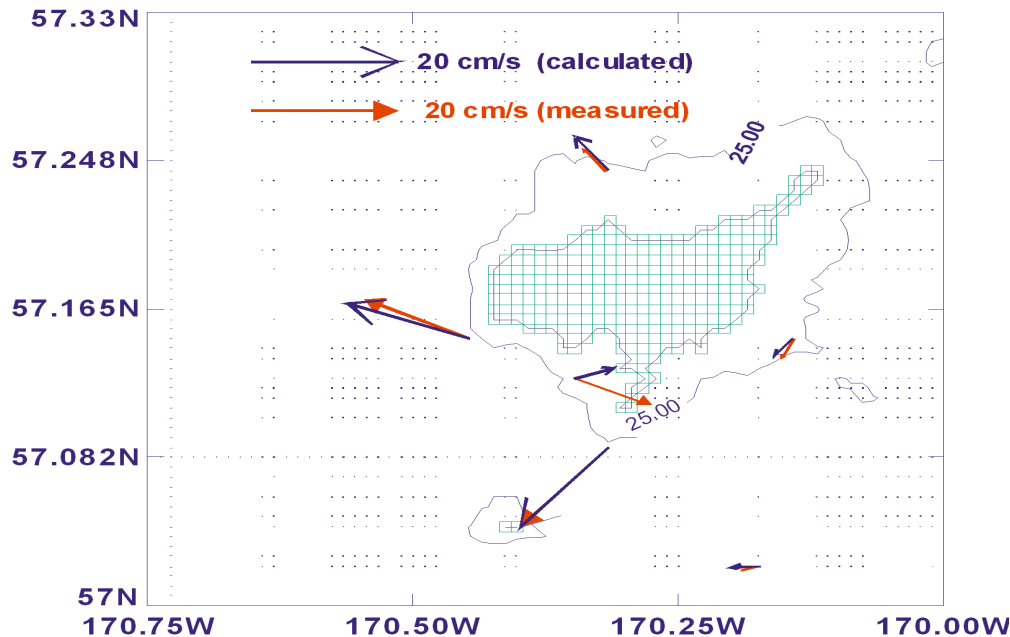


**Figure II.9. Comparison of the measured and calculated residual currents in the vicinity of St. Paul Island.**

To depict pattern of the tidal motion in the island's proximity, a set of particles is released around St. Paul. Position of a water particle located at a point with coordinates  $(x_0, y_0)$  at time  $t = t_0$  is tracked in time via the Lagrangian velocity. **Lagrangian velocity** is defined as superposition of Eulerian velocity (i.e., velocity given from tidal computation) and Stokes velocity. The change in position of a specific particle in the horizontal plane during time step  $dt$  is described as the total effect due to Eulerian and Stokes velocities (**Longuet-Higgins, 1969**).

$$dx = udt + 0.5\left(u\frac{\partial u}{\partial x} + v\frac{\partial u}{\partial y}\right)(dt)^2 \quad (11a)$$

$$dy = vdt + 0.5\left(u\frac{\partial v}{\partial x} + v\frac{\partial v}{\partial y}\right)(dt)^2 \quad (11b)$$

From experiments carried out we can conclude that the primary factors are Eulerian oscillatory and residual velocity. Stokes velocity is of secondary importance in the particle motion around St. Paul Island.

The initial locations and trajectories of the particles are given in Figure II.10. Out of five particles released, the one initially located 1 km from the shore describes the fastest trajectory. The particle released closest to the island is slowed down by the local coastal eddies. Only particles within 6 km of the island describe major features of the clockwise trapped motion. Particles initially located greater than 8 km west of the island were trapped into local offshore eddy generated around shallow bank, see Figure II.8.

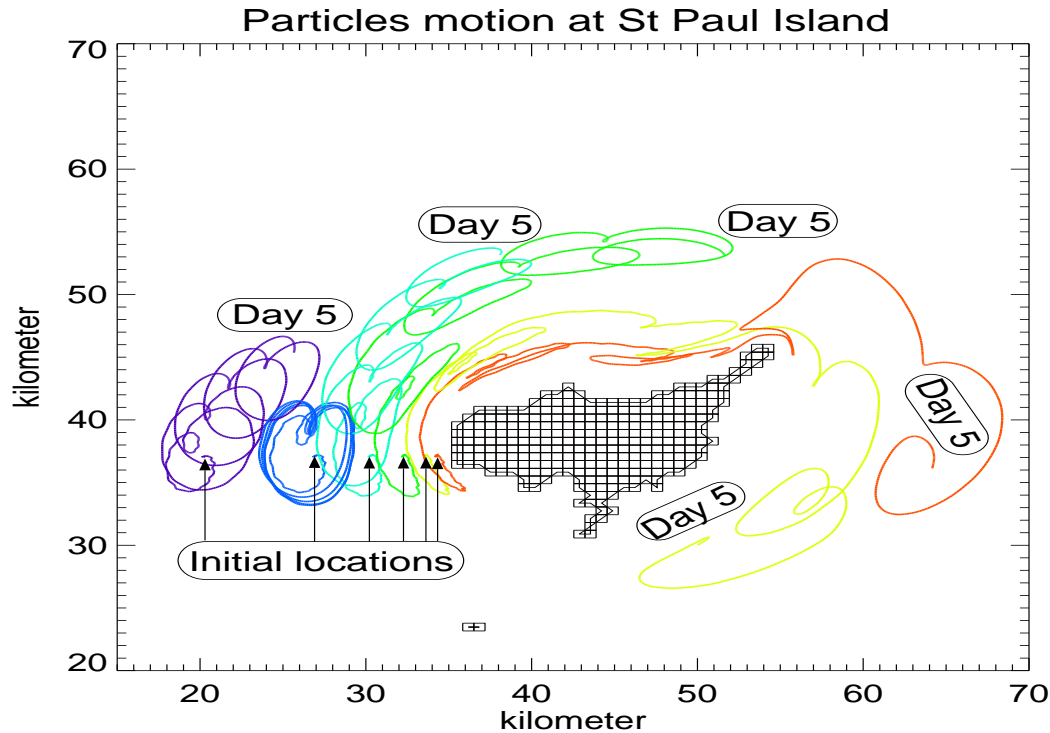
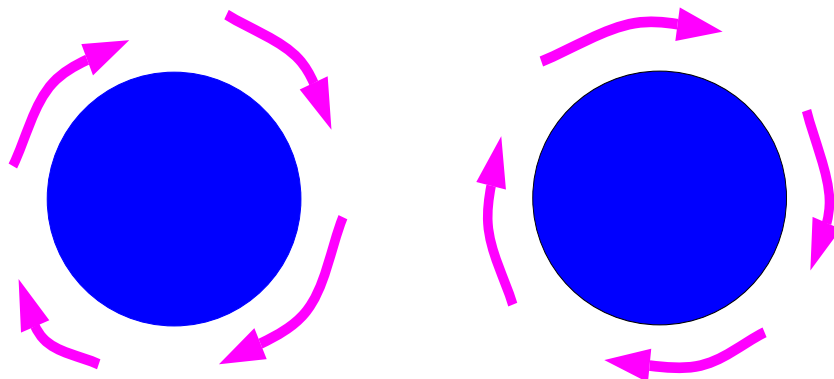


Figure II.10. Calculated trajectories during 5-day period. Particles are released west of St. Paul Island. Lagrangian particle motion is a superposition of tidal motion (oscillatory and residual) and Stokes drift. Mean velocity varies from  $10 \text{ cms}^{-1}$  to  $15 \text{ cms}^{-1}$ .

The type of circulation observed around one island can be extended to the island chain like Aleutian Islands. Tidally generated shelf-trapped waves at the shelf break and large tidal currents between Aleutian Islands generate strong nonlinear effects, resulting in complicated spectra of the tidal motion. The basic tidal constituents, through nonlinear interactions, generate long-term and short-term oscillations and residual currents. The role of tides in the exchange of the water between North Pacific and Bering Sea is especially important. Due to strong tidal currents, permanent residual motion has been established between islands (Kowalik, 1999) influencing exchange between the North Pacific and Bering Sea. Tidally driven residual motion around islands establishes a clockwise circulation (Fig.II.11). Thus in every pass between Aleutian Islands along with the northward transport on the eastern side of a pass, the southward directed transport exists on the western side of the same pass (Reed and Stabeno, 1999).



**Figure II.11. Tidally driven residual motion around pair of islands**

## References

- Abraham, G., H. Gerritsen, and G. J. H. Lindijer, 1987. Subgrid tidally induced residual circulation, *Cont. Shelf Res.*, 7, 285–305.
- Cartwright, D. E., 1969. Extraordinary tidal currents near St. Kilda, *Nature*, 223, 928–932.
- Defant, A., 1960. *Physical Oceanography*, Pergamon Press, v 2, 598pp.
- Francis, O., and P. Mazzega, 1990. Global charts of ocean loading effects. *J. Geophys. Res.*, 95, 11,411–11,424.
- Gill, A. E., 1982. *Atmosphere–Ocean Dynamics*, Academic Press, 662 pp.
- Hendeshott, M. C. 1977. Numerical models of ocean tides. In: *The Sea*, vol. 6, John Wiley & Sons, New York, 47–96.
- Henry, R. F. and M. G. G. Foreman, 2001. A representation of tidal currents based on energy flux, *Marine Geodesy*, 24(3), 139–152.
- Hunkins, K., 1986. Anomalous diurnal tidal currents on the Yermak Plateau. *J. Mar. Resear.*, 44, 51–69.
- Huthnance, J.M. 1981. Large tidal currents near Bear Island and related tidal energy losses from the North Atlantic. *Deep Sea Res.*, 28(1A), 51–70.
- Huthnance, J. M., 1974. On the diurnal tidal currents over Rockall Bank. *Deep Sea Res.*, 21, 23–35.
- Jayne, S. R. and L. S. St. Laurent, 2001. Parameterizing tidal dissipation over rough topography. *Geoph. Res. Letters*, 28(5), 811–814.

- Kantha, L. H., 1995. Barotropic tides in the global oceans from a nonlinear tidal model assimilating altimetric tides. 1. Model description and results. *J. Geophys. Res.*, 100, 25,283–25,308.
- Kowalik, Z. 1979. A note on co-oscillating  $M_2$  - tide in the Arctic Ocean. *Deutsche Hydrographische Zeitschrift* 32(3):100-112.
- Kowalik, Z., 1999. Bering Sea Tides. In: *The Bering Sea: Physical, Chemical and Biological Dynamics*, T. R. Loughlin and K. Ohtani, Eds., Alaska Sea Grant Press, Fairbanks, AK., 93–127.
- Kowalik, Z. and A. Marchenko, 2002. Tidal motion enhancement around islands. *J. Mar. Res.*, 60, 551-581.
- Kowalik, Z., and T. S. Murty, 1993. *Numerical modeling of ocean dynamics*, World Scientific Publ., 481 pp.
- Kowalik, Z. and P. Stabeno. 1999. Trapped motion around the Pribilof Islands in the Bering Sea. *Journal of Geophysical Research*, 104, C11, 25,667-25-684.
- Kowalik, Z., and A. Yu. Proshutinsky, 1995. Topographic enhancement of tidal motion in the western Barents Sea. *J. Geophys. Res.*, 100, C2, 2613–2637.
- Kowalik, Z and N. Untersteiner. 1978. A study of the  $M_2$  tide in the Arctic Ocean. *Dtsch. Hydrog. Z.*, 31, H.6, 216–229.
- Lamb, H. 1945. *Hydrodynamics*, 6th ed. Dover Publ. N.Y. 738 pp.
- Larsen, J. C, 1977. Cotidal charts for the Pacific Ocean near Hawaii using f-plane solutions. *J. Phys. Oceanogr.*, 7, 100109
- Lee, S. H., and K. Kim, 1993. Scattering of a Kelvin wave by a cylindrical island. *J. Oceanogr. Soc. Korea*, 28, 177–185.
- Le Provost, C. and F. Lyard, 1997. Energetics of the  $M_2$  barotropic ocean tides: an estimate of bottom friction dissipation from a hydrodynamic model. *Prog. Oceanog.*, 40, pp. 37-52.
- Loder, J.W., and D. G. Wright, 1985. Tidal rectification and front circulation on the sides of Georges bank. *J. Mar. Res.*, 43, 582–604.
- Longuet-Higgins, M. S., 1969. On the transport of mass by the time-varying ocean currents, *Deep Sea Res.* 16, 431–447.
- Marchuk, G. I. and B. A. Kagan, 1977. *Oceanic Tides*. Gidrometizdat. Leningrad, 296 pp.
- Mei, C. C., 1989. *The Applied Dynamics of Ocean Surface Waves*. World Scientific, 740 pp.
- Mofjeld, H. O., 1980. Effect of vertical viscosity on Kelvin waves. *J. Phys. Ocean.*, 10, 1039–1050.
- Mofjeld, H. O., 1984. Recent observations of tides and tidal currents from the Northeastern Bering Sea shelf. *NOAA Technical Memorandum ERL PMEL-57*, 36pp.
- Mooers, C., N. K. and R. L. Smith, 1968. Continental shelf waves off Oregon. *J. Geophys.*

*Res.*, **73**, 549–557.

Nekrasov, A. V., 1992. On tidal energy horizontal circulation. *The Journal of the Korean Society of Coastal and Ocean Engineers*, 4(3), 168–177.

Pearson, C. A., H. O. Mofield, and R. B. Tripp, 1981. Tides of the Eastern Bering Sea shelf, In: *The Eastern Bering Sea Shelf: Oceanography and Resources*, 1, 111–130.

Proudman, J., 1914. Diffraction of tidal waves on flat rotating sheets of water. *Proc. Lond. Math. Soc.*, 14, 89–102.

Rabinovich, A.B., and R.E. Thomson, 2001. Evidence of diurnal shelf waves in satellite-tracked drifter trajectories off the Kuril Islands, *J. Phys. Oceanogr.*, 31 (9), 2650–2668.

Ray, R. D., and B. V. Sanchez. 1989. Radial deformation of the earth by oceanic tide loading. NASA Technical Memorandum 100743. 51p.

Reed, R. K. and P. J. Stabeno, 1999. The Aleutian North Slope Current. In: *The Bering Sea: Physical, Chemical and Biological Dynamics*, T. R. Loughlin and K. Ohtani, Editors, Alaska Sea Grant Press, Fairbanks, AK, 177–191.

Rhines, P. B., 1969. Slow oscillations in an ocean of varying depth. 1. Islands and seamounts. *J. Fluid Mech.*, 37, 191–205.

Smagorinsky, J., 1963. General circulation experiments with the primitive equations, I. The basic experiment, *Mon. Weather Rev.*, 91, 99–164.

Sunderman, J. 1977. The semidiurnal principal lunar tide  $M_2$  in the Bering Sea. *Deutsche Hydrog. Zeitschrift* 30: 91–101.

Sverdrup, H. W. 1926. Dynamics of tides on the North-Siberian shelf. *Geofys. Publ. Norske Videnskaps-Akad.*, Oslo, 4, 175.

Taylor, G. I., 1919. Tidal friction in the Irish Sea. *Phil. Trans. Royal Soc. A.*, v. 220.

Taylor, G. I., 1921. Tidal oscillations in gulfs and rectangular basins. *Proc. London Math. Society* (2nd series), 20, 148–181.

Wahr, J., 1981. Body tides on an elliptical, rotating, elastic and oceanless earth. *Geophys. J. R. Ast. Soc.*, 64, 677–703.

Yefimov, V. V., Ye. A. Kulikov, A. B. Rabinovich, and I. V. Fine, 1985. *Ocean Boundary Waves*, Gidrometeoizdat, Leningrad, 280 pp.

Zimmerman, J. T. F., 1978. Topographic generation of residual circulation by oscillatory (tidal) currents. *Geophys. Astrophys. Fluid Dyn.*, 11, 35–47.

## CHAPTER III: TIDAL CURRENT

## 1. Bottom boundary layer

The tidal flow depicts to the large degree a constant current from the surface to the bottom. In proximity to the bottom the eddy viscosity diminishes the flow, influencing both magnitude and phase of the tidal current. If the tidal waves dynamics was limited to a simple oscillatory motion as is the case of the short wind waves, the decay of such motion is associated with an alternating oscillatory movement (**Lamb, 1932**). The influence of the Coriolis force brings an additional complication since the water particles in the tidal wave travel around an ellipse or circle in one tidal cycle. Tidal flow in proximity to the bottom is described by the following set of equations

$$\frac{\partial u}{\partial t} - fv = -g \frac{\partial \zeta}{\partial x} + \frac{\partial}{\partial z} N_z \frac{\partial u}{\partial z} \quad (\text{III.1})$$

$$\frac{\partial v}{\partial t} + fu = -g \frac{\partial \zeta}{\partial y} + \frac{\partial}{\partial z} N_z \frac{\partial v}{\partial z} \quad (\text{III.2})$$

In the above equations the horizontal components of velocity  $(u, v)$  have been related to the sea level  $(\zeta)$ . The motion is modified by the Coriolis force and the vertical friction. Here  $t$  is the time,  $z$  is the vertical coordinate,  $g$  gravity acceleration,  $N_z$  vertical eddy viscosity and  $f = 2\Omega \sin \phi$ ,  $\Omega$  is the Earth's rotation frequency and  $\phi$  is the geographical latitude.

The first step is to assume that velocity is a combination of the zero-order geostrophic solution and the first order solution, which represents changes caused by friction (**Munk et al., 1970**). For the zero-order, assumption is that the horizontal velocity does not vary along the vertical direction,

$$\frac{\partial u_0}{\partial t} - fv_0 = -g \frac{\partial \zeta}{\partial x} \quad (\text{III.3})$$

$$\frac{\partial v_0}{\partial t} + fu_0 = -g \frac{\partial \zeta}{\partial y} \quad (\text{III.4})$$

The first-order velocity is defined by,

$$\frac{\partial u_1}{\partial t} - fv_1 = \frac{\partial}{\partial z} N_z \frac{\partial u_1}{\partial z} \quad (\text{III.5})$$

$$\frac{\partial v_1}{\partial t} + fu_1 = \frac{\partial}{\partial z} N_z \frac{\partial v_1}{\partial z} \quad (\text{III.6})$$

The total velocity  $u = u_0 + u_1$  and  $v = v_0 + v_1$  away from the bottom will be expressed by the  $u_0$  and  $v_0$  only, while at the bottom, due to the friction  $u = 0$ , and  $v = 0$ . Therefore, the boundary conditions for the first-order velocity are

$$u_1 = -u_0, \quad v_1 = -v_0 \quad \text{at} \quad z = 0 \quad \text{and} \quad u_1 = 0 \quad v_1 = 0 \quad z \rightarrow \infty \quad (\text{III.7})$$

In the above equations the vertical coordinate is pointing upward and for convenience the origin of  $z$ -coordinate is located at the bottom. **Thorade (1928)** demonstrated (cf. **Defant, 1960**) that the vertical scale of the bottom boundary layer (BBL) depends on the tidal ellipse rotation, and for the clockwise (CW) and counterclockwise (CCW) rotation the two different scales occur. Following **Sverdrup (1926)** the **clockwise  $q$  and counterclockwise  $r$  components** are defined as

$$q = u_q + iv_q, \quad \text{and} \quad r = u_r - iv_r \quad (\text{III.8})$$

These components are defined through the Cartesian velocity as,

$$u = u_q + u_r, \quad \text{and} \quad v = v_q + v_r \quad (\text{III.9})$$

Also for  $q$  and  $r$  to display constant amplitudes

$$u_q = iv_q, \quad \text{and} \quad u_r = -iv_r \quad (\text{III.10})$$

With the above definition the Cartesian velocity components in terms of the CW and CCW components, can written as,

$$u = \frac{q + r}{2}, \quad \text{and} \quad v = \frac{q - r}{2i} \quad (\text{III.11})$$

or

$$q = u + iv, \quad \text{and} \quad r = u - iv \quad (\text{III.12})$$

Thus the CCW component is the complex conjugate of CW component. Equations of motion (III.5) and (III.6) can be redefined for  $q$  and  $r$  components by multiplying second equation by  $i$  and taking a sum and difference,

$$\frac{\partial q_1}{\partial t} + ifq_1 = \frac{\partial}{\partial z} N_z \frac{\partial q_1}{\partial z} \quad (\text{III.13})$$

$$\frac{\partial r_1}{\partial t} - ifr_1 = \frac{\partial}{\partial z} N_z \frac{\partial r_1}{\partial z} \quad (\text{III.14})$$

Here  $q_1 = u_1 + iv_1$  and  $r_1 = u_1 - iv_1$ . The boundary conditions (III.7) needs to be reformulated for the rotating components, and also the boundary condition at the free surface ought to be changed, since the distance from the bottom to the free surface is finite. At the free surface we assume zero stress condition,

$$\frac{\partial q}{\partial z} = 0 \quad \text{and} \quad \frac{\partial r}{\partial z} = 0 \quad \text{at} \quad z = H \quad (\text{III.15})$$

At the bottom the total velocity vanishes and the first-order velocity is defined by the zero-order velocity

$$q_1 = -q_0 \quad \text{and} \quad r_1 = -r_0 \quad \text{at} \quad z = 0 \quad (\text{III.16})$$

Here  $q_0 = u_0 + iv_0$  and  $r_0 = u_0 - iv_0$ . Solution to equation (III.13) and (III.14) for the constant eddy viscosity  $N_z$  and for the all dependent variables changing in time as  $\exp -i\omega t$ , can be written as (Mofjeld(1980)):

$$q_1 = -q_0 Q \quad \text{and} \quad r_1 = -r_0 R \quad (\text{III.17})$$

Here

$$Q = \frac{\cosh[\alpha_q(z - H)]}{\cosh(\alpha_q H)} \quad \text{and} \quad R = \frac{\cosh[\alpha_r(z - H)]}{\cosh(\alpha_r H)} \quad (\text{III.18})$$

The total velocity as defined by eqs (III.1) and (III.2) is

$$q = q_0 + q_1 = q_0(1 - Q) \quad \text{and} \quad r = r_0 + r_1 = r_0(1 - R) \quad (\text{III.19})$$

Here

$$\alpha_q = (1 + i)[(f - \omega)/2N_z]^{1/2}, \quad \text{if } \omega < f$$

$$\alpha_q = (1 - i)[(\omega - f)/2N_z]^{1/2}, \quad \text{if } \omega > f \quad (\text{III.20})$$

$$\alpha_r = (1 - i)[(\omega + f)/2N_z]^{1/2}, \quad \text{for all } \omega, \quad \text{and } f > 0 \quad (\text{III.21})$$

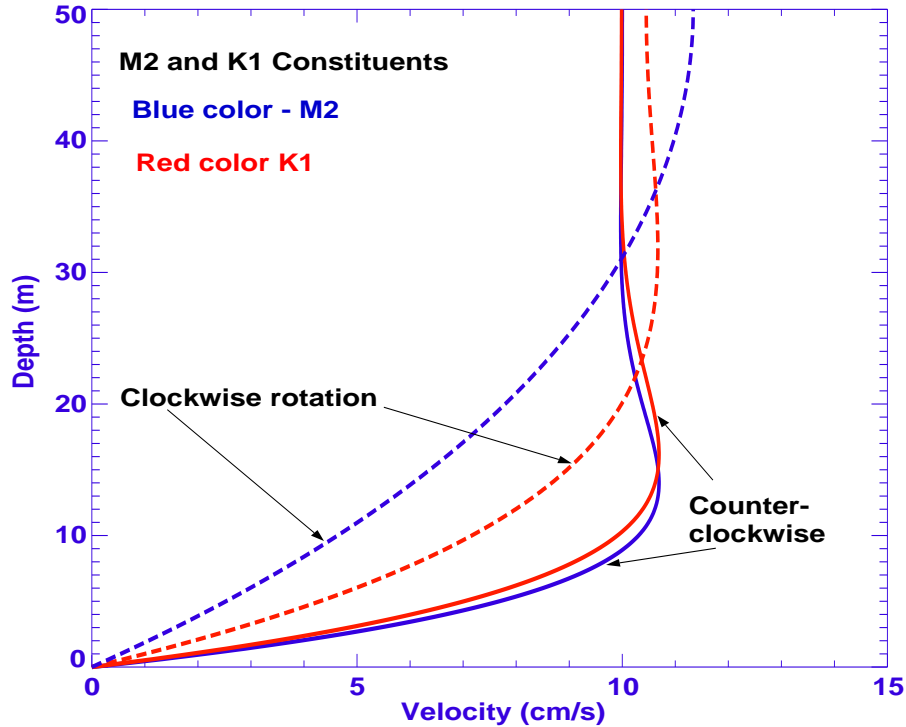


Figure 1. Vertical structure of the magnitude of the tidal current for the constant eddy viscosity coefficient.

The magnitude of the thickness of the BBL can be evaluated from the exponent in the above solution assuming decay of  $e^{-\alpha_q \delta}$  and  $e^{-\alpha_r \delta}$  is equal to  $e^{-1}$ ;

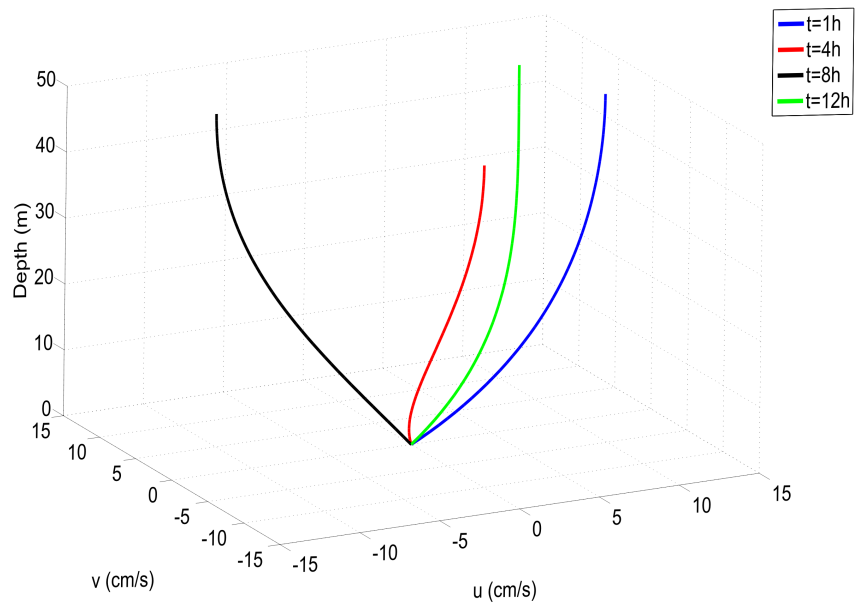


Figure 2a. 3D vertical structure of the clockwise component in the  $M_2$  current.

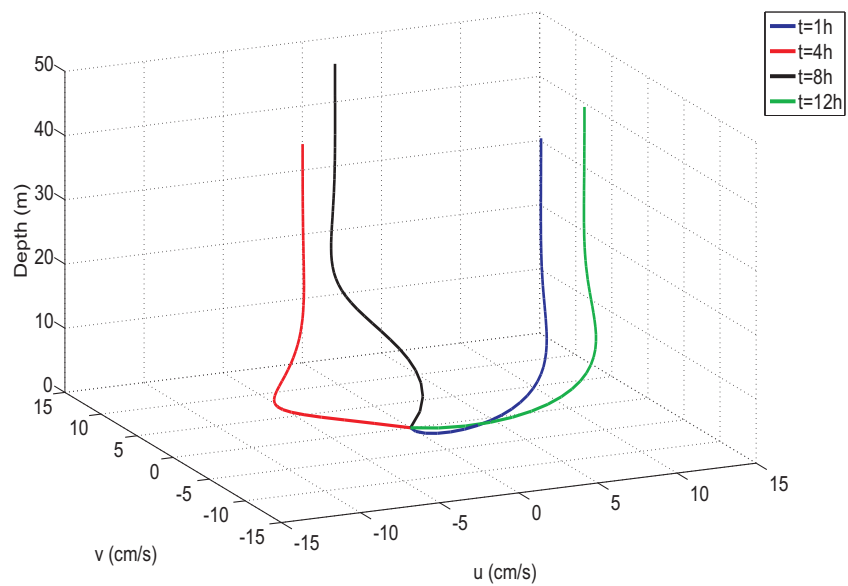


Figure 2b. 3D vertical structure of the counterclockwise component in the  $M_2$  current. Courtesy of Ying-Chih Fang.

$$\delta^\pm \simeq \sqrt{\frac{2N_z}{\omega \pm f}} \quad (\text{III.22})$$

Here minus is for the clockwise and plus is for the counterclockwise rotation. At the latitude  $60^\circ\text{N}$  the disparity between two scales is quite strong, since  $\delta^-/\delta^+ \simeq 4$ . In the Fig.1 the vertical distribution of the magnitude of velocity is shown for the clockwise and counterclockwise motion. The motion is considered in the shallow water of 50 m depth and is generated by circular current whose components for the clockwise motion are  $u_0 \sin(\omega t)$  and  $v_0 \cos(\omega t)$ . The amplitude is 10 cm/s and is equal to  $\sqrt{(u_0^2 + v_0^2)}$ . The constant eddy viscosity is  $50 \text{ cm}^2/\text{s}$ , latitude is  $60^\circ\text{N}$ . The blue color depicts  $M_2$  constituent and the red color is for  $K_1$ . The strong disparity in the behavior between clockwise and counterclockwise motion is well noticed.

Because the  $M_2$  wave is located in the subinertial frequency domain and its period ( $T_{M_2}=12.42 \text{ hr}$ ) is close to the inertial period ( $T_i = 13.82\text{hr}$ ), while the  $K_1$  wave is located in the superinertial domain and its period ( $T_{K_1} = 23.93 \text{ hr}$ ) is much larger than the inertial period, the thickness of the BBL for  $M_2$  flow is greater than for  $K_1$  flow. The strong differences between CC and CCW motion in the  $M_2$  currents are well observed in the time dependent 3-D motion plotted in Figures 2a and 2b.

A few conclusions follow from the above figures and solution. Consider for example two velocity profiles with circular motion imparted at the seafloor. We consider profiles of the 1)  $M_2$  CW motion and 2)  $M_2$  CCW motion, both forced with the same magnitude. Comparison of these two profiles shows that the dominant component of velocity at the free surface is rotating clockwise, while close to the bottom the CCW rotation is stronger. The relation between  $M_2$  and  $K_1$  components can be deduced in the similar manner. Again considering the same forcing the large differences between clockwise rotating currents can be observed. This leads to conclusion that  $M_2$  will dominate in the surface layer, but  $K_1$  is stronger in the bottom layer.

## 2. Vertical changes in the eddy viscosity

Above conclusions were deduced for the constant eddy viscosity which expresses conditions in the well mixed water column. As suggested by **Prandle (1982)** the properties of the BBL are further elucidated by the use of a variable eddy viscosity. The exchange of turbulent motion in the stratified water column is better described through the variable eddy viscosity. The problem of the tidal BBL and its dependence on the vertical exchange of momentum and mass will be considered by eqs (III.5) and (III.6), together with the following boundary conditions,

$$u_1 = -u_0, \quad v_1 = -v_0 \quad \text{at} \quad z = 0 \quad \text{and} \quad \frac{\partial u_1}{\partial z} = 0 \quad \frac{\partial v_1}{\partial z} = 0 \quad \text{at} \quad z = H \quad (\text{III.23})$$

Here for the clockwise (and circular) motion with the radius equal to 10 cm/s;  $u_0 = 10 \sin(\omega t)$  and  $v_0 = 10 \cos(\omega t)$ . To find the variability of the eddy viscosity in the tidal

flow the additional equations will be considered. To account for the vertical variations of the density the equation for temperature and salinity are solved,

$$\frac{\partial T}{\partial t} = \frac{\partial}{\partial z} D_z \frac{\partial T}{\partial z}, \quad \text{and} \quad \frac{\partial S}{\partial t} = \frac{\partial}{\partial z} D_z \frac{\partial S}{\partial z} \quad (\text{III.24})$$

In eddy viscosity parameterization we follow **Galperin et al. (1988)**. The eddy viscosity ( $N_z$ ) and eddy diffusivity ( $D_z$ ) are computed according to

$$N_z = lqS_m \quad \text{and} \quad D_z = lqS_H \quad (\text{III.25})$$

Where  $l$  is the mixing length,  $q$  the square root of twice the kinetic energy, and  $S_M$  and  $S_H$  are functions of the vertical stratifications. The definition of these functions is given in **Blumberg and Mellor (1987)** and **Galperin et al. (1988)**. The equation for the turbulent energy

$$\frac{\partial q}{\partial t} = 2N_z \left[ \left( \frac{\partial u}{\partial z} \right)^2 + \left( \frac{\partial v}{\partial z} \right)^2 \right] + 2D_z \frac{g}{\rho} \frac{\partial \rho}{\partial z} - \frac{2q^3}{B_1 l} \quad (\text{III.26})$$

and the equation for the length  $l$

$$\frac{\partial q^2 l}{\partial t} = lE_1 N_z \left[ \left( \frac{\partial u}{\partial z} \right)^2 + \left( \frac{\partial v}{\partial z} \right)^2 \right] + lE_2 D_z \frac{g}{\rho} \frac{\partial \rho}{\partial z} - \frac{q^3}{B_1} \tilde{W} \quad (\text{III.27})$$

complete the turbulence closure.

Here  $B_1 = 16.6$ ,  $E_1 = 1.8$ ,  $E_2 = 1.33$ .  $\tilde{W}$  defines a wall proximity function, see formulas (III.13) and (III.14) in **Blumberg and Mellor (1987)**. Thus the problem of the tidal BBL and its dependence on the vertical exchange of momentum and mass will be considered by eqs (III.5) and (III.6) together with boundary conditions (III.23) and the turbulence closure problem expressed by (III.24)–(III.27). Similar problems were solved for the tides by **Mofjeld et al., (1984)** and **Marchuk and Kagan, (1977)**.

First, the vertical exchange is considered in the uniform water column. The results of numerical computations are shown in Fig. 3a for the  $M_2$  wave and in Fig. 3b for the  $K_1$  wave. All parameters are defined for the geometry considered in Fig. 1. For comparison, the previous results for the constant eddy viscosity are given as well. The influence of the depth-dependent eddy viscosity is expressed in the narrowing of the BBL, both for the semidiurnal and diurnal tides and for the clockwise and counterclockwise rotations. As before the motion imparted at the bottom influences higher levels of the water column through the clockwise  $M_2$  component. For the variable eddy viscosity the magnitude of the  $M_2$  current even at the water surface is still growing (Fig. 3a), whereas the clockwise  $K_1$  component reaches constant magnitude away from the free surface (Fig. 3b).

The vertical distribution of the eddy viscosity coefficient for the clockwise and counterclockwise rotation of the  $M_2$  wave is shown in Fig. 4. The velocity distribution given in Fig. 3 influences the vertical pattern of the eddy viscosity as well. For the clockwise motion the maximum value of the eddy viscosity is greater and also it is located higher above the bottom than the maximum for the counterclockwise rotation. The vertical distributions for the  $K_1$  wave, differ in magnitude and location of the maximum, but the general shape of the distributions is similar to the presented in Fig.4.

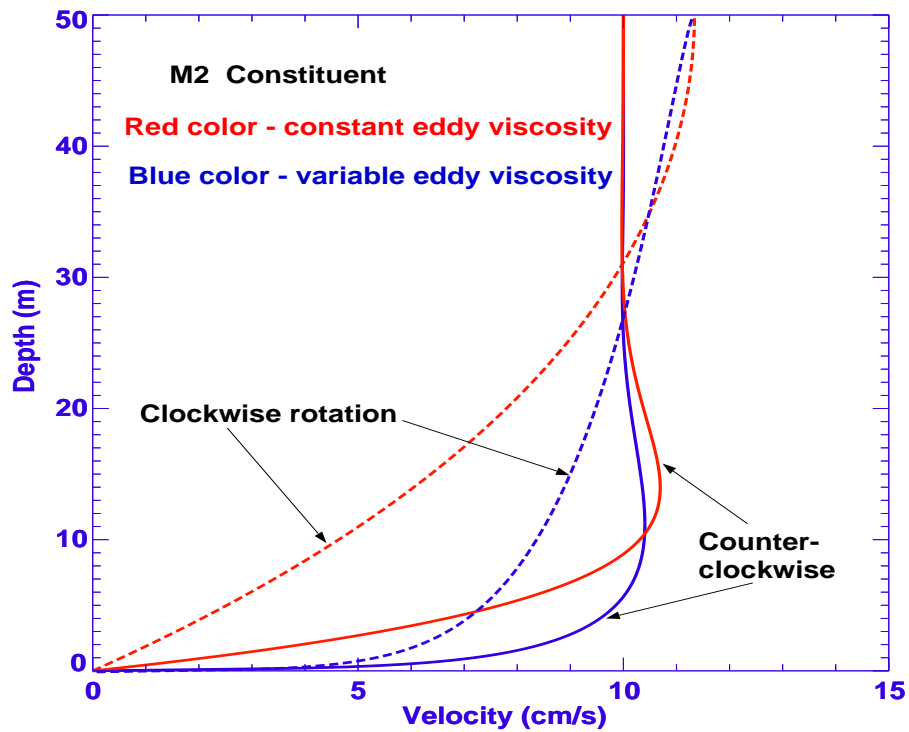


Figure 3a. Vertical structure of the magnitude of the  $M_2$  current for the constant (red color) and the variable (blue color) of the eddy viscosity coefficient.

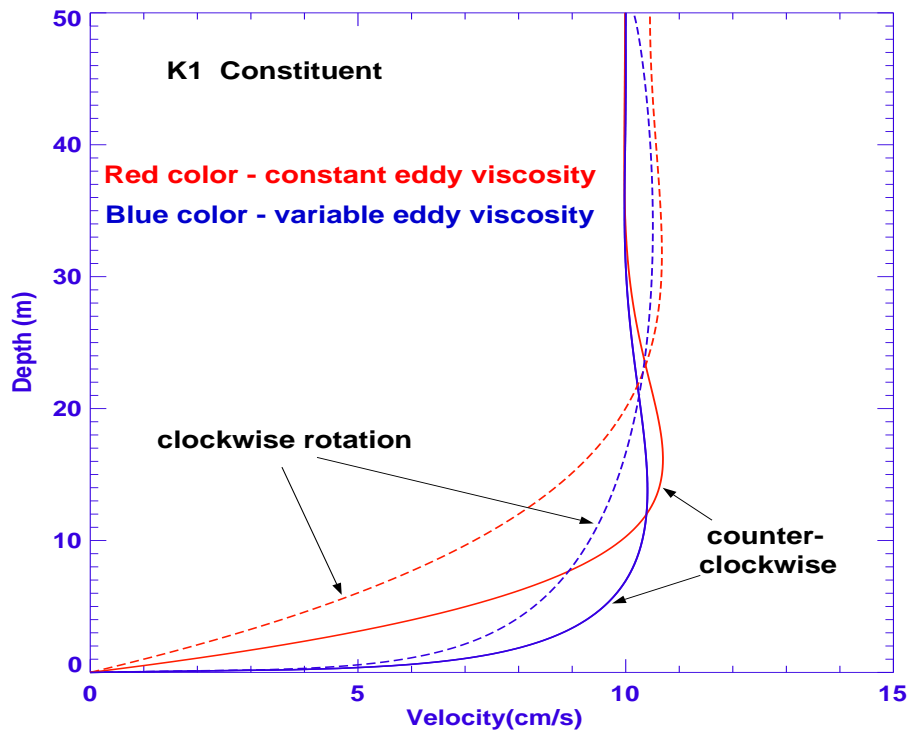


Figure 3b. Vertical structure of the magnitude of the  $K_1$  current for the constant (red color) and the variable (blue color) of the eddy viscosity coefficient.

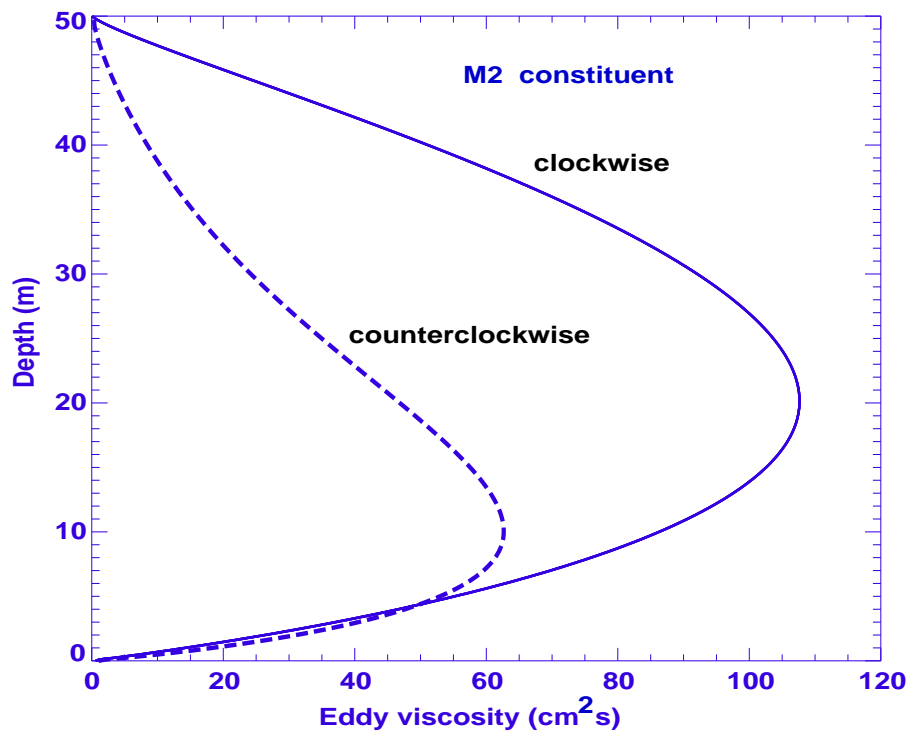
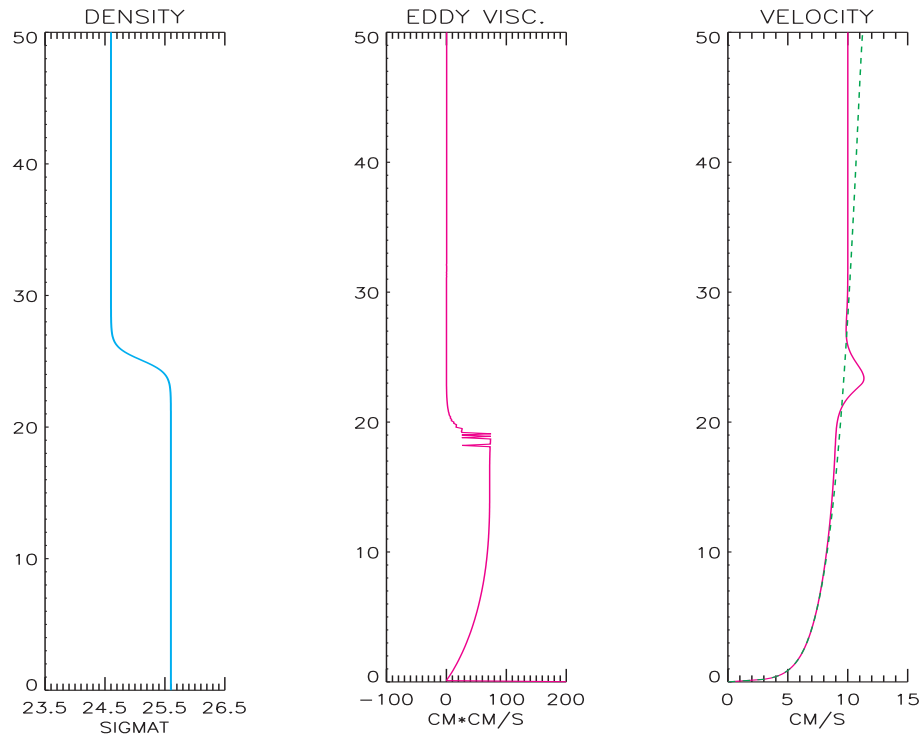


Figure 4. Vertical structure of the eddy viscosity coefficient for the clockwise (continuous line) and counterclockwise (dashed line) motion in the  $M_2$  wave.

### 3. Influence of the stratification

Observation of the tidal currents in the shallow water region of freshwater influence (outflowing from the Rhine river) show a strong difference for the stratified and well mixed conditions (Visser et al., 1994). The observations were taken in the shallow (less than 20 m) water and close to the shoreline. On the other hand the tidal currents around St. Lawrence Island were observed at the greater depth and at some distance from the island. The influence of the well mixed and stratified conditions is well observed but the difference is not very strong. The key factor seems to be location of the pycnocline in relation to the BBL. Let us consider a slightly modified model which takes into account a modification of the velocity due to the density stratification. Typical density profile south of St. Lawrence Island at the late summer shows very strong fresh water influence. The water column structure depicts two-layers of the well-mixed density which are divided by the very narrow pycnocline layer. This density distribution is introduced into eqs.(III.26) and (III.27) to calculate modified distribution of the eddy viscosity and next through eqs.(III.5) and(III.6) a new velocity is computed. With respect to the CW and CCW components, the density effect will be small on the CCW components since they have a narrow BBL and above this layer the velocity remains constant. The effect will be stronger on the clockwise components (especially on  $M_2$  wave) due to their variability along the vertical direction.



**Figure 5.** Vertical structure of the density (sigmat), eddy viscosity coefficient and magnitude of the velocity in the  $M_2$  wave.

In Fig. 5 the effect of the density stratification on the velocity distribution of the  $M_2$  wave is shown. The density stratification resulted in the new profile of the eddy viscosity. Due to the density stratification, the turbulence generated in the BBL, has been strongly reduced and at about 20 m above the bottom it is completely damped. Therefore, the eddy viscosity changes only in the near-bottom region, above 20 m from the bottom the eddy viscosity is reduced to the constant, close to zero value. Such distribution of the turbulence generates the velocity profile (continuous line) which has a small maximum at the pycnocline and constant magnitude above. For comparison (broken line) the velocity profile without stratification is given as well. In Fig.6 the influence of the density stratification on the  $K_1$  wave is depicted. Although the velocity profile shows a small variations at the pycnocline, the overall influence is negligible. The different behavior of the  $M_2$  and  $K_1$  waves is related to the different thickness of the boundary layers. The boundary layer thickness of the  $K_1$  wave is smaller than the distance to the pycnocline, therefore the pycnocline region is encountered by the constant velocity profile without any gradients. On the other hand the boundary layer for the  $M_2$  wave is greater than the distance to the pycnocline. The  $M_2$  wave profile depicts quite strong gradient in the pycnocline region. Above pycnocline the eddy viscosity is strongly reduced and the new vertical structure depicts there a constant velocity. This is in contrast with the profile computed without density stratification (cf. broken line in Fig. 5).

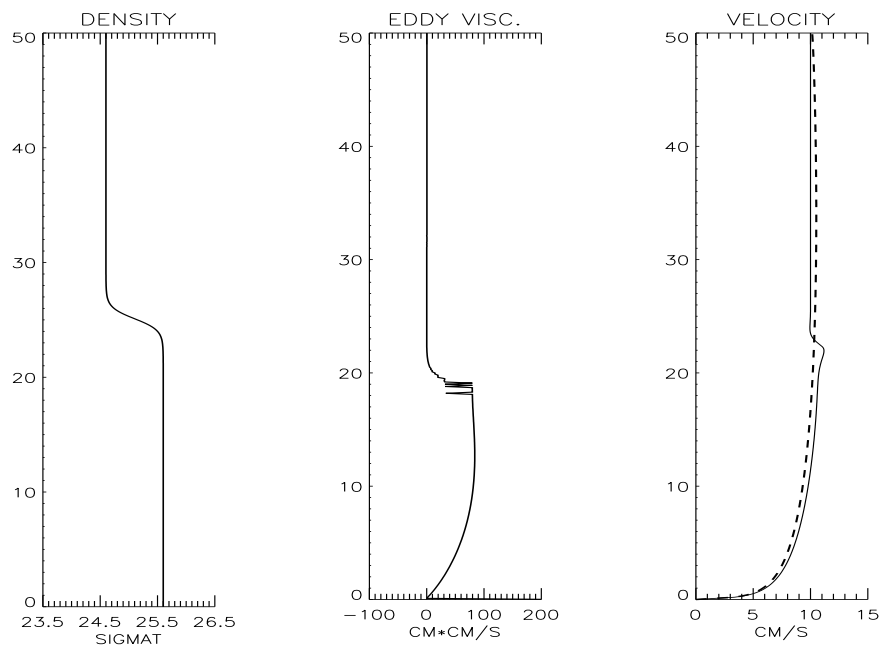


**Figure 6.** Vertical structure of the density (sigmat), eddy viscosity coefficient and magnitude of the velocity in the  $K_1$  wave.

Up till now we investigated the vertical structure of the magnitude of tidal velocity. Let us consider the vertical structure of velocity. The usual approach is to construct the ellipses of the tidal currents (we consider circles) and to analyze the changes in the water column due to the bottom stress, eddy viscosity and stratification. In Fig.7, top panel the  $M_2$  tidal current circles are given at the three levels. The vertical structure of the current magnitude corresponding to this case is given in Fig. 2. The small break in the circular motion in Fig. 7 is marking the beginning and end of the tidal cycle. The circular motion imparted at the bottom is transferred towards the surface, while the current is increasing towards the surface the motion remains circular. The radius vectors drawn from the center of the circle to the border denote both the velocity magnitude and the phases at the initial time. The phase difference between the  $M_2$  currents at the surface and at the bottom is approximately  $9^\circ$ . Somewhat different picture emerges for the density stratified column – Fig. 7, bottom panel. The phase difference between surface and the middle depth (25 m from the bottom) is negligible, thus the upper portion of the water (above halocline) is moving back and forth as one column. The phase difference from the upper water column to the bottom is approximately  $33^\circ$ . Because the period of the  $M_2$  wave is close to 12 hr the phase difference corresponds to about 2 hr difference between the surface and bottom currents. Comparison of the surface and the middle depth current show that the current at the surface does not remain circular, but assumes an elliptical shape; and the middle depth currents are stronger than the surface currents (this conclusion follows from the Fig. 5 as well).

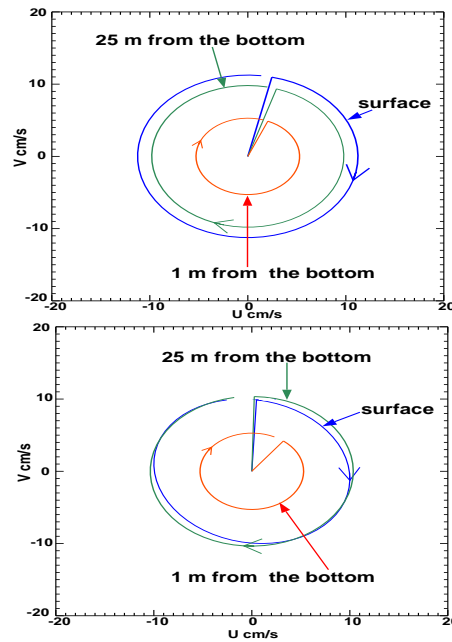


Figure 7. Vertical structure of the tidal current circles/ellipses. Upper panel for the uniform density. Lower panel for the density distribution given in Figs. 5 and 6.

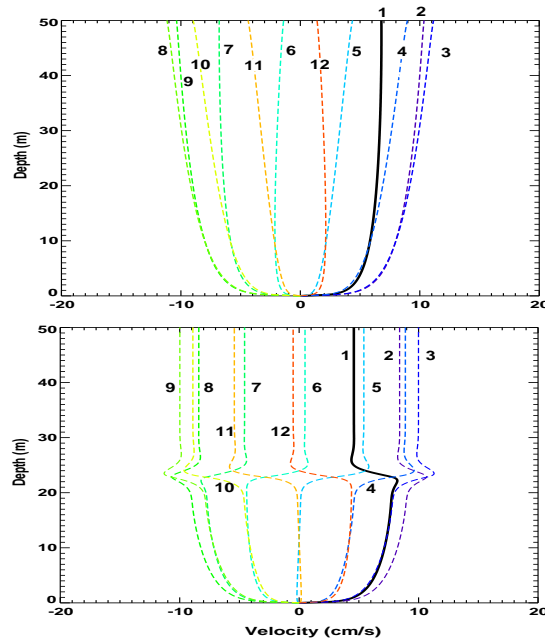


Figure 8.  $U$  component of the tidal current. Upper panel for the uniform density. Lower panel for the density distribution given in Figs. 5 and 6. Numbers denote hours in 12hr periodic motion.

Let us consider the component of the current in the vertical cross-sections along the  $x$ -axis. This is of course  $u$  component in the Cartesian system of coordinates. In the Fig. 8 the progression of the velocity for the 12 phases of the  $M_2$  tide period is plotted. While in

the uniform water column (Fig. 8, top panel) the u-velocity is described by the continuous profile with small changes along the vertical direction, in the stratified water column the velocity depicts rapid change in the region of halocline.

In summary, the influence of the density stratification will lead to the changes in the vertical structure of the tidal currents. The two-layer density structure causes reduction of turbulence in the column above pycnocline. Therefore the motion in the upper portion of fluid often show strong phase lag in relation to the near-bottom motion. The vertical structure of the current tends to develop rapid changes with the maximum velocity in the pycnocline region.

#### 4. St. Lawrence Island region

Above theory we will apply to the vertical variability of tidal currents in the northern part of the Bering Sea near St. Lawrence Island. Since the vertical distribution of the current, due to density stratifications, varies in time the long time-series of measurements are considered. St. Lawrence Island is situated on the Bering Sea shelf about 250 km south of Bering Strait and 500 km northeast of the shelf break (Figure 9). Fall storms tend to mix and cool the water column until by December the northern shelf waters are vertically homogeneous and at the freezing point. Ice cover progresses from north to south (Niebauer, 1999) and by the end of December the entire northern shelf is ice covered. During the winter, a polynya is generated immediately to the south of St. Lawrence Island by periodic strong northerly wind events (Schumacher et al., 1983; Johnson and Kowalik, 1986). Opening and closing of the polynya occurs until late April, when increasing solar radiation and warmer air temperatures melt the sea ice. Spring and summer insolation, the fresh ice melt and the spring river freshets progressively stratify the water column so that by the end of summer the northern shelf is essentially a two layer fluid: a homogeneous lower layer of cold, salty water remnant from the previous winter (mixed by tidal currents) and a homogeneous upper layer (mixed by winds) comprised of relatively fresh and warm waters. Fall storms then break down this stratification and the cycle begins anew. The unique location of the northern Bering Sea as a transition zone between the mid-latitudes and the Arctic results in three different water types (Alaska Coastal Water, Bering Shelf Water and Anadyr Water, (Coachman et al., 1975) that pass through Bering Strait to their eventual fate in the layers of the Arctic Ocean. A table depicting the annual cycle of the physical environment in the northern Bering Sea region is given in Table 1. Tides are an important and consistent driving force in the Bering Sea. About 90% of the kinetic energy over the south-east Bering Sea shelf and 10-40% in the St Lawrence Island region is of tidal origin (Coachman, 1986). Tide waves enter the Bering Sea as progressive waves from the North Pacific Ocean, mainly through the central and western passages of the Aleutian-Komandorski Islands (Sünderman, 1977; Pearson et al., 1981; Kantha, 1995). The Arctic Ocean is a minor secondary source of tides, and therefore tides in the northern Bering Sea are considered to be the result of co-oscillation with the Pacific and, to a lesser degree, with the Arctic Ocean.

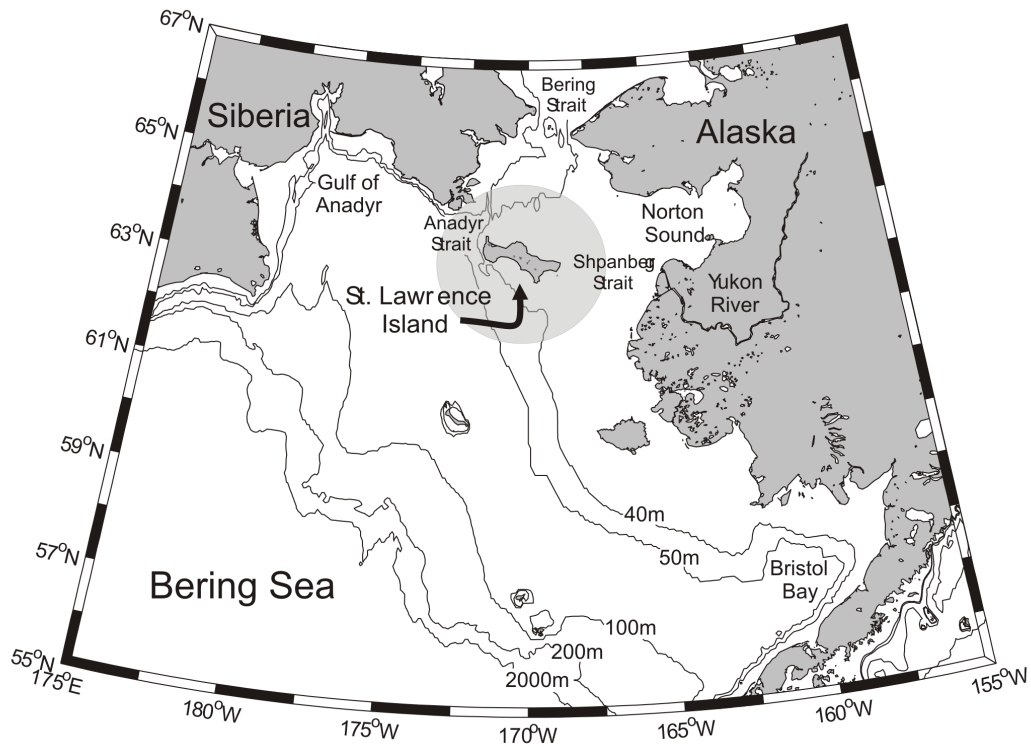


Figure 9. Map of the eastern Bering Sea with place names and bathymetric contours. The study area is denoted by a shaded circle around St. Lawrence Island.



Table 1. Basic environmental components of the St. Lawrence Island region and their approximate annual distributions. Shaded boxes denote nominal months of influence by relevant processes.

Pearson et al. (1981) constructed empirical charts for four major tidal constituents

( $M_2$ ,  $N_2$ ,  $K_1$ , and  $O_1$ ) over the Bering Sea shelf. **Mofjeld (1984, 1986) and Mofjeld et al. (1984)** analyzed data for three diurnal components ( $O_1$ ,  $P_1$ ,  $K_1$ ) and three semidiurnal components ( $M_2$ ,  $S_2$ ,  $N_2$ ) over the northeastern Bering shelf and made comparisons against numerical models and tidal theory. Observations show that over most of the shelf regions, the tides are primarily semidiurnal. However, near some of the Aleutian Islands, in Norton Sound and at some locations along the shelf break, diurnal tides are dominant. The tides on the northeastern Bering Sea shelf are in a transitional regime, between low tides in the Chukchi Sea and high tides along the Bering shelfbreak.

The major semidiurnal constituent  $M_2$  displays approximately 20 cm amplitude near St. Lawrence Island. The  $M_2$  tide is under the influence of amphidromic systems located near Bering Strait, southeast of St. Lawrence Island and in the Gulf of Anadyr (**Kowalik, 1999**). The dynamics of diurnal tides can be described using the major constituent  $K_1$ . Although the  $K_1$  wave has a maximum amplitude of approximately 40 cm in the region of the shelf break, this amplitude decreases from the shelf break to about 7-8 cm in the St. Lawrence Island region. **Mofjeld (1984)** has suggested that such behavior of the  $K_1$  tidal wave on the Bering Sea shelf resembles a Sverdrup wave generated by an incident wave from the deep Bering basin. The Sverdrup wave model predicts well the amplitudes and phases of the tides on the Bering Sea shelf. These waves, in a frictionless ocean below the critical latitude (for  $K_1$  tide,  $\Phi_{cr}=30^\circ$ ), propagate as free waves; above this latitude they change to subinertial evanescent waves. Data described by **Mofjeld (1986)** from the northwestern shelf show that the tidal harmonic constants change seasonally. The diurnal amplitude increased and semidiurnal amplitude decreased during winter. The increase and decrease amounted to a few percent of the mean values. The maximum change in amplitude is close to 3 cm and the maximum change in phase is up to  $15^\circ$  for the  $M_2$  tide in Bering Strait. The relatively large changes in amplitude (37% of the mean amplitude) at this site possibly expresses damping of the tides by the sea ice in the Arctic Ocean (**Kowalik and Proshutinsky, 1994**). Observations on ice drift and deformation in the Bering Sea indicate possible strong nonlinear ice–water coupling in the tidal band of oscillations since the  $M_4$  tidal component of the ice velocity is relatively much stronger than the  $M_4$  in the ocean currents (**Pease and Turet, 1989**).

Five current meter stations located near St. Lawrence Island were described by **Pearson et al. (1981) and Mofjeld (1984)**. Mooring NC25A, located 40 km to the south of the island at 46 m depth, displays weak tidal currents. Here, the  $M_2$  semi-major axis value is 4.8 cm/s and  $K_1$  is 1.8 cm/s. However, mooring LD2 located off Northeast Cape in a total water depth of 28 m shows much stronger currents: for the  $M_2$  wave the semi-major axis is 15.4 cm/s and for the  $K_1$  wave, 7.5cm/s. For comparison to the observations made in 1998-1999, the moorings deployed in the 1970s and 1980s (NC19B, NC25A, NC26B, LD2 and LD3) are reproduced in Table 2 and Table 3. These historical measurements give broader spatial coverage than the newer observations but none of the historical records were made over the course of an entire calendar year.

Here we describe tidal analyses from 12 additional year-long stations in the vicinity of St. Lawrence Island reported by **Danielson and Kowalik (2005)**.

## 5. Tidal data and comparison of full records against the vertically averaged model.

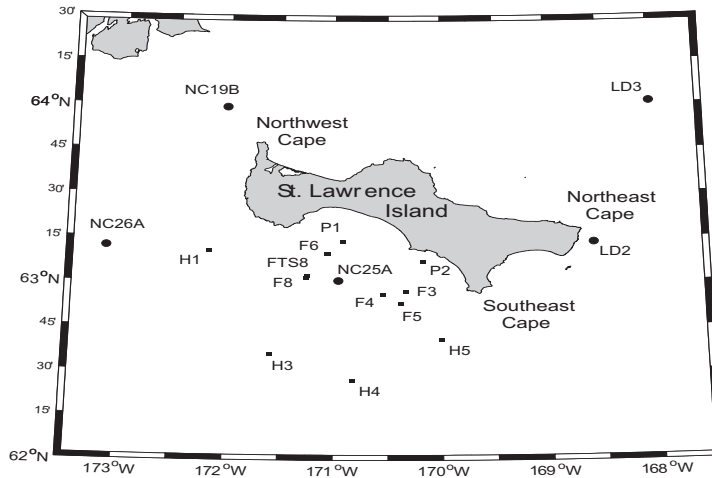


Figure 10. Map of the St Lawrence Island region with place names. Mooring locations with tidal analyses new to this study are marked with squares and historical mooring locations are marked with circles.

Mooring Name	Latitude (°N)	Longitude (°W)	Water Depth (m)	Instr. Depth (m)	Instr. Type	Record Length (hr)
P1	63.216320	-170.919255	33	29	RCM	8760
P2	63.105798	-170.175357	33	28	RCM	8760
F3	62.939492	-170.332632	44	40	RCM	8760
F4	62.920650	-170.550217	44	40	RCM	8760
F5	62.867403	-170.383040	45	41	RCM	8760
F6	63.150860	-171.065913	44	39	ADCP	8760
FTS8	63.015542	-171.264042	50	45	RCM	8760
F8	63.017197	-171.259847	50	45	ADCP	8760
H1	63.162092	-172.167453	60	22	RCM	8760
H1	63.162092	-172.167453	60	55	RCM	8760
H3	62.584617	-171.585850	48	43	RCM	8760
H3	62.584617	-171.585850	48	20	RCM	8760
H4	62.437383	-170.828100	42	24	RCM	8760
H4	62.437383	-170.828100	42	37	RCM	8760
H5	62.667317	-170.000883	42	37	RCM	8760
H5	62.667317	-170.000883	42	24	RCM	8760
<i>NC19B</i>	63.966667	-172.016667	55	45	RCM	5496
<i>NC25A</i>	63.000000	-170.966667	46	36	RCM	5496
<i>NC26A</i>	63.183333	-173.133333	67	57	RCM	5496
<i>LD2</i>	63.216667	-168.583333	28	24	RCM	696
<i>LD3</i>	64.000000	-168.000000	37	33	RCM	696

Table 2.

Table 2. Mooring names, locations, water column depth, instrument depth, instrument type and record lengths are given. Historical mooring names and parameters (Pearson et al.,1981; Mofjeld, 1984) are denoted with italics. RCM = Aanderaa RCM-4 and RCM-7 instruments, ADCP = RDI 300 KHz Acoustic Doppler Current Profiler.

A total of twelve moorings were deployed to collect velocity data at hourly intervals over the period of one year from September 1998 to September 1999. Figure 10 shows a detailed map of the St. Lawrence Island region with these mooring locations and the five historical mooring locations taken from [Pearson et al. \(1981\)](#) and [Mofjeld \(1984\)](#). Table 2 summarizes the mooring names, instrument types, spatial coordinates, current meter depths, water column depths and record lengths for the records used in the comparison with the numerical model. Tidal ellipse parameters were not recomputed for the historical records. Rather, we have taken the previously published findings for these moorings ([Pearson et al., 1981](#); [Mofjeld, 1984](#)), adjusting the inclination (and phase when necessary) to conform to the current standard of reporting ellipse inclination with respect to due east. New results in Table 2 have been computed in a consistent manner to these historical analyses for ease of comparison. The essence of this analysis approach is consecutive 29-day harmonic analyses spaced every 15 days from the beginning of the record. Results from moorings LD2 and LD3 were only published with one months worth of record, so the standard deviation entry in Table 3 is blank for these moorings. LD2 and LD3 represent mid-summer conditions. The moorings NC19B, NC25A and NC26A represent tidal currents from the November through June time frame, see Table 1 and discussion below for ramifications of these temporally restricted sample periods.

Analysis software T-TIDE by [Pawlowicz et al. \(2002\)](#), was used for all tidal harmonic fit computations. Two selected depths, one near-surface and one near-bottom are given for the ADCP instruments.

The yearlong analysis shows that the  $M_2$  constituent contains the most energy, with current speeds between 3.1 and 16.0 cm/s.  $K_1$  is the largest diurnal constituent, with current speeds between 1.8 and 7.5 cm/s. For records with an entire years worth of data, the  $M_2$  ( $K_1$ ) current speed maxima and minima are 16.0 (4.1) and 6.2 (2.0) cm/s respectively. At ADCP mooring F8, the second through tenth largest constituents resolved from vertically averaged currents are all in the range between 1.2 and 3.8 cm/s. The first ten constituents at this mooring, in order of magnitude, are  $M_2$ ,  $K_1$ ,  $N_2$ ,  $MM$ ,  $MSM$ ,  $MF$ ,  $O_1$ ,  $S_2$ ,  $SSA$  and  $P_1$ . All ten constituents have a signal to noise ratio greater than 2. The sum of these first ten amplitudes is about 38 cm/s. The mean current speed of a year-long tidal prediction that includes all resolved constituents is about 12 cm/s.

Propagation of the time of maximum  $M_2$  current generally progresses from east to west for the region to the south of the island with the notable exception of mooring H5 off Southeast Cape. The three moorings located off Northwest, Northeast and Southeast Capes have the three largest Greenwich phase values, indicating that these promontories may act to disrupt the wave propagation with increased phase lag. Given the similarity in phase amongst all southerly mooring locations, it is not possible to discern a direction of propagation for the  $K_1$  wave. As with the  $M_2$  phase, the  $K_1$  phase measured at H5 (bottom instrument) is a bit of an outlier.

M2									
Mooring Name	Depth (m)	Semi-Major Axis (cm/s)		Semi-Minor Axis (cm/s)		Inclination (degrees)		Greenwich Phase (degrees)	
		Mean	Std. Dev.	Mean	Std. Dev.	Mean	Std. Dev.	Mean	Std. Dev.
P1	29	6.7	1.5	1.3	0.7	147.9	9.3	74.0	7.3
P2	28	7.2	1.3	2.8	1.3	134.3	8.2	49.6	7.9
F3	40	11.5	3.6	1.5	0.9	137.3	4.4	53.2	5.2
F4	40	10.1	3.3	0.9	0.8	143.1	5.6	57.5	6.0
F5	41	10.6	3.7	0.9	0.9	145.4	6.8	54.3	5.1
F6	37	9.9	1.6	2.2	0.8	146.5	12.6	41.0	11.8
F6	10	16.0	2.0	-3.5	1.2	163.6	6.1	64.8	6.4
FTS8	45	8.3	2.3	0.4	0.6	132.8	6.8	68.7	8.2
F8	43	10.5	1.3	0.1	0.8	145.7	9.3	44.7	8.2
F8	10	15.0	1.0	-3.9	0.8	153.6	5.1	59.6	3.1
H1	22	8.7	2.7	-2.5	1.1	142.9	2.1	114.9	4.8
H1	55	7.1	1.9	0.0	0.5	136.0	7.8	99.6	8.2
H3	43	6.2	2.4	-2.8	1.3	158.8	4.7	60.3	6.3
H3	20	7.1	2.7	-3.9	1.5	162.2	8.9	72.3	4.7
H4	24	8.0	2.9	-3.8	1.5	164.6	35.9	58.7	38.2
H4	37	8.3	2.4	-3.0	1.4	169.0	5.9	42.0	7.0
H5	37	10.9	3.6	-0.3	1.0	62.0	81.4	157.7	95.4
H5	24	12.2	2.7	-2.1	0.9	9.2	3.3	228.7	7.8
<i>NC19B</i>	<i>45</i>	<i>5.3</i>	<i>0.4</i>	<i>0.6</i>	<i>0.5</i>	<i>28.0</i>	<i>8.0</i>	<i>190.0</i>	<i>12.0</i>
<i>NC25.4</i>	<i>36</i>	<i>4.8</i>	<i>0.7</i>	<i>0.2</i>	<i>0.5</i>	<i>151.0</i>	<i>5.0</i>	<i>242.0</i>	<i>6.0</i>
<i>NC26.4</i>	<i>57</i>	<i>3.1</i>	<i>0.7</i>	<i>1.1</i>	<i>-0.4</i>	<i>101.0</i>	<i>4.0</i>	<i>104.0</i>	<i>5.0</i>
<i>LD2</i>	<i>24</i>	<i>15.4</i>		<i>8.5</i>		<i>59.0</i>		<i>130.0</i>	
<i>LD3</i>	<i>33</i>	<i>4.9</i>		<i>3.5</i>		<i>128.0</i>		<i>78.0</i>	

Table 3a

K1									
Mooring Name	Depth (m)	Semi-Major Axis (cm/s)		Semi-Minor Axis (cm/s)		Inclination (degrees)		Greenwich Phase (degrees)	
		Mean	Std. Dev.	Mean	Std. Dev.	Mean	Std. Dev.	Mean	Std. Dev.
P1	29	2.0	0.7	-0.3	0.3	154.8	33.8	231.9	41.0
P2	28	2.1	0.6	0.0	0.3	151.5	10.2	187.0	17.2
F3	40	3.6	1.4	-1.1	0.7	140.4	41.6	192.2	56.7
F4	40	3.4	1.3	-1.2	0.5	155.9	8.7	207.4	15.8
F5	41	3.4	1.3	-1.1	0.6	150.9	32.4	198.1	42.0
F6	37	3.1	0.7	-0.6	0.5	151.8	47.8	197.2	48.9
F6	10	3.6	0.8	-0.7	0.5	134.7	41.5	199.4	50.2
FTS8	45	3.0	0.8	-0.6	0.3	147.4	7.2	222.9	17.3
F8	43	3.5	0.7	-1.0	0.3	158.1	6.0	207.7	14.9
F8	10	3.9	1.0	-1.4	0.4	141.8	5.9	199.0	14.5
H1	22	2.6	0.8	-0.7	0.3	140.3	9.3	234.3	18.7
H1	55	2.7	1.0	-0.6	0.4	154.2	9.1	244.8	18.4
H3	43	2.7	0.8	-1.8	0.7	142.2	38.6	219.6	36.7
H3	20	2.7	1.0	-1.7	0.7	143.0	41.4	203.1	43.1
H4	24	3.2	0.8	-2.1	0.7	113.2	71.1	205.7	87.2
H4	37	3.4	0.9	-2.4	0.7	78.0	73.2	231.6	114.0
H5	37	3.8	1.1	-1.6	0.7	22.5	9.3	227.0	160.9
H5	24	4.1	1.0	-1.6	0.5	21.4	8.3	297.4	113.7
<i>NC19B</i>	<i>45</i>	<i>3.0</i>	<i>0.4</i>	<i>0.0</i>	<i>0.2</i>	<i>44.0</i>	<i>4.0</i>	<i>355.0</i>	<i>9.0</i>
<i>NC25.4</i>	<i>36</i>	<i>1.8</i>	<i>0.4</i>	<i>0.4</i>	<i>-0.2</i>	<i>158.0</i>	<i>9.0</i>	<i>214.0</i>	<i>10.0</i>
<i>NC26.4</i>	<i>57</i>	<i>1.3</i>	<i>0.2</i>	<i>0.7</i>	<i>-0.2</i>	<i>146.0</i>	<i>14.0</i>	<i>219.0</i>	<i>17.0</i>
<i>LD2</i>	<i>24</i>	<i>7.5</i>		<i>-0.7</i>		<i>79.0</i>		<i>29.0</i>	
<i>LD3</i>	<i>33</i>	<i>4.0</i>		<i>-1.7</i>		<i>17.0</i>		<i>24.0</i>	

Table 3b

Table 3. Tidal parameters derived from both the model and overlapping 29-day analyses of the current meter records of the St. Lawrence Island region. Given are semi-major and semi-minor ellipse axes (cm/s), the phase angle (degrees) referred to Greenwich and the inclination (degrees) of the semi-major axis referenced in a counter-clockwise fashion to due east. Positive (negative) sign of the semi-major axis denotes counterclockwise (clockwise) rotation. Mean and standard deviations are computed with respect to the ensemble of 29-day analyses, beginning 15 days from the start of the record. Historical mooring names and parameters (Pearson et al., 1981; Mofjeld, 1984) are denoted with italics.

The model delineates regions of stronger currents in the St. Lawrence Island domain, in particular sites off the Northwest, Northeast and Southeast capes. The stronger tidal currents of these locations are probably due to shallower bathymetry which conforms to the cape structure. It is of interest to see that Anadyr Strait, located between the island and Siberia, strongly controls the tidal motion both in the semidiurnal and diurnal bands by changing the flow from elliptical to rectilinear, whereas off of Southeast cape  $K_1$  is much more elongated than  $M_2$ . The  $K_1$  wave has approximately twice the wavelength of the  $M_2$  wave so it is not surprising that the  $K_1$  ellipses are less able to exhibit rotational character within the straits. The wider nature of Shpanberg Strait (approx. 200 km) apparently allows for more rotation of the  $M_2$  wave than does Anadyr Strait (approx. 75 km).

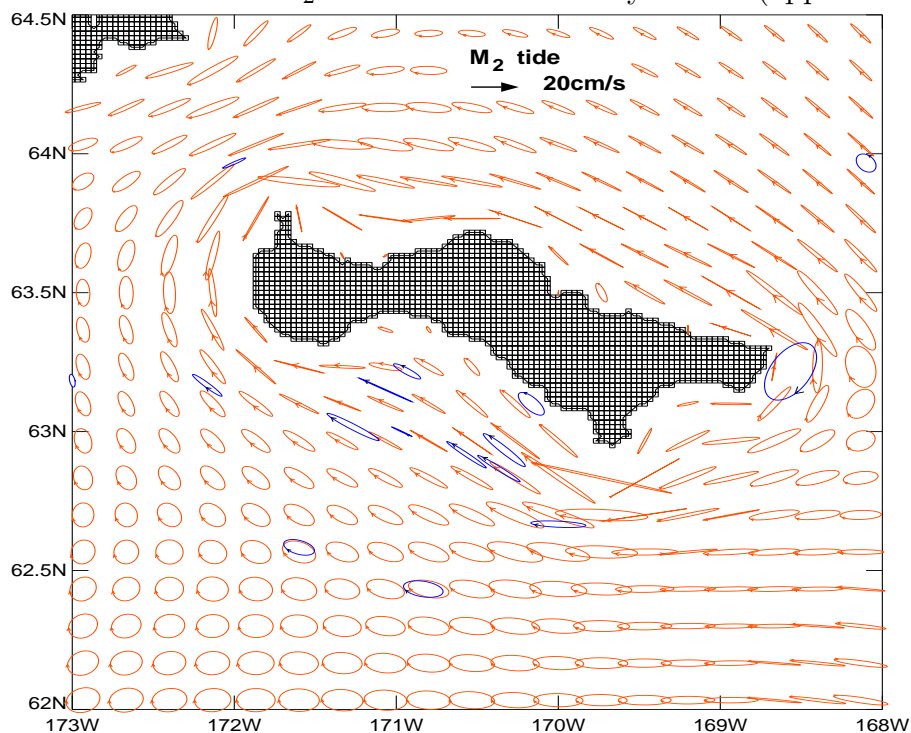


**Figure 11.  $M_2$  observed and estimated tidal ellipses. Red ellipses are from the model, blue ellipses are from the current meter records.**

We compare tidal current ellipses from the measurements against the local tidal model constructed around St. Lawrence Island. The numerical model uses a spatial resolution of approximately 1.85 km. The boundary conditions for the local model were taken from a large scale model for the entire Bering Sea (Kowalik, 1999). The ellipses for the  $M_2$  tide are shown in Figure 11 and ellipses for the  $K_1$  tide in Figure 12. The computed ellipses turned out to be in reasonable agreement with those obtained from the observations, thus implying that the tidal regime is mainly of barotropic nature. Deviations of ellipse eccentricity and magnitude may be due in part to 1) deviations from true depths of the bathymetric data set employed, 2) proximity of the recording instrument to the sea floor and 3) local density structure. These deviations especially are strong for the  $M_2$  constituent. Historical currents, usually measured close to the bottom, are smaller than the computed ellipses. Ellipse orientation is generally parallel to the bathymetric contours and ellipses are more rectilinear for locations closer to the shore and in the straits.

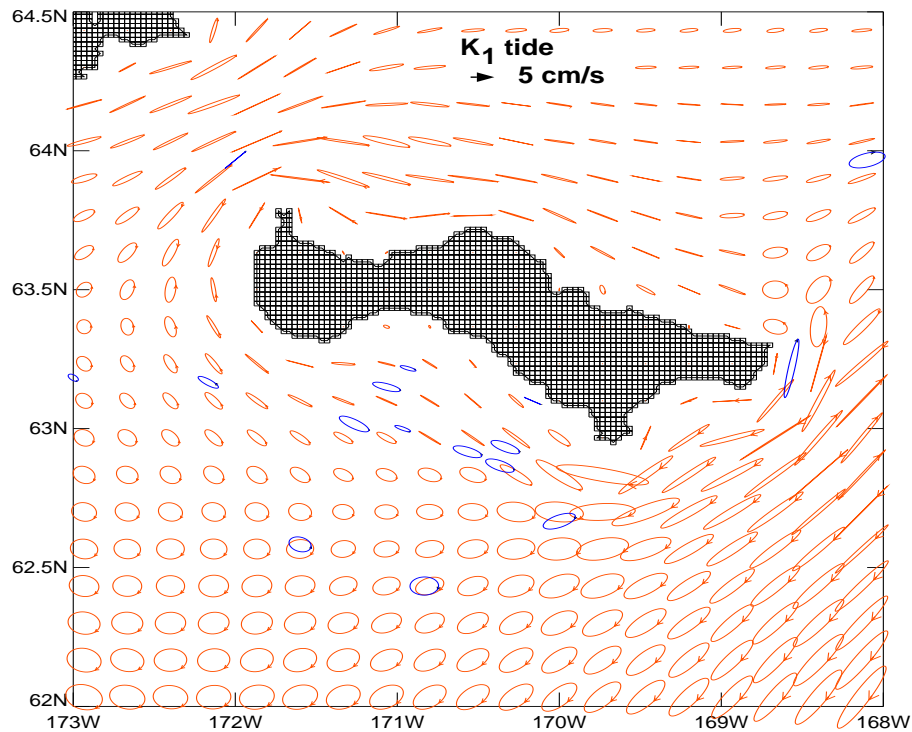


**Figure 12.  $K_1$  tidal ellipses. Red ellipses are from the model, blue ellipses are from the current meter records.**

## 6. Structure of temporal and vertical variability.

To examine the primary characteristics in the tidal current distribution along the vertical direction we describe yearlong analyses at mooring F8. Structure of the tidal currents through the water column based on the annual analysis for all depths at mooring F8 is shown in Figure 13.  $M_2$  tidal currents are relatively constant ( $15 \pm 2$  cm/s) from the surface down to approximately 15 m depth, depict a slight maximum around 20 m, and then decay to the instrument depth of 43 m. This character is seen in both the semi-major and semi-minor axes. The direction of rotation for the  $M_2$  ellipse is negative (CW) and only in close proximity to the instrument the direction changes to positive rotation (CCW). This reflects that in the entire layer of decreasing current magnitudes, progressing toward the bottom, the sense of rotation tends more and more to the CCW direction. The current ellipse only slightly changes eccentricity in the surface layer, as both major and minor axes are relatively constant. Below 25 m, the eccentricity decreases until at about 10 m above the bottom the ellipse becomes rectilinear, indicative of the change in sense of rotation. The  $M_2$  inclination and phase both are constant in the upper 15 m of the water column then undergo a linear decrease of about  $15^\circ$  to the instrument depth. In contrast to the  $M_2$  currents, the  $K_1$  tidal current semi-major and semi-minor axes are invariant over the course of the water column. The phase and inclination of  $K_1$  progress from the surface to the instrument depth over a range of about  $20^\circ$  in an opposite sense to the change of the  $M_2$  parameters. The diurnal BBL must be located below the deepest measurement depth, i.e., 6 m above the bottom. Mean variations through the water column are in the range of

$\pm 10^\circ$  and  $\pm 0.5$  cm/s. The direction of rotation for the  $K_1$  ellipse does not change from CW throughout the water column. The profile shape for the  $K_1$  tide does not significantly change character through the course of the year.

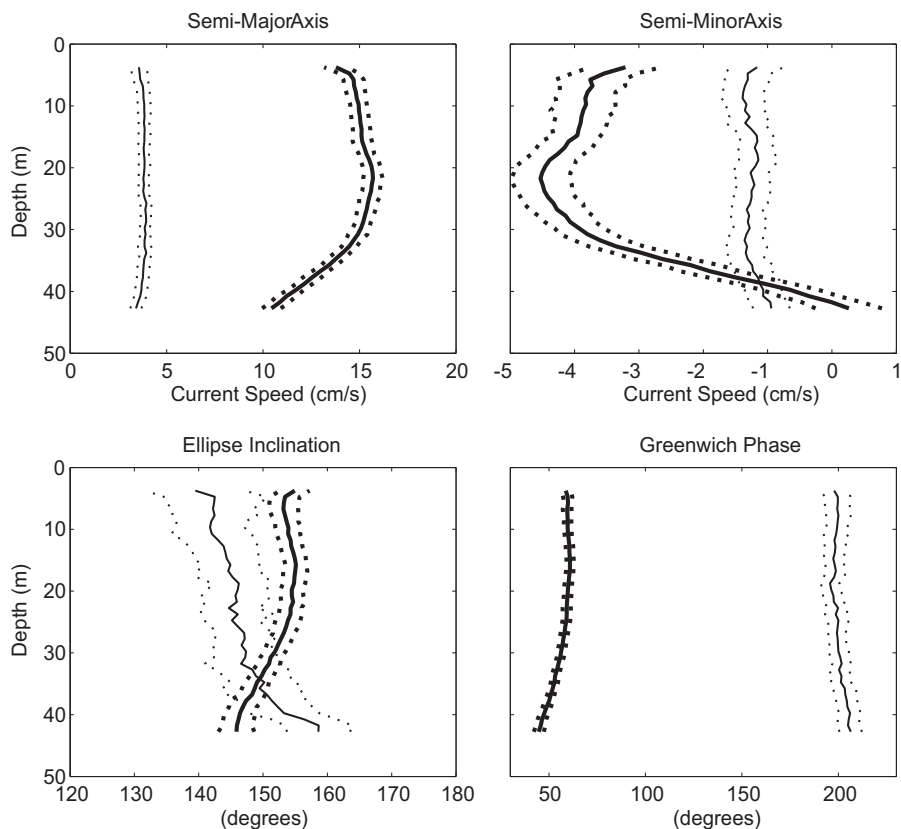


**Figure 13.** Vertical profiles of velocity parameters for  $M_2$  (heavy lines) and  $K_1$  (light lines) tidal currents. Dotted lines depict the  $\pm 95\%$  confidence limits for each parameter.

For the two moorings with profiling ADCPs (F6 and F8), we also computed overlapping monthly tidal harmonic analyses for the year-long series. This allows us to assess the seasonal character in conjunction with the vertical structure for a comprehensive description of the tidal currents. Figure 14 describes the yearly cycle of the  $M_2$  tidal currents from F8 and shows the development of a strong baroclinic tide during the summer. The character of the  $M_2$  tidal currents changes over the course of the year from the cold, salty, ice covered winter conditions between January and March and the two-layer, sharply stratified conditions of July through September. For  $M_2$ , the time periods of October to December and May to June are transition periods between these two extremes. The main periodicity is a yearly cycle with weaker winter currents and stronger summer currents. The month-long analyses reveal that the  $M_2$  currents varied from as little as 7 cm/s (near the bottom in the winter) to as much as 21 cm/s (near the surface in the summer). Minimum values were observed near the bottom during all months, the smallest values occurring between January and March. Tidal currents were fairly constant between the surface and about 25m

during this time. During the stratified period (approximately June through September) at mooring F8 a subsurface maximum of the  $M_2$  currents occurred between 20 and 25m, whereas at F6 the  $M_2$  currents are maximal at the surface and decay throughout the water column toward the bottom. From March to October, ellipse inclination and phase both are constant in the upper 20m and then decay from 20m to the bottom. From November through April the phase and inclination are less variant through the water column.

The diurnal tidal currents are smaller than the  $M_2$  currents and exhibit markedly different seasonal character.  $K_1$  does not have an annual modulation. Constituent  $K_1$  ( $T=23.934522$  h) is not typically resolved from constituent  $P_1$  ( $T=24.065873$  h) in a 29-day analysis, so instead  $P_1$  was inferred from  $K_1$  using the relationship determined by the yearlong analysis (Foreman and Henry, 1989; Pawlowicz et al., 2002). Linear interaction of  $K_1$  and  $P_1$  creates a beat period of 1/2 year (Pugh, 1987). In the St Lawrence Island region, the manifestation of this semi-annual period (Figure 15) results in an envelope of current speed with minimum of approximately 2.5 cm/s in March/September and maximum of about 5cm/s in November/May. Although 5 cm/s is not a particularly energetic flow, it is of the same order as the mean background flow (3.6 cm/s) at NC25A (Schumacher et al, 1983) and is approximately 40% of the annual mean tidal flow and 14% of the peak tidal flow. Thus the major seasonal cycle for the diurnal currents is not the annual cycle of baroclinic tide generation which dominates behavior of  $M_2$  but the semi-annual cycle of interacting constituents. Beating of close constituents also occurs for semi-diurnal tides; we will show later that  $M_2$  and  $N_2$  exhibit a monthly beat that dominates the total tidal energy profiles.

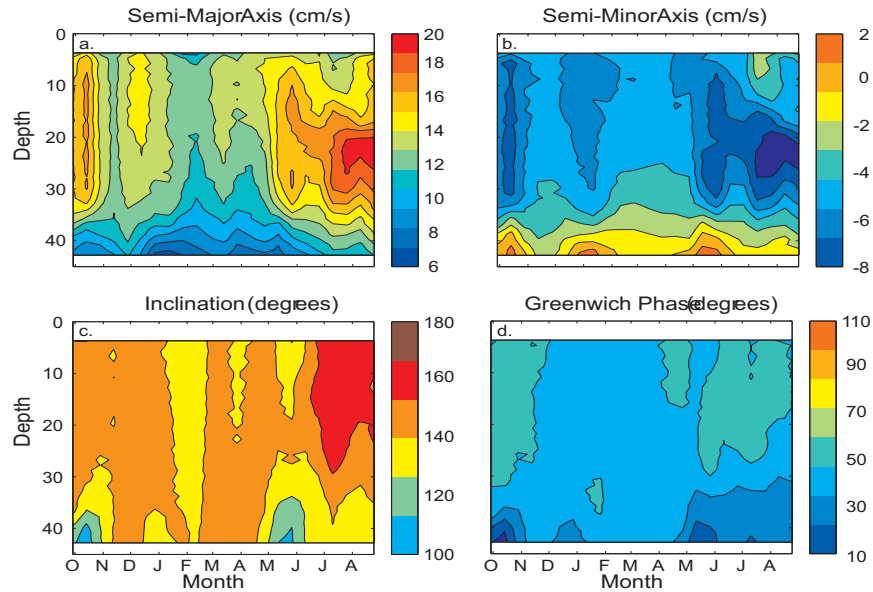


**Figure 14.** Contours of harmonic constants for the  $M_2$  currents at stations F8 from September 1998 to September 1999. Shown are: semi-major axis (a), semi-minor axis (b), inclination (c) and Greenwich phase (d). The horizontal axes denote the month of the year, the vertical axes denote depth through the water column.

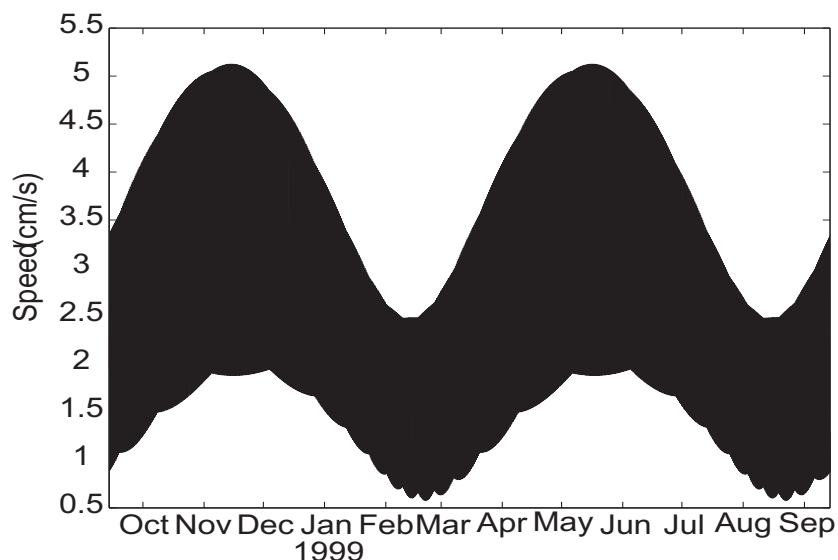


**Figure 15.** Semi-annual modulation due to constituents  $K_1$  and  $P_1$  at mooring F8. The envelope shown indicates the range of current speeds seen on a daily basis.

## 7. Rotary spectra

Tidal current parameters were also evaluated based on rotary spectra analysis (Gonella, 1972; Mooers, 1973; Emery and Thomson, 2001). Figure 16 depicts the rotary spectra for the 10 m and 43 m depths at mooring F8. Rotary spectral analysis for the total energy in diurnal and semidiurnal bands shows that the energy of semidiurnal tides dominates both the upper and lower water column. The contribution of diurnal tides to the total energy is smaller, although the second strongest maximum in the energy spectra belongs to the  $K_1$  tide. Tidal maxima show some slight seasonal variability, but it is not the strongest feature of the tidal regime depicted by the rotary spectra.

The feature which sets apart the tidal currents in the upper and lower water column are the CW and CCW components of rotation. At 10 m depth, the energy of the CW component at the  $M_2$  period is more than two times greater than the energy of the CCW component, while at 43 m depth the CCW component slightly dominates (Table 4). The same behavior, i.e., prevalence of CW motion at the surface and growth of the CCW motion towards the bottom can be discerned for both seasons as well as the other semidiurnal tides, cf.,  $S_2$  and  $N_2$ . The ratios of CW to CCW energy in the diurnal band do not appreciably change with depth.

	M2		K1	
	Winter	Summer	Winter	Summer
10m	3.25	2.17	3.71	3.65
43m	0.85	0.97	3.25	3.72

Table 4. Ratio of CW to CCW power in summer and winter seasons for constituents M2 and K1 at near-surface and near-bottom depths.

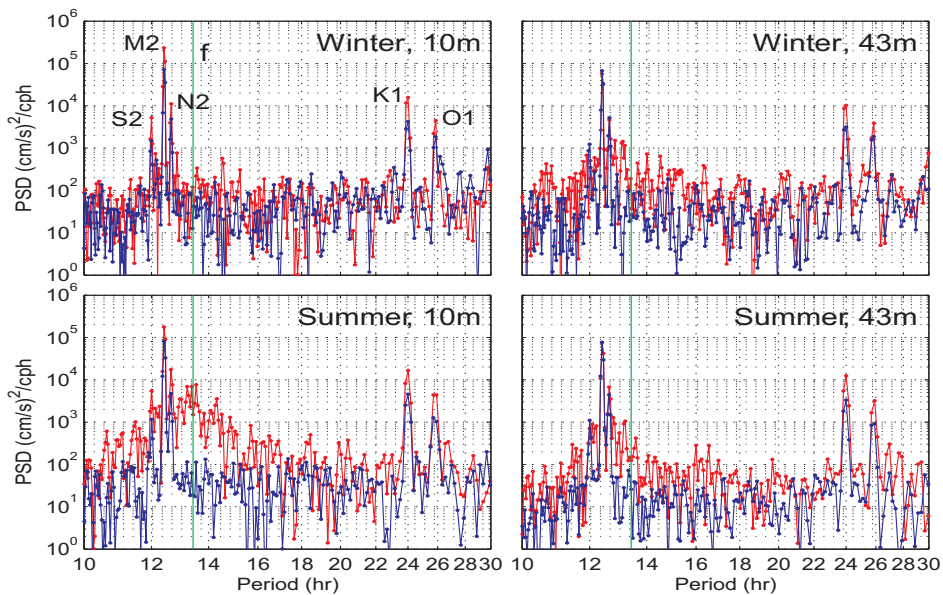


Figure 16. Rotary power spectra of the currents at mooring F8. Panels depict spectra from a) Winter, 10m depth, b) Winter, 43m depth, c) Summer 10m depth and d) Summer 43m depth. Red (blue) traces correspond to CW (CCW) rotation. Vertical green line locates inertial period (f).

The broad inertial oscillation maximum in Figure 16c exhibits strong seasonal variability. Amplification of near-inertial clockwise currents in the upper layer of the water column during the summer period is seen in this figure. Wind-generated motion supplies energy only through the surface layer of the ocean in the wide frequency band around the inertial frequency, but we have seen that baroclinic tidal effects are also primarily limited to the upper portion of the water column. The strong summer stratification appears to limit the enhancement of near-inertial motion to the upper layer. Figure 16c also suggests that the summer enhancement is not limited to inertial motion, as the clockwise currents at the  $N_2$  frequency have been magnified with respect to the  $N_2$  currents shown in panel 16a. However, the noise floor of the semi-diurnal band in the near-surface winter spectrum (16a) appears depressed with respect to the other three spectra, so such observations are difficult to assess. In winter, the near-surface maximum in the power spectra around the inertial period of oscillation is absent. One might like to draw the conclusion that the probable cause of the diminished energy is reduced air-sea coupling due to sea ice cover, but this has to be reconciled with the measurements in ice free regions. [Maas and van Haren \(1987\)](#) demonstrated a dramatic increase in energy of the inertial oscillations, in the central part of the North Sea, from the unstratified winter conditions to the stratified summer conditions, despite the facts that there is no ice cover during the winter and that the wind forcing during both seasons is not significantly different.

## 8. Elliptical motion along the vertical direction

Initial investigations of the BBL were made for circular motion where the relative input of the CW and CCW motion was the same. To consider the possibility of generating an elliptical CCW motion in close proximity to the bottom by elliptical CW motion imparted at the surface we take the surface currents from the F8 mooring and use them as the forcing function for the boundary layer currents. We consider motion generated by the  $M_2$  surface current whose components are  $u_0 \cos(\omega t - g_u)$  and  $v_0 \cos(\omega t - g_v)$ . Amplitudes and phases of the current are:  $u_0 = 14.0\text{cm/s}$ ,  $g_u = 239^\circ 20'$ ,  $v_0 = 5.3\text{cm/s}$ ,  $g_v = 88^\circ 54'$ . The density distribution for this computations is the same as in Figure 5.

The  $M_2$  tidal current ellipses have been plotted in Figure 17 at four levels (distances are given from the sea surface). In the surface layer (10 m), near the pycnocline (24 m), below the pycnocline (36 m) and close to the bottom(44 m). While in the upper layer (10-15 m from the surface) the current ellipses conserve the shape, magnitude, and sense of rotation. In the lower layer the ellipses change magnitude, shape and sense of rotation. The clockwise motion dominates in the entire water column with an exception of the narrow bottom layer where the  $M_2$  current rotates counterclockwise. The decrease of the current towards the bottom is associated with the changes in the ellipse shape. Close to the bottom, due to the different decay rate of the CC and CCW components the flow becomes more rectilinear. Especially interesting is the behavior of the tidal current ellipses in the pycnocline region where a maximum of the current occurs both in observation and model, although the model predict smaller values than the observed ones.

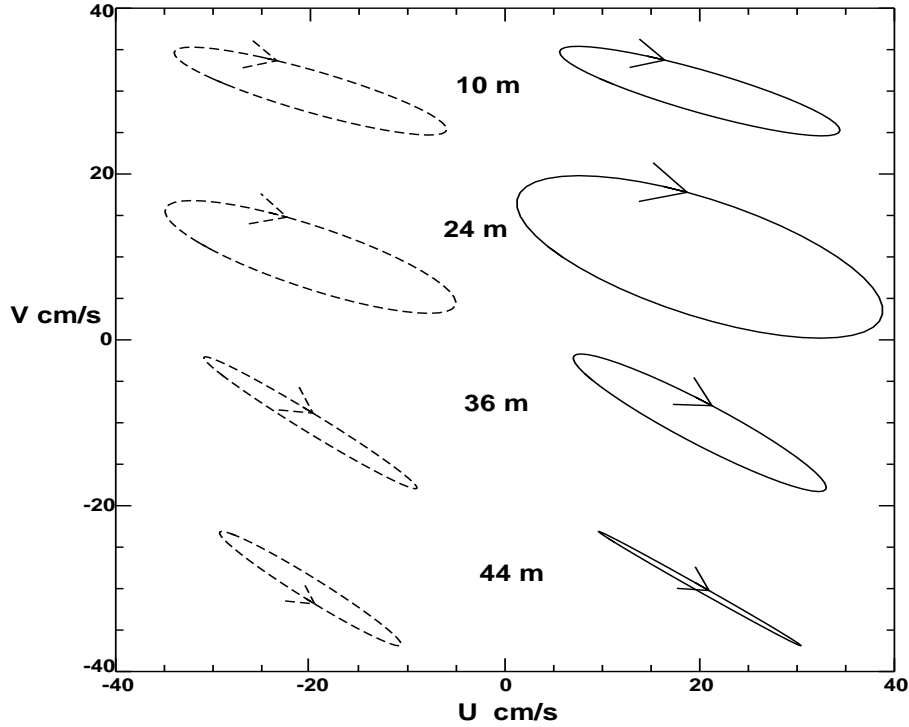


Figure 17.  $M_2$  tidal ellipses at the mooring F8 during summer period. Calculations are given by broken lines, observations by continuous lines. Depth is shown as distance from the free surface.

## 9. Tidal ellipses

Tidal currents expressed along the east-west direction as

$$u = u_0 \cos(\omega t - g_u) \quad (\text{III.28a})$$

and along the north-south as

$$v = v_0 \cos(\omega t - g_v) \quad (\text{III.28b})$$

depict in the  $u$ - $v$  system of coordinate an ellipse. Now we investigate some of the ellipse properties in the rectangular (Descarte) system of coordinate and in the polar system of coordinates. To deal with concrete ellipse the data from the previous section will be used again. With  $u_0 = 14.0\text{cm/s}$ ,  $g_u = 239^\circ 20'$ ,  $v_0 = 5.3\text{cm/s}$ ,  $g_v = 88^\circ 54'$ . The plot of velocities in time for the 12.4 h period is given in Figure 18.

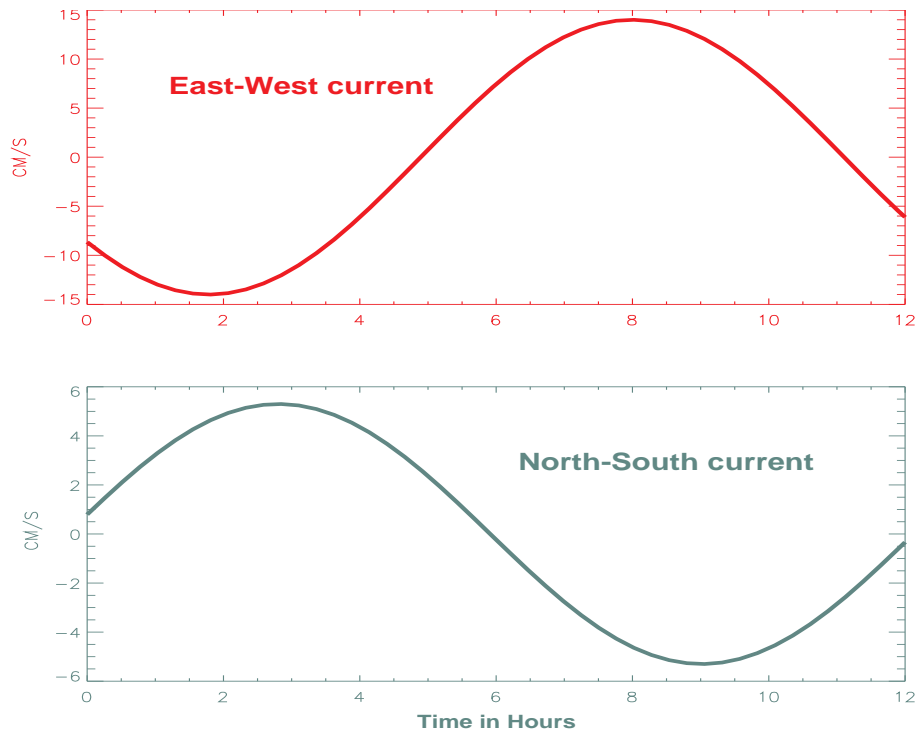


Figure 18. The north-south and the east-west constituents of the tidal current.

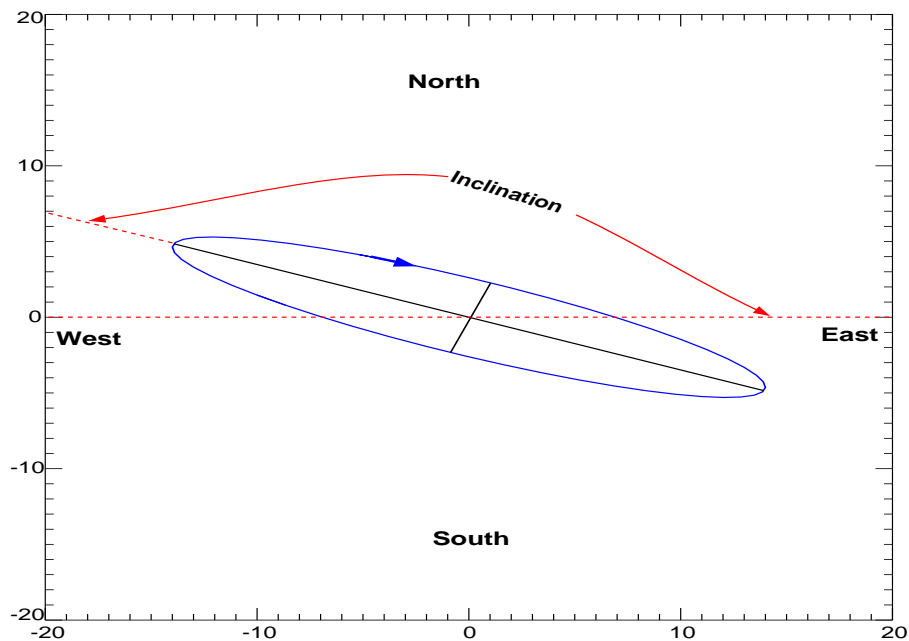


Figure 19. Tidal ellipse constructed from the current given in Fig.18.

The notation used to describe tidal ellipse is shown in this figure. Besides major and minor axes the CW sense of rotation is shown by arrow. Often ellipse is related to the geographical directions to this serve an inclination an angle between the major axis and the East. In an older notation the angle was given between the North and the major axis. Velocity displayed by the tidal ellipse moves the water particles in an elliptical fashion as

well. The displacement ellipse can be easily calculated since:

$$u = \frac{dx}{dt} = u_0 \cos(\omega t - g_u) \quad (\text{III.29a})$$

$$v = \frac{dy}{dt} = v_0 \cos(\omega t - g_v) \quad (\text{III.29b})$$

Thus denoting displacement along  $x$  direction as  $D_x$  and along  $y$  direction as  $D_y$ , we arrive at

$$D_x = \frac{u_0}{\omega} \sin(\omega t - g_u) \quad (\text{III.30a})$$

and

$$D_y = \frac{v_0}{\omega} \sin(\omega t - g_v) \quad (\text{III.30b})$$

Substituting the values for the ellipse considered above and  $\omega = 1.4051910^{-4}$  of  $M_2$  from the Table I.4.

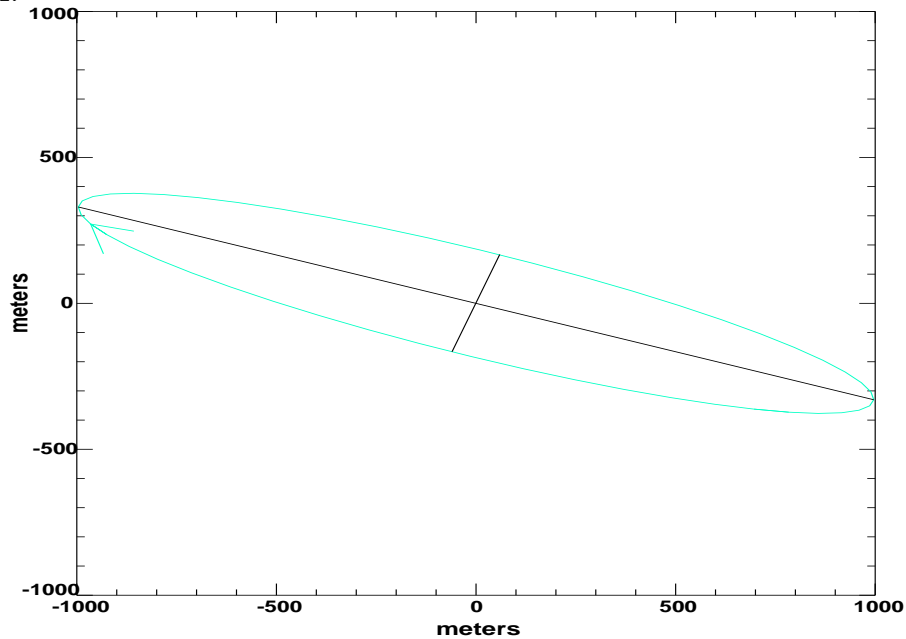


**Figure 20.** Tidal ellipse of displacement constructed from the current given in Fig.18.

Ellipses of velocity from Fig.19 and displacement from Fig.20 depict the same shape, orientation and rotation, while ellipse of velocity is expressed in cm/s the displacement ellipse is given in meters. We can conclude from Fig. 20 that the particle travels during one tidal period more than 4 km.

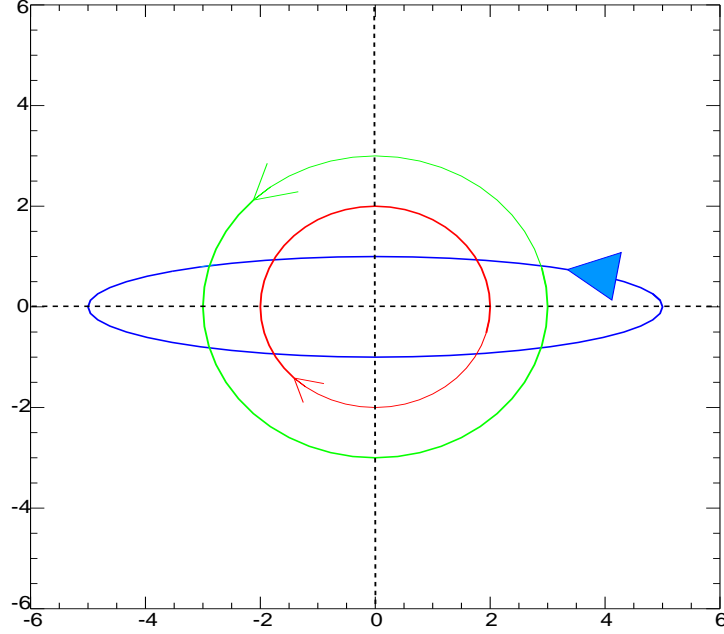


**Figure 21. Tidal ellipse constructed from two circles of CW and CCW rotation.**

Investigation of the tidal currents is closely related to the geometrical properties of an ellipse. Therefore, starting from the velocity component given by III. 28 we shall calculate the ellipse parameters. First using, a simple example, we demonstrate that the elliptical motion is a combination of CW and CCW circular rotations. The rotary velocity (cf. eq.III.8) are superposition of CW and CCW motion. For the CCW motion we can write as  $re^{i\omega t}$  and for the CW as  $qe^{-i\omega t}$ . The Cartesian components  $u$  and  $v$  of the velocity expressed in the complex form can be related to the rotary components, as

$$V = u + iv = re^{i\omega t} + qe^{-i\omega t} \quad (\text{III.31})$$

$$u = (r + q) \cos(\omega t) \quad \text{and} \quad v = (r - q) \sin(\omega t) \quad (\text{III.32})$$

The magnitude squared of the velocity vector is obtained from  $u + iv$  by multiplying it by complex conjugate  $u - iv$ , at any given time,

$$(\vec{V})^2 = u^2 + v^2 = (r + q)^2 \cos^2(\omega t) + (r - q)^2 \sin^2(\omega t) \quad (\text{III.33})$$

hence the maximum current equals to  $V_{max} = r + q$  and the minimum is current is  $V_{min} = r - q$ . These are the respectively, the major and minor semiaxis of the tidal current ellipse. To deduce the direction of rotation we return to the total velocity in the complex notation

$$V = u + iv = (r + q) \cos(\omega t) + i(r - q) \sin(\omega t), \quad (\text{III.34})$$

therefore the direction of rotation will depend on the sign of  $r - q$  in the above expression. If  $r > q$  (or  $V_{min} > 0$ ) the CCW rotation occurs, on other hand if  $r < q$  the CW rotation dominates. As an illustration let's take  $r = 3\text{cm/s}$  and  $q = 2\text{cm/s}$ . These two circles combines into one CCW rotating ellipse given in Fig. 21 with the major semiaxis equal to

$r + q = 5\text{cm/s}$  and minor semiaxis equal to  $r - q = 1\text{cm/s}$ . This is quite simple example since the argument  $\omega t$  starts from  $t = 0$ , i.e. from the East direction. Expressions for the current (III.29) include phase differences ( $g_u$  and  $g_v$ ) which complicate algebra, but describe a general behavior. Taking again velocity as a complex number we can include III.29 in the following way,

$$\begin{aligned} V &= u + iv = u_0 \cos(\omega t - g_u) + iv_0 \cos(\omega t - g_v) \\ &= \frac{u_0}{2} [e^{i(\omega t - g_u)} + e^{-i(\omega t - g_u)}] + i \frac{v_0}{2} [e^{i(\omega t - g_v)} + e^{-i(\omega t - g_v)}] \\ &= \left[ \frac{u_0}{2} e^{-ig_u} + i \frac{v_0}{2} e^{-ig_v} \right] e^{i\omega t} + \left[ \frac{u_0}{2} e^{ig_u} + i \frac{v_0}{2} e^{ig_v} \right] e^{-i\omega t} \\ &= V_{cc} e^{i(\omega t + g_{cc})} + V_c e^{-i(\omega t - g_c)} \end{aligned} \quad (\text{III.35})$$

Thus the general expression for the complex velocity has been subdivided into CCW and CW rotations. The amplitude of the CCW rotation is

$$V_{cc} = 0.5 [u_0^2 + v_0^2 + 2u_0v_0 \sin(g_v - g_u)]^{1/2}, \quad (\text{III.36a})$$

and phase is equal to

$$g_{cc} = \text{Arctan} \frac{v_0 \cos g_v - u_0 \sin g_u}{v_0 \sin g_v + u_0 \cos g_u} \quad (\text{III.36b})$$

For the CW rotation the amplitude is

$$V_c = 0.5 [u_0^2 + v_0^2 + 2u_0v_0 \sin(g_u - g_v)]^{1/2}, \quad (\text{III.37a})$$

and phase

$$g_c = \text{Arctan} \frac{v_0 \cos g_v + u_0 \sin g_u}{-v_0 \sin g_v + u_0 \cos g_u} \quad (\text{III.37b})$$

Above simple example of CCW rotating current along the circle of the radius of 3cm/s and CW rotating current along the circle of the radius of 2cm/s was represented as ellipse with the following velocity components

$$u = 5 \cos(\omega t) \quad \text{and} \quad v = 1 \cos(\omega t - \pi/2)$$

Thus taking  $u_0 = 5\text{cm/s}$ ,  $g_u = 0$ ,  $v_0 = 1$  and  $g_v = \pi/2$  and introducing these values into III.36 and III.37 the CCW and CW rotating circle are defined as

$$V_{cc} = 3\text{cm/s}; \quad g_{cc} = 0; \quad V_c = 2\text{cm/s}; \quad g_c = 0 \quad (\text{III.38})$$

As we have seen in III.34 the maximum of tidal current (major semiaxis) is defined by the sum of CC and CCW amplitude,

$$V_{max} = V_{cc} + V_c =$$

$$0.5[u_0^2 + v_0^2 + 2u_0v_0 \sin(g_v - g_u)]^{1/2} + 0.5[u_0^2 + v_0^2 + 2u_0v_0 \sin(g_u - g_v)]^{1/2} \quad (\text{III.39})$$

These two circular component ought to be aligned along the same direction at the time when the maximum currents occur, therefore from III.35,

$$\omega t_m + g_{cc} = -\omega t_m + g_c \quad (\text{III.40})$$

Here  $t_m$  is the time when the maximum occurs. From the III.39

$$\omega t_m = \frac{g_c - g_{cc}}{2} \quad (\text{III.41})$$

and introducing this phase value into III.35 the maximum current is

$$\begin{aligned} V_{max} &= V_{cc}e^{i(\omega t_m + g_{cc})} + V_c e^{-i(\omega t_m - g_c)} \\ &= (V_{cc} + V_c)e^{i\frac{g_c + g_{cc}}{2}} \end{aligned} \quad (\text{III.42})$$

Thus the direction (inclination) of semimajor axis, is

$$\begin{aligned} \delta &= \frac{g_c + g_{cc}}{2} = \\ &0.5 \left[ \text{Arctan} \frac{v_0 \cos g_v - u_0 \sin g_u}{v_0 \sin g_v + u_0 \cos g_u} + \text{Arctan} \frac{v_0 \cos g_v + u_0 \sin g_u}{-v_0 \sin g_v + u_0 \cos g_u} \right] \end{aligned} \quad (\text{III.43})$$

The direction of the semiminor axis is differs from  $\delta$  by  $\pi/2$  and the minimum velocity is defined by the difference of the CCW and CW amplitudes,

$$V_{min} = V_{cc} - V_c \quad (\text{III.44})$$

Checking above formulas through the simple example given by III.38, the time of maximum is  $t_m = 0$ , the inclination of the major semiaxis is  $\delta = 0$ , the direction of semiminor axis is  $\delta = \pi/2$ , the maximum current is  $V_{max} = 5\text{cm/s}$  and the minimum current is  $V_{min} = 1\text{cm/s}$ .

## 10. Nonlinear effects in the tidal currents.

The ellipse representation of the tidal currents is based on an assumption that the currents is a linear superposition of the various constituents. This assumption works well until the stronger currents occur giving the way to the nonlinear interactions. Usually the tides which propagate over a deep basin depict small currents and amplitudes. Upon impinging onto the shelf break, the tide changes velocity due to changes in bathymetry. Numerical models and observations show striking differences in enhancement between diurnal and semidiurnal tides in the region of the shelf break. While the semidiurnal currents show gradual increase in currents the diurnal tides sometimes display the local maxima in proximity to the shelf break thus suggesting the presence of trapped or partially trapped diurnal shelf waves. Trapped tidal waves often occur at the edges of continental shelves, in

the canyons, and at the seamounts, and therefore are important in the dynamical coupling and exchange of properties between the shelf and the deep ocean.

Velocity patterns of diurnal and semidiurnal tidal motions are also quite different in the shelf and shelf break domains. An examination of the vertical and horizontal variability of measured tidal currents along the shelf break show further contrast in the behavior of the semidiurnal and diurnal constituents, namely: (1) Maximum semidiurnal currents are observed in the upper layer or at depths of 40 to 70 m, and for regions with large depths, the energy of the semidiurnal currents decreases rapidly with depth; (2) the energy of diurnal currents remains almost the same (at the shelf) or even significantly increases (at the shelf break). As a result, semidiurnal currents prevail in the upper layer and diurnal currents dominate in the near-bottom layer. This behavior, as we demonstrated above, is related to the different BBL for the diurnal and semidiurnal tides in the middle latitudes.

In the very shallow waters both semidiurnal and diurnal currents are significantly enhanced resulting in enhanced local mixing and tidal fronts. In proximity to the shelf, islands, headlands and around banks, due to nonlinear interactions, tidal motion can generate a new oscillations and the residual permanent currents which are often observed as permanent eddies. Residual currents play an important role in small and meso-scale exchange of properties between shelf and ocean and also in small scale transport of nutrients and plankton ([Pingree and Maddock, 1985](#)). Sediment transport forced by tides plays important role in the engineering practice since channel widening and deepening alters the tidal flow as well. The nonlinear interaction of the sediment transport and tidal velocity may cause unexpected directions of the sediment transport into and out of inlets ([Walton, 2002](#)).

To elucidate some nonlinear interactions we shall start with tidal equations given in Ch. II

$$\frac{\partial u}{\partial t} + u \frac{\partial u}{\partial x} + v \frac{\partial u}{\partial y} - fv = -\frac{1}{\rho} \frac{\partial p_a}{\partial x} - g \frac{\partial \alpha \zeta}{\partial x} + g \frac{\partial \beta \zeta_0}{\partial x} + \tau_x^s / D - \tau_x^b / D + N_h \Delta u \quad (\text{II.22, III.45})$$

$$\frac{\partial v}{\partial t} + u \frac{\partial v}{\partial x} + v \frac{\partial v}{\partial y} + fu = -\frac{1}{\rho} \frac{\partial p_a}{\partial y} - g \frac{\partial \alpha \zeta}{\partial y} + g \frac{\partial \beta \zeta_0}{\partial y} + \tau_y^s / D - \tau_y^b / D + N_h \Delta v \quad (\text{II.23, III.46})$$

Additionally we shall need to express explicitly the bottom stress as it is proportional to the square of the average velocity:

$$\tau_x^b = ru \sqrt{u^2 + v^2} \quad \text{and} \quad \tau_y^b = rv \sqrt{u^2 + v^2} \quad (\text{II.3, III.47})$$

The transformation of the tidal flow in the shallow water is taken place through the advective nonlinear term and the bottom stress.

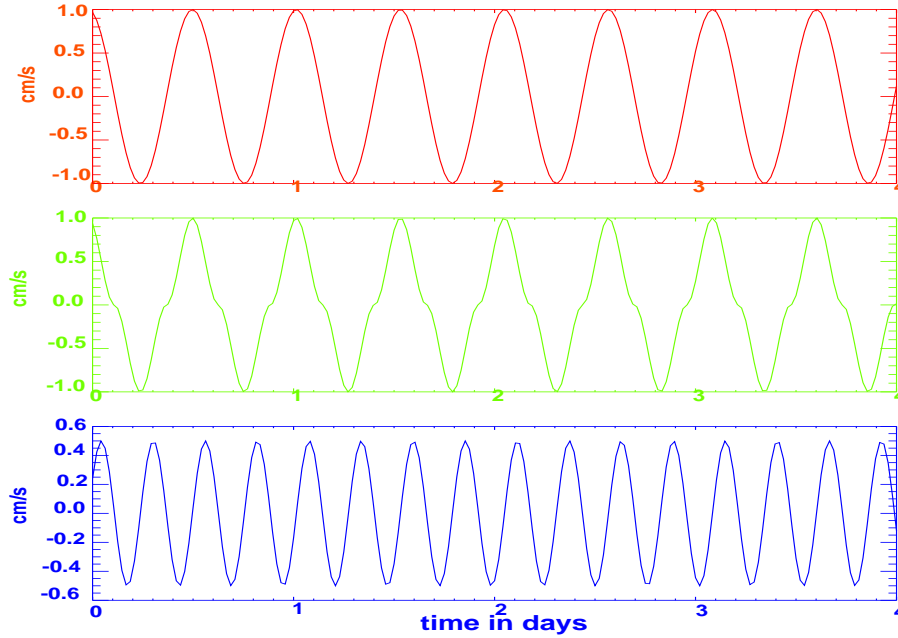


**Figure 22. Upper panel (red): U component of the  $M_2$  tidal current, middle panel (green): nonlinear U velocity due to the bottom friction, lower panel (blue): nonlinear U velocity due to the advective term.**

Interactions of the various nonlinear terms in the equation of motion when the tidal flow is composed of many tidal constituents leads to the complicated tidal currents which changes spatially and temporarily. To investigate the principal features of the nonlinear interaction let's consider flow along the east-west direction only and the nonlinear interaction will take place only for the one component –  $M_2$ . In such case only two nonlinear terms are present, i.e. the advective term  $u \frac{\partial u}{\partial x}$  and the bottom friction  $\tau_x^b = ru|u|$ . Assuming  $M_2$  current has a simple form  $\cos(\omega t)$  we shall investigate how nonlinear terms change this wave. For this purpose the advective term is taken as multiplication of  $\cos(\omega t) \sin(\omega t)$  and the bottom friction is calculated as  $\cos(\omega t) |\cos(\omega t)|$ . The results of computations are given in Fig. 22. The original  $M_2$  wave depicted in the upper panel is only slightly deformed by the bottom friction as can be seen in the middle panel, and the main period still remains 12.42 h. The power spectra of the time series from the middle pane shows that the deformation is located at the 4.1 h. Therefore, we can conclude that each basic constituent produces through the bottom friction the new constituents called overtides. Overtides due to nonlinear bottom friction are (Parker, 1991):

$$T_{OM_2} = T_{M_2}/(2i + 1) \quad (\text{III.48a})$$

Here  $i=1,2,3,\dots$ . Thus for the  $M_2$  tide the major overtides are located at 4.14 h and 2.48 h. This has been confirmed by the maximum in the power spectra. Different behavior show the advective term (lower panel). There is no more oscillations with the basic period, the main oscillation is close to 6 h period. These are overtides generated by advective terms, their periods are defined as,

$$T_{OM_2} = T_{M_2}/(2i) \quad (\text{III.48b})$$

Here  $i=1,2,3,\dots$ . For the  $M_2$  tide the major overtides are located at 6.21 h and 3.105 h. By changing  $M_2$  period in formulas III.48 to the period of any constituent the overtides for every tidal wave can be easily estimated.

Above results are easily obtained by considering simple trigonometrical identities. First, let us notice that the absolute magnitude of  $|\cos(\omega t)|$  can be (in the first approximation) taken as  $0.5(1 + \cos(2\omega t))$ , see Fig.23.

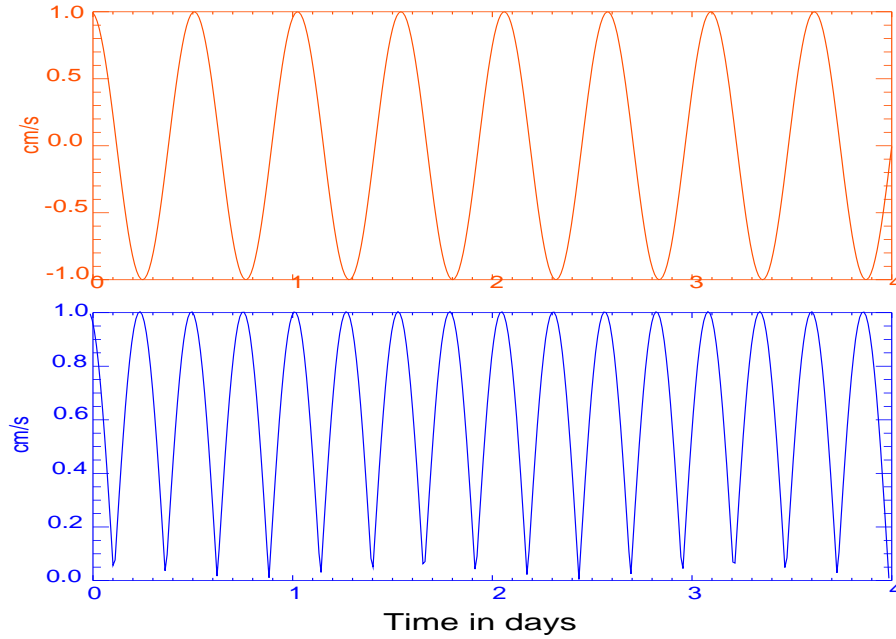


**Figure 23.** Upper panel (red): U component of the  $M_2$  tidal current, lower panel (blue): absolute value of U component.

For the bottom friction term  $u|u|$

$$\begin{aligned} \cos(\omega t)0.5[1 + \cos(2\omega t)] &= 0.5[\cos(\omega t) + \cos(2\omega t) \cos(\omega t)] = \\ &0.5[\cos(\omega t) + 0.5[\cos(3\omega t) + \cos(\omega t)]] = \\ &0.5[1.5 \cos(\omega t) + 0.5 \cos(3\omega t)] \end{aligned} \quad (\text{III.49})$$

This show that the friction produces oscillations with the main frequency of  $\omega$  and a new frequency of  $3\omega$ . The latter frequency for the  $M_2$  wave generates overtide of approximately 4 h. Advective term leads to the following

$$\cos(\omega t) \sin(\omega t) = 0.5 \sin(2\omega t) \quad (\text{III.50})$$

Thus producing oscillation with a frequency of  $2\omega$  which for  $M_2$  wave results in 6 h overtide.

## 11. Nonlinear tidal interactions in the Sea of Okhotsk.

The Sea of Okhotsk is bounded by Hokkaido, the Kuril Islands, the Kamchatka Peninsula, Siberia, and Sakhalin Island (Fig. 24). The two major domains of the sea are a broad

shelf area along the Siberian coast and a relatively flat central basin with depths of approximately 1000–1500 m. The Kuril Basin is the deepest region with depths of 3000 to 3200 m. The nonlinear tidal interactions are going to be demonstrated in the region of the Kashevarov Bank. It is located at the northern shelf break between 200 m and 500 m isobaths with the top of the bank at about 100 m depth.

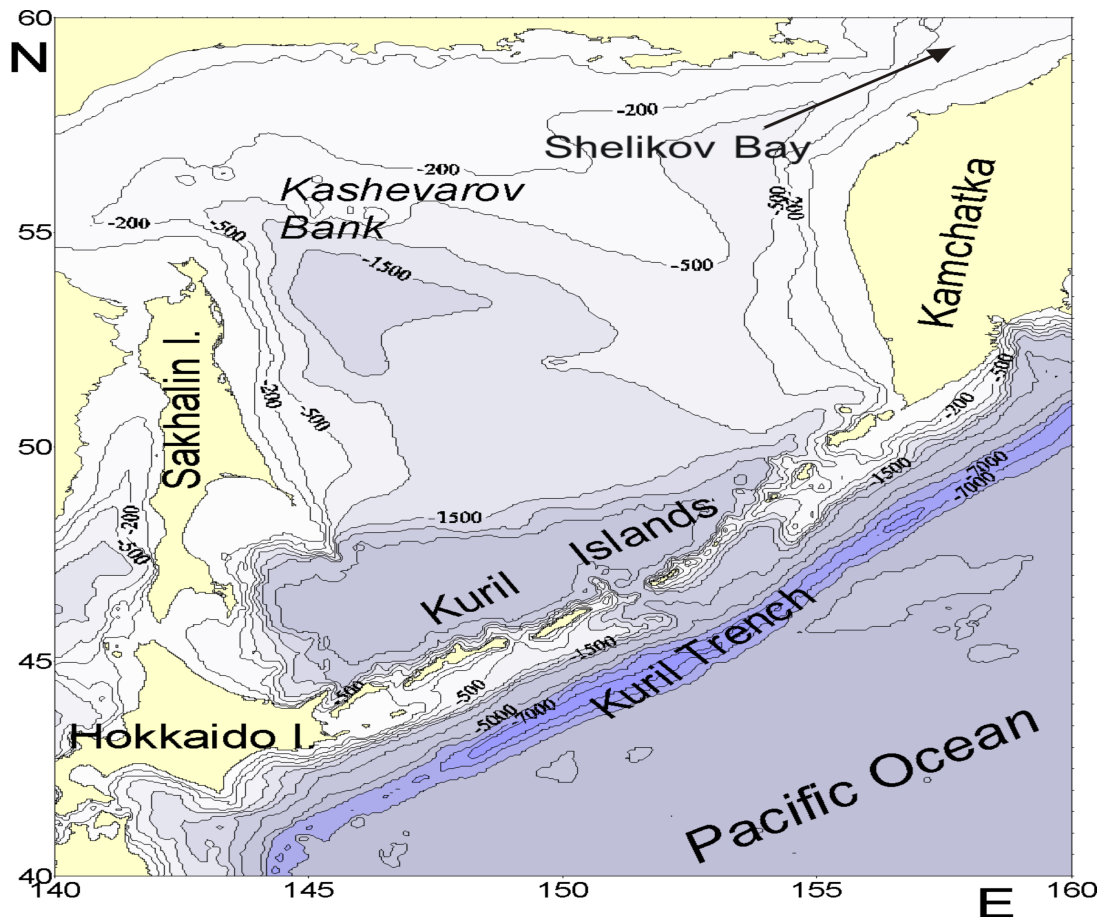


**Figure 24. Bathymetry of the Sea of Okhotsk.**

The Sea of Okhotsk is a region of large tidal sea level oscillations and strong tidal currents. In shallow Penzhinskaya Guba, total tidal sea level oscillations reach 13 m. The tides are dominated by the diurnal constituents. In Figure 2 the major diurnal constituent  $K_1$  is given from [Kowalik and Polyakov, 1998 \(K&P\)](#) computations. This constituent shows enhancement of the  $K_1$  tides towards shallow and narrow domains of Shelikow Bay and Penzhinskaya Guba. In the latter the amplitude is close to the 4 m. This shallow area generates the strongest diurnal tides in the entire World Ocean. The area of the Kashevarov Bank shows typical pattern of the trapped diurnal wave with the local maximum of the amplitude and the associated change of the phase.

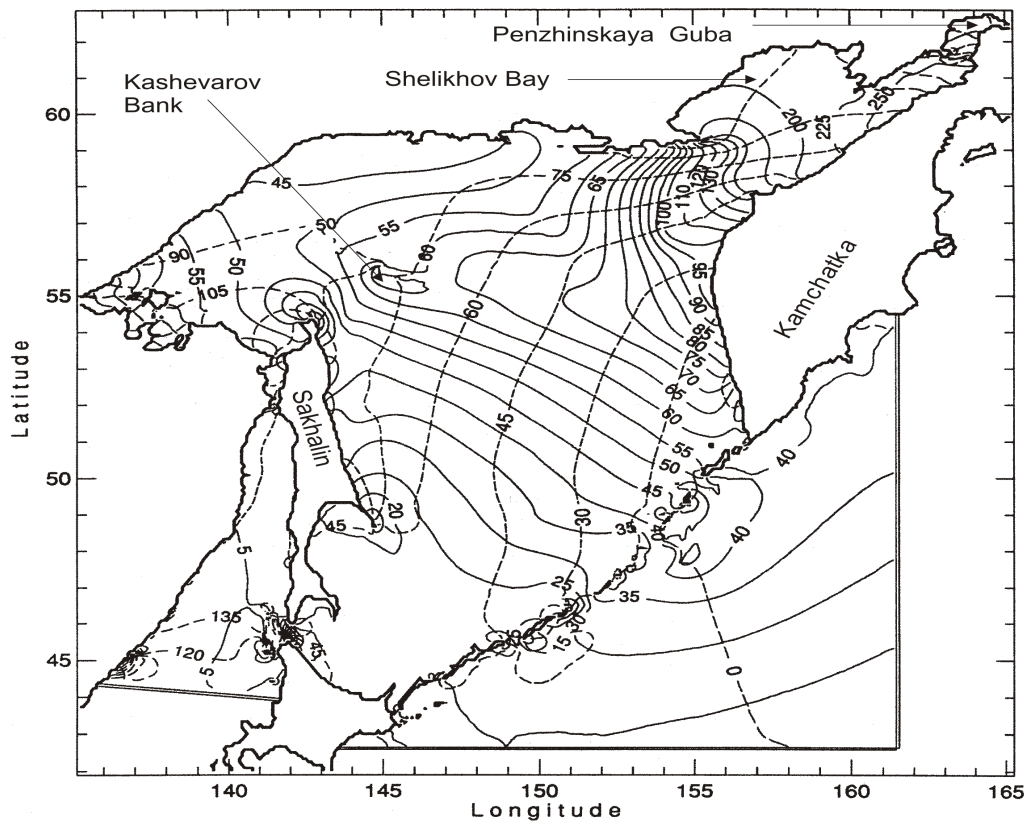


**Figure 25.** Computed amplitudes (solid lines, cm) and phases (dashed lines, degrees) of surface elevation for the diurnal  $K_1$  tide. The phases are referred to Greenwich; the phase contours are plotted every  $15^\circ$ .

The maximum tidal currents computed for the eight tide constituents in Figure 26 connect enhanced tidal currents in both the semidiurnal and diurnal bands to the shallow areas of Shelikhov Bay and Penzhinskaya Guba. The strong currents occur as well along the deeper domains of Kashevarov Bank, in proximity to the Kuril Islands and at a few smaller locations. In the diurnal band of oscillations the maximum current can also be associated with the occurrence of shelf waves. Enhanced velocity along the shelf break and over isolated seamounts (see summary by [Foreman et al. 1995](#)) is caused by near-resonant amplification of diurnal currents by topography. Investigations of the resonance band of frequencies over seamounts by [Chapman \(1983, 1989\)](#), [Brink \(1989\)](#), [Hunkins \(1986\)](#) and [Haidvogel et al. \(1993\)](#) delineated the dependence of trapped waves on the range of topographic sizes and stratification. From their results one can conclude that regions of local resonance are more likely to be found in the polar oceans, where large values of the Coriolis parameter occurs. Nonlinear interactions of diurnal currents were investigated by ([K& P, 1998](#)) through  $K_1$  and  $O_1$  constituent behavior over Kashevarov Bank. These interactions generate residual circulation of the order of  $10 \text{ cm s}^{-1}$ , major oscillations at semidiurnal and fortnightly periods (13.66 day) and higher harmonics of

basic tidal periods. The  $M_2$  tidal current, caused by the nonlinear interaction of the diurnal constituents over Kashevarov Bank, constitutes approximately a half of the total  $M_2$  tide current there.

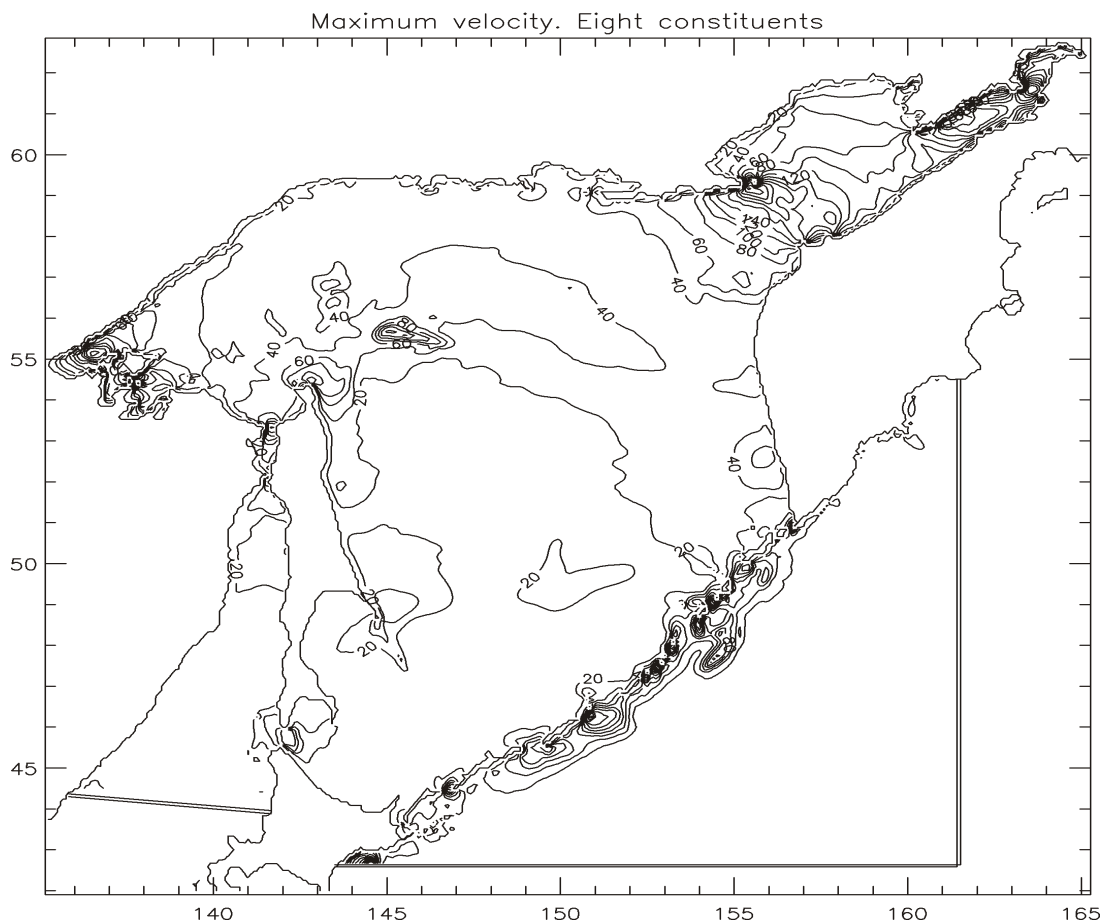


**Figure 26.** Contours of the maximum tidal current (solid lines,  $\text{cm s}^{-1}$ ) based on the eight constituents.

The fortnightly current, through nonlinear interactions, also influences basic diurnal tidal currents by inducing fortnightly variations in the amplitude of these currents.

A noticeable transformation of the diurnal amplitudes and currents is evident. Results are discussed for the dominant  $K_1$  constituent. The cotidal chart of the  $K_1$  constituent for the Kashevarov Bank region is shown in Fig. 27. The amplitude at the top of bank increases, reaching a maximum of 70 cm. A similar pattern in the  $O_1$  tidal level oscillations occurs as well. The maximum current for  $K_1$  and  $O_1$  is 85 and 75  $\text{cm s}^{-1}$ , respectively, relative to off-bank values of 5–10  $\text{cm s}^{-1}$ . The circular shape of the tidal current ellipses above the bank changes to rectilinear oscillations at the steepest slopes of the bank, located south and southwest from the top of the bank. This tidal flow behavior is typical for trapping or partial trapping of tidal energy by bottom irregularity (Kowalik, 1994).

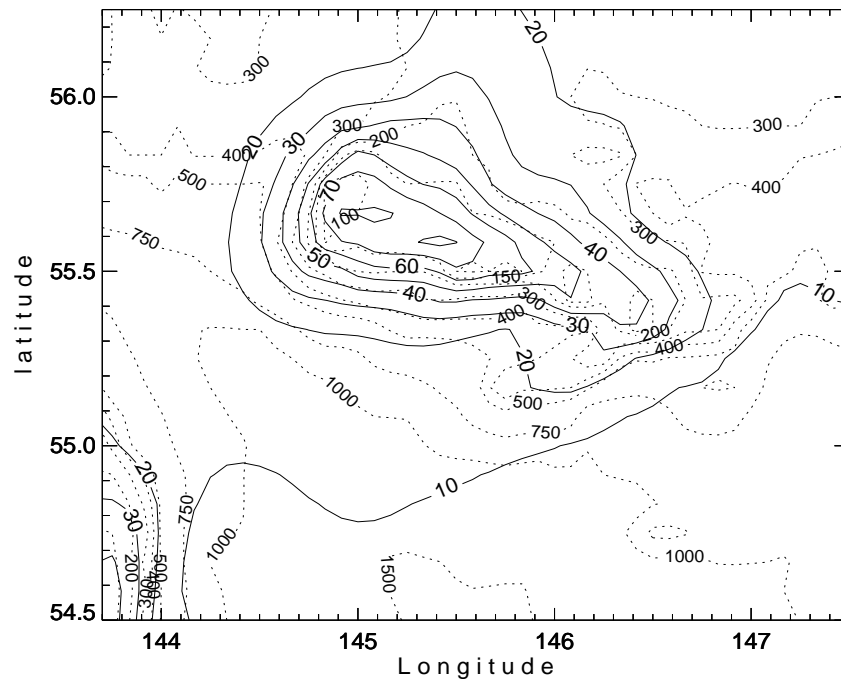


**Figure 27.** Computed amplitudes (solid lines, cm) of surface elevation for the  $K_1$  constituent above Kashevarov Bank. Bathymetry in meters is given by dotted lines. The top of the Bank denotes location for the time series analysis.

Local behavior of tidal oscillations often depends on the resonance phenomena in local water bodies (e.g., [Platzman 1972](#)). To demonstrate the possibility of resonance K&P, 1998 depicted the distribution of natural oscillations in the Sea of Okhotsk and especially at Kashevarov Bank over the range of diurnal and semidiurnal tides.

The natural period of 26.3 hours occurs in the entire SO both in the sea level and in velocity spectra. This period is very close to the  $O_1$  period (25.82 h), therefore enhancement of the  $O_1$  tide occurs, but the 26.3 h resonant peak is broad and some enhancement of oscillations takes place at the  $K_1$  period (23.93 h) as well. Observations taken near Sakhalin Island ([Rabinovich and Zhukov 1984](#)), off Hokkaido ([Odamaki 1994](#)) and at the Kuril Islands ([Yefimov et al. 1985](#)) show that the  $O_1$  constituent is much more amplified than the  $K_1$  constituent, corroborating the possibility of resonance enhancement in the entire Sea of Okhotsk through a 26.3 h oscillation.

Over Kashevarov Bank the periods in the diurnal range of oscillations and especially the period of 26.3 hours, shows the resonant amplification of velocity.

The nonlinear interaction of tidal constituents above a seamount is an important element of tidal dynamics. Recent studies, based on current observations over Fiebering Guyot in the North Pacific ([Brink 1995](#)) and on investigations by [Butman et al. \(1983\)](#), show that the nonlinear interaction of diurnal constituents  $K_1$  and  $O_1$  results in new oscillations with periods at the semidiurnal  $M_2$  tidal frequency (sum of  $K_1$  and  $O_1$  frequencies) and a fortnightly tide (difference of  $K_1$  and  $O_1$  frequencies) with a 13.66-day period. The rectification of the strong diurnal currents produces a mean (residual) clockwise circulation around the seamount.

K&P 1998 applied this mechanism to study nonlinear tidal interaction over Kashevarov Bank due to the two major constituents  $K_1$  and  $O_1$ . A series of experiments was carried out to assess the effects of nonlinear interactions of these constituents and to demonstrate the balance between a linear and nonlinear tendency in the tidal velocity.

Two sets of experiments were carried out: a) all nonlinear terms are included, and b) nonlinear advective terms are rejected and bottom friction terms are linearized. Comparison of results with and without advective terms and nonlinear bottom friction in the equations of motion shows that their omission removes the residual circulation. To investigate the differences between linear and nonlinear tidal dynamics, we considered the temporal variability of the tidal currents. The time series of the tidal currents at top of Kashevarov Bank after 30 days of simulation is shown in Fig. 28 for both the nonlinear and linear cases.

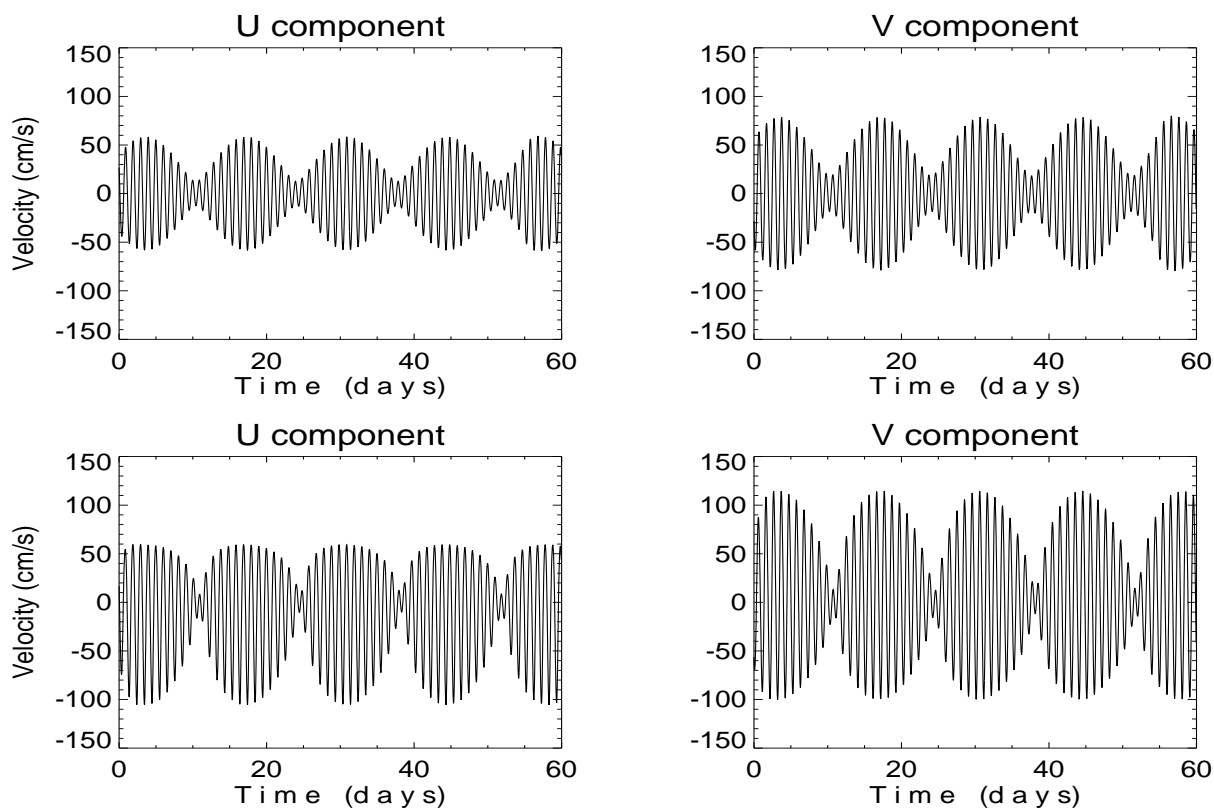


**Figure 28.** Time series of the U (east–west) and V (south–north) components of tidal current at the top of Kashevarov Bank (see Fig. 27) for the linear (upper panel) and nonlinear (lower panel) simulations. Forcing is due to  $K_1+O_1$ .

The temporal variability of the tidal currents resulting from the interaction of  $K_1$  and  $O_1$  constituents exhibits a fortnightly (13.66-day) oscillation which constitutes the upper and lower envelope of the diurnal signals (Fig. 28). In the linear case (Fig. 28, top) the fortnightly envelopes of the positive and negative values are symmetrical and no residual currents are generated. In the nonlinear case the upper and lower envelopes of the tidal currents are asymmetrical (Fig. 28, bottom). The values of the upper envelope of the north–south (V) velocity component are greater than those of the lower envelope, resulting

in a 13–14  $\text{cm s}^{-1}$  residual current. Particularly striking is the difference of 45  $\text{cm s}^{-1}$  between the upper and lower envelopes of the east–west (U) velocity component.

The nonlinear interaction of the diurnal tides influences the pattern of the  $M_2$  constituent. The  $K_1$  and  $O_1$  tides generate a rather strong current at the  $M_2$  frequency. The current shows a maximum of approximately 9  $\text{cm s}^{-1}$  at the top of Kashevarov Bank where the nonlinear interactions are greatest and rapidly diminishes to 1  $\text{cm s}^{-1}$  off the bank where the nonlinear terms are small. The 9  $\text{cm s}^{-1}$  current is approximately a half of the total  $M_2$  tidal current above the bank as computed by the model which incorporated the eight tidal constituents. The nonlinear interaction of the diurnal tides has no significant effect on sea level at the  $M_2$  tidal frequency and the maximum of amplitude is approximately 1 cm at the bank top.

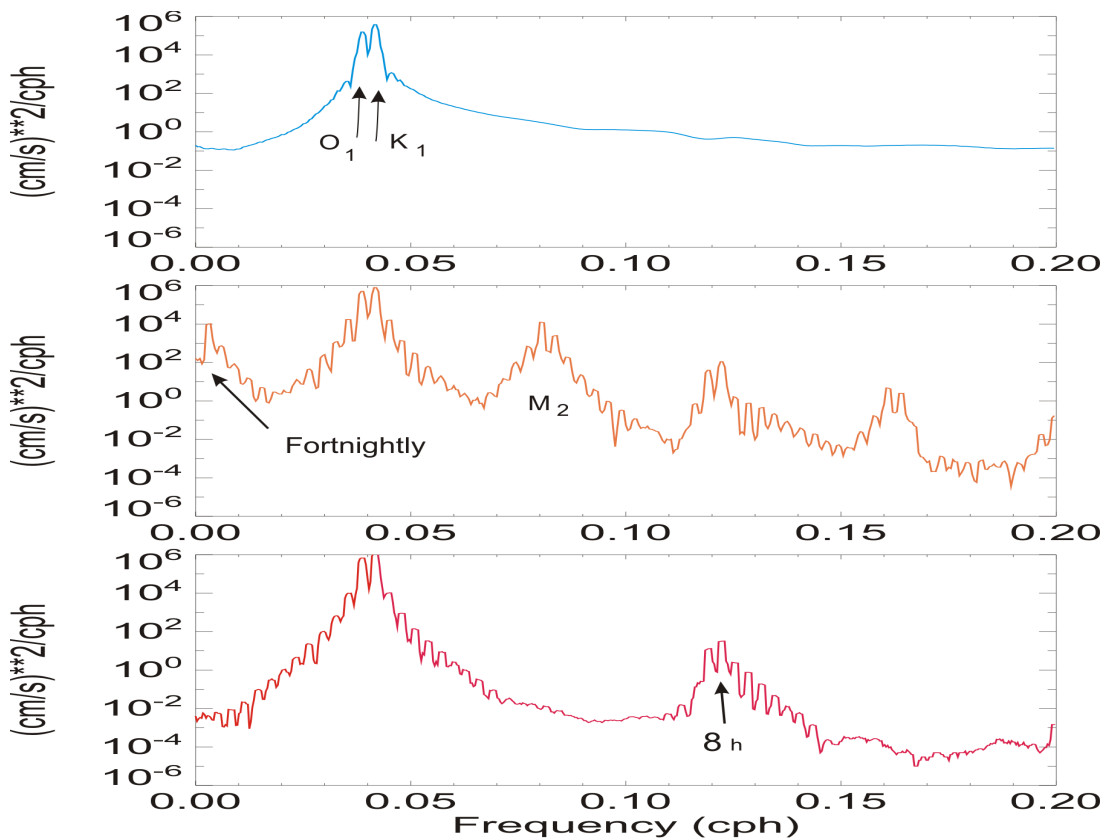


**Figure 29.** Power spectra of the U (east–west) component of the tidal current at Kashevarov Bank. (top) Linear simulation, (center) fully nonlinear simulation and (bottom) partly nonlinear simulation, due to the bottom friction. Forcing is due to  $K_1+O_1$ .

To identify additional important aspects of the interaction of  $K_1$  and  $O_1$  constituents, power spectra was employed. The purpose of these experiments was to learn how energy is redistributed from the major tidal constituents,  $K_1$  and  $O_1$ , to various parts of the tidal spectra for the linear and nonlinear interactions. Magnitudes of the energy spectra at  $O_1$  and  $K_1$  periods for the nonlinear and linear experiments are governed by different physics. These magnitudes are controlled by bottom friction, and only nonlinear bottom friction

reproduces tidal amplitude well. The linearized formula is based on mean values which do not take local conditions into account.

The power spectra of the east–west component of the tidal current at the top of the bank are given in Fig. 29. The linear result is shown in the top panel, the full nonlinear interaction is given in the center panel, and the nonlinear interaction without advective terms (only nonlinear bottom friction remains in the equation of motion) is depicted in the bottom panel.

The power spectrum for the linear problem (Fig. 29, top) shows only one major maximum with energy at  $K_1$  and  $O_1$  wave-periods. In the case of nonlinear interaction, the existence of several major and minor maxima in the power spectra (Fig. 29, center) is revealed. The major maxima occur at the semidiurnal, diurnal and fortnightly periods. Minor maxima are located close to 8 h and 6 h. The major maxima can be explained by nonlinear interaction of two original tidal constituents (the so-called compound tides). Moreover, each basic constituent ( $K_1$  or  $O_1$ ) produces, through the nonlinear terms, overtides represented in the power spectra as both major and minor maxima. Assuming the  $K_1$  period to be  $T_{K1}$ , this constituent through the advective terms, generates overtide oscillations whose periods are  $T_{K_i} = T_{K1}/2i$  (**Parker 1991**). Overtides due to nonlinear bottom friction are  $T_{K_i} = T_{K1}/(2i + 1)$ . Here  $i=1,2,3,\dots$ . Thus, for the  $K_1$  tide, the major overtides are located at 11.96 h and 5.98 h (due to advective terms) and 7.98 h (due to bottom friction) and for the  $O_1$  tide the major overtides are at 12.91 h and 6.45 h (due to advective terms) and 8.61 h (due to bottom friction). In the semidiurnal band, the power spectra depict a large maximum of energy caused by several oscillations: a compound tide at the  $M_2$  tide period, an overtide due to the  $K_1$  tide at 11.96 h, and an overtide due to the  $O_1$  tide at 12.91 h. In the bottom plot, the nonlinear interaction is caused by the bottom friction only (i.e. advective terms are neglected), the dominant oscillation is located at the diurnal band, and the first higher harmonic is, as one would expect, close to 8 h. The latter maximum is of secondary magnitude and one can conclude that the bottom frictional terms do not transfer energy as effectively as advective terms. In summary, the nonlinear terms transfer energy from the  $K_1$  and  $O_1$  constituents towards longer and shorter periods. It can be deduced from Fig. 29 (center panel) that the energy from these waves mainly sustains oscillations in the fortnightly and semidiurnal bands. At the shorter periods, the magnitudes of energy maxima are very small.

**References**

- Blumberg A. F. and G. L. Mellor, 1987. A description of a three-dimensional coastal ocean model. In *Three-Dimensional Coastal Models*, N. S. Heaps, Editor, AGU, 1–16.
- Brink, K. H., 1989. The effect of stratification on seamount-trapped waves. *Deep-Sea Res.*, **36**, 825–844.
- Brink, K. H., 1995. Tidal and lower frequency currents above Fieberling Guyot. *J. Geophys. Res.*, **100**, 10 817–10 832.
- Butman, B., M. Noble, D. C. Chapman, and R. C. Beardsley, 1983. An upper bound for the tidally rectified current at one location on the southern flank of Georges Bank. *J. Phys. Oceanogr.*, **13**, 1452–1460.
- Chapman, D. C., 1983. On the influence of stratification and continental shelf and slope topography on the dispersion of subinertial coastally trapped waves. *J. Phys. Oceanogr.*, **13**, 1641–1652.
- Chapman, D. C., 1989. Enhanced subinertial diurnal tides over isolated topographic features. *Deep-Sea Res.*, **36**, 815–824.
- Coachman, L. K. 1986. Circulation, water masses, and fluxes on the southeastern Bering Sea shelf, *Cont. Shelf Res.*, **5**, 23–108
- Coachman, L. K., K. Aagaard, and R. B. Tripp, 1975. *Bering Strait: The Regional Physical Oceanography*, University of Washington Press, Seattle, WA, 172 pp.
- Danielson, S., and Z. Kowalik, 2005. Tidal currents in the St. Lawrence Island region. *J. Geophys. Res.*, **110**, C10004, doi:10.1029/2004JC002463.
- Defant, A. 1960. *Physical Oceanography*, Pergamon Press, **2**, 598 pp (see page 326).
- Emery, W.J., and R.E. Thomson, 2001. *Data Analysis Methods in Physical Oceanography*, 2nd and Revised Edition, Elsevier, Amsterdam, 638 p.
- Foreman, M. G. G., and R. F. Henry, 1989, The harmonic analysis of tidal model time series, *Adv. Water Resour.*, **12**, 109–120.
- Foreman, M. G. G., W. R. Crawford, and R. F. Mardsen, 1995. De-tiding: Theory and practice, in *Coastal and Estuarine Studies*. R. Lynch and A. M. Davies, Eds., AGU, **47**, 203–239.
- Galperin, G., L.H. Kantha, S. Hassid and A. Rossati, 1988. A quasi-equilibrium turbulent energy model for geophysical flows. *J. Atmosph. Sciences*, v.45, No.1, 55–62.
- Gonella, J., 1972. A rotary-component method for analysing meteorological and oceanographic vector time series, *Deep-Sea Res.*, **19**, 833–846.
- Haidvogel, D. B., A. Beckmann, D. C. Chapman, and R.-Q. Lin, 1993. Numerical simulation of flow around a toll isolated seamount. Part II: Resonant generation of trapped waves. *J. Phys. Oceanogr.*, **23**, 2373–2391.
- Hunkins, K., 1986. Anomalous diurnal tidal currents on the Yermak Plateau. *J. Mar. Sci.*, **44**, 51–69.

- Johnson, W. and Z. Kowalik. 1986. Modeling of storm surges in the Bering Sea and Norton Sound. *J. Geophys. Res.* 91(C4), 5119–5128.
- Kantha, L. H., 1995. Barotropic tides in the global oceans from a nonlinear tidal model assimilating altimetric tides. 1. Model description and results. *J. Geophys. Res.*, 100, 25,283–25,308.
- Kowalik, Z., 1994. Modeling of topographically-amplified diurnal tides in the Nordic Seas. *J. Phys. Oceanogr.*, **24**, 1717–1731.
- Kowalik, Z., 1999. Bering Sea Tides. In: *The Bering Sea: Physical, Chemical and Biological Dynamics*, T. R. Loughlin and K. Ohtani, Eds., Alaska Sea Grant Press, Fairbanks, AK., 93–127.
- Kowalik, Z., and A. Yu. Proshutinsky, 1994. The Arctic Ocean Tides, In: *The Polar Oceans and Their Role in Shaping the Global Environment: Nansen Centennial Volume*, Geoph. Monograph 85, AGU, 137–158.
- Kowalik, Z. and I. Polyakov, 1998. Tides in the Sea of Okhotsk. *J. Phys. Oceanogr.*, **28(7)**, 1389–1409.
- Lamb, H. 1945. *Hydrodynamics*, 6th ed. Dover Publ. N.Y. 738 pp.
- Maas, L. R. M. and J. J. M. van Haren, 1987. Observations on the vertical structure of tidal and inertial currents in the central North Sea. *J. Mar. Res.*, 45, 2, 293–318.
- Marchuk, G. I. and B. A. Kagan, 1977. *Oceanic Tides*. Gidrometizdat. Leningrad, 296 pp.
- Mofjeld, H. O., 1980. Effect of vertical viscosity on Kelvin waves. *J. Phys. Ocean.*, 10, 1039–1050.
- Mofjeld, H. O., 1984. Recent observations of tides and tidal currents from the Northeastern Bering Sea shelf. *NOAA Technical Memorandum ERL PMEL-57*, 36pp.
- Mofjeld, H. O., 1986. Observed tides on the Northeastern Bering Sea shelf. *J. Geophys. Res.*, **91**, 2593–2606.
- Mofjeld, H. O., J. D. Scumacher and D. J. Pashinski, 1984. Theoretical and observed profiles of tidal currents at two sites on the southeastern Bering sea shelf. NOAA Tech. Memo. ERL, PMEL-62, PMEL, Seattle, 60 pp.
- Mooers, C.N.K., 1973. A technique for the cross spectrum analysis of pairs of complex-valued time series, with emphasis on properties of polarized components and rotational invariants, *Deep-Sea Res.*, 20, 1129–1141.
- Munk W., F. Snodgrass and M. Wimbush, 1970. Tides off-shore: Transition from California coastal to deep-sea waters. *Geop. Fluid Dyn.*, v.1, 161–235.
- Niebauer, H. J., N. A. Bond, L. P. Yakunin, V. V. Plotnikov, 1999. An Update on the Climatology and Sea Ice of the Bering Sea, In: *Dynamics of The Bering Sea: A summary Physical, Chemical and Biological Characteristics, and a Synopsis of Research on the Bering Sea*, T. R. Loughlin and K. Ohtani, Editors, Alaska Sea Grant Press, Fairbanks, AK, 29–59.
- Odamaki, M., 1994: Tides and tidal currents along the Okhotsk coast of Hokkaido. *J.*

*Oceanogr. Soc. Japan*, **50**, 265–279.

Parker, B. B., 1991. The relative importance of the various nonlinear mechanisms in a wide range of tidal interactions. In: *Tidal Hydrodynamics*, B. B. Parker, Ed., Wiley and Sons, 237–268.

Pawlowicz, R., B. Beardsley, and S. Lentz, 2002. Classical tidal harmonic analysis including error estimates in MATLAB using T\_TIDE. *Computers and Geosciences* **28**, 929–937.

Pearson, C. A., H. O. Mofield, and R. B. Tripp, 1981. Tides of the Eastern Bering Sea shelf, In: *The Eastern Bering Sea Shelf: Oceanography and Resources*, **1**, 111–130.

Pease, C.H. and P. Turet, 1989. Sea ice drift and deformation in the Western Arctic. *EEE Publ. N. 89CH2780/5*, 1276–1281.

Pingree, R.D. and L. Maddock, 1985. Rotary currents and residual circulation around banks and islands. *Deep-Sea Res.*, **32**, 929–947.

Platzman, G. W., 1972. Two-dimensional free oscillations in natural basins. *J. Phys. Oceanogr.*, **2(2)**, 117–138.

Prandle, D., 1982. The vertical structure of tidal current. *Geophys. Astrophys. Fluid Dyn.*, **22**, 22–49.

Pugh, D. T., 1987. *Tides, Surges and Mean Sea-Level*, John Wiley & Sons, 472pp.

Rabinovich, A. B., and A. Ye. Zhukov, 1984. Tidal oscillations on the shelf of Sakhalin Island. *Oceanology*, **24(2)**, 184–189.

Schumacher, J. D., K. Aagaard, C.H. Pease and R.B. Tripp, 1983. Effects of a shelf polynya on flow and water properties in the northern Bering Sea, *J. Geophys. Res.*, **88**, No. C5, 2723–2732.

Sunderman, J. 1977. The semidiurnal principal lunar tide  $M_2$  in the Bering Sea. *Deutsche Hydrog. Zeitschrift* **30**: 91–101.

Sverdrup, H. W. 1926. Dynamics of tides on the North-Siberian shelf. *Geophys. Publ. Norske Videnskaps-Akad.*, Oslo, **4**, 175.

Thorade, H. 1928. Gezeitenuntersuchungen in der Deutschen Bucht der Nordsee. *Deutsche Seewarte*, **46**, **3**, 85pp.

Visser, A.W., A. J. Souza, K. Hessner and J. H. Simpson, 1994. The effect of stratification on tidal current profiles in the region of freshwater influence. *Oceanologica Acta*, **17**, **4** 369–381.

Walton, T., 2002. Tidal Velocity Asymmetry at Inlets. *Coastal and Hydraulics Engineering Technical Note -IV-47*. US Army Corps of Engineers, 17 pp.

Yefimov, V. V., Ye. A. Kulikov, A. B. Rabinovich, and I. V. Fine, 1985. *Ocean Boundary Waves*. *Gidrometeoizdat*, Leningrad, 280 pp.

## CHAPTER IV: TIDE DISTRIBUTION AND TIDAL POWER

### 1. Introduction

Currently tidal power plants (TPP) use both potential (tidal sea level) and kinetic energy (tidal currents). Both usages have their roots in small tide mills constructed along tidal shores. In a tidal mill a small pond is connected to the open ocean through a sluice. During flood tides a gate in the sluice is lowered so the pond is filled up with incoming water. This water is stored in the pond until the ebb tide when the gate is lifted up and the water head generated is applied to move a waterwheel ([Bernshtein, 1961](#)). Since modern tidal plants tap both potential and kinetic energy, knowledge of tide distribution in the World Ocean is critical in development of tidal power on a site-specific basis. To illustrate basic tidal physics which govern the large tidal levels, a few locations with very large tides has been singled out. While tidal sea levels are quite easy to understand and predict, the tidal currents are less amenable to investigations. Currents are strongly modified by the local bathymetry and shoreline geometry. Strong flows occur in relatively shallow water and in constrained passages. Tides change in density-stratified waters by generating internal tides which locally enhance tidal currents ([Wunsch, 1975](#)). Exploitation of the tidal energy is usually restricted to limited sites which display large range of tidal elevations, or strong tidal currents, or both. Consequently, it is important to understand the balance of the tidal energy at such sites. The balance includes an accounting of the energy inflow and outflow to and from the local domain, and sources and sinks of energy inside the local domain ([Nekrasov, 1992](#); [LeProvost and Lyard, 1997](#)). An example of energy balance approach is discussed for the Okhotsk Sea, where one of the largest tidal ranges have been recorded (13.9 m) in the Penzhinskaya Guba.

Potential energy generated by the sea level difference has been used to produce electricity through construction of barrages to dam water passages so that the water head necessary for the turbine operation can be established. Knowledge for such constructions has been achieved mainly through the investigations of French scientists and engineers and it was implemented to the 240 MW TPP at La Rance, Brittany, France, in 1967 ([Gibrat, 1966](#)). The power plant taps tidal energy during a limited time period when the sea level difference between basin and open ocean is large enough to drive turbines. A simple consideration based on the conservation of volume connects thus generated power to the sea level changes in the basin and the discharge through the dam.

Older use of tidal power by blocking the entrance to a bay with a dam was implemented very slowly, because of the prohibitive costs of such construction. The new approach is to use tidal currents similar to the way wind-mills are used to tap the wind energy. This relatively inexpensive method is stimulating tidal power development and has the potential to provide large amounts of energy ([Garrett and Cummins, 2004](#)). A simple theory shows that the maximum power available from the moving fluid is proportional to the fluid density times velocity cubed. Because density of the sea water is approximately 900 times

greater than the air density the same amount of energy generated by wind can be achieved by relatively much slower water movement.

## 2. Short description of tides in the World Ocean

Distribution of the tidal amplitude and phase in the World Ocean based on the Topex/Poseidon satellite observations and on the global numerical models has been summarized by **Shum et al. (1997)** with the final products recorded on the diskette titled *A Collection of Global Ocean Tide Models*, available at email: [podaac@podaac.jpl.nasa.gov](mailto:podaac@podaac.jpl.nasa.gov). In Figs. 1 – 4 the charts of amplitude and phase of the four major tidal constituents ( $M_2$ ,  $S_2$ ,  $K_1$  and  $O_1$ ) are shown based on the satellite observations. The data and figures were compiled by G. Musiela from National Tidal Facility, Adelaide, Australia. To simplify description, the reference will be often made to the  $M_2$  tide – the semidiurnal constituent due to the moon attraction with the period equal to half of the mean lunar day. This is the strongest constituent in the entire spectra of the tidal oscillations. The tide producing force at this frequency is two times stronger than for the  $K_1$  tide, the major diurnal constituent (cf. Chap. I and **Pugh, 1987**).

It is useful to notice that in the charts the same color denotes the different amplitudes for the different constituents. Both  $M_2$  and  $K_1$  wave in the Pacific and Atlantic Oceans propagate around amphidromic points, where amplitude of the tidal wave is close to zero. According to the simple long wave dynamics represented by Kelvin wave propagating in a wide channel, counterclockwise rotation is expected in the northern hemisphere and clockwise rotation in the southern hemisphere (**Godin, 1988; Pugh, 1987; Taylor, 1921**). As can be seen in the figures, not all waves in the Pacific and Atlantic oceans rotate according to expected patterns. Color coded amplitudes filter out the locations of the higher tidal amplitudes in the World Ocean. The largest surface area covered by the red color for the semidiurnal tides is observed in the north-eastern Atlantic Ocean at the coast of north-west Africa, western Europe and Greenland. The high amplitudes of semidiurnal tides occur also around South America in the Amazon Basin and close to southern Argentina. The largest surface area of the relatively high semidiurnal tides in the Pacific Ocean occurs in the Gulf of Alaska, at equatorial South America and around New Zealand. Other regions of high semidiurnal tides are located in off western Australia and between Madagascar and Africa.

The diurnal tides, as expressed by the  $K_1$  wave, have relatively large amplitudes in the North Pacific, with the largest surface area covered by red and yellow-red colors in the Gulf of Alaska and southern part of the Bering Sea, but these amplitudes are much smaller than the  $M_2$  amplitude. The highest diurnal tides have been observed in the Okhotsk Sea. The regions of the Persian Gulf, Java Sea, west coast of New Guinea, northern Australia and Antarctica also display stronger diurnal tides. Diurnal tide distribution is contrasting the semidiurnal tide distribution, while semidiurnal waves depict maxima both in the open ocean and in the coastal regions, the diurnal waves are very small in the open ocean and only in proximity to the continents their amplitude is growing.

To describe the total tidal range we shall use the largest observed tidal range, defined as mean spring range (**Pugh, 1987**). In the open ocean the tidal range is about 0.5–1m. The change of depth and coastal line has a strong influence on the tidal amplitude (and even stronger on the tidal current).

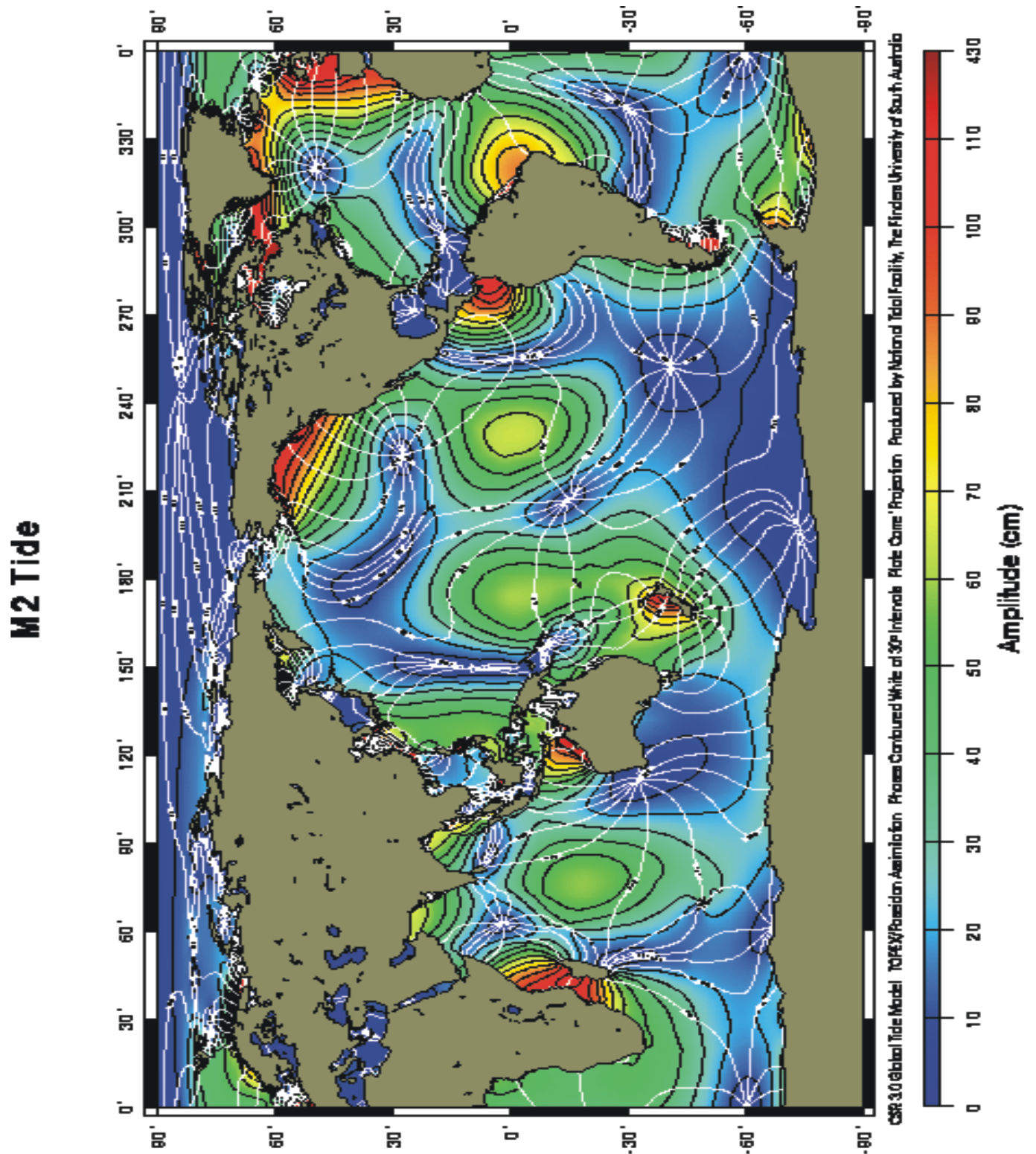


Figure 1.  $M_2$  tide in the World Ocean. Amplitude (black lines) is given in cm and phase (white lines, degree) is referred to Greenwich. Courtesy of G. Musiela, NTF, Australia.

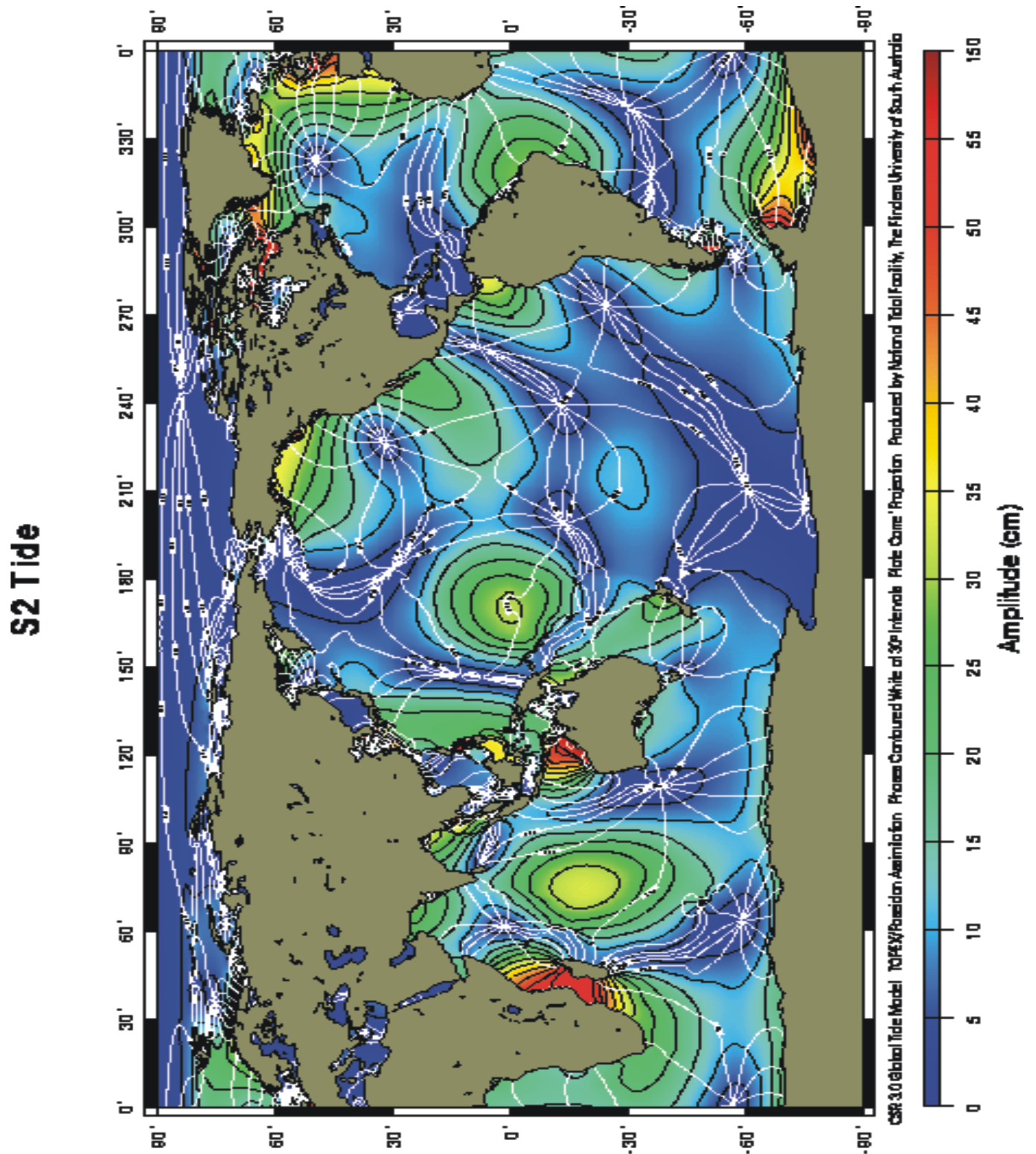


Figure 2.  $S_2$  tide in the World Ocean. Amplitude (black lines) is given in cm and phase (white lines, degree) is referred to Greenwich. Courtesy of G. Musiela, NTF, Australia.

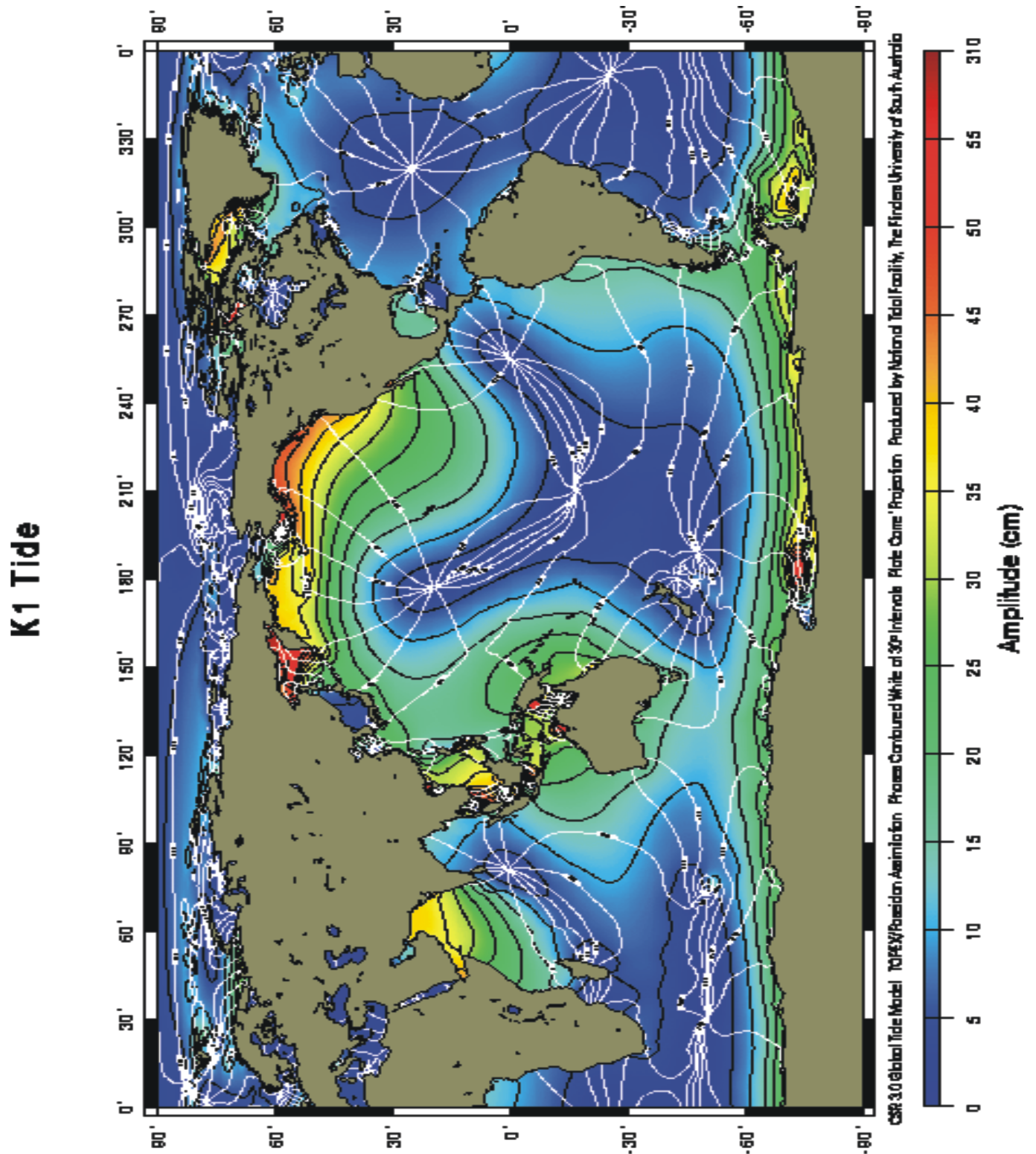


Figure 3.  $K_1$  tide in the World Ocean. Amplitude (black lines) is in cm and phase (white lines, degree) is referred to Greenwich. Courtesy of G. Musiela, NTF, Australia.

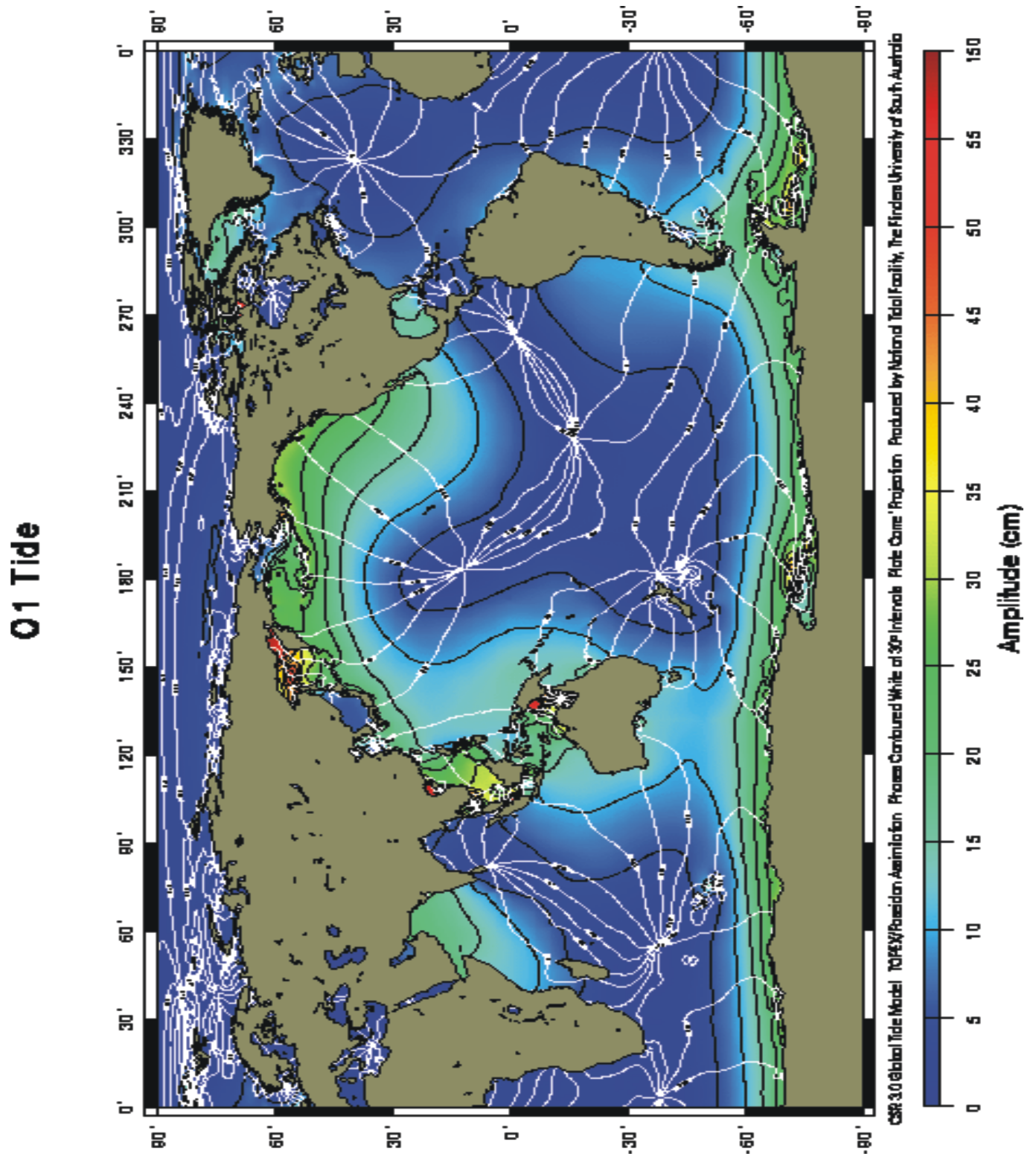


Figure 4. O<sub>1</sub> tide in the World Ocean. Amplitude (black lines) is in cm and phase (white lines, degree) is referred to Greenwich. Courtesy of G. Musiela, NTF, Australia.

Generally along the ocean coast the tidal range is less than 1.5–2 m. Tidal ranges exceeding 5–6 m were observed only in the narrow bays or channels where depth is changing quite smoothly from the mouth to the head (cf., [Defant, 1960](#); [Godin, 1988](#)). Usually the bays with the large tides, like Bay of Fundy on the Atlantic coast of North America, White Sea in the Northern Russia, Penzhinskaya Guba in the Okhotsk Sea or Cook Inlet in the Gulf of Alaska, depict amplification of the tide that occurs from the mouth to the head of the bays. Such tidal patterns may be attributed either to the gradual shallowing and narrowing of the bay or resonance condition, when natural period (eigenperiod) of oscillations of the bay is close to the tidal period ([Defant, 1960](#)).

The brief description of the tides is aimed here to delineate locations with the high tidal range for possible tidal power exploitation. Along with the potential energy expressed by the tidal range, the kinetic energy expressed by the current can be used as well. Construction of the charts for the tidal currents is quite difficult because currents display strong spatial variability. The general oceanic tidal models (cf. [LeProvost et al., 1994](#); [Kantha, 1995](#); [Shum et al., 1997](#)) calculate distribution of currents as well, but the spatial grid applied in such calculations (20–40 km) is not adequate for the small scale resolution. Therefore, we mention here a few important properties of the tidal currents. Obviously, the high tidal range generates the large currents, but the relatively strong currents can be generated by the coastal and bathymetry constraints even if tidal elevations are small. The most conspicuous topographic enhancement of the flow occurs in Cook Inlet, Alaska where  $M_2$  tide current increases up to 3–4 m/s ([Patchen et al., 1981](#), [US Coast Pilot, 1995](#)). This current enhancement is related to the large tides whose range is close to 10 m. On other hand, in the passages between the Aleutian Islands, strong currents of the order of 2.5–3 m/s are not associated with the high tides because the tidal range there is about 1 m.

Semidiurnal and diurnal tidal currents behave sometimes similarly, but often are different. Tides propagating from the deep ocean onto the continental shelf change velocity due to changes in the bathymetry. The shelf break also induces a strong vertical motion and, in the stratified ocean, large amplitude internal tides are generated as well. These waves can display large currents but they do not influence the sea level. Large amplitude internal wave packets are often observed at the shelf break region ([Holloway, 1987](#)). All tidal waves impinging on the shelf break become slightly deformed and additionally, at the middle latitudes, diurnal tides are also selectively trapped over shelf break region. The resonant phenomenon in the diurnal band of oscillation can generate enhanced current and trap tidal energy away from the shelf domain as well. Trapped diurnal tidal waves often occur at the edges of continental shelves, in the canyons and at the seamounts ([Cartwright, 1969](#); [Kowalik and Proshutinsky, 1993](#)). This trapping of diurnal tides at the local bathymetry leads to enhancement of the tidal currents, while the change of the sea level is quite small. Over the shelf and in the shallow bays, in the passages between islands, close to headlands and around banks the tidal currents, both in diurnal and semidiurnal band of oscillations can be strongly amplified leading often to strong nonlinear interactions.

### 3. Short description of extreme tide ranges.

Here the brief description of the highest tides in a few locations of the World Ocean, is given. Although the tidal constituents (amplitude and phase) are constant, the resultant

tides depend on many time dependent factors which tend to generate variable sea level elevations. The highest tidal ranges given below are expected to occur at least once per year.

1. **The Bay of Fundy. Tidal range 17m.** The bay is located on the Atlantic coast of Canada and it has the highest tides observed in the World Ocean. Tides in the bay are dominated by the semi-diurnal oscillations with high waters and low waters each approximately of the same range. The high tides have been attributed to the fact that the natural period of the Gulf of Maine-Bay of Fundy system is close to, but slightly above, the  $M_2$  period (Garrett and Greenberg, 1977; Greenberg, 1979). The evidence for this came from an examination of the tidal amplification at the various ports as a function of the frequency and existence of the highest amplification peak at the  $M_2$  frequency. In the Bay of Fundy proper the amplitude of  $M_2$  tides changes from approximately 2 m at the entrance to more than 5 m in Minas Basin and to more than 4.5 m in Chignecto Bay (see Fig. 5). Along with the high tides, strong tidal currents occur which can be used for tidal power generation as well. The half-flood tide currents at the south shore of the Bay of Fundy are close to  $100 \text{ cm s}^{-1}$  and at the north shore about  $75 \text{ cm s}^{-1}$ . The obvious locations for the strong currents are narrow passages like Cape Split, dividing Minas Channel from Minas Basin; here the maximum flood tide current is close to  $4 \text{ m/s}$ . Flood tides entering rivers cause strong currents and bores. The Saint John River empties through a shallow sill about 4 m deep, tides here cause a strong current alternating in direction, known as "reversing falls". Strong tides and narrow passages seem to be ideal for tidal power utilization, therefore, in the Bay of Fundy a small pilot plant for tidal power generation has been constructed at the Annapolis Royal, Nova Scotia. The mean tidal amplitude of the  $M_2$  tide at this site is more than 3 m.

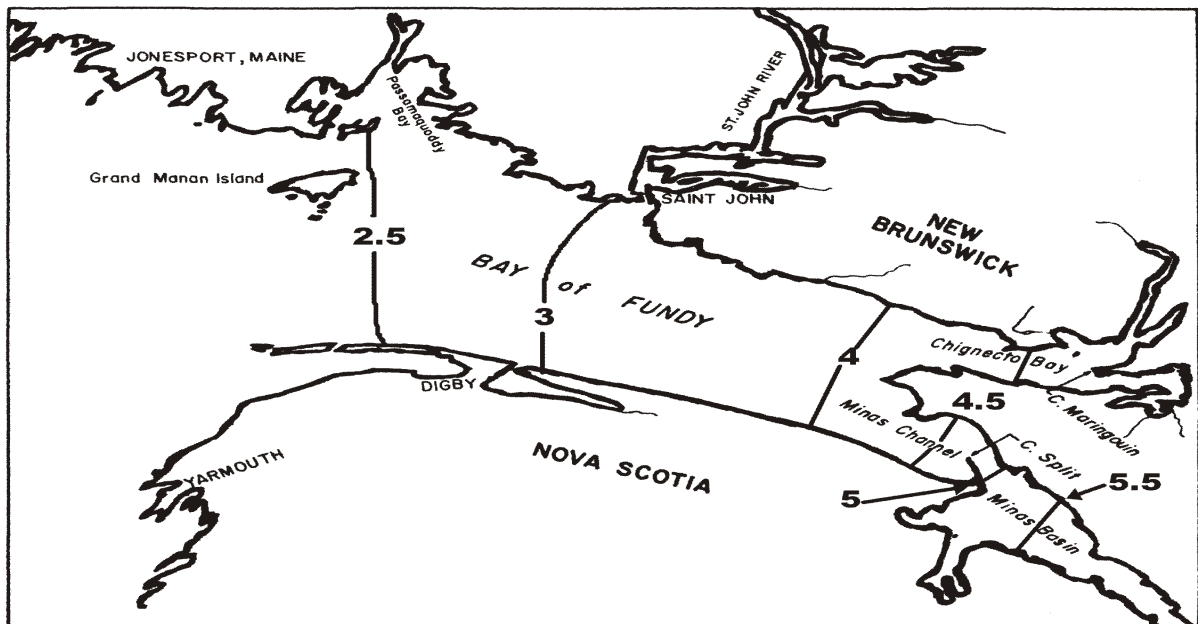


Figure 5. Amplitude (in meters) of  $M_2$  tide in the Bay of Fundy.

2. **Penzhinskaya Guba. Tidal range 13.9 m.** This bay is located in the north-eastern part of the Okhotsk Sea (Fig. 6). The Okhotsk Sea's natural period of oscillations is close to 26 h, therefore the diurnal tides are resonantly enhanced and dominate over semidiurnal tides. Both  $M_2$  and  $K_1$  waves are generated by tides entering the Okhotsk Sea through the passages between the Kuril Islands, and both tides show similar amplitude in the North Pacific. The system of Shelikhov Bay and Penzhinskaya Guba amplifies all tidal waves. At the entrance to Shelikhov Bay the  $K_1$  wave amplitude is close to 150 cm, the  $O_1$  is about 100 cm and  $M_2$  is 50 cm. While  $K_1$  is amplified to about 250 cm (about two times),  $K_1$  to about 180 cm (about two times) and  $M_2$  to about 120 cm, thus suggesting that the system of Shelikhov Bay and Penzhinskaya Guba is better tuned to the semidiurnal periods.

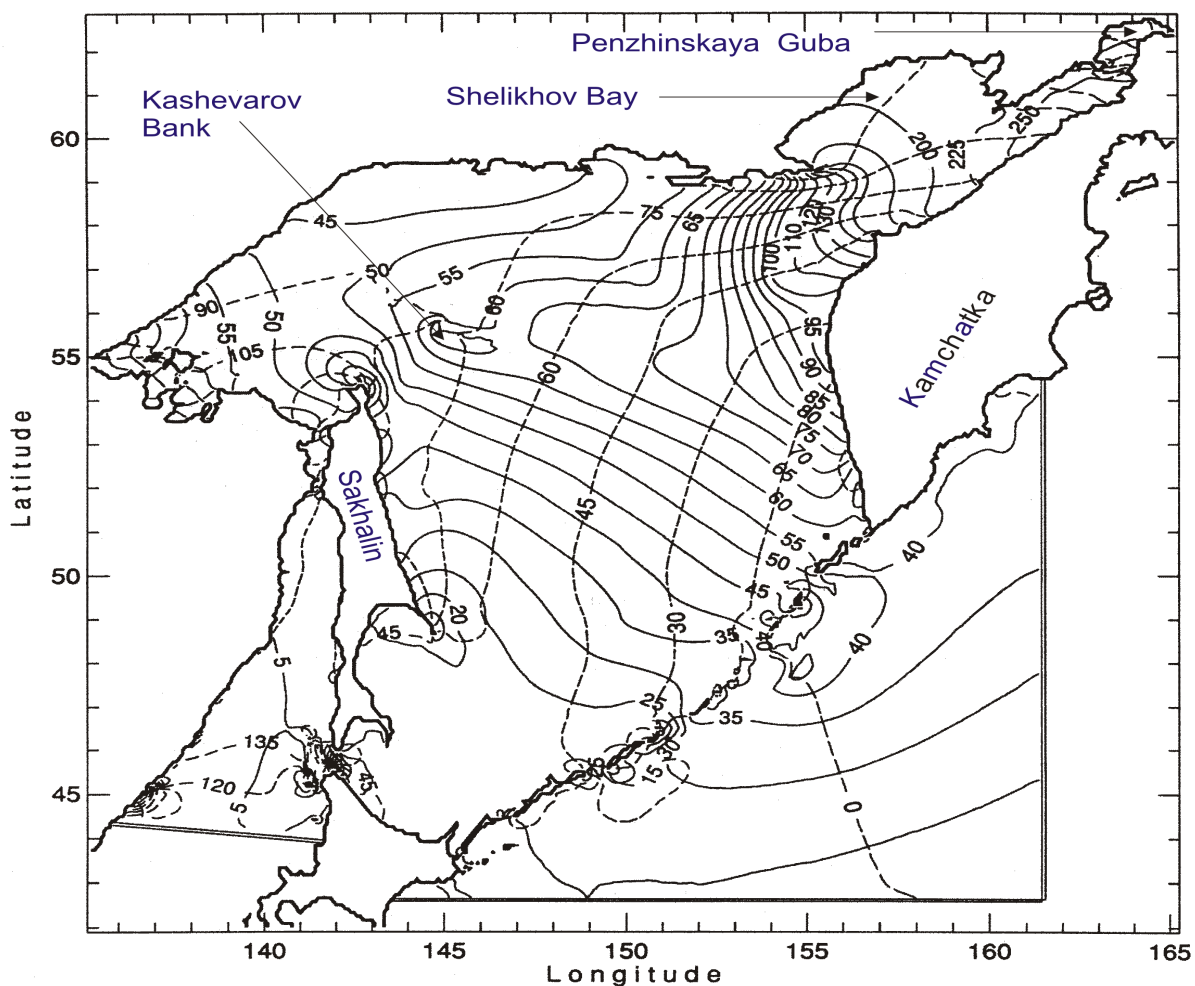
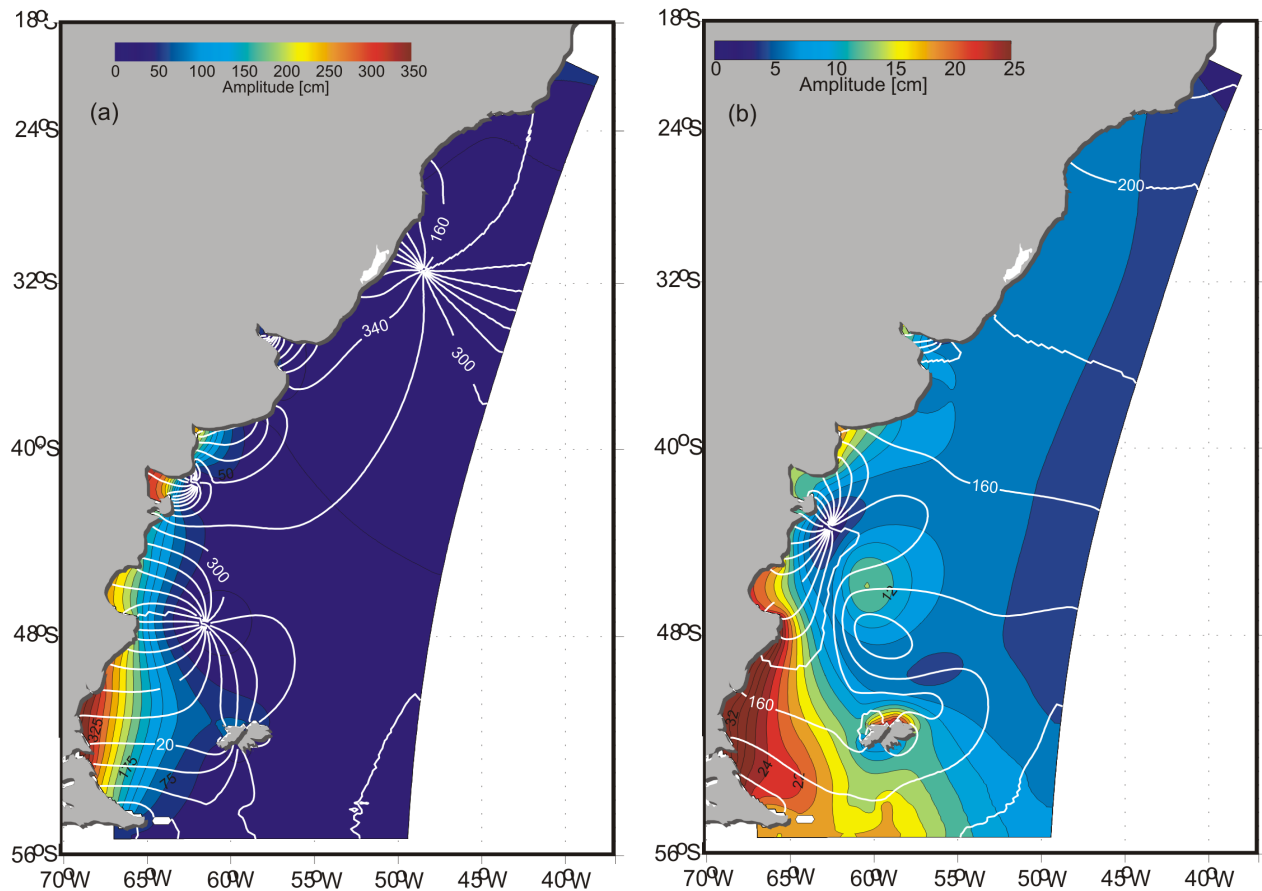


Figure 6. Amplitude and phase of the  $K_1$  tide in the Okhotsk Sea based on Kowalik and Polyakov (1998). Amplitude (solid lines) is in cm and phase (dashed lines, degree) is referred to Greenwich

An interesting and important phenomenon for tidal power exploitation, are regions of trapping diurnal tides, where tidal currents are enhanced. This phenomenon is called

tidally induced trapped shelf wave. Because tidal frequencies ( $\omega$ ) straddle the local Coriolis frequency, diurnal and semidiurnal constituents have different tidal wave dynamics for given Coriolis force, gravity, and bathymetry. In particular, in the Okhotsk Sea, diurnal tides are subinertial and semidiurnal tides are superinertial. The inertial frequency ( $\omega = f$ , where  $f = 2\Omega \sin \phi$ ,  $\Omega$  is the Earth's rotation frequency and  $\phi$  is the geographical latitude), separates physically different types of wave motions: gravity forces determine wave behavior at  $\omega > f$ , while gyroscopic forces prevail at  $f > \omega$  (LeBlond and Mysak, 1978). A noticeable location for diurnal tide trapping is Kashevarov Bank (depth about 100 m). While  $K_1$  amplitude above this bank increases only about 10 cm (see Fig. 6), the current at the top of the bank reaches 85 cm/s, while off-bank values are 5–10 cm/s. The maximum current of  $K_1$  and  $O_1$  is close to 160 cm/s at the bank's top.

**3. Puerto Rio Gallegos, southern Argentina (Lat.  $51^\circ 36'$  S Long.  $69^\circ 01'$  W) . Tidal range close to 12 m.**



**Figure 7. Main tidal constituents: (a) M2 constituent, amplitudes (color), Contour Interval (CI) = 25 cm, Greenwich phase (white solid lines), CI = 20 deg; (b) K1 constituent, amplitudes (color), CI = 2 cm. Courtesy of E. Palma, Universidad Nacional del Sur, Bahia Blanca, Argentina.**

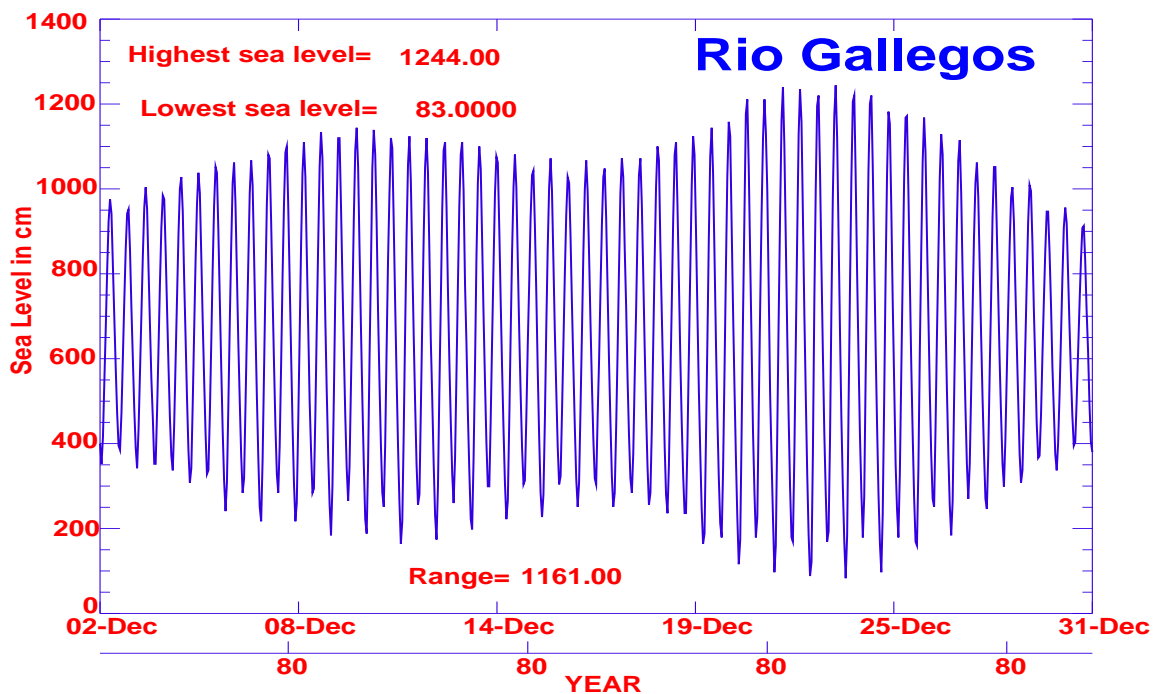


**Figure 8.** Tide gauge records from Muelle El Turbio (Rio Gallegos) Lat.  $51^{\circ}37'S$ , Long.  $68^{\circ}13'W$ , courtesy Departamento Oceanografia, Servicio de Hidrografia Naval, Argentina.

The general chart of the  $M_2$  tide (Fig. 1) shows strong amplification of this wave at the southern Argentina coast line. Such amplification is due probably to the wide shelf (Glorioso and Flather, 1997). The width of this shelf is close to a quarter wavelength of the  $M_2$  tide and therefore resonant conditions may be at work in this system. In Fig. 7 the amplitude and phase of the major diurnal ( $K_1$ ) and semidiurnal ( $M_2$ ) constituents are given based on the computations by Palma et al. (2004). The amplitudes of the diurnal waves are one order smaller than the amplitude of the semidiurnal waves. The semidiurnal wave propagates from the south to the north and the largest amplitude of more than 4 m occurs along the shore between  $48^{\circ}S$  and  $54^{\circ}S$  in the Bahia Grande. Smaller bays to the north also enhance semidiurnal tides, and especially around  $41^{\circ}S$  (Golfo San Matias) the  $M_2$  wave is strongly amplified so that the total tide range is close to 10 m. The largest tides occur in the estuary of Rio Gallegos. Measurements taken at the point Lat.  $51^{\circ}37'S$ , Long.  $68^{\circ}13'W$ , during the month of December 1980 (see Fig. 8) by Departamento Oceanografia, Servicio de Hidrografia Naval show range of 11.6 m, but up river from this point the range exceeds 13 m. Fig. 8 shows that, indeed, the dominant tidal constituent is semidiurnal tide, but it also depicts a strong change of amplitude in the two-week time period, which suggests that the tidal energy is highly variable in time.

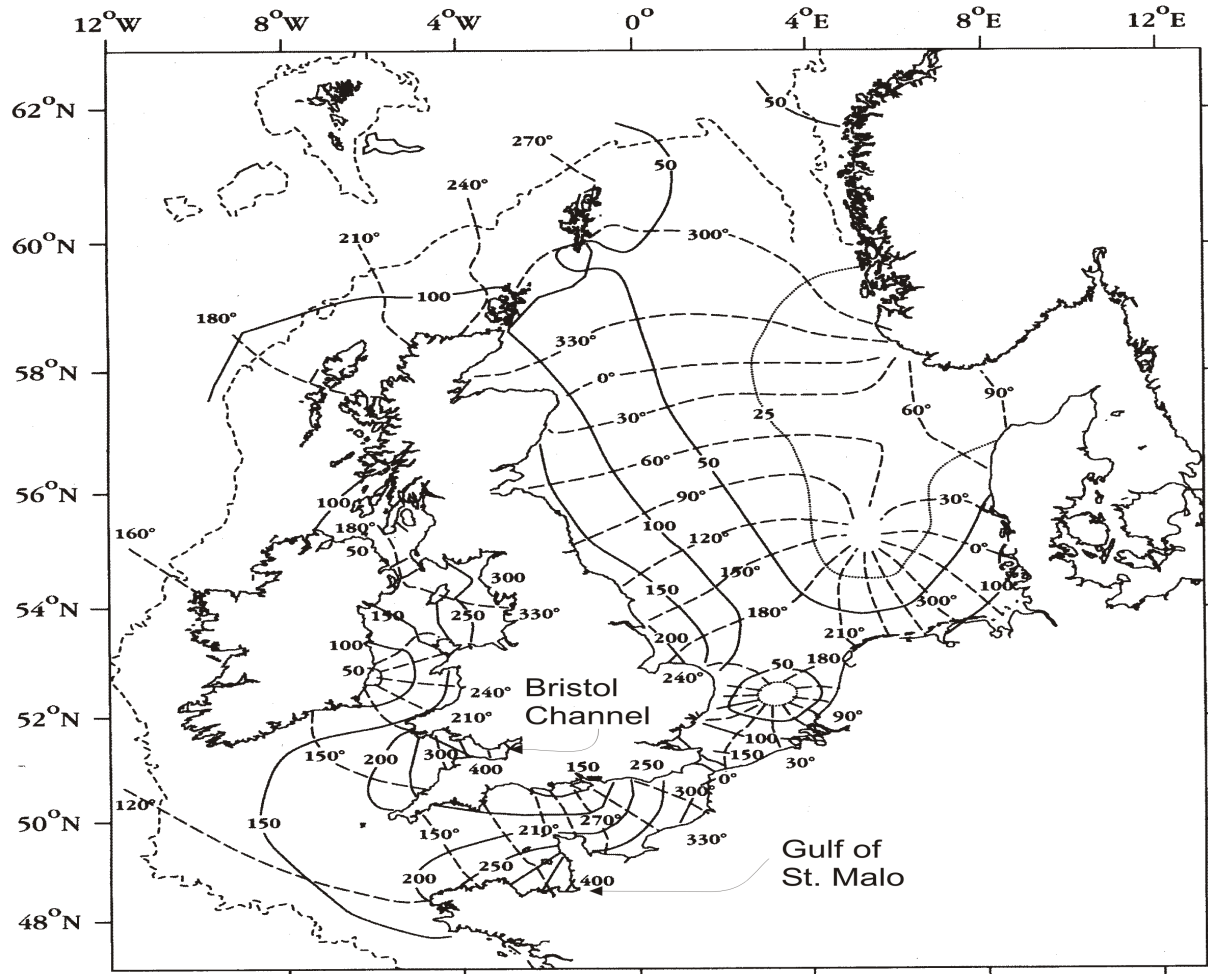


Figure 9. Amplitude and phase of the  $M_2$  tide at the N. W. European Shelf Seas, based on Flather (1976). Amplitude (solid lines) is in cm and phase (dashed lines, degree) is referred to Greenwich

4. **Gulf of St. Malo, coast of France.** At the port of Granville the maximum tide range of the spring tide reaches 14.7 m.

5. **Bristol Channel, coast of England.** The maximum tidal range in the Severn River estuary reaches 14.5 m.

$M_2$  tide at the coasts of Scotland, England and France is strongly amplified as shown in Fig. 9. These data were derived by Flather (1976) through an application of the 2-D model. Computed amplitudes and phases are in close agreement with the observations. In this figure, the two locations of the extreme tidal amplitude have been marked, the heads of the Gulf of St. Malo and the Bristol Channel. The English Channel/La Manche (between France and England) and Irish Sea (between England and Ireland) are two channels where  $M_2$  wave is generated through the interaction of two traveling waves entering these channels from the south and north (Defant, 1960).

As both channels narrow, the tide is amplified, and it seems that, both in the Gulf of St. Malo located in the English Channel/La Manche and the Bristol Bay located in

the Irish Sea, the resonance phenomenon is at work. The resonance interaction between co-oscillating water-masses of the Gulf of St. Malo and the oscillations in the English Channel can be easily deduced from the Fig. 9. At the entrance to the Gulf of St. Malo the amplitude is only about 200 cm to 250 cm, while it increases to more than 400 cm at the head of the Bay. A similar situation occurs in the Bristol Channel; the amplitudes at the entrance of about 200 cm are amplified at the head of the Bay to approximately 450 cm.

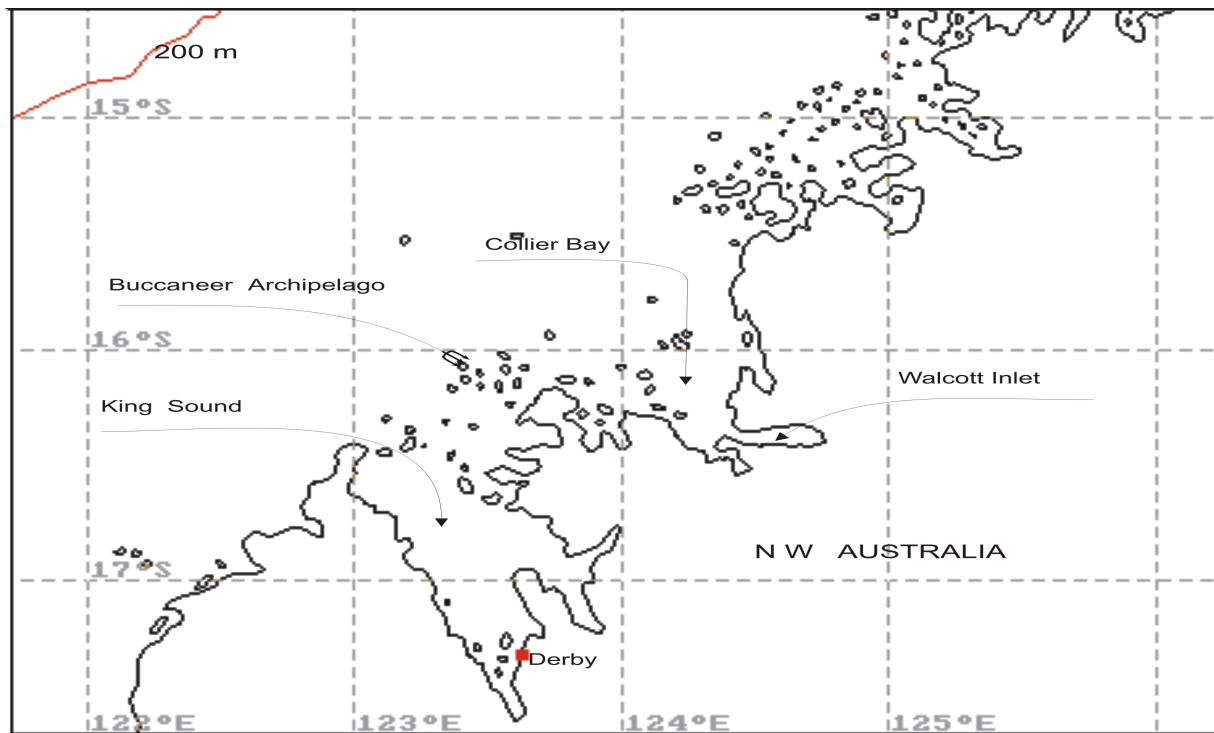


**Figure 10. North west Australia. Geographical locations of the largest tides in the Australia. Notice the extent of the shelf given by 200 m isobath.**

#### **6. Western Australia. Tidal range 11 m.**

As can be gleaned from the Figs. 1 and 2, Northwestern Australia has very large tides. The major tidal constituents belong to the semidiurnal tides. As in many cases considered before, the tidal behavior over an adjacent ocean shelf defines to a large degree the tides along the coastline. The largest tides occur in the two semi-closed water bodies: Collier Bay and King Sound (Fig. 10).

The largest recorded ranges in Australia are those for Lizard Island (11.352 m) and Shale Island (11.556 m) located in the Collier Bay, see Fig. 11. This is based on data obtained in 1977 and 1963, respectively (NTF, 2000). A common misconception is that the highest tides are around Derby, King Sound (10.468 m). The tides in King Sound and Collier Bay travel through narrow passages. A narrow passage to Talbot Bay (in Buccaneer Islands) depicts very strong tidal currents. Tidal flow generates a waterfall effect as water piles up against one side of this narrow passage (50 m wide).

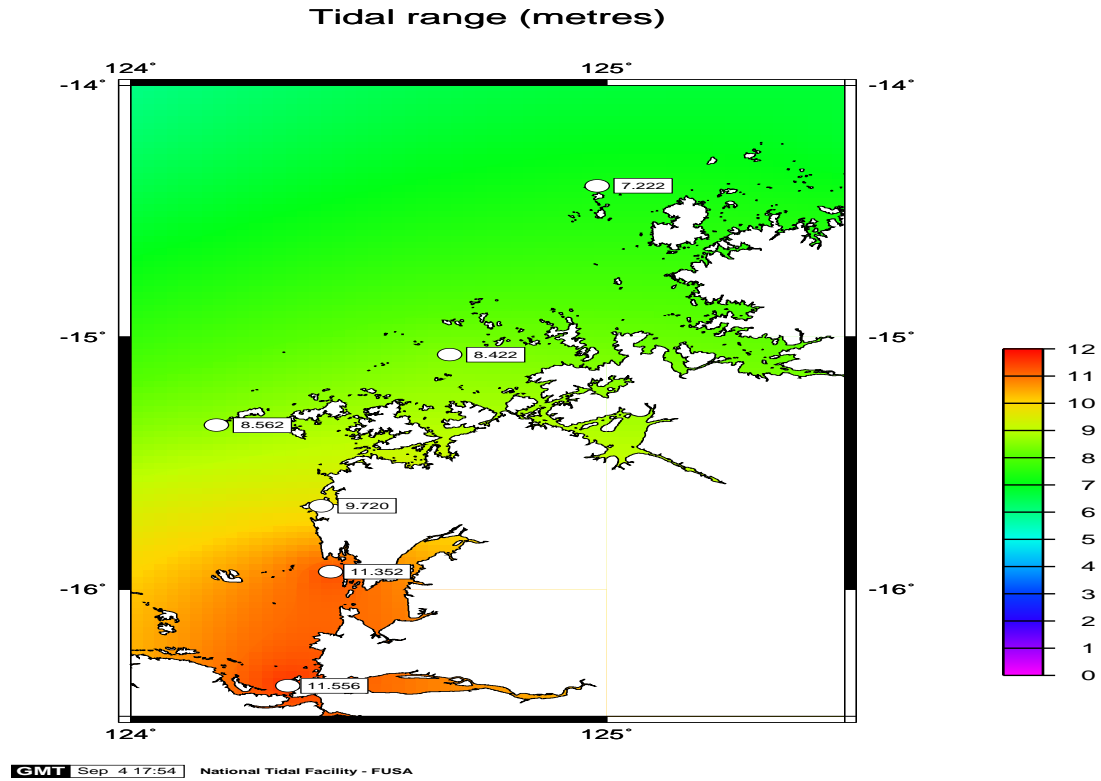


Figure 11. Collier Bay, Northwest Australia. Tide range in meters. Courtesy NTF, Australia

#### 4. Rudimentary notions related to transfer of energy

The force  $F$  applied to a water particle displaces this particle from position  $l$  to position  $l + dl$ , and therefore this force does small work  $dW$

$$dW = Fdl \quad (\text{IV.1})$$

The work done on the particle of water by the various forces is equal to the change in the kinetic energy of the particle. To understand this important connection between work and energy let us start with the general equation of motion,

$$\rho \frac{Du}{Dt} = F_x \quad (\text{IV.2})$$

$$\rho \frac{Dv}{Dt} = F_y \quad (\text{IV.3})$$

Here  $\rho$  denotes the density of the sea water,  $u$  and  $v$  are the components of the velocity vector along  $x$  (East-West) and  $y$  (South-North) directions, respectively, and  $F_x$  and  $F_y$  are the components of force. Multiplying the first equation by  $dx$  and the second equation by  $dy$  the work along  $x$  and  $y$  direction is obtained

$$\rho \frac{Du}{Dt} dx = \rho \frac{Du}{Dx} \frac{Dx}{Dt} dx = \rho \frac{Du}{Dx} u dx = F_x dx = dW_x \quad (\text{IV.4})$$

$$\rho \frac{Dv}{Dt} dy = \rho \frac{Dv}{Dy} \frac{Dy}{Dt} dy = \rho \frac{Dv}{Dy} v dy = F_y dy = dW_y \quad (\text{IV.5})$$

Adding the above equations by sides

$$\rho d(u^2/2 + v^2/2) = dW_x + dW_y = dW \quad (\text{IV.6})$$

and integrating we arrive at the conclusion that the work done by all forces in the system, such as pressure, tidal forces and friction resulted in the change of kinetic energy of the system.

$$\rho(u^2/2 + v^2/2)_2 - \rho(u^2/2 + v^2/2)_1 = W \quad (\text{IV.7})$$

To continue this consideration, one needs a system of units to measure forces, work and energy. The force defined by equations IV.2 and IV.3 is density multiplied by acceleration. This is due to the fact that we consider the mass of the unit volume. Thus, assuming force as mass times acceleration,

$$F = m \frac{Du}{Dt}; \quad \text{units in CGS are} \quad 1g \times 1 \frac{cm}{s^2} \quad (\text{IV.8})$$

This unit is called dyne. Since  $1\text{kg}=10^3\text{g}$  and  $1\text{m/s}^2 = 10^2 \text{ cm/s}^2$  the larger unit is introduced called newton.  $1\text{N}=1\text{kg} \times 1\text{m/s}^2 = 10^5 \text{ dyne}$ . The unit of work is defined as the work done by a unit force moving a water particle a unit distance. In CGS the unit of work is  $1\text{dyne} \times \text{cm}$ , which is called erg. Finally, the notion of power is defined as the time rate at which work is done,

$$P = \frac{dW}{dt} = Fu; \quad \text{units in CGS are} \quad 1\text{J/s} = 10^7\text{erg/s} = 10^7\text{g} \times \frac{cm^2}{s^3} \quad (\text{IV.9})$$

From above, the power can be also expressed as force multiplied by velocity. The  $1\text{J/s}$  is called watt (W).

It is of interest to evaluate an amount of the tidal energy which can be used for the tidal power. Here different avenues can be taken; the easiest approach is to define potential energy as it is expressed by sea level change, and the average numbers for this change are easily accessible from measurements. The kinetic energy is expressed by currents and, therefore, it is a less known part of the energy balance. Besides kinetic and potential energy, the consideration of dissipated energy due to friction may also be important, because redirecting this energy into tidal power seems to sustain the tidal regime. The average dissipated power due to tides is equal to 4 TW (**Munk, 1997; Egbert and Ray, 2000**) and the major portion of approximately 3TW is associated with the lunar tides (**Kagan, 1997**), (1 Terawatt= $10^{12}$  W). Generally, we assume that the work done by the Moon and Sun is in balance with the tidal energy dissipated in the World Ocean. Efforts made by oceanographers to evaluate the energy dissipated through the work done by the frictional forces and through other sinks of tidal energy are still in progress (**Munk, 1997**). The exploitation of tidal energy should reinvest this dissipated energy into tidal power with the tacit assumption that such an approach should not strongly disturb the tidal regime. The large changes introduced by tidal power tapping may defy the entire purpose of tidal

power. The present-day tidal current and tidal elevation may remain unchanged if tidal dissipation is substituted for tidal energy tapping. While the amount of dissipated energy is relatively easy to account for, the spatial (geographic) distribution of dissipation will be difficult to preserve (or conform to the natural dissipation), since the tidal energy must be tapped strongly at the smaller domain to be economically viable. To estimate available tidal energy, the kinetic and potential energy of tides ought to be known. The potential energy is given by

$$\frac{1}{2} \iint \rho g \zeta^2 dx dy = const \quad (\text{IV.10})$$

This energy is expressed in  $g \times \frac{cm^2}{s^2}$ , therefore to change it into power the above ought to be divided by time, i.e., the tidal period. The sea level  $\zeta$  changes from 0 to the tidal range, or  $2\zeta_a$  during one tidal period. Where  $\zeta_a$  is the amplitude. The major input into this expression is the surface area of a domain. Let's estimate the potential energy in Cook Inlet, Alaska, where the maximum tide range is close to 11m and the average range over the inlet can be taken as 6m. Surface area of the inlet is approximately  $2 \times 10^4 km^2$ . Substituting these numbers into an equation for the potential energy we arrive at  $3.5 \times 10^{15} J = 3.5 \times 10^3 TJ$ . Assuming that this energy can be changed into power at a constant rate in time during the  $M_2$  tide period, the power extracted will be  $7.8 \times 10^{10} W = 7.8 \times 10^7 kW$ . Similar calculations for the entire World Ocean with an average tide amplitude of 50 cm will set a global energy equal to  $3.5 \times 10^5 TJ$ . Changing this energy into power, we arrive at approximately  $8 \times 10^9 kW$ . This power is only 100 times larger than the power available in the Cook Inlet, although the surface of the World Ocean ( $5 \times 10^8 km^2$ ) is about  $2.5 \times 10^4$  times larger than the Cook Inlet. Finally, a word of caution, the formula (IV.10) used for the potential energy calculations gives only an approximate estimate. The formula is correct, but it requires detailed knowledge of the sea level distribution.

Actually, the above calculated energy cannot be extracted into power uniformly in time. The tide is variable in time, and in Cook Inlet it exhibits a marked diurnal inequality with the consecutive high waters and low waters varying strongly. The tidal regime in all local waters display strong fortnightly (neap-spring) variability. Usually the amplitudes from spring to neap tides change by a factor of 2, which means that the energy changes by a factor of 4. These variabilities make the utilizing of tidal energy quite difficult and necessitate large investments into complicated machinery for the tidal power generation, which differs from the hydro-power generation. However, we have to realize that "available" tidal energy cannot be completely used for power generation; the best approach will be to utilize the portion which is dissipated in the local water body. This guarantees (to some degree) that the old tidal regime will stay undisturbed. A different approach is to extract the tidal energy only in a small section of the basin (bay), so even if the tidal regime is changed in this small section the remaining area of the basin will sustain strong tides and deliver energy for power tapping.

## 5. Tidal energy balance in local water bodies

Mean energy balance averaged over the tidal period includes sources of energy i.e., energy generation due to the work of external forces, as well as sinks of energy, this is energy dissipated by the internal and bottom friction. Sources and sinks of energy are

connected by transport of energy expressed by the energy flux (**Munk, 1997**). The well established principle of energy conservation declares that the tidal energy averaged over the tidal period and over the surface of the local water body must remain constant, therefore the flux of tidal energy into domain (through the open boundaries) and the tidal energy generated in the local domain ought to be in equilibrium with the dissipation. Hence, for the energy balance over the tidal period and over the domain surface and boundaries, a simple equation holds (**Nekrasov, 1990; Leprovost and Lyard, 1997; Kowalik and Murty, 1993**)

$$\frac{1}{T} \int \left\{ \int \int \left[ E_g + \frac{\partial E_{hx}}{\partial x} + \frac{\partial E_{hy}}{\partial y} = E_d \right] dx dy \right\} dt \quad (\text{IV.11})$$

Here:  $dx dy$  element of surface in the  $x$  and  $y$  coordinates,  $t$  is time,  $T$  denotes the tidal period,  $E_g = E_{gx} + E_{gy}$  is surface density of the energy generated in the domain. It is expressed in  $\text{W cm}^{-2}$ . Therefore, to derive the total energy, it is multiplied by the domain surface area.  $E_{hx}$  and  $E_{hy}$  are components of the energy flux through the boundary between the local water body and the ocean. It is expressed in  $\text{W cm}^{-1}$  and to derive total inflowing energy it is multiplied by the length of a boundary.  $E_d$  is surface density of the energy dissipated in the domain. It is expressed in  $\text{W cm}^{-2}$ . Hence, to derive total dissipated energy, it ought to be multiplied by the surface area of a domain. Usually, the tidal energy generated in a local domain is very small in comparison to the energy flux, so that an even simpler equation of energy conservation can be written, namely

$$\frac{1}{T} \int \left\{ \int \int \left[ \frac{\partial E_{hx}}{\partial x} + \frac{\partial E_{hy}}{\partial y} = E_d \right] dx dy \right\} dt \quad (\text{IV.11a})$$

The energy flux is a vector with two components defined as (**Nekrasov, 1992; Henry and Foreman, 2001**),

$$\mathbf{E}_h = \{ \rho g H u \zeta, \rho g H v \zeta \} \quad (\text{IV.12})$$

Here the following notation is used:  $\rho$  is the water density,  $g$  is the earth's gravity acceleration,  $H$  is the water depth,  $\zeta$  is the sea level and  $u$  and  $v$  are components of velocity along west-east ( $x$ ) and south-north ( $y$ ) directions. Investigation of the progressive tidal wave established the mean (over tidal cycle) energy flux along the  $x$  direction as (see Chap. II)

$$\bar{E}_{hx} = \frac{1}{2} \rho g H u_a \zeta_a \cos(\phi_u - \phi) \quad (\text{IV.13})$$

A similar formula can be written for the  $y$  coordinate

$$\bar{E}_{hy} = \frac{1}{2} \rho g H v_a \zeta_a \cos(\phi_v - \phi) \quad (\text{IV.14})$$

Measured sea level and velocity are represented here as cos function of frequency  $\omega = 2\pi/T$  ( $T$  is tidal period), and time  $t$ . The sea level and velocity in the tidal wave are given in the following way

$$\zeta = \zeta_a \cos(\omega t - \phi)$$

$$u = u_a \cos(\omega t - \phi_u)$$

$$v = v_a \cos(\omega t - \phi_v) \quad (\text{IV.15})$$

$\zeta_a$  is amplitude and  $\phi$  is phase of a tidal wave. For each tidal constituent the amplitude and phase are called harmonic constants.  $u_a$  and  $\phi_u$  are amplitude and phase for the  $u$  component of current (u harmonic constants).  $v_a$  and  $\phi_v$  are amplitude and phase of the  $v$  component of current (v harmonic constant).

The tidal energy dissipation takes place through bottom friction, horizontal friction and transfer of the tidal energy into internal tides or turbulence (cf. **Munk, 1997**). The most important terms are due to dissipation by the bottom friction :

$$E_{dx} = \rho u \tau_x^b \quad \text{and} \quad E_{dy} = \rho v \tau_y^b \quad (\text{IV.16})$$

Here  $\tau_x^b$  and  $\tau_y^b$  are components of the bottom stress. The bottom stress depends on the current velocity and is expressed as

$$\tau_x^b = \rho c_d u \sqrt{u^2 + v^2} \quad \text{and} \quad \tau_y^b = \rho c_d v \sqrt{u^2 + v^2} \quad (\text{IV.17})$$

A dimensionless bottom drag coefficient  $c_d$ , equals approximately to  $3 \times 10^{-3}$ . The total dissipated energy

$$E_d = E_{dx} + E_{dy} = \rho c_d u^2 \sqrt{u^2 + v^2} + \rho c_d v^2 \sqrt{u^2 + v^2} = \rho c_d (u^2 + v^2)^{3/2} \quad (\text{IV.18})$$

is proportional to velocity cubed.

This term ought to be first averaged over tidal period and subsequently integrated over the surface of the entire domain. The rate of energy dissipation is expressed in  $\text{erg}/(\text{s cm}^2)$ , while net energy flux through a transect is expressed in the  $\text{erg s}^{-1} \text{ cm}^{-1}$ . We shall demonstrate the distribution of energy in the Okhotsk Sea for the  $K_1$  wave. The energy flux for the  $K_1$  constituent, calculated by **Kowalik and Polyakov (1998)**, is shown in Fig. 12. The energy flux through the eastern open boundary brings  $100.5 \times 10^{16} \text{ erg/s}$  into computational domain (this domain also includes a portion of the Pacific), while the flux of  $27.8 \times 10^{16} \text{ erg/s}$  through the southern boundary is directed into the Pacific from the Okhotsk Sea. Also, a very small flux of  $0.3 \times 10^{16} \text{ erg/s}$  is directed from the Japan Sea into the Okhotsk Sea domain. The net flux of tidal energy is directed from the open boundary located in the Pacific Ocean through Kuril Straits towards the region of high frictional dissipation in Shelikhov Bay and Penzhinskaya Guba. Big open arrows in Fig. 12 show net energy fluxes (energy flux multiplied by the length of a transect) crossing several transects. The general pattern of energy flow is broken by larger and smaller domains of a circular or semicircular flux of energy. These are regions of trapped tidal energy and enhanced flux. The areas around the Kuril Islands (especially on the Pacific side), Kashevarov Bank and the entrance to Shelikhov Bay, are major domains of trapped energy. Lesser domains are located at escarpments between Kashevarov Bank and the entrance to Shelikhov Bay, along Kamchatka and Sakhalin.

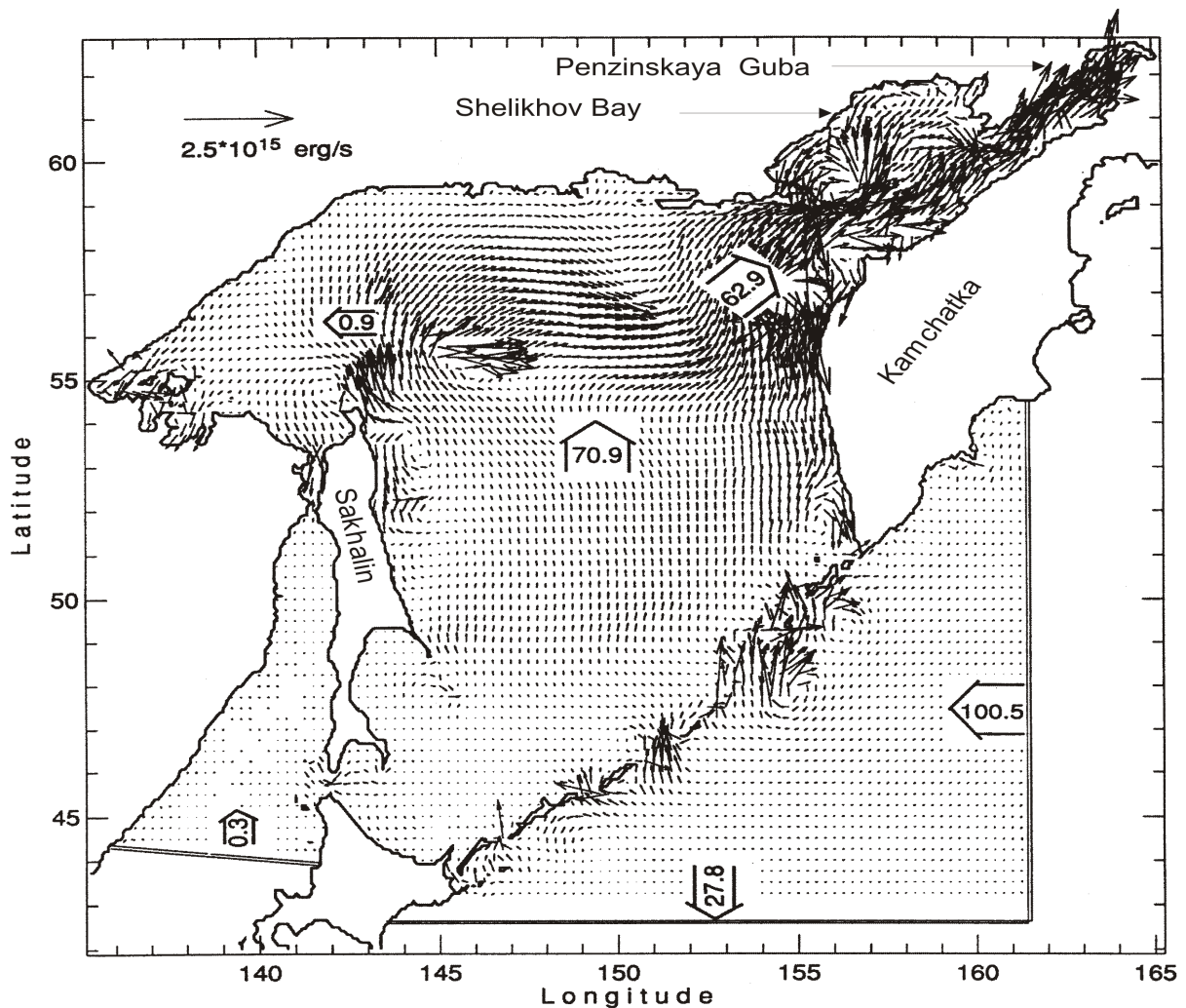


Figure 12. Tidal energy flux for  $K_1$  tide in the Okhotsk Sea based on [Kowalik and Polyakov \(1998\)](#). Large arrows show the net energy flux through transects. The values inside arrows should be multiplied by  $10^{16}$  erg  $s^{-1}$ .

Fig. 13 depicts the rate of energy dissipation per unit surface in the Okhotsk Sea due to  $K_1$  constituent. The trapping of the energy flux over local bathymetry depicted in Fig. 12 for the  $K_1$  constituent resulted in the local maxima for the rate of energy dissipation. The overall rate of energy dissipation of the  $K_1$  wave due to the bottom friction is obtained by integrating over the surface of the entire domain given in Fig. 13. In Table 1 the total energy balance is shown for the four tidal constituents  $K_1$ ,  $O_1$ ,  $M_2$  and  $S_2$ . For major constituent  $K_1$  the total energy source (i.e. inflow and generation by astronomical forcing) equals  $77.7 \times 10^9$  W, and is close to the energy sink caused by the bottom and horizontal friction dissipation. The total flux of energy across open boundaries and the overall rate of energy generation due to astronomical tidal forcing is balanced by the total rate of energy dissipation.

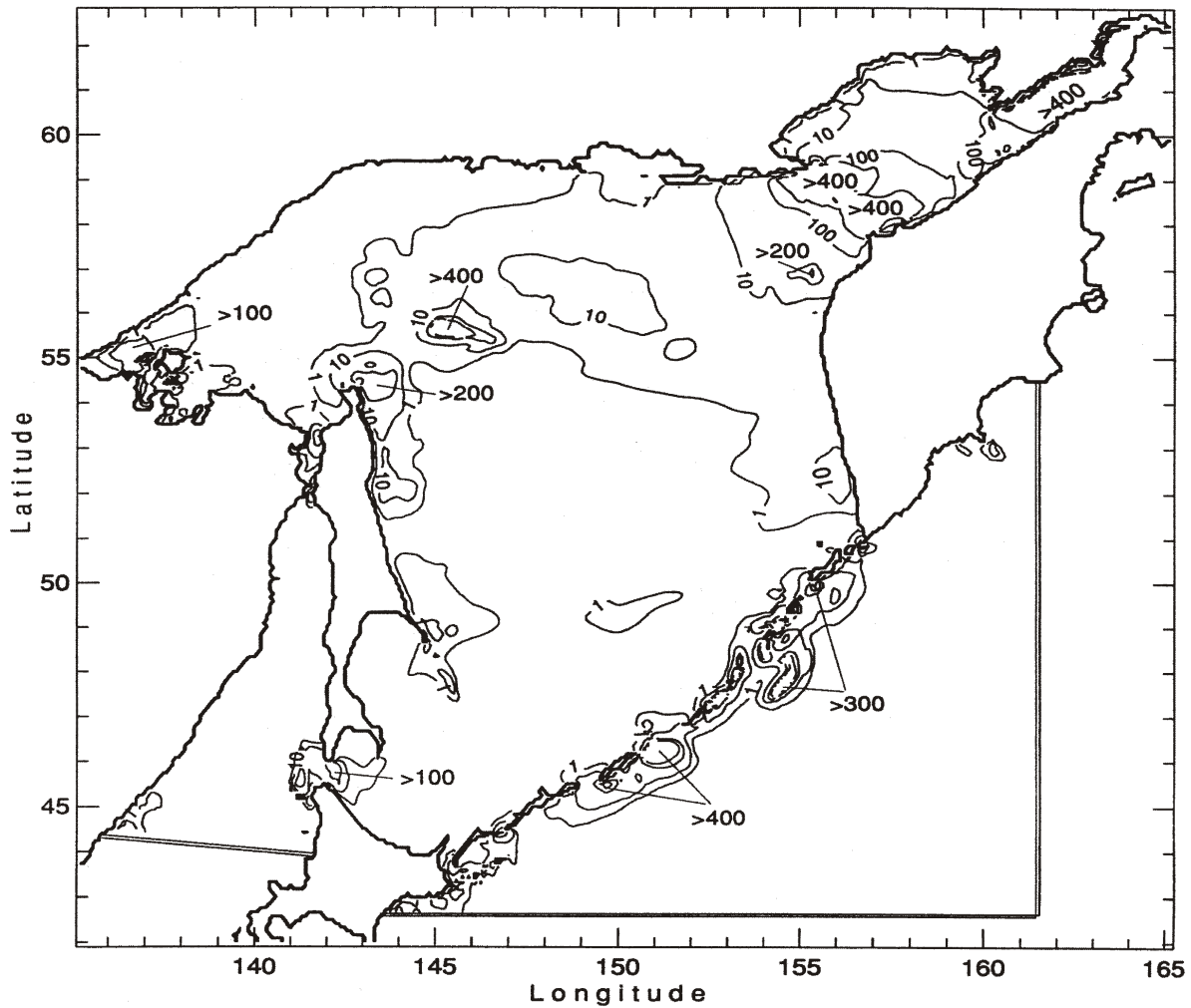


Figure 13. The rate of energy dissipation per unit surface due to  $K_1$  tide ( $\text{erg s}^{-1} \text{cm}^{-2}$ ) in the Okhotsk Sea based on Kowalik and Polyakov (1998).

Table 1. Energy balance for the major tidal constituents

Net flux through open boundary:	Sources $\times 10^9$ Watt				Rate of energy dissipation due to:	Sinks $\times 10^9$ Watt			
	$K_1$	$O_1$	$M_2$	$S_2$		$K_1$	$O_1$	$M_2$	$S_2$
Japan Sea	0.3	0.3	-0.05	0.0	bottom friction	58.1	17.5	39.9	3.4
Southern boundary	-27.8	-11.4	-15.8	-1.3	horizontal friction	20.2	7.8	9.3	1.1
Eastern boundary	100.5	34.4	56.3	5.4					
Energy generation by astronomical force	4.7	1.3	8.1	0.5					
Total	77.7	24.6	48.6	4.6		78.2	25.2	49.2	4.5

The net energy flux through the open boundaries is the principal source of energy. The overall rate of energy generated by astronomical forces is relatively small. For the  $K_1$  tide, astronomical forces generate only  $4.7 \times 10^9 \text{ W}$ , approximately 6% of the total energy. The total rate of energy dissipation due to  $K_1$  tide dominates the dissipation due to  $M_2$  tide, since the overall rate of energy dissipation due to  $M_2$  wave is only  $49.2 \times 10^9 \text{ W}$ .

## 6. Tidal power from bays of high tidal energy

Consider a bay with a large tidal range (Fig. 14) connected through a relatively narrow entrance to the open ocean. Here we would like to investigate various methods of tapping the tidal energy and possible consequences of a closure placed across the entrance to the bay. Generally, construction placed across the entrance may be directed either to tapping potential energy and utilizing the power through the difference of the sea level generated by the dam; or a number of generators can be placed to tap kinetic energy. Computations related to tidal power extraction need to estimate the effects of construction placed in the entrance on the tides in the bay. Usually, bays with large tides, like Cook Inlet in the Gulf of Alaska, Bay of Fundy on the Atlantic coast of North America or White Sea in Northern Russia depict amplification of the tide from the mouth to the head of the bay. Such tidal patterns may be attributed either to the gradual shallowing and narrowing of bays or resonance conditions, when own period of oscillations of the bay has the period close to the tidal period. Any construction in the upper reaches of such a bay may result in a change of the tidal pattern which either tunes the bay closer to resonance, and therefore results in larger tidal ranges, or it can tune the bay away from resonance, causing smaller tidal ranges (**Garrett, 1984**). For the Bay of Fundy the estimate is that the bay is a little too long for full resonance; similarly the estimates for Cook Inlet suggest that the inlet is somewhat too long for resonance. Blocking off part of the bays may bring a different tidal regime: both in the Bay of Fundy and in the Cook Inlet a higher tide range will occur, since further shortening of the bays may tune it closer to full resonance. Complete blocking of the upper end of the Minas Basin in the Bay of Fundy (see Fig. 5) made in a numerical model by **Greenberg (1979)** does not generate such a clear picture as one would expect from the simple resonance consideration. A drop in the sea level occurs close to the barrier, but the sea level increased in the rest of the Bay of Fundy. To offset such a tidal range reduction, usually a larger number of generating units is installed at a tidal power station. This, in turn, will lead to further sea level reduction due to partial blocking of the flow by the turbines.

The environmental changes induced by a dam or barrage result in changing patterns of tidal currents as well. Cook Inlet is known for large and variable deposits of sediments, as tidal currents often are in the range of a few knots. A barrage may introduce even stronger currents leading to the complete scouring of sediments in some locations and the redeposition of them in other locations. It is important to use sediment transport models that will simulate the influence of the construction on the net sediment transport; the shipping channels cannot become areas of deposit and the sand cannot be removed from the beaches. The study of the sedimentation patterns in the Bay of Fundy and Minas Basin by **Pelletier and McMullen (1972)** showed that sedimentary regime in the Minas Basin is in equilibrium. If a tidal regime were to be changed by a dam, the delicate equilibrium

would be destroyed, leading to large deposits in some locations. Therefore, in choosing a construction site and a method of extraction of tidal power, a balance must be achieved between cost of construction, environmental changes and quantity of generated energy. The latter is quite easy to evaluate, based on the simple computation we have made above. Environmental consequences can be deduced with the help of numerical models (see [Kantha and Clayson, 2000](#)).

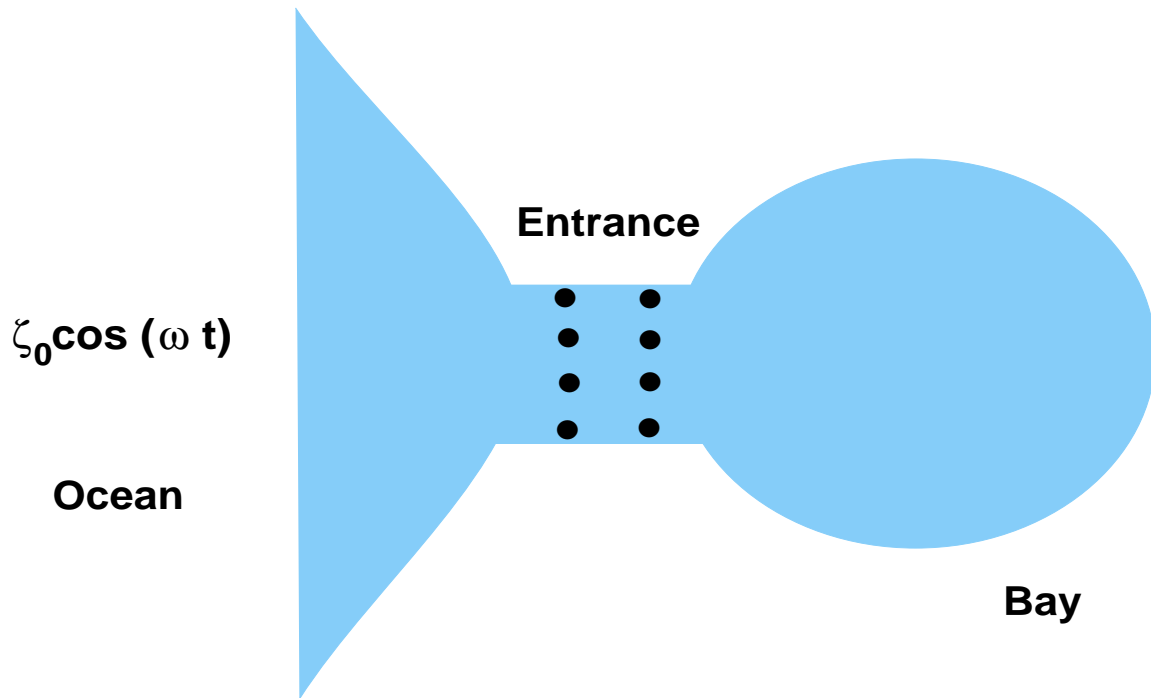


**Figure 14.** Schematic representation of a TPP and hydrodynamical modeling in a bay with a large tidal range. In the ocean the tide is prescribed as  $\zeta_0 \cos(\omega t)$ , dots depict tidal barrage or tidal current generators.

Since the introduction of a dam or turbines into the tidal flow will introduce a resistance into this flow, we can assume that the current and sea level will become smaller far from the construction. Close to dams the currents are very strong and turbines create a lot of turbulence. There is potential for the multiple passage of fish through the turbines and sustaining strong damage. In the region of strong currents, the methods ought to be defined for impact predictions on fish and marine life and measures should be implemented to avoid the area of strong currents and turbulence. On other hand, the smaller currents away from a dam will influence a flushing rate of the bay, which in turn may influence a pollution rate.

Thermal conditions in the bay may change as well. These conditions often change due to mechanical mixing. Sluggish currents in the bay will cause less mixing which may result in more extreme seasonal temperatures. Thus, the consequences of tidal power structures are many and often difficult to predict. The basic prediction may be supported by equations of motion and continuity described in [Kowalik and Murty, 1993](#). Three subdomains shown in Fig. 14 are components of hydrodynamical-numerical model for predicting elevations and currents. All subdomains ought to be connected by the boundary

conditions. Starting from the open ocean the time-variations of sea level at the open boundary can be prescribed from observations or larger scale models (in Fig. 14 it is given as  $\zeta_0 \cos(\omega t)$ ). Next through numerical solutions, the sea level and velocity can be calculated in the entrance to the bay. Before this calculation can be tackled, the flow rate through a dam, barrage or turbines must be given. The flow through turbines ought to be connected with the inner subdomain represented by the bay. Such an approach will allow the evaluation of currents and sea level distribution, before and after a construction is placed across the entrance to the bay. More sophisticated equations, taking into account the sediment motion and heat transport, will answer more complicated environmental questions.

## 7. Tidal power from the sea level difference

Generation of power from tides is not very different from hydro power generation using river flow. The main requirement is the difference in the water level to drive turbines. There are many schemes of tidal power generation; the simplest one is presented in Fig. 15. The single basin (bay) is cut from the open ocean by dykes (barrages). The dyke incorporates sluice gates and a power house which includes turbines. The barrages create the water head necessary for turbine operation. The power house includes turbines connected with electric generators. The sluices will control the water flow for power generation, navigation and sometimes for fish migration. In the so-called one-way (single-effect) generation, the incoming tide enters the bay through the sluice gates and turbines and on the ebb tide the water exits through turbines. To keep the maximum level inside the bay the sluice gates are locked and power generation is achieved during ebb tide ([Gibrat, 1966](#); [Bernshtein, 1996](#)).

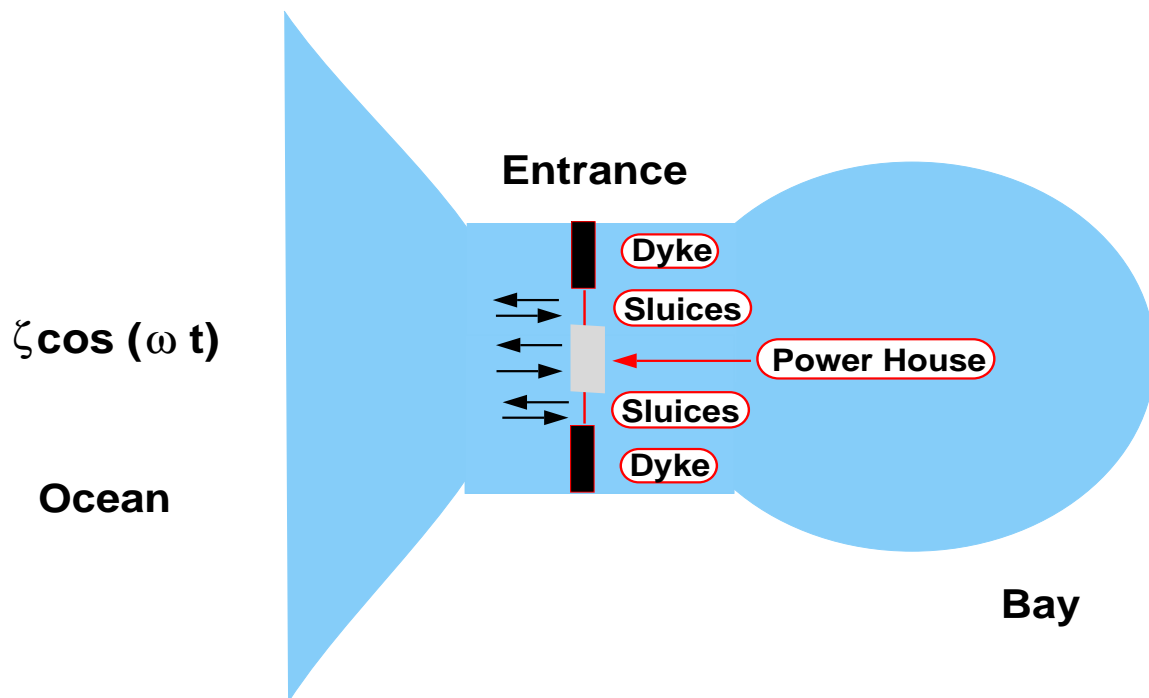


Figure 15. Tidal power plant constructed at the entrance to a single bay.

To start power generation, a minimum sea level difference (minimum head) between ocean tides and basin tides is required (Fig. 16). To generate the minimum head of economical value for power production a tidal range of the 4 to 6 m is needed. Typical sea level variations at the outside and inside of the basin are shown for the semidiurnal tide in Fig. 16, upper panel. The presence of sluices and turbines limits the flow of water between the bay and the ocean. This results in the reduced range of the sea level change inside the bay as compared to the sea level before the TPP construction. The time span when sufficient sea level differences exist for power generation is limited by the minimum head required. The power generation time is also limited by the time needed for the basin to be filled on the rising tide. For the minimum head assumed in the Fig. 16 the generation time (from  $T_1$  to  $T_2$ ) equals approximately 5.5 hours. During each generation cycle, as can be seen in the lower panel of Fig. 16, the generators do not deliver constant power in time. The power output slowly increases with the increasing of the head up to a level when constant power is achieved. Often, due to the high available head the turbine output needs to be cut back to avoid overloading.

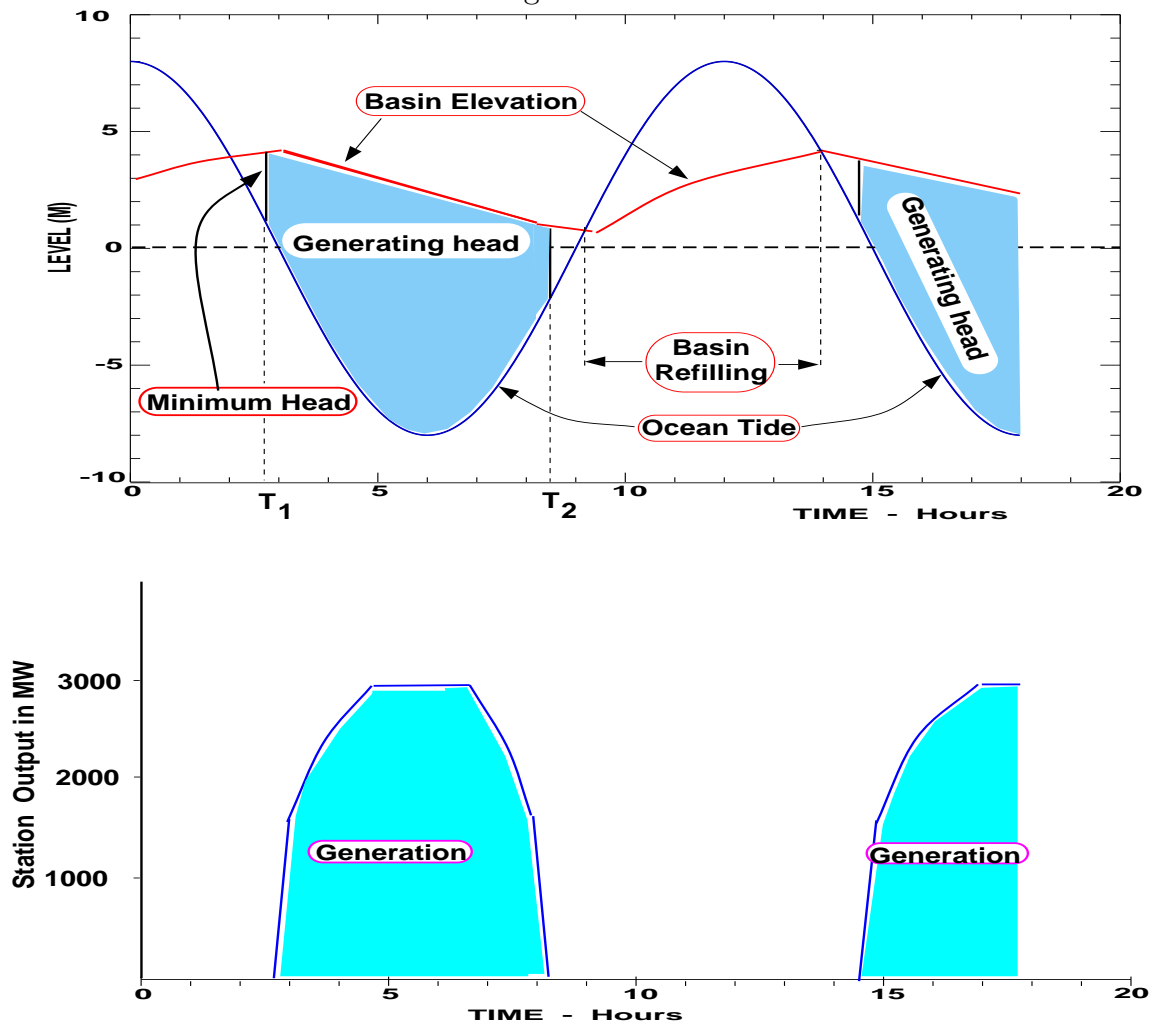
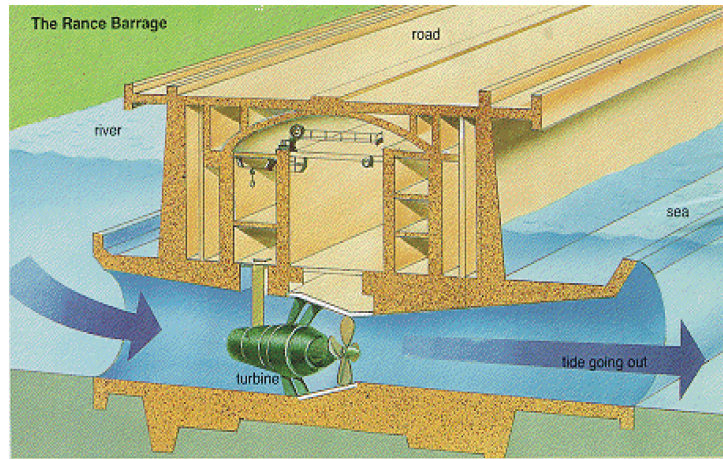


Figure 16. Tidal power generation: typical one-way cycle for a single bay. Upper panel, sea level inside and outside of bay. Lower panel, power output in time.



**Figure 17. La Rance tidal power station. Courtesy Electricite de France.**

The general picture from the above scheme is that the available power is highly variable in time, which points toward development of various schemes of economical and controllable utilizations of the tidal power.

Such schemes have been achieved mainly through the investigations of French scientists and engineers and implemented to the 240 MW TPP at La Rance, Brittany, France, constructed in 1967 (**Gibrat, 1966**). The La Rance estuary with a width of about 750 m, was an ideal site considering a  $18,000 \text{ m}^3/\text{s}$  flow at the flood tide. The estuary (behind the dam in Fig. 17) is capable of containing about 180 million  $\text{m}^3$  of water with the basin area  $22 \text{ km}^2$ . The estuary was blocked by a 13 m high dam. This dam (Fig. 17) also serves as a highway bridge between St. Malo and Dinard. The power station operates in a one-way mode, demonstrated in Fig. 17, although two-way operation (both on ebbing and flooding tides) is possible. In two-way operation the turbine in Fig. 17 changes direction to follow the ebb/flood cycle. 240MW is probably the maximum output (which cannot be sustained all the time), even if an average is only 50% of the maximum, La Rance delivers per year  $120 \times 10^3 \text{ kW} \times 8760 \text{ h} = 1.05 \times 10^9 \text{ kWh}$ . To estimate the number of homes that this quantity of electricity will provide for in a year, the average household consumption is assumed to be about 4500 kWh/year. Thus La Rance tidal power station supplies about 222 thousand households.

The French investigations served well in developing a TPP at the Kislaya Guba in the Barents Sea on the Kola Peninsula, Russia in 1968, with installed power of 0.4 MW and a small artificial basin of area  $1.1 \text{ km}^2$ . An 18 MW plant was built in 1984, at Annapolis Royal (entrance to the Annapolis river in the Bay of Fundy), Nova Scotia, Canada. The area of the basin behind the barrage is only  $15 \text{ km}^2$ . China constructed, in 1985, a small plant at Jiangxia with 4MW output and a small basin area of  $1.4 \text{ km}^2$ .

New tidal power plants are being considered, including the Severn project in England and in Garolim Bay, Korea.

A more efficient use of sea level difference is to generate power on both the rising and falling tides (**Gibrat, 1966; Bernshtein, 1996**). This is called a single-basin two-way generation. Previously, the power was generated on the falling (ebb) tide only when the minimum head required for power generation occurred at time  $T_1$  and lasted till the time  $T_2$  (cf, Fig. 16). In the new regime, at the time  $T_2$  the turbines are stopped, rotated

the opposite direction and restarted again at the time  $T_3$ , when the minimum sea level difference on the rising (flood) tide will occur.

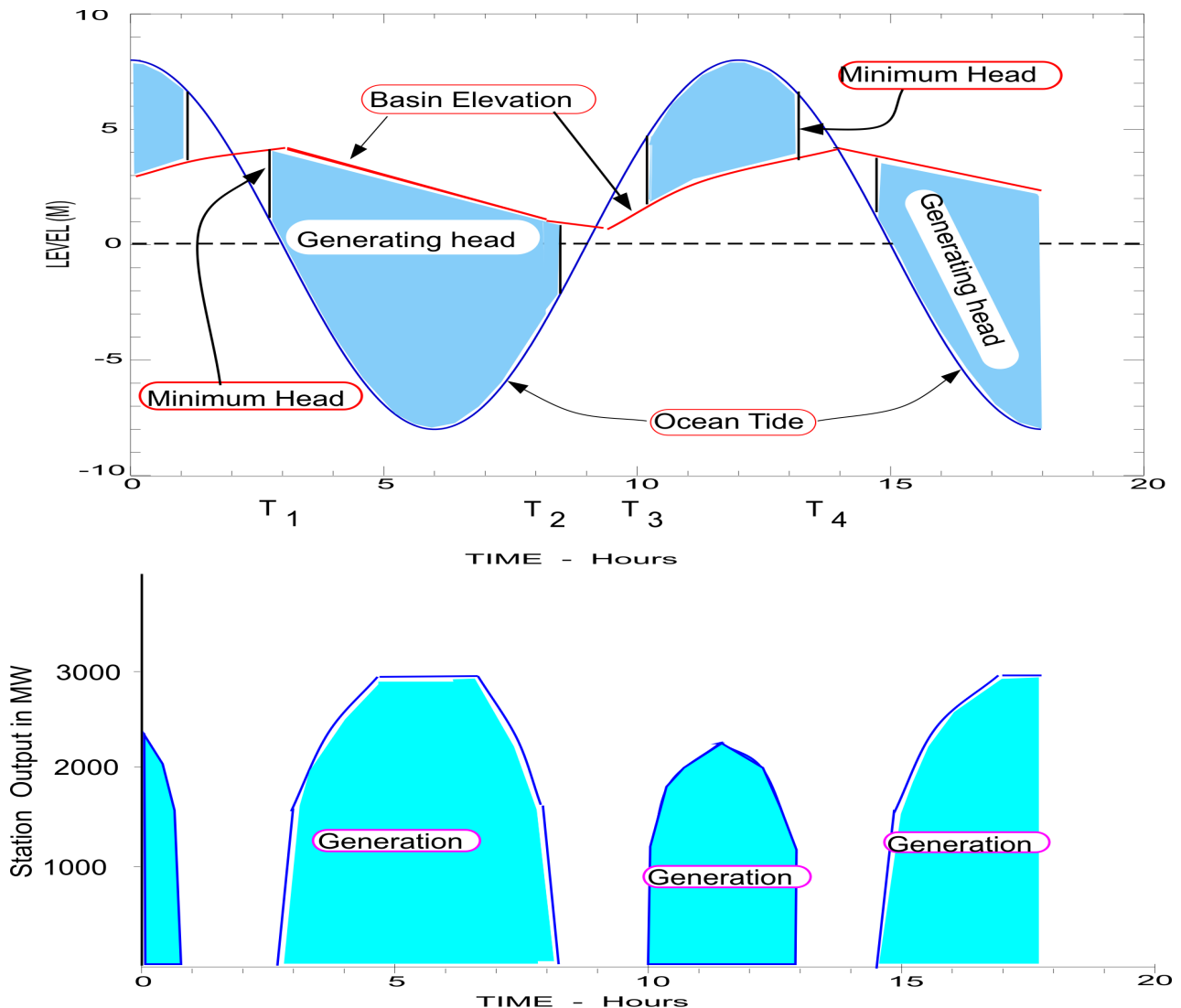


**Figure 18.** A typical two-way cycle for the single bay. Upper panel, sea level inside and outside of bay. Lower panel, power output in time.

This regime will last until time  $T_4$  when the turbines will be stopped and rotated. From Fig. 18 it can be deduced that the TPP working in the two-way regime delivers power during 8.5h, compared to the one-way generation time of 5.5h.

The efficiency of the TPP can be improved in many ways: the use of pumping is very popular method which increases the sea level inside the basin and, therefore, gives better power output. In connection with the utilization of tidal power in the Bay of Fundy, many utilization schemes were suggested, because of the proximity of two bays with high tides. The paired-basin schemes open the possibility of continuous power generation, [Lawton \(1972\)](#).

A simple theory for designing a TPP has been described by [Gibrat \(1966\)](#), [Prandle \(1984\)](#) and [Godin \(1988\)](#). This theory connects generated power to the sea level changes

in the basin and discharge through the dam. The water level inside the basin will be denoted as  $Z(t)$  and the sea level in the ocean as  $\zeta = \zeta_0 \cos \omega t$ . The sea level difference or head ( $H_d$ ) is given by

$$H_d(t) = Z(t) - \zeta_0 \cos \omega t \quad (\text{IV.19})$$

Denoting discharge through the turbines during the power generation phase as  $Q$  and assuming it is constant in time, we can write equation of continuity in the following form,

$$S \frac{\partial Z}{\partial t} = -Q \quad (\text{IV.20})$$

Here,  $S$  is the surface of the basin,  $\frac{\partial Z}{\partial t}$  is the vertical velocity of the free surface. The positive direction of discharge is from the basin to the ocean. An additional assumption is that the surface area of the basin, while moving up or down, does not change in time. Neglecting losses, the principal parameter for the tidal plant evaluation, the power produced (PW) is given as

$$PW = \rho g H_d Q \quad (\text{IV.21})$$

Thereby, the energy extracted during one tidal period (see Fig. 16) is

$$E = \rho g \int_{T_1}^{T_2} H_d Q dt \quad (\text{IV.22})$$

Introducing definition for the head given by eq.(IV.19) and assuming that the discharge is constant

$$\begin{aligned} E &= \rho g Q \int_{T_1}^{T_2} H_d dt = \rho g \int_{T_1}^{T_2} (QZ(t) - Q\zeta_0 \cos \omega t) dt = \\ &\rho g \int_{T_1}^{T_2} (QZ(t) - Q\zeta_0 \cos \omega t) dt = \rho g \int_{T_1}^{T_2} \left( -S \frac{\partial Z}{\partial t} Z(t) - Q\zeta_0 \cos \omega t \right) dt = \\ &\rho g \left[ -S \int_{Z_1}^{Z_2} Z dZ - Q\zeta_0 \int_{T_1}^{T_2} \cos \omega t \right] = \\ &-\rho g S \left[ \frac{Z_2^2 - Z_1^2}{2} - \left( \frac{Z_2 - Z_1}{T_2 - T_1} \right) \frac{\zeta_0}{\omega} (\sin \omega T_2 - \sin \omega T_1) \right] \end{aligned} \quad (\text{IV.23})$$

where  $Z_1$  and  $Z_2$  are sea level in the bay at times  $T_1$  and  $T_2$ . Thus, the energy is extracted through the complicated interaction of the levels inside and outside of the bay. When the question about the possibility of tidal energy tapping from a semi-enclosed bay was asked, we used for the evaluation of this energy the expression for the potential energy (IV.10). This expression obviously gave the maximum available energy. The total available energy is present in the above expression; this is the term related to  $(Z_2^2 - Z_1^2)$ . Portion of the total available energy is fluxed back to the ocean by the last term in (IV.23). The relation of this term to the energy flux given by eq.(IV.12) is easily established since the discharge  $Q$  is actually the horizontal velocity integrated over the cross section of a channel.

Eq.(IV.23) defines extracted energy during the ebbing cycle in Fig. 16. The basin refilling regime, when the sluice gates are open, is given by the following discharge

$$Q = \epsilon G \sqrt{2gH_d} \quad (\text{IV.24})$$

Where,  $G$  is sluice gate area,  $\epsilon$  is a flow contraction coefficient depending on the shape of the structure.  $G_\epsilon = \epsilon G$ , here  $G_\epsilon$  is an effective gate area. Introducing this discharge into (IV.20) and taking into account the equation for the head

$$S \frac{\partial Z}{\partial t} = -G_\epsilon \sqrt{2g(Z - \zeta_0 \cos \omega t)} \quad (\text{IV.25})$$

From the above we can conclude that the effective sluice gate area is a function of the square root of the head during sluicing time, while the power produced by the turbine is proportional to the head value. This exemplifies the difference between the sluicing and the generating phases of the process. The large tidal waves (large heads) increase efficiency of the tidal power generating. On the other hand, using a large basin with a large surface will increase the extracted energy, but it also increases the losses for the sluice gate operation. Gates are required to open and close during each tidal cycle, which can bring as many as 700 operations per year, while in the regular hydro-power station the gates will be open a few times per year. With both gains and losses of energy variable in time, optimization methods were applied to obtain maximum energy yield from the tidal power plants (see, [Gibrat, 1966](#) and [Bernshtein, 1996](#)).

## 8. Tidal power from currents

**8.1 The future of tidal power.** The older approach to power generation was to block the entrance to the bay with a dam and use the difference of the sea level in front and behind the dam to move the turbines. The cost of building dams and tidal generating stations is often prohibitive. The estimated cost of the proposed tidal station on the Severn River in England would be in the range of \$15 billion. The recent approach is to place turbines (tidal flow generators), devices similar to wind-mills, into the tidal current. The construction, operating and maintenance costs of such tidal flow generators is much lower compared to barrages. Additionally, environmental changes introduced by turbines are much smaller than the changes caused by damming of the entire bay entrance. The propeller of the tidal flow generator is quite slow, with 4 to 6 rotations per minute. Since the power generated from the flow is a function of the fluid density, the propellers constructed for the water do not need to be as large as in the air. The new types of water turbine with the helical shape has been patented by [Gorlov \(2001\)](#). This turbine captures 35 percent of the water's energy (<http://www.gcktechnology.com/GCK/pg2.html>). A few tidal power plants already use the tidal power from currents. A TPP with the helical turbines has been tested at the Uldolmok Strait, Korea, where the speed of tidal currents reaches  $6 \text{ m s}^{-1}$ . New York Power Authority and Columbia University are deploying a demonstration turbine system in the East River in New York City. This system also will be used for field testing and design prototyping. In tidal currents of up to 7.5 knots, the generator with 10-foot diameter blades, will be capable of generating up to 25

kW (<http://www.verdantpower.com/Initiatives/eastriver.shtml>). In 2002, the Norwegian company Hammerfest Stroem deployed tidal flow generators in northern Norway close to the small town Hammerfest. The 300kW turbines are located at the bottom of a narrow strait, well below the surface, so that safe shipping can take place. The blades of the propellers can rotate to adjust for the tidal current direction (Stone, 2003). Future TPP construction and exploitation will depend on the existence of a large-current location in close proximity to local users.

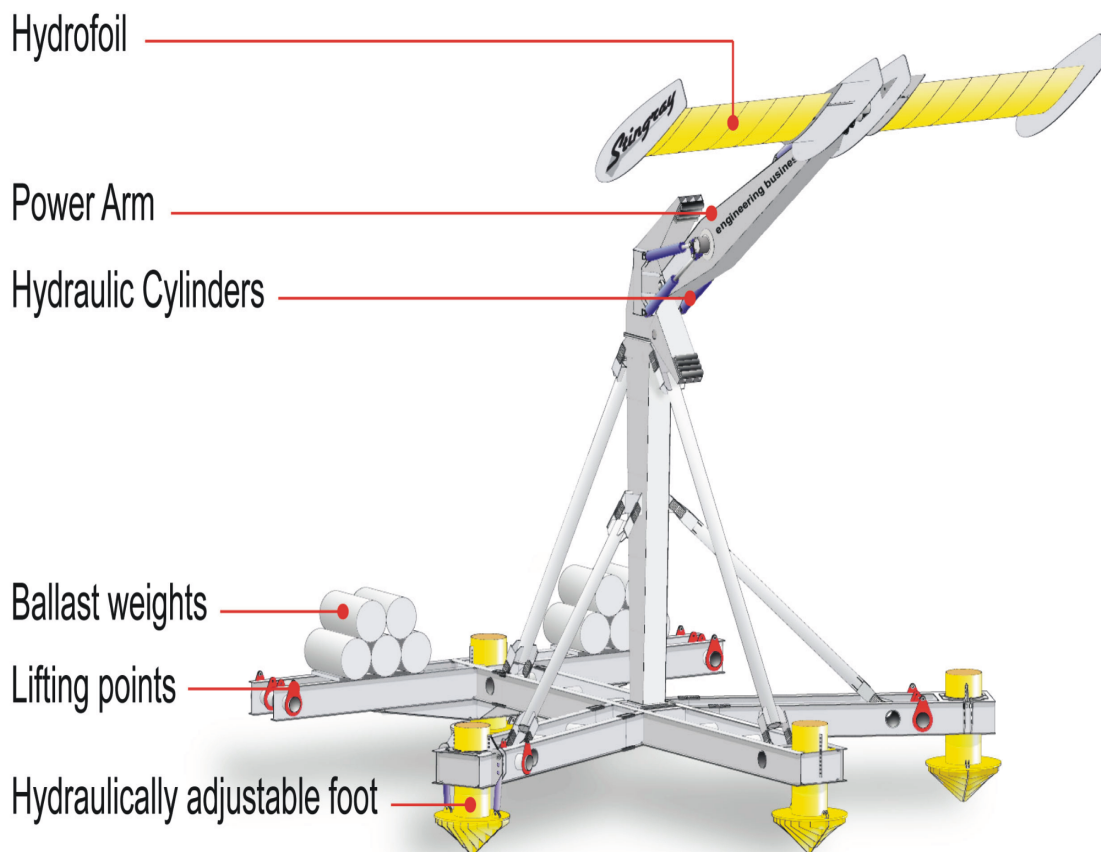


**Figure 19. Stingray tidal current generator. Courtesy, The Engineering Business Limited ([www.engb.com](http://www.engb.com)).**

Tidal power plants have the potential to provide large amounts of energy. The European Commission estimated that 42 sites of large tidal currents around the UK could produce 48-terrawatt hours of electricity per year. The Commission has identified large tidal-current at 106 sites around Europe.

One of the most interesting tidal flow generators and the one that is stimulating tidal

power development is the Stingray constructed by the Engineering Business (Northumberland, UK). Let's carefully analyze the many facets involved in the construction, testing and operating such generators. The kinetic energy of tides is changed into electricity by a hydraulic generator system. The key feature of this machine is a large horizontal hydrofoil which through the pitch control (angle of attack) can oscillate up and down (Fig. 19). This motion forces a support arm to oscillate up and down as well. The arm is restrained by hydraulic cylinders, which produce high-pressure oil that drives a hydraulic motor and then hydraulic pressure rotates the generator. The generator output feeds an industrial drive system giving a dc output. In a Stingray farm, the output from a number of devices feed a dc bus which typically connects through a submarine cable to land, where an inverter produces ac power for users. The initial planning (**Trapp and Watchorn, 2001**) was to develop a machine of a 150kW time-averaged output in a 2m/s current. Stingray had to be designed so that the whole assembly could be installed and recovered easily at low cost, and as often as required. Since hydroplane design and control was very important in achieving high power output from Stingray, the EB performed the extensive dynamic modeling of the hydroplane and arm movement. The second stage was preliminary testing of the constructed machine, as well as the launch and recovery system, which can set a 180 tonn on the seabed in 36 m water depth in a high current location in Yell Sound in Shetland (**Trapp, 2002**).

While developing and testing Stingray, EB is also trying to estimate the likely cost of the future tidal farm. The costs involved in the 2002 Stingray program allow them to predict the costs for a 5MW tidal farm. The value of the power produced by such a farm will be slightly higher than the power delivered by other sources, as technology of tidal power is developed and refined the cost of power will be greatly reduced.

## 8.2 Power generation from currents.

A simple theory constructed by **Garret and Cummins (2004)** emphasized that the power generation by current cannot occur without generation of a pressure difference across the turbines, similar to the sea level difference across the water dam. To investigate the power potential of turbines moored across an entrance to the bay, let's use the Bernoulli's theorem which states that in the steady flow of the ideal fluid, the combination of pressure, velocity and gravity force is constant along the given stream-line (cf, **Kundu, 1990**),

$$p/\rho + \frac{u^2 + v^2}{2} + gz = Const \quad (\text{IV.26})$$

The change along the vertical direction  $z$  will be omitted from further considerations.

On the flood-tide when the flow takes place from the ocean into the bay, the pressure in the entrance in front of turbines is  $p_0$  and the upstream velocity is  $u_0$ . Assuming that pressure and velocity along the stream-line, which just passed the row of turbines is  $p_1$  and  $u_1$  (Fig. 20), we can write for the pressure difference across the turbine

$$dp = p_1 - p_0 = \frac{1}{2}\rho(u_0^2 - u_1^2) \quad (\text{IV.27})$$

According to (IV.9) the power generated by this pressure head (per unit area of the turbine) is equal to

$$P = dp u_1 = \frac{1}{2}\rho u_1(u_0^2 - u_1^2) \quad (\text{IV.28})$$

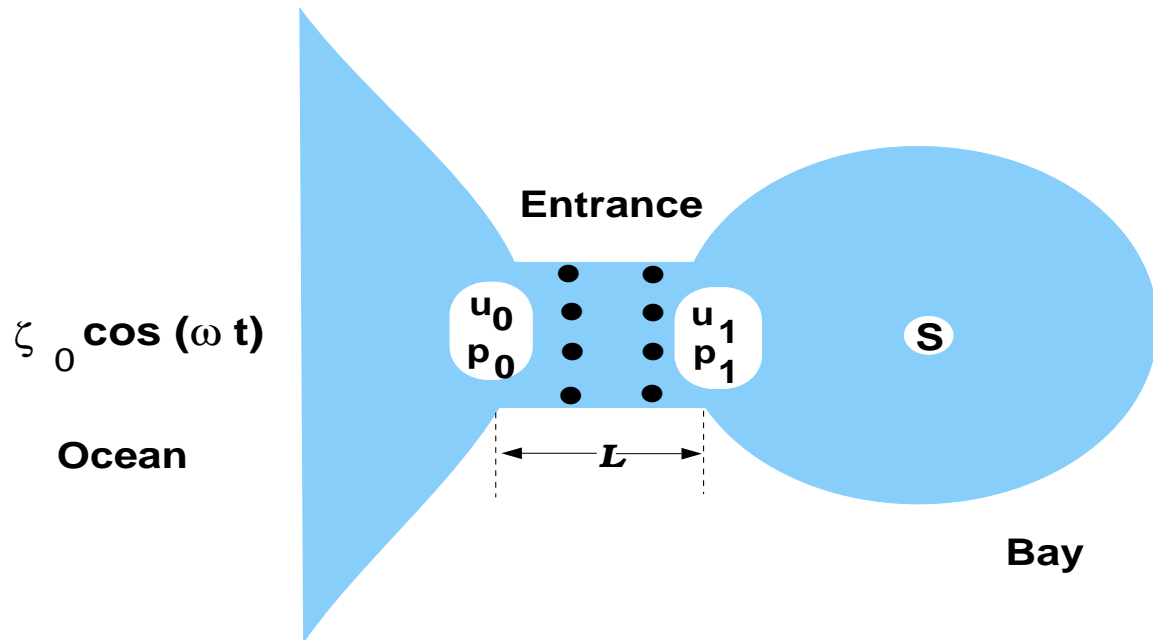


Figure 20. Schematic representation of tidal power construction and hydrodynamical modeling in the bay. At the ocean side the tide is prescribed as  $\zeta_0 \cos(\omega t)$ , dots depict the tidal current generators located in the entrance to the bay.

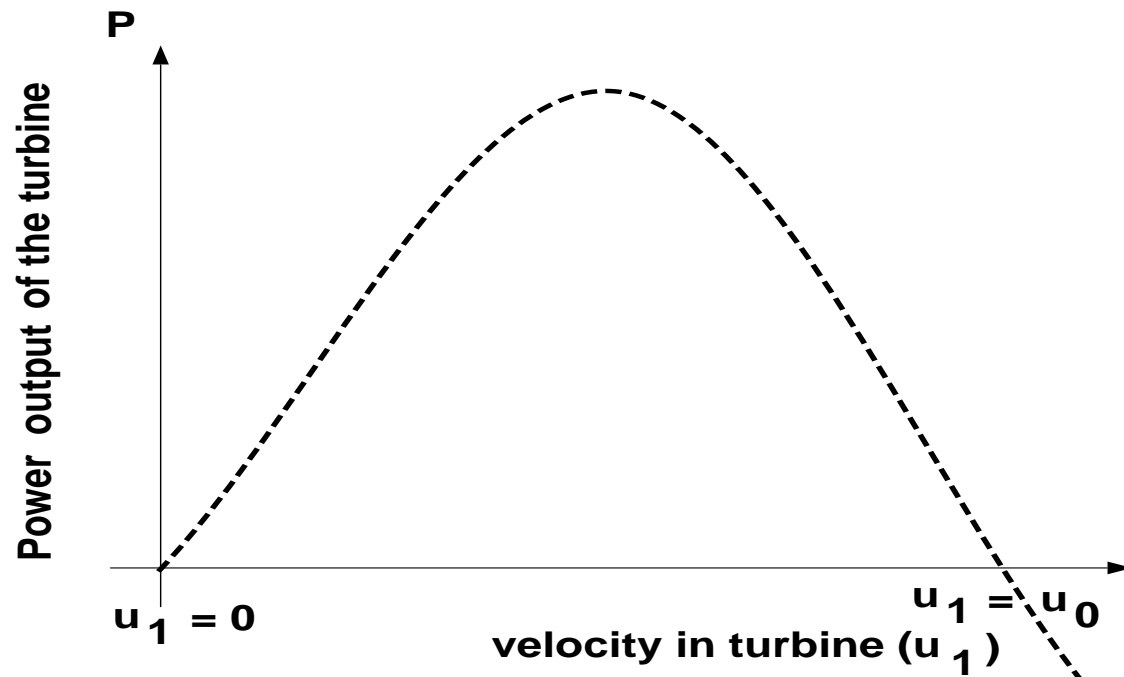


Figure 21. Power generated by the turbine as the function of flow velocity ( $u_1$ ) in the turbine.

The turbine stops to generate power when velocity diminishes to zero ( $u_1 = 0$ ), and also when the downstream velocity  $u_1$  is greater than the upstream velocity  $u_0$ . The behavior of the generated power as the function of velocity  $u_1$  clearly illustrates Fig. 21. The power achieves maximum at the point where derivative  $\frac{\partial P}{\partial u_1} = 0$

$$\frac{\partial P}{\partial u_1} = \frac{1}{2}\rho(u_0^2 - u_1^2 - 2u_1^2) = 0 \quad (\text{IV.29})$$

or when the flow through the turbine ( $u_1$ ) and in the front of the turbine ( $u_0$ ) are related as  $u_1 = \frac{u_0}{\sqrt{3}}$ . The maximum power available at this velocity is

$$P_{max} = \frac{1}{2}\rho\frac{u_0}{\sqrt{3}}(u_0^2 - \frac{u_0^2}{3}) \simeq 0.2\rho u_0^3 \quad (\text{IV.30})$$

This is the upper limit of the power generated per unit (cross-sectional) area of the turbine and it is expressed through the readily available upstream velocity of a free flow ( $u_0$ ) in front of the turbine. It is interesting to notice that up to this point we did not mention what kind of fluid is flowing through the turbines. It can be air or water, the difference is in the density.

Since the water/air density ratio is equal to approximately 900, the water velocity can be quite small compared to the air velocity, to achieve the same power.

The dissipated tidal power, defined as the time rate at which work is done by the bottom friction forces (see IV.18), is proportional to the  $u^3$ , as we can glean from the above formula the available power for electricity generation is proportional to velocity cubed as well. Because of this similarity the exploitation of tidal energy should be directed to reinvesting the dissipated power into the tidal power. Henceforth, the generation of electricity by kinetic energy tapping may be better tuned to the natural dissipation and towards preservation of the natural tidal regime. Unfortunately, the dissipated power is distributed rather smoothly in space while the tidal energy ought to be tapped in small domains to be economically viable.

Tidal power tapping by generators moored at the bay entrance leads to a decrease in the flow. Adding more turbines will lead to even stronger change of the tidal pattern. To answer basic questions related to interactions of the flow and turbines a simple theory was constructed by **Garret and Cummins (2004)**. A schematic representation of TPP is given in Fig. 20.

Tidal wave elevation in the open ocean is  $\zeta_0 \cos(\omega t)$ . The local balance of the forces in the entrance includes the pressure due to the sea slope and the resistance force ( $F$ ) due to turbines

$$g(Z - \zeta_0 \cos \omega t)/L = -F \quad (\text{IV.31})$$

Here  $L$  denotes the length of the entrance, where the turbines are moored. The resistance force is assumed to be a linear function of velocity  $F = ru$ , and  $r$  is resistance coefficient.

The change of the sea level in the bay is assumed to be uniform over the entire bay, therefore the continuity equation can be written as (cf, eq. IV.20)

$$S\frac{\partial Z}{\partial t} = Eu \quad (\text{IV.32})$$

Here  $E$  is a cross-sectional area of the entrance and  $S$  is the surface area of the bay. Combining (IV.31) and (IV.32), an equation for sea level in the bay follows,

$$\frac{\partial Z}{\partial t} + \frac{Eg}{rSL}(Z - \zeta_0 \cos \omega t) = 0 \quad (\text{IV.33})$$

Introducing a new variable  $q = Eg/(rSL)$ , the above equation is rewritten as

$$\frac{\partial Z}{\partial t} + qZ - q\zeta_0 \cos \omega t = 0 \quad (\text{IV.34})$$

$q$  denotes the frequency of the natural (own) oscillations in the bay/entrance system. The solution to this nonhomogenous ordinary differential equation can be searched in the form

$$Z = C_1 \sin \omega t + C_2 \cos \omega t \quad (\text{IV.35})$$

Introducing (IV.35) into (IV.34) and comparing coefficients at the sin and cos functions, the following expressions are derived for the coefficients,

$$C_1 = \frac{q\omega\zeta_0}{\omega^2 + q^2}; \quad C_2 = \frac{q^2\zeta_0}{\omega^2 + q^2} \quad (\text{IV.36})$$

Analytical expression (IV.35) allows us to answer the basic question, namely what will be the sea level change in the bay induced by the turbines located in the entrance. To simplify this solution two cases can be considered: a)  $\omega \gg q$ , and b)  $q \gg \omega$ . Thus, the first case assumes that the period of the tide is much shorter than the period of the natural oscillations in the bay/entrance system. Actually, the second case is more realistic since usually the tidal period is longer than the local period of oscillations. In the second case, the coefficient  $C_2 \gg C_1$  and solution for the sea level simplifies to

$$Z \simeq \zeta_0 \cos \omega t \quad (\text{IV.37})$$

Eq. (IV.37) states an intuitive result, that when tidal period is much longer than the own period, the sea level oscillations inside the bay are repeating the tidal oscillations in the open ocean. If such a solution can be achieved through a construction of the tidal power generators in the entrance, this will be an important result suggesting that while tidal power is tapped the tides could be maintained close to the natural regime.

Frequency  $q$  can be represented as

$$q = Eg/(rSL) = \omega_H^2/r \quad (\text{IV.38})$$

where  $\omega_H^2$  is the square of the frequency of natural oscillations of the bay. It is called Helmholtz frequency (**Kowalik and Murty, 1993, 384p**). The assumption that  $q \gg \omega$  can be rewritten as

$$\omega_H^2/r \gg \omega \quad \Rightarrow \quad \frac{\omega_H^2}{\omega^2} \gg \frac{r}{\omega} \quad (\text{IV.39})$$

The requirement that  $\omega_H^2/r \gg \omega$  is equivalent to relations between the period of the natural oscillations and the tidal period. The natural oscillations occur for the joint system of the bay/entrance. The role of the bay natural oscillations can be investigated through the Helmholtz frequency. It is important to see that the simplified solution derived above is valid only when  $q \gg \omega$  is fulfilled. In general, the full solution given by (IV.35) and (IV.36) should be investigated.

The power gained by the turbines is defined by the time rate at which work is done by the resistance forces averaged over the tidal cycle:

$$P = \rho EL \int_0^T F u dt \quad (\text{IV.40})$$

Here  $F = ru$ , and from (IV.32)  $u$  can be calculated as

$$u = \frac{S}{E} \frac{\partial Z}{\partial t} \quad (\text{IV.41})$$

Introducing from (IV.35) the sea level  $Z = C_1 \sin \omega t + C_2 \cos \omega t$ , the above velocity is

$$u = \frac{S}{E} (C_1 \omega \sin \omega t - C_2 \omega \cos \omega t) \quad (\text{IV.42})$$

and the following result is obtained for the power,

$$P = \rho EL \left(\frac{S}{E}\right)^2 r \omega \frac{T}{2} (C_1^2 + C_2^2) \quad (\text{IV.43})$$

The simplified case considered above ( $C_2 \gg C_1$ ) defines  $C_2 \simeq \zeta_0 \cos(\omega t)$ ; therefore the power gained by the turbines is proportional to  $\zeta_0^2$  - square of amplitude of the tidal wave in the open ocean.

## 9. Conclusion

Assuming that the total energy produced by work of the Moon and Sun in the amount of 4 TW is dissipated in the World Ocean, the question is, how much of this energy can be tapped for the electricity generation. Currently, the world production of electricity is in the range 1.5-2 TW. Therefore, at first glance, the available tidal energy seems to be very large. This great amount of energy is distributed over the vast geographical domain. The power available for tapping is probably in the range of 1% to 2% of the total amount, i.e., about 0.04 to 0.08 TW.

In this chapter, we presented various aspects of the tidal power generation. We have considered the tapping into the potential and kinetic energy of the tides and the changes such tapping will introduce in the tidal regime of a small water body connected to the ocean. Tide in the open ocean was "given" as a boundary condition. We can extend this problem and ask what will happen to the tidal regime in the open ocean when the local potential and kinetic energy start to change. This is not easy question to answer since we are dealing with the small (initial) changes in the vast tidal system. While the

tidal energy tapping will proceed ahead, it is important to develop a new branch of tidal dynamics which will help to better understand the interaction between the natural tidal regime and the future changes to be introduced by tapping the tidal power. Especially, it is important to construct tools for evaluation the effect of local changes on the global tidal regime. After all, the tidal machine has not only practical application for delivering the tidal power, some of the 4 TW dissipated in the Oceans has relevance for the present and future climate of the earth (Munk and Wunsch, 1998).

10. The last page from Gibrat's *L'énergie des mares*

## POSTFACE

### La mer et l'énergie des marées

Pendant vingt-cinq années ce fut le dialogue avec la mer : Amie, elle apportait avec les marées l'énergie dont l'homme avait besoin et facilitait les travaux de génie civil par son rythme de marées hautes et basses, de vives eaux et de mortes eaux, permettant de prévoir, donc de ruser avec sa puissance ; ennemie, elle menaçait de disloquer les batardeaux par la tempête, de détruire les machines par la corrosion de l'eau de mer ou l'érosion des sables, d'abaisser les rendements par des dépôts ou de gêner l'exploitation par l'envasement, etc.

Elle ne s'est laissé conquérir, comme il convient, que lentement et a joué quelques tours ; mais pour l'amoureux de l'énergie des marées, la mer a été et restera guide, maître et seigneur.

*Tu duca, tu signore e tu maestro*

écrivait déjà Dante (*Enfers*, II, 140).

R. GIBRAT

211

14\*

## 11. Acknowledgements

I would like to express my deep gratitude to all who helped in my task by offering data, figures and valuable knowledge on tides. I am grateful to: J. Luick, Bill Mitchell and G. Musiela, National Tidal Facility, Adelaide, Australia; R. Flather, Proudman Oceanographic Laboratory, United Kingdom; E. Palma, Universidad Nacional del Sur, Baha

Blanca, Argentina; E. D'Onofrio Departamento Oceanografia, Servicio de Hidrografia Naval, Argentina; A. V. Nekrasov Hydrometeorological University, St. Petersburg, Russia; C. Garrett, University of Victoria, Victoria, Canada; F. Henry and M. Foreman, Institute of Ocean Science, Sidney, Canada; H. Mofjeld, PMEL, Seattle and A. Proshutinsky, WHOI.

## References

- Bernshtein L. B., 1961, *Tidal Energy for Electric Power Plants*, Israel Program for Scientific Translations, Jerusalem, 378 pp.
- Bernshtein L. B., 1996, *Tidal Power Plants*, Korea Ocean Res. and Development Institute, Seoul, 444 pp.
- Cartwright D. E., 1969, *Extraordinary tidal currents near St. Kilda*, Nature, 223, 928–932.
- Defant A., 1960, *Physical Oceanography*, Pergamon Press, v 2, 598 pp.
- Egbert, G. D., Ray R.D., 2000, *Significant dissipation of tidal energy in the deep ocean inferred from satellite altimeter data*, Nature, 405, 775–778.
- Flather R. A., 1976, *A tidal model of the north-west European continental shelf*, *Memoires Societe Royale des Sciences de Liege*, 6(10), 141–164.
- Garrett, C., 1984, *Tides and tidal power in the Bay of Fundy*, Endeavour, New Series, v.8, No.2., 160–167.
- Garrett C., Cummins P., 2004, *Generating tidal power from currents*, J. Waterw., Port, Coastal, Ocean Eng., 130(3), 114–118.
- Garrett, C., Greenberg D. A., 1977, *Predicting changes in tidal regime: The open boundary problem*, J. Phys. Oceanogr., 7, 171–181.
- Gibrat R., 1966, *L'energie des marées*, Presses Universitaires de France, Paris, 219 pp.
- Glorioso P. D., Flather R. A., 1997, *The Patagonian Shelf tides*, Prog. Oceanog., 40, 263–283.
- Godin G., 1988, *Tides*, CICESE, Ensenada Baja California, 290 pp.
- Gorlov A. M., 2001, *Tidal energy*, In *Encyclopedia of Ocean Sciences*, Academic Press, London, 2955–2960.
- Greenberg D.A., 1979, *A numerical model investigation of tidal phenomena in the Bay of Fundy and Gulf of Maine*, Marine Geodesy, 2(2), 161–187.
- Henry R. F., Foreman M. G. G., 2001, *A representation of tidal currents based on energy flux*, Marine Geodesy, 24(3), 139–152.
- Holloway P. E., 1987, *Internal hydraulic jumps and solitons at a shelf break region on the Australian North West Shelf*, J. Geophys. Res., C95, 5405–5416.
- Kagan B. A., 1997, *Earth–Moon tidal evolution: model results and observational evidence*, Prog. Oceanog., 40, 109–124.

- Kantha L. H., 1995, *Barotropic tides in the global oceans from a nonlinear tidal model assimilating altimetric tides. 1. Model description and results*, J. Geophys. Res., 100, 25,283–25,308.
- Kantha L. H., Clayson C. A., 2000, *Numerical Models of Oceans and Oceanic Processes*, Academic Press, 940 pp.
- Kowalik Z., Murty T. S., 1993, *Numerical modeling of ocean dynamics*, World Scientific Publ., 481 pp.
- Kowalik, Z., Polyakov I., 1998, *Tides in the Sea of Okhotsk*, J. Phys. Oceanogr., 28(7), 1389–1409.
- Kowalik Z., Proshutinsky A. Yu., 1993, *Diurnal tides in the Arctic Ocean*, J. Geophys. Res., 98, 16449–16468.
- Kundu P., 1990, *Fluid Dynamics*, Academic Press, 638 pp.
- Lawton F. L., 1972. *Economics of tidal power*, In: *Tidal Power*, Gray T. J. and O. K. Gashus, Eds., Plenum Press, 105–130.
- LeBlond P.H., Mysak L.A., 1978, *Waves in the Ocean*, Elsevier, Amsterdam, 602 pp.
- LeProvost C., Genco M. L., Lyard F., 1994, *Spectroscopy of the world ocean tides from a finite element hydrodynamic model*. J. Geoph. Res., 99, 24,777–24,797.
- LeProvost C., Lyard F., 1997, *Energetics of the  $M_2$  barotropic ocean tides: an estimate of bottom friction dissipation from a hydrodynamic model*, Prog. Ocean., 40, 37–52.
- Munk W., 1997, *Once again: once again–tidal friction*, Prog. Oceanog., 40, 7–35.
- Munk W. H., Wunsch C., 1998, *Abysal recipes II: Energetics of tidal and wind mixing*, Deep-Sea Res., 45, 1977–2010.
- Nekrasov A. V., 1990, *Energy of Ocean Tides*, Leningrad, Gidrometeoizdat, 288pp.
- Nekrasov A. V., 1992, *On tidal energy horizontal circulation*, The Journal of the Korean Society of Coastal and Ocean Engineers, 4(3), 168–177.
- NTF, Australia, 2000, *Western Australian Sea Level Variability due to Tides, Weather and Extreme Events*, A report to The Government of Western Australia, Coastal Management Branch, Department of Transport by NTF Australia, 46pp.
- Palma E. D., Matano R. P., and Piola A. R., 2004, *A numerical study of the Southwestern Atlantic Shelf circulation. Part I: The barotropic response to tidal and wind forcing*, J. Geophys. Res., (Oceans), .109, C08014, doi:10.1029/2004JC002315.
- Patchen R. C., Bruce J. T., Connolly M. J., 1981, *Cook Inlet Circulatory Survey: 1973-75*, NOS Oceanographic Circulatory Survey Rep. No. 4, Rockville, Md., 89 pp.
- Pelletier R. R., McMullen R. M., 1972, *Sedimentation patterns in the Bay of Fundy and Minas Basin*, In: *Tidal Power*, Gray T. J. and O. K. Gashus, Eds., Plenum Press, 153–188.
- Pugh D. T., 1987 *Tides, Surges and Mean Sea-Level*, John Wiley & Sons, 472pp.
- Prandle D., 1984, *Simple theory for designing tidal power schemes*, Adv. Water Resources, 7, 12–27.

- Shum C. K., *et al.*, 1997, *Accuracy assessment of recent ocean models*, J. Geoph. Res., 102, 25,173–25,194.
- Stone R., 2003, *Norway goes with the flow to light up its nights*, Science, v. 299, p.399.
- Taylor, G. I., 1921. *Tidal oscillations in gulfs and rectangular basins*, Proc. London Math. Society (2nd series), 20, 148–181.
- Trapp T. Watchorn M., 2001, *EB Development of Tidal Stream Energy*, The Institute of Marine Engineers, MAREC 2001 Conference, The Engineering Business Limited (www.engb.com), 6pp.
- Trapp T., 2002, *The Stingray Programme 2002*, The Engineering Business Limited, M02-151-01.doc, 4pp.
- United States Coastal Pilot, 1995, *Pacific and Arctic Coasts of Alaska*, NOAA, Washington, DC, 334 pp.
- Wunsch C., 1975, *Internal tides in the ocean*, Rev. Geophys. Space Phys., 13, 167–182.